THERMOMECHANICAL MILLING OF LITHICS
IN VOLCANIC CONDUITS

by

MICHELLE CAMPBELL

B.Sc. (Hons), McGill University, 2007

A THESIS SUBMITTED IN PARTIAL FULFILLMENT OF
THE REQUIREMENTS FOR THE DEGREE OF

MASTER OF SCIENCE

in

THE FACULTY OF GRADUATE STUDIES

(Geological Sciences)

THE UNIVERSITY OF BRITISH COLUMBIA

(Vancouver)

December, 2012

Abstract

Pyroclastic deposits resulting from explosive volcanic eruptions commonly contain clasts originating from the conduit wall rocks, which were entrained into the rapidly ascending stream of erupting material. These particles are termed accessory lithic clasts. Previous studies of the relative abundances and compositions of accessory lithic clasts have been used to identify the subsurface wall rocks of the volcanic conduit, to document variations in eruptive intensity, or to track changes in conduit or vent geometry over the course of the eruption. However, the morphological properties of accessory lithic clasts are largely ignored and offer an unused means of studying the processes operating in the conduit during explosive eruptions. During a volcanic eruption, wall rocks are violently fragmented to produce clasts that are incorporated into a hot, high velocity, particle-laden gas jet. There the clasts are subjected to elevated temperatures, blasting by volcanic ash, and occasional collisions with other large particles or with the conduit walls. The resultant morphologies of the accessory lithic clasts will be influenced by 1) the intrinsic physical properties of the clasts in question; 2) the specific physical and thermal processes to which the clasts were subjected within the conduit; and 3) the residence times of the clasts within the conduit. The 2360 B.P. Pebble Creek Formation of the Mount Meager Volcanic Complex in SW British Columbia is the product of the most recent explosive eruption in Canada. This formation includes a widespread pumice fallout deposit containing anomalously rounded and smoothed monzogranite accessory lithic clasts. In this study, I seek to explain the unusual shapes and surface textures of these clasts through detailed field work, analysis of sample morphology, and the computation of likely conditions within the conduit. My aim is to produce a comprehensive, mechanistic model of how these lithic clasts were reshaped within the volcanic conduit.

Table of Contents

List of Tables

List of Figures

List of Symbols

a	long axis
a_{image}	image major axis
b	intermediate axis
b_{image}	image minor axis
c	short axis
d	clast diameter
g	gravitational acceleration
m	molecular gas weight
n_f	exsolved weight fraction of gas
A_{convex}	image convex hull area
A_{image}	image area
A_{meas}	measured surface area
A_{proj}	projected surface area
A_{surf}	whole rock surface area
C	circularity
C_D	drag coefficient
C_{vx}	convexity
D	volcanic conduit diameter
E	ellipticity
H	height of volcanic plume
M_{dry}	dry mass
M_{wet}	wet mass
Md_φ	median grain diameter
M_f	mass flux
P	lithostatic pressure
$P_{ellipse}$	image ellipse perimeter
P_{image}	image perimeter
Q	universal gas constant
S_{max}	maximum surface smoothness
T	temperature
U_G	gas velocity
U_R	clast velocity relative to a fixed point
U_T	clast terminal velocity
V	sample volume
φ	phi
ρ_B	bulk density
ρ_c	clast density
ρ_g	gas density
ρ_m	magma density
ρ_s	sample density
ρ_w	water density
σ_φ	graphical standard deviation

Ψ_p	maximum projection sphericity
Ψ_t	true sphericity
masl	meters above sea level
B.P.	before present
Ka	thousand years
Ma	million years
MMVC	Mount Meager Volcanic Complex
PCF	Pebble Creek Formation
SEM	Scanning Electron Microscope
XRD	X-Ray Diffraction

Acknowledgements

First and foremost, I would like to thank my co-supervisors, Kelly Russell and Lucy Porritt, for all of their guidance, encouragement and feedback over the last two years. Kelly, thank you for all of your patience as my fledgling project began taking shape, for your eagerness to discuss any new findings with me, no matter how trivial, and for sharing your passion for volcanology. The only reason I chose this topic for my Masters project was because you seemed so amazed and fascinated by these weird round rocks; I think that fascination with the natural world is at the heart of all good science. Lucy, your uncanny ability to understand my half-formed ideas and poorly plotted data, and to somehow distill the most meaningful conclusions from them, has been greatly appreciated. Thanks for all of your insights, for your extremely prompt feedback, and for pushing me to the finish line.

I would also like to thank my third committee member, Bern Klein, for his valuable insights and discussions, and for bringing an engineer's perspective to the table.

Many thanks to James Welles for driving around Mount Meager with me, and most especially for all of your hard work in the lab.

A very appreciative thanks to all of my Volcanology & Petrology labmates from the last two years. I learned so much and received so much valuable feedback from all of you, but most importantly, you helped make my time at UBC some of the best years of my life. Special thanks to Alex Kushnir, for all of your encouragement and positivity during the last few hectic months.

I also gratefully acknowledge the funding for my Masters provided by the Fonds Québécois de Recherche sur la Nature et les Technologies, and a W.H. Mathews scholarship from the Department of Earth and Ocean Sciences.

To my Family,
for always encouraging my pursuit of science,

and to Daniel Norton,
for listening to me ramble on about round rocks
since the day we met.

1. Introduction

A volcano, in the simplest sense, is the intersection of magmatic material or gases with the surface of the Earth. As such, most studies of volcanoes have focussed on the magmatic products deposited around the volcano following the eruption. In reality, volcanic deposits may contain material from three different sources: (1) juvenile material, which originated from the erupting magmatic system; (2) accidental clasts, which were entrained from the Earth's surface by volcanic flows; and (3) accessory lithic clasts, which were country rock clasts ripped from the walls of the volcanic conduit and incorporated into the stream of erupting volcanic material (Wright et al., 1980). Each of these clast categories contains information relevant to the dynamics of volcanic eruption and emplacement.

In typical volcanological studies, the accessory and accidental lithic clast types present are mentioned in passing, by briefly listing major properties of the clasts such as the composition, the qualitative overall roundness (e.g. angular, subrounded), the size range observed, and the relative abundance estimates. Accessory lithics may also be used to infer the nature of the lithologies underlying the vent (e.g. Varekamp, 1993), and may include samples of hydrothermal systems or ancient volcanic landforms subsequently destroyed by the eruption (e.g. Pittari et al., 2008). The relative abundances of lithics have been used to distinguish different phases of a volcanic eruption, including vent opening and widening events (e.g. Druitt and Sparks, 1984; Rust and Cashman, 2007). The study of accessory lithics has also been used to gain insights into the evolution or migration of the volcanic vent during an eruption (e.g. Calder et al., 2000), and to make inferences about the fluctuations in mass discharge rates and conduit width over the course of an eruption (e.g. Wilson et al., 1980). Accessory lithic clasts can therefore provide valuable information about many parameters related to volcanic eruptions, but to date the information carried by accessory lithic clasts has not been fully explored. One important characteristic of accessory lithic clasts is particle morphology, although few if any studies have focussed on how morphology relates to volcanic processes.
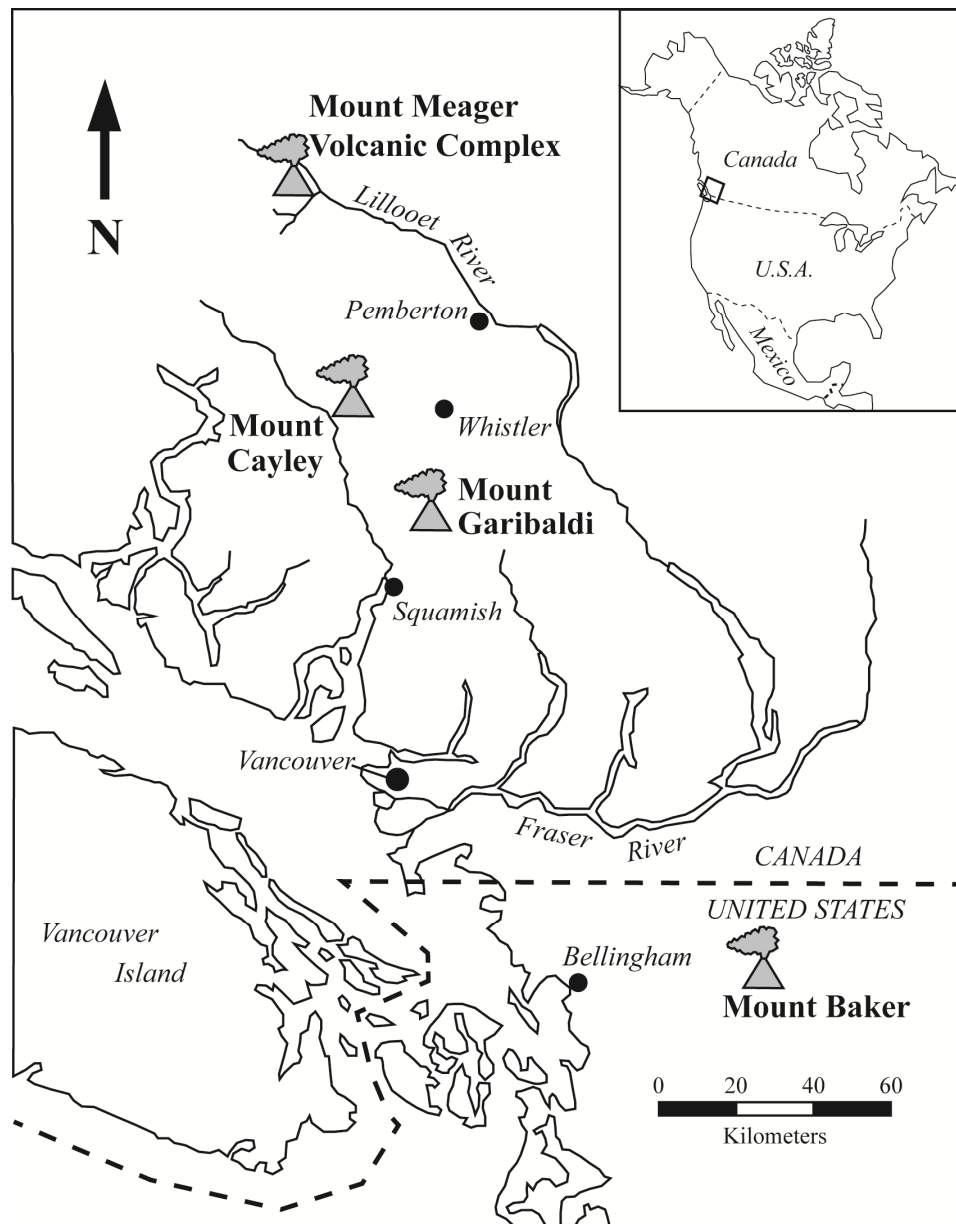
Figure 1-1. Location of the Mount Meager Volcanic Complex in southwestern British Columbia, Canada. Mount Meager, Mount Cayley, Mount Garibaldi and Mount Baker are located in the northernmost section of the Cascade Volcanic Arc.

The pumiceous pyroclastic fallout deposits of the 2360 B.P. Pebble Creek Formation of the Mount Meager Volcanic Complex, located in SW British Columbia (Figure 1-1), provide an exciting example of the potential usefulness of accessory lithics in our understanding of volcanic eruption dynamics. The initial phase of the 2360 B.P. event was an explosive, subplinian eruption that was similar in scale to the 1980 Mount St. Helens eruption. The most abundant type of accessory lithic

found in the Pebble Creek Formation fallout deposits is a suite of subangular, irregular and rough dacite lava clasts (Figure 1-2b), which originated from the 100 Ka Plinth Assemblage deposits directly underlying the vent of the 2360 B.P. eruption (Read, 1990). The relatively blocky, angular and rough nature of these clasts appears to correlate well to the traditional view of the incorporation of accessory lithics into the stream of erupting material, whereby lithic clasts are produced through violent fragmentation of the conduit wall and rapidly ejected from the vent. However, the fallout deposits of the Pebble Creek Formation also contain a very peculiar type of accessory lithic clast: anomalously rounded and smoothed clasts of monzogranite (a type of granite), sourced from the basement rocks underlying the Plinth Assemblage (Figure 1-2a). Although pyroclastic density current deposits may contain highly rounded lithic clasts, scoured from stream beds or till deposits (i.e. incorporated accidental clasts), pyroclastic fallout deposits do not entrain significant quantities of accidental clasts. The monzogranite clasts also have very fresh appearances, and do not feature chemically altered or partially melted rinds. Therefore, the morphologies of these highly rounded and smoothed accessory lithic clasts must be the result of mechanical processes operating within the volcanic conduit, in addition to thermal effects caused by the exposure of the clasts to intense heat within the conduit. The conduit processes which acted upon these clasts also did so during a very limited timeframe: from the moment that they were ripped from the walls of the conduit, to their final ejection from the volcanic vent.

During a subplinian eruption, a stream of gas, ash, pumice and rock clasts exits a volcanic conduit at high velocities (100's of m/s) to form an expanding column above the volcanic vent. The hot, particle-laden jet within the volcanic conduit would act on any entrained accessory lithic clasts, subjecting them to a combination of physical processes, including mechanical reshaping (sandblasting by ash and small pumice clasts, fractures caused by collisions with lithic clasts or the conduit walls) and thermal effects. The unique morphological features of the accessory lithic clasts represent a 'textural fingerprint' reflecting these specific processes. In addition to the influence of the intrinsic physical properties of the clasts, the extent of clast rounding is expected to be a function of the intensity and effectiveness of the volcanic comminution processes which affected these clasts, as well as the residence times of these clasts within the volcanic conduit. The textural fingerprints of accessory lithics may therefore provide insights into eruption conditions and conduit processes. Thus, the study

of accessory lithic morphology could potentially have great uses for forensic volcanological studies. Here, I present a detailed study of the morphological properties of the two main accessory lithic types from the 2360 B.P. eruption of the Mount Meager Volcanic Complex, with the aim of understanding the processes that have influenced the morphologies of the clasts.
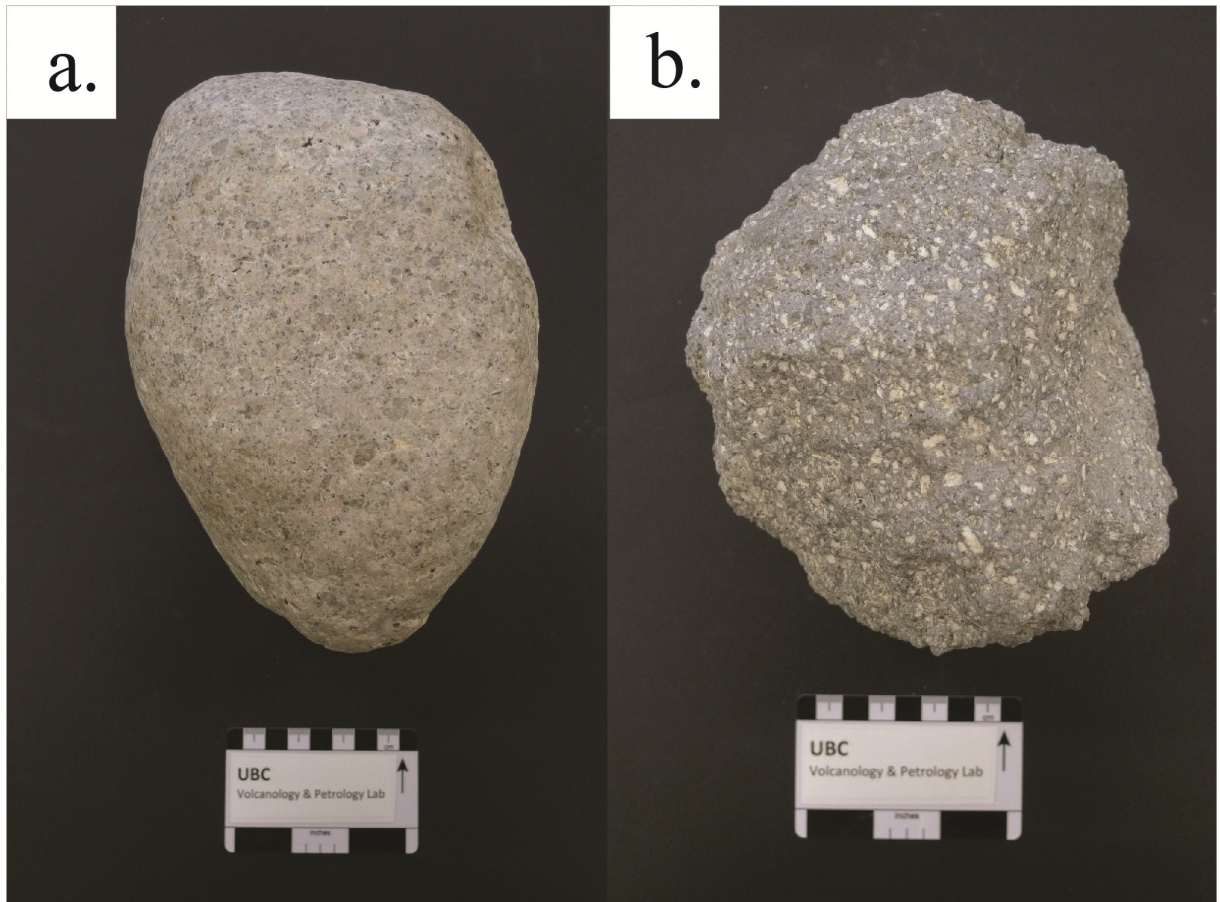
Figure 1-2. Accessory lithic clasts from the Pebble Creek Formation fallout deposits. a) Monzogranite clast displaying high degrees of smoothing and rounding. b) Dacite clast exhibiting typical subangular shape and rough surface texture.

1.1 Research Objectives

The first goal of this research project is to provide thorough, quantitative descriptions of the morphologies of the two most abundant accessory lithic clast types from the Pebble Creek Formation fallout deposits: the rounded and smoothed monzogranite clasts, and the subangular and rough dacite

4

clasts. These properties consist of all relevant aspects of morphology, including: size, form, sphericity, surface roughness, and any macroscopic or microscopic surface textures observed.

The second goal of this study is to understand the mechanical and thermal processes which produced the final morphologies of these two clast types. Attaining this objective requires estimates of the depths at which these clast types were incorporated into the flux of erupting material, of the residence times and relative velocities of these clasts within the volcanic conduit, and of the thermal equilibration timescales of these clasts.

The final objective of this study is the generation of a comprehensive, mechanistic model of how accessory lithics were reshaped within the conduit of the 2360 B.P. eruption of the Mount Meager Volcanic Complex, which may then be applied to the deposits of other volcanoes. Therefore, an important subset of this objective is the explanation of how a single overall process (the 2360 B.P. eruption of the Mount Meager Volcanic Complex) produced two suites of accessory lithic clasts with such vastly differing morphological features, and what influence intrinsic rock properties and conduit residence time has on the final clast morphology. To date, no scientific studies have linked quantitative accessory lithic morphology data to processes operating within the volcanic conduit. This model will be the first to do so, combining the morphological and textural data gathered from the lithic clasts with our understanding of the mechanical and thermal processes operating within the volcanic conduit, in order to explain how the clasts were reshaped within the volcanic flux.

1.2 Thesis Outline

Chapter 2 contains a literature review of the existing systems used to quantify the morphologies of rock clasts, of the natural processes known to reshape rock clasts, and of volcanic processes that have previously been documented to produce clast rounding.

Chapter 3 is a review of the field area of this study, the Mount Meager Volcanic Complex. This includes descriptions and stratigraphic relationships of the various lithological units present in the Pebble Creek Formation, the pre-Pebble Creek Formation volcanic deposits, and the basement rocks.

Chapter 4 contains the results of the field work conducted for this study, including graphic logs, grain size distributions and componentry data for outcrops of the Pebble Creek Formation fallout deposits and lithological descriptions of the clast types present in the fallout deposits.

Chapter 5 presents the results from the morphological analysis of the two most abundant accessory lithic clast types in the Pebble Creek Formation fallout deposits: the Plinth Assemblage dacite and the Fall Creek Stock monzogranite. Morphological analyses included the quantification of the mass, density, volume, form, ellipticity, circularity, convexity, sphericity and surface roughness of the clasts, and the qualitative assessment of macroscopic and microscopic surface textures. The effect of the exposure of the clasts to sudden, intense heat is also discussed.

In Chapter 6, the implications of the field and morphological results from this study are discussed. Velocities of the clasts within the volcanic conduit during the eruption are computed, along with the approximate residence times of clasts incorporated at various depths within the conduit. A mechanistic model of accessory lithic reshaping within the volcanic conduit is then presented, which combines the morphological clast data with the computed conduit velocities and residence times.

Finally, Chapter 7 reviews the main findings and conclusions from this research, and summarizes the important implications for conduit dynamics from this study.

2. Morphology and Rounding of Lithic Clasts

Morphology is a term that encompasses the entire outward appearance of an object and, in geology, is a fundamental property of all clastic particles. Natural processes leave a variety of morphological imprints on rock surfaces. There have been two main approaches to the investigation of rock clast morphology. The empirical approach involves the analysis of clasts from known environments (e.g. Ehlmann et al., 2008; Van Hoesen and Orndorff, 2004), whilst the experimental approach employs apparatuses such as rock tumblers to experimentally recreate rounding processes analogous to natural ones (e.g. Attal and Lavé, 2009; Kuenen, 1956). Both of these approaches require methods to fully describe the external appearance of the clasts. The following section reviews the systems devised for the qualitative and quantitative description of clast morphology.

2.1 Clast Morphology

There are a variety of systems designed to describe and quantify clast morphology, which are usually based on a set of distinct, measurable features (Krumbein, 1941; Sneed and Folk, 1958; Wadell, 1932; Wentworth, 1919; Winkelmolen, 1982). A simplified classification system of clast morphology was provided by Barrett (1980), who postulated that external morphology could be expressed as three main features: form, roundness and surface texture. The term form is used, in the sense described by Sneed and Folk (1958), for the overall shape of a particle, independent of roundness or surface roughness. Form relates principally to the ratios between the three orthogonal main axes (long, intermediate and short) of a clast. Roundness relates to the corners, edges and faces of the clast, and how pointed, linear or planar these features are. Surface texture encompasses overall surface roughness, as well as any characteristic textural marks. Form, roundness, surface texture and size are all independent properties which can describe the full range of variations in clastic particle morphology (Figure 2-1) (Barrett, 1980). However, clast modification due to a given natural process may affect two or more of these features simultaneously. A fourth feature of morphology, size, is also an important parameter in the study of any clast population.

To date, few volcanological studies have focussed on the properties of the lithic clasts found within volcaniclastic deposits (e.g. Calder et al., 2000; Mellors and Sparks, 1991; Rust and Cashman,

2007), and even within these, the descriptions of particle morphology have been quite limited and qualitative. Clast form might be described by such terms as equant, elongate, tabular or platy. Degree of roundness might be described as angular, subangular, subrounded or rounded. Modern textbooks and field reference guides still contain the charts developed by Krumbein (1941) and Powers (1953) to visually assign numerical roundness and sphericity values to clasts, a semi-quantitative method at best. Surface textures are oftentimes not mentioned.

Advances in computer sciences and image analysis techniques during recent decades have allowed for quantitative morphological data to be collected on a scale not previously possible. Early authors relied on metrics that measured only the form of a particle, for example the ratios between the three orthogonal axes of a clast (e.g. Sneed and Folk, 1958; Wadell, 1932). More recent methods include the 2-D and 3-D shape quantification of clasts. 2-D shape quantification involves the analysis of photographs of clasts, where the outlines of the clasts found on an image are digitally detected and traced using computer software. The digital clast outlines may then be used to generate metrics based on geometrical parameters of each clast, which relate to the dimensionality or roundness of each clast (e.g. Durian et al., 2007; Manga et al., 2011; Roussillon et al., 2009). Alternatively, methods such as Fourier grain shape analysis may be employed to generate complex mathematical characterizations of the clast contours (e.g. Bowman et al., 2001; Diepenbroek et al., 1992; Hu and Stroeven, 2006). Economical 3-D imaging techniques have only recently become available. 3-D laser scanners may be used to digitally replicate the full external morphology of lithic clasts. The produced 3-D shape files can then be analyzed in order to precisely measure parameters, such as the surface area of the scanned sample, as well as metrics relating to these parameters (Anochie-Boateng et al., 2011; Hayakawa and Oguchi, 2005). Furthermore, a variety of different techniques have been employed to generate 3-D profiles of a discrete region of a rock sample's surface, including 3-D laser scanning (Ehlmann et al., 2008), digital photogrammetry (Lee and Ahn, 2004) and profilometry (Develi et al., 2001). These scanned regions are used to characterize the surface topography and overall roughness of the sample in question.

In order to fully characterize the morphology of a sample set, it is necessary to obtain quantitative data relating to as many aspects of morphology as possible. A basic understanding of the natural rounding processes that affect lithic clasts is also necessary to understand the development and

significance of clast morphology. In the following section (Section 2.2), I review the literature on: (1) natural mechanical processes which commonly alter clasts morphologies, (2) thermochemical processes that can affect clast morphology, and (3) the characteristic textural features imposed on clast surfaces by these natural processes. In the subsequent section (Section 2.3), I will review the existing literature on rounding processes in volcanic systems.
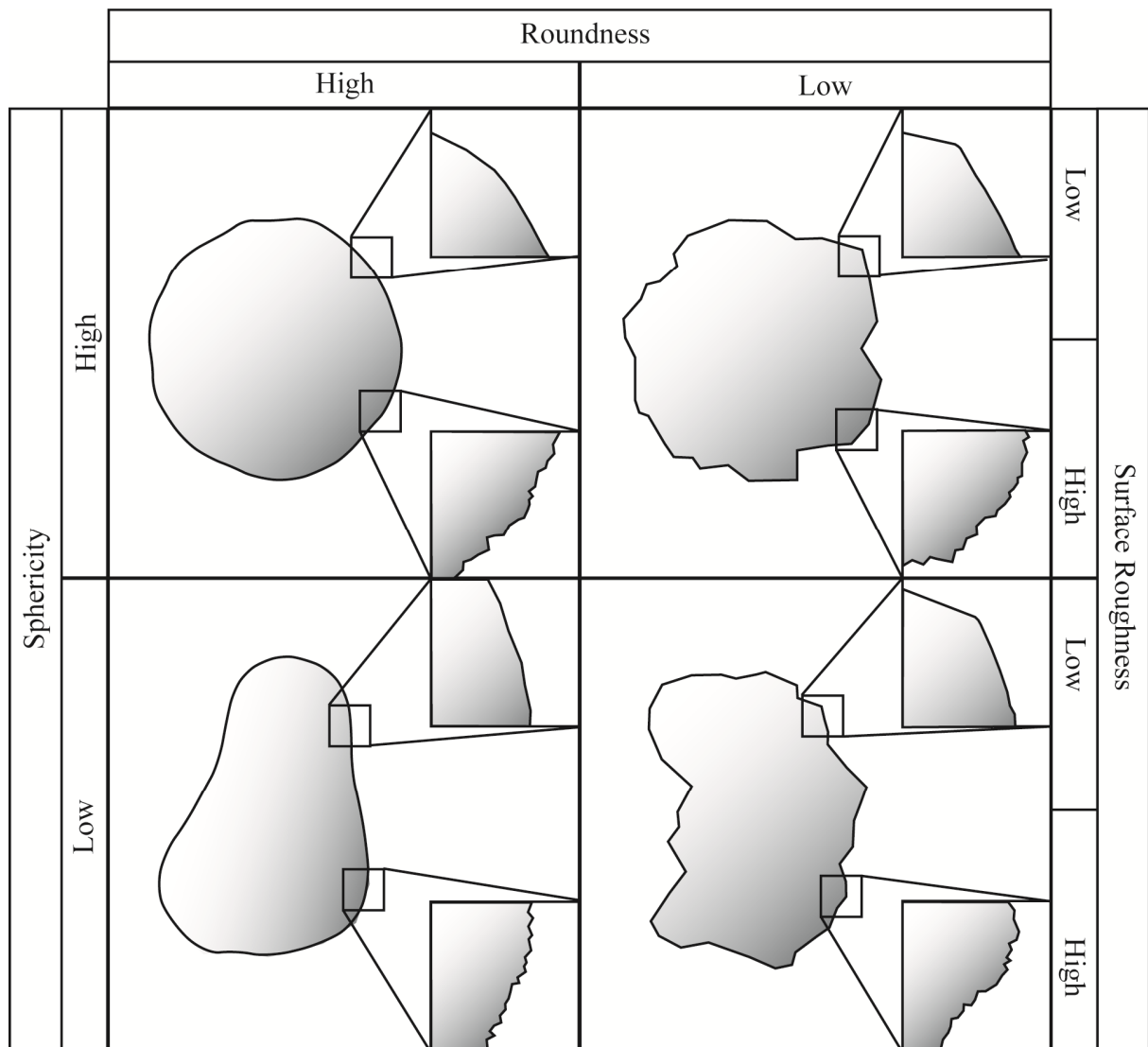
Figure 2-1. Comparison of the mutually independent morphology characteristics of sphericity, roundness and surface roughness.

2.2 Natural Rounding Processes

In sedimentology, the terms "immature" and "mature" are often applied to a given clast population. The term immature applies to clasts or particles which are blocky, angular and rough; the implication (and source of the word immature) is that these are relatively young clasts, having either only recently broken apart from their host rock source, or having undergone little movement or weathering since this event. Mature clasts, on the other hand, are relatively rounded and smoothed when compared to their immature counterparts, and have likely been extensively transported or weathered. A variety of different natural processes are capable of transforming a rough and angular particle into a smooth and rounded one, including the actions of rivers, oceans, wind, glaciers, weathering processes, etc. Intuitively, anyone who has ever walked upon a beach covered in pebbles of relatively uniform shape, roundness and smoothness might also guess that specific environments produce characteristic morphological imprints upon the clasts that they affect. Sedimentologists have long sought to identify surficial imprints which might allow one to determine the exact provenance and erosional history of a clast observed out of geological context. Such relationships would greatly facilitate the interpretation of paleodeposits and paleoenvironments.

The natural mechanisms capable of affecting rock clast morphology can be divided into two broad categories: (1) mechanical processes, and (2) thermal or chemical processes, which I will collectively refer to as thermochemical processes. Overviews of the types of mechanisms associated with each of these two categories, and the typical morphological expressions of these mechanisms, are found in the following subsections.

Term	Definition
Comminution	The gradual diminution of a substance to a fine powder or dust by crushing, grinding, or rubbing.[1]
Abrasive Wear, or Abrasion	Wear due to hard particles or hard protuberances forced against and moving along a surface.[2] The mechanical wearing, grinding, scraping, or rubbing away (or down) of rock surfaces by friction and impact, in which the solid rock particles transported by wind, ice, waves, running water, or gravity are the tools of abrasion.[1]
Abradant	A material that is producing, or has produced, abrasive wear.[2]
Impingement	A process resulting in a continuing succession of impacts between (liquid or solid) particles and a solid surface.[2]
Solid Impingement Erosion	Progressive loss of original material from a solid surface due to continued exposure to impacts by solid particles.[2]
Blasting	Abrasion or attrition effected by the impact of fine particles moved by wind or water against or past an exposed, stationary surface.[1]
Sandblasting	A type of blasting in which the particles are hard mineral grains (usually quartz) of sand sizes.[1]
Disruptive Collision	High-energy collision between a clast and an impacting particle, producing a fragment > 25% of the original volume of the clast.[3]
Non-Disruptive Collision	Low-energy collision between a clast and an impacting particle, resulting in a loss of $\leq$ 25% of the original volume of the clast.[3]
Exfoliation	The process by which concentric scales, plates, or shells of rock, from less than a centimeter to several meters in thickness, are successively spalled or stripped from the bare surface of a large rock mass. It is caused by physical or chemical forces producing differential stresses within the rock, as by expansion of minerals as a result of near-surface chemical weathering, or by the release of confining pressure of a once deeply buried rock as it is brought nearer to the surface by erosion (pressure-release jointing). It often results in a rounded rock mass or dome-shaped hill.[1]
Spheroidal Weathering	A form of chemical weathering in which concentric or spherical shells of decayed rock (ranging in diameter from 2 cm to 2 m) are successively loosened and separated from a block of rock by water penetrating the bounding joints or other fractures and attacking the block from all sides. Synonyms: onion-skin weathering; concentric weathering.[1]
Spalling	The separation of macroscopic particles from a surface in the form of flakes or chips.[2]
Spall	Chip or flake produced via spalling.

Table 2-1. Glossary of terminology related to clast morphology modification. Definitions are taken from: [1] Neuendorf et al. (2011) , [2] ASTM Standard (2010), and [3] Dufek et al. (2012). The first 9 terms are related to mechanical processes that lead to the breakup of lithic clasts, while the last 4 terms relate mainly to thermochemical processes.

2.2.1   Mechanical Processes

The evolution of the shape of a clast or particle through mechanical processes can be viewed as a succession of breakages or surficial cuts or fractures of the body that remove a given amount of material (Durian et al., 2007). These processes involve brittle failure of parts of the clast caused by physical contact with other solid particles, converting young, polyhedral-like clast shapes with a small number of large sides and sharp corners and edges into more mature shapes with a relatively high number of small sides and smooth vertices (Durian et al., 2007). A variety of different natural mechanical breakage processes exist (see Table 2-1 for a glossary of terms relevant to mechanical wear), operating in a wide range of different environments. For example, cobbles on a beach will rub against each other as the waves come in and out, gradually becoming rounder by the resulting abrasion, clasts in a desert environment will become smoothed by the action of sandblasting, and clasts in a rock avalanche will energetically impact each other, breaking into multiple large fragments.

Clearly, the overall energy of the particle-particle interaction has an important influence on the resulting morphologies of the impacted clasts. Relatively low-energy collisions that result in the loss of a small amount of the volume of the impacted clast are termed "non-disruptive collisions," while relatively high-energy collisions that result in the loss of a larger amount of the impacted clast's volume, potentially breaking the clast into many small fragments, are termed "disruptive collisions" (Dufek et al., 2012). Dufek et al. (2012) defined non-disruptive collisions as those resulting in a loss of $\leq$ 25 % of the original volume of the clast, and disruptive collisions as those resulting in a loss of > 25% of the original clast volume. Whether two lithic particles will undergo a disruptive or non-disruptive collision is a function of the strength and intrinsic physical properties of the particles (i.e. composition, grain size, degree of weathering or alteration, textures, structures, etc.) and the energy of the impact. The energy associated with a collision between particles is, in turn, a function of the relative velocities and sizes of the particles. The number of collisions suffered by a clast, which is proportional to the duration of the exposure of the clast to the process or environment in question, will also have a great influence on final particle morphology. For example, an angular clast placed on a beach will not differ perceptibly after a day, but might become substantially rounder after many years.

In summary, the morphological imprints that are borne by a lithic clast affected by mechanical processes are a function of three parameters: (1) the intrinsic properties of the clast; (2) the properties

of the external processes that have affected the clast; and (3) the duration of the clast's exposure to these processes, i.e. the residence time of the clast within a certain environment.

2.2.2   Thermochemical Processes

The morphologies of lithic particles are not solely affected by mechanical processes; they are also subject to modification by heat and fluids. Thermochemical processes do not involve physical contact with other solid particles, but instead involve the loss of lithic material through mechanisms such as dissolution by a fluid, etching via acidic fluids, brittle failure due to thermal stresses, or melting via proximity to a heat source. Table 2-1 contains a glossary of some important terms related to the thermochemical modification of lithic clast morphology. One notable process which may lead to the formation of rounded clasts is exfoliation, which is the detachment of flakes or plates from a rock body (Ollier, 1971). The best known geological example of exfoliation is spheroidal weathering, also known as onion-skin weathering, which is the transformation of a competent rock mass to a series of concentric shells around a central corestone (Ollier, 1967, 1971). Spheroidal weathering is thought to be due to the cyclic infiltration of water along joint surfaces in rock masses, which causes a "weathering front" to progressively infiltrate the rock via a series of chemical reactions (hydration, solution, hydrolysis and oxidation) (Arribas et al., 2007; Mabbutt, 1961). Spheroidal weathering typically occurs in hard, uniform lithologies such as granite, dolerite, basalt, gabbro, and sandstone (Ollier, 1971). The concentric shells characteristic of spheroidal weathering are typically a few mm or cm thick, and may be highly decomposed, or relatively fresh (Arribas et al., 2007). Similarly, the rounded central corestone may be quite altered, but there is often a very abrupt change between a relatively hard and fresh corestone and the surrounding altered concentric shells (Ollier, 1971).

It has long been noted that the exposure of rock clasts to sudden intense heat is also capable of exfoliating, or spalling, rock clasts (e.g. Norton, 1925). For example, wildfires have been observed to cause the exfoliation of large boulders (Blackwelder, 1926; Dorn, 2003). This exfoliation typically occurs via the formation of 1-5 cm thick spalls, which commonly taper to a thin edge (Blackwelder, 1926). Following the onset of a volcanic eruption, the wall rocks surrounding the volcanic conduit are suddenly exposed to a tremendous amount of heat (temperatures exceeding $1200^{o}C$ for certain

magmatic compositions). Therefore, the effects of thermal stresses on accessory lithic clasts should not be ignored. The process and effects of thermal spalling are discussed in the following subsection.

2.2.2.1 Thermal Spalling

Definitions of spalling in the literature enclose a variety of types of fracturing of the material in question, from fine-grained disintegration of the sample, to the formation of small surficial chips, to the development of large fractures through the entire specimen (e.g. Norton, 1925; Ollier, 1971). For the purposes of this study, I define spalling as the sudden explosive emission of chips or flake-shaped particles ("spalls") from the surface of spallable materials, which include rocks, ceramics and brick (Table 2-1).

Early studies of thermal spalling often investigated the spalling of industrial materials such as bricks and ceramics. Norton (1925), who investigated the thermal spalling of firebricks, noted that a typical spalling fracture on the exposed corner of a brick showed an approximately spherical surface; he proposed that this demonstrated that spalling fractures occur along isothermal surfaces within the sample. Preston and White (1934) studied the thermal spalling of ceramic spheres. They found that ceramic spheres introduced into an oven at 815°C emitted multiple small, thin spalls, while those introduced into an oven at 760°C emitted fewer, thicker spalls. Furthermore, at 930°C, violent spalling was observed, while a paucity of spalling was noted for those spheres introduced into an oven at only 540°C. Preston and White (1934) proposed that the sudden heating of these spheres caused their rinds to be in a state of tangential compression and their cores to be in a state of radial tension. Strain building up within the sphere could then be partially released by the separation of the rind from the core: in essence, by spalling.

In an early investigation of the spalling of rocks, Thirumalai (1969) attempted to induce spalling in three different rock types (quartzite, granite and basalt), using an oxyhydrogen torch. In this study, continuous thermal spalling of the quartzite samples was found to be easily attained, while the thermal spalling of the granite samples would be intermittently disrupted by the onset of partial melting of the surface layer; mechanical removal of the melt on the surface was necessary to maintain progressive spalling. No spalling was achieved with the basalt samples, which simply melted at all experimental conditions. Two scanning electron micrographs of the thermally spalled surface of a

quartzite sample were included in Thirumalai (1969); these micrographs appear to indicate that smooth areas of failure occurred during spalling. Rauenzahn and Tester (1989) also investigated the thermal spalling of rocks. Although they focused their experimental studies on granite samples from two sources, the Westerly granite and the Barre granite, they included a list of various rock types along with their respective physical properties and spalling ratings. These ratings range from Poor/Fair (e.g. basalt, marble, schist, tuff) to Good/Excellent (e.g. dolomite, quartzite, and quartz-rich varieties of granite, gneiss and diorite). The presence of quartz appears to have a significant effect on the spallability of rocks. Other rock spalling papers have presented studies of topics such as the influence of steam pressure on the spalling of sedimentary rocks (Hettema et al., 1998), and the acoustic emissions associated with thermal cracking of quartz-bearing rocks (Glover et al., 1995). However, to date no studies have been published on the effects of thermal spalling on the clasts of explosive volcanic deposits, or focused on the microscopic textural appearance of spalled surfaces.

2.2.3   Common Natural Textural Imprints on Rock Surfaces

Sedimentologists have long sought to identify surface textures of rock particles that are diagnostic of a given process. The advent of the scanning electron microscope (SEM) in the 1960's allowed for detailed, high resolution studies of the microscopic surface features of lithic particles that were previously impossible. A few studies have been published on the microscopic surface textures of pebbles or cobbles in natural rounding environments (e.g. Caballero and Capra, 2011; de Vries Klein, 1963; Judson and Barks, 1961; Krinsley and Donahue, 1968; Pearce, 1971; Van Hoesen and Orndorff, 2004). However, to date, studies of diagnostic sedimentary surface features have focussed primarily on individual quartz grains from various environments (e.g. Brown, 1973; Bull, 1981; Bull et al., 1987; Culver et al., 1983; Krinsley and Doornkamp, 1973; Mahaney, 2002; Mahaney et al., 2001; Margolis and Krinsley, 1974). The study of the textures produced by natural processes on a single mineral species, as opposed to whole rocks, greatly simplifies matters, as grains of a single mineral have roughly uniform intrinsic properties (Marsland and Woodruff, 1937).

#	Microscopic Surface Feature	Subaqueous			Aeolian			Glacial			Regolith & Weathering		
		Low Energy	Medium Energy	High Energy	Coastal	Tropical	Periglacial	Continental	Marine	Fluvial	Temperate	Tropical	Marine
1	Small blocks (< 1μm)					■	■						
2	Small conchoidal fractures (< 1μm)		■		■	■							
3	Large blocks (> 1μm)										■		
4	Large conchoidal fractures (> 1 μm)			■							■		
5	Straight scratches		■		■								
6	Curved scratches	■		■	■					■			
7	Striations									■			
8	Step-like fractures												
9	Arc steps										■		
10	Meandering ridges			■	■		■	■	■	■			
11	V-shaped impact pits	■								■			
12	Fracture plates (crack propagation)												
13	Angular outline	■	■		■	■							
14	Rounded outline								■	■	■	■	
15	Low relief (< 0.5 μm)		■	■					■				
16	Medium relief	■						■					
17	High relief (> 1 μm)		■		■		■						■
18	Oriented etch pits			■	■					■			
19	Irregular pitted surface					■	■	■	■				
20	Diagenetic etching						■	■		■			
21	Smooth fracture surfaces						■		■	■			
22	Crystal overgrowth												

Table 2-2. Modified from Margolis and Krinsley (1974). Summary of the environmental occurrence of 22 common microscopic surface features visible on quartz grains. Features #1 to 12 are mechanical in origin, #13 to 17 represent the grain's outline and relative surface relief, and features #18 to 22 are chemical in origin. Descriptions of each of the 22 surface features are found in Margolis and Kennett (1971). Solid black infill indicates that > 75% of the grains analyzed from this environment displayed the surface feature; solid gray infill indicates that 25 – 75% of the grains displayed the feature; small black squares indicate that 5 – 25% of the grains displayed the feature; and blank squares indicate that < 5% of the grains displayed the feature.

Quartz, as a relatively abundant mineral, widespread in nearly every environment and resistant to both mechanical and chemical breakdown, is a logical candidate for extensive study (Bloss and Gibbs, 1963; Bull, 1981). Table 2-2 contains a selection of the most common surface texture features identified on quartz grains via scanning electron microscopy, along with the main environments associated with each textural class (Margolis and Krinsley, 1974). The features listed in Table 2-2 are separated into three categories: relative relief, mechanically-derived features and chemically-derived features. Due to the relative paucity of studies documenting the typical surface features on pebble- to cobble-sized rocks, terminology borrowed from this study of quartz grain surface features will be utilized to characterize the microscopic surface features observed on the samples from this study.

One key observation that can be made from Table 2-2 is that most of the observed textures can be created in multiple environments, and presumably by different specific processes. This issue is termed the problem of equifinality of textures (Bull, 1981). Thus, it is important to keep in mind that specific textures may not be indicative of only a single process or environment.

2.3 Volcanic Rounding Processes

The rounding processes that occur in volcanic settings have certain similarities and certain differences with rock rounding processes occurring in other environments. Firstly, the most common abradants in both settings are lithic particles. The main types of abradant in explosive silicic eruptions will be shards of volcanic glass (ash) and pumice lapilli and blocks, along with fragments of country rock. The main abradant types in other environments, for example fluvial, littoral or glacial, will vary depending on the location and energy of the environment, but will commonly be composed of competent rock fragments or crystals, and will rarely be composed predominantly of volcanic ash and pumice. The non-disruptive solid impingement erosion of accessory lithic clasts by ash (i.e. ash-

blasting) within the volcanic conduit may be analogous to the non-disruptive solid impingement erosion of rocks by sand grains (sandblasting) caused by aeolian action, for example in desert environments. Ash-blasting may, however, occur at significantly higher impact velocities, up to several hundred meters per second. A certain number of disruptive collisions are also to be expected during a volcanic eruption, as relatively large particles (large pumice or accessory lithic clasts) impact one another or impact the walls of the conduit at high velocities.

One significant additional consideration about particles incorporated into the stream of erupting material during a volcanic eruption is that these particles are subjected to very high temperatures for a finite period of time. Therefore, the potential effect of thermal modification to particle morphology should not be overlooked.

2.3.1   Volcanic Rounding: Literature Review

To date, no studies have specifically addressed the shaping or rounding of accessory lithic clasts within a volcanic conduit. A variety of other forms of volcanic rounding, or processes which reshape volcanic clasts, have however been described in the literature. Here, I have subdivided the existing literature into three categories, according to the type of material being reshaped: (1) juvenile clasts, (2) xenolithic and xenocrystic material, and (3) lithic clasts.

2.3.1.1 Juvenile Clasts

As magma rises through a volcanic conduit, the volatiles it bears will begin to exsolve and expand, with vesiculation increasing as the magma continues rising. Eventually, the magmatic material in the conduit transitions from a frothy, highly viscous liquid to a turbulent particle-laden gas traveling at velocities up to the speed of sound. This transitional zone is referred to as the fragmentation front, or fragmentation level (e.g. Parfitt and Wilson, 2008) (Figure 2-2). The discrete particles formed at the fragmentation front are termed juvenile clasts, and typically include rock types such as pumice and scoria. The size distribution of the particles in volcaniclastic deposits has previously been attributed to this initial fragmentation (Büttner et al., 2006; Wohletz et al., 1989). However, Dufek et al. (2012) argue that the confined nature of the volcanic conduit, along with the high particle density and high particle velocities, mean that a large number of particle collisions and associated comminution are

likely to occur as the juvenile clasts ascend through the volcanic conduit. The authors combine experimental data with analytical and numerical simulations to show that disruptive collisions can severely affect the primary grain size distribution of the pumice particles generated at the fragmentation front, depending on the depth of this front. For example, less than 2% of the original 10 cm size pumice clasts formed at a 3 km deep fragmentation front are predicted to exit the vent intact (i.e. without having undergone any disruptive collisions) (Dufek et al., 2012).

A significant amount of work has been conducted on the fragmentation and comminution of ash-sized particles in volcanic systems (Dufek and Manga, 2008; Heiken, 1972; Walker, 1981). SEM imaging and descriptions of volcanic ash have also been conducted by multiple studies, which have shown that ash-sized volcanic particles are typically quite angular and irregular, and include glass shards from broken bubble walls, equant mineral grains, and small pumice clasts (Heiken, 1972; Heiken and Wohletz, 1985; Riley et al., 2003; Rose et al., 1973). The nature of ash-sized volcanic particles is potentially important to the study of accessory lithic reshaping, as they are the dominant abradant particles in volcanic systems.
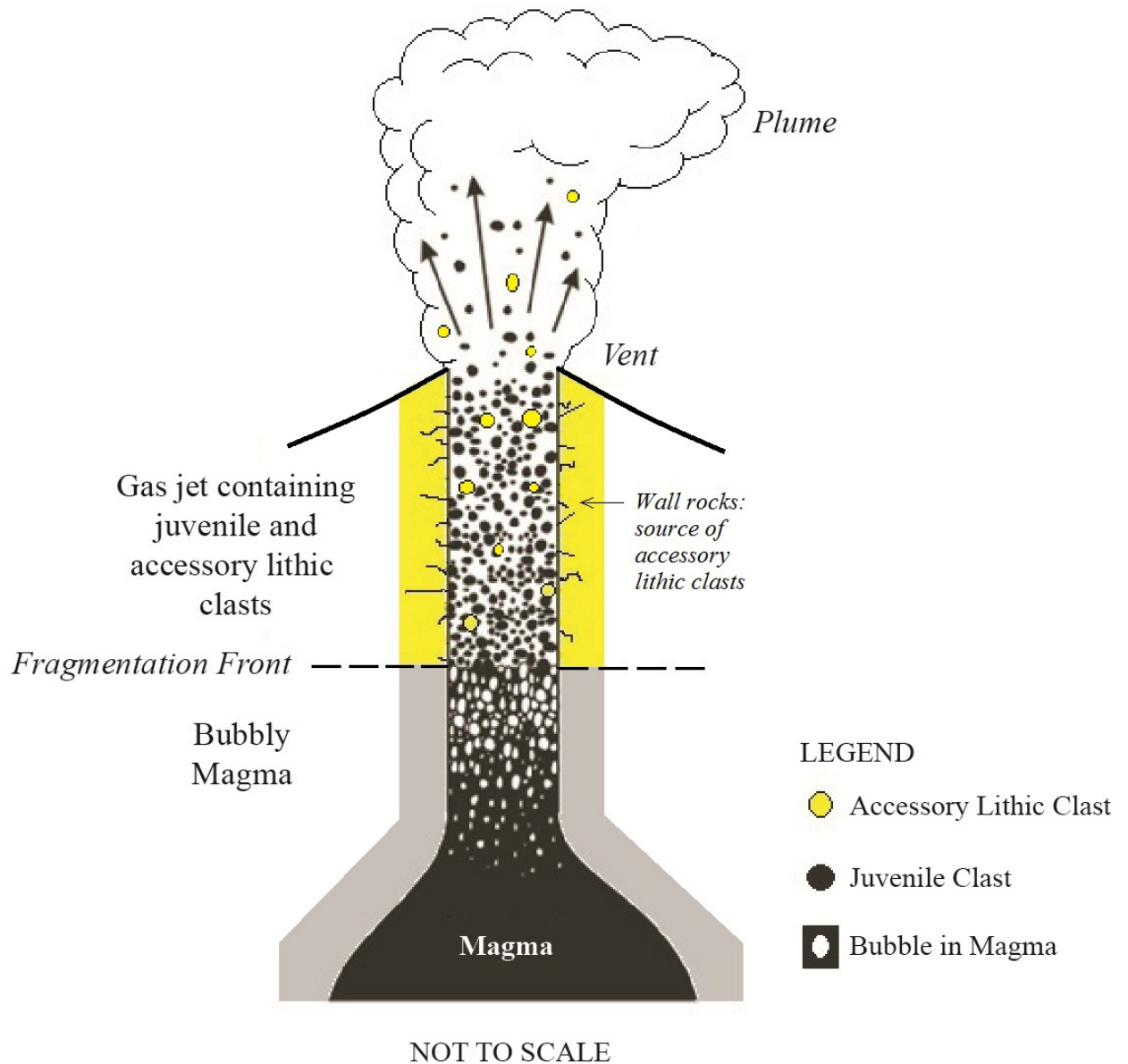
Figure 2-2. Schematic diagram of a volcanic conduit, illustrating the fragmentation front. Modified from Mastin (2002).

The behaviour of juvenile clasts following their ejection from the vent largely depends on the post-fragmentation properties of the erupting magma, including parameters such as the magma's composition and volatile content, and the size of the clast. Juvenile clasts from mafic systems may become highly rounded, but not necessarily due to mechanical process. For example, Pele's tears and spheres are small mafic juvenile clasts whose highly rounded morphologies are usually ascribed to the effects of viscous relaxation and surface tension forces on molten clots (Porritt et al., 2012; Walker and

Croasdale, 1971). Carracedo Sánchez et al. (2009) also described composite spheroidal bombs present at Cabeza Seguro volcano, Spain; the authors postulate that these rounded clasts formed via the agglutination and welding of non-vesicular juvenile droplets within the volcanic conduit. Otherwise mafic clasts may be breadcrusted, or be fragmented upon deposition, but usually do not undergo extensive reshaping or remobilization immediately following deposition. The very high-energy events associated with large-volume, explosive felsic eruptions, however, allow for more clast reshaping opportunities outside of the vent. The rounding of pumice clasts from pyroclastic density currents has been used to demonstrate the occurrence of significant transport and abrasion within these currents (e.g. Wilson and Hildreth, 1998). Manga et al. (2011) performed a series of laboratory experiments, tumbling natural pumice clasts in a rock tumbler, to study the effects of prolonged mechanical wear on pumice. The aim of the study was to reproduce the comminution and abrasion experienced by pumice clasts within pyroclastic density currents, and to establish an empirical relationship between the mass lost from the clasts and their final degree of roundness. Dufek and Manga (2008) found that the tumbled clasts consistently became progressively rounder up to a certain steady degree of roundness. This maximum degree of roundness was dependent on the lithological properties of the clasts being tumbled (Manga et al., 2011).

Finally, the morphologies of juvenile volcanic clasts can also be modified following deposition, long after the eruption, by surficial remobilization and resedimentation processes (Carey et al., 2000; Carey and Sigurdsson, 1978). These post-depositional processes tend to increase the roundness of the modified clasts, at least for relatively fragile clasts such as pumice, by decreasing their surface roughness and decreasing their shape complexity (Carey et al., 2000; Carey and Sigurdsson, 1978).

2.3.1.2 Xenoliths

Xenoliths and xenocrysts are rock fragments and single crystals, respectively, which have been incorporated into a host magma body from an outside source. Xenoliths may originate from the mantle ('mantle xenoliths'), or from any part of the crust through which the magma body in question contacted ('country rock xenoliths'). Mantle xenoliths and xenocrysts are typically found in mafic to ultramafic intrusive or volcanic bodies, such as basalts, kimberlites, or carbonatites, and are typically

subrounded to rounded (e.g. Brett et al., 2009; Dawson et al., 1970; Guest et al., 1995). However, it is unclear whether the roundness of these mantle xenoliths is due to mechanical or thermochemical processes operating during the magma's long ascent to the Earth's surface. Country rock xenoliths occur in intrusive and extrusive rocks of all composition types, and vary from angular to rounded in shape (e.g. Shamberger and Hammer, 2006). This variability in morphology likely depends on a range of factors, such as the lithology and intrinsic properties of the clasts, to the depth of the clasts' incorporation into the magma, and the temperature and composition of the magma. Many crustal xenoliths show significant degrees of melting, dissolution or chemical alteration induced by their host magmas. Brown et al. (2007) also showed that the emplacement of kimberlite dykes can result in significant deformation and alteration of the country rock they intrude. Area of significant alteration exist in the country rock adjacent to kimberlite intrusions of the Swartruggens Kimberlite Dike Swarm, South Africa, expressed as brecciated zones (containing angular, centimeter-sized fragments), dyke-parallel fractures, and spheroidal alteration zones. The dolerite and quartzite country rock of the latter zones contain rounded cores (5 cm to > 1 m in diameter) which are surrounded by in situ, concentric foliated and altered rock. Rounded country rock clasts have also been found in the volcanic deposits within many kimberlite pipes (e.g. Porritt and Cas, 2009).

2.3.1.3 Accessory Lithic Clasts

Accessory lithic clasts in a volcanic deposit are, as previously stated, wall rock fragments incorporated into the stream of erupting material during a volcanic eruption (Wright et al., 1980) (Figure 2-2). As discussed in the previous chapter, accessory lithics are an important source of information about the nature of the country rock underlying volcanic systems, as well as the processes operating within the volcanic conduit over the course of an eruption (e.g. Calder et al., 2000; Pittari et al., 2008; Rust and Cashman, 2007; Suzuki-Kamata et al., 1993; Varekamp, 1993).

Certain types of pyroclastic deposits, termed lag breccias, are anomalously rich in accessory lithics (Calder et al., 2000; Druitt, 1985; Nairn et al., 1994). While the morphologies of these lithic clasts are not usually described in detail in the studies, some are known to be quite rounded. Nairn et al. (1994) noted, while describing the lag breccias interbedded with the Kaingaroa Ignimbrites (Taupo Volcanic Zone, New Zealand), that the dense lithic clasts of the lag breccias are typically 20 – 30 cm in

size and angular to subrounded, and that the larger lithic clasts (up to 50 cm) were usually the most rounded. Proximal lag breccias on Santorini, Greece, have also been observed to contain subangular to rounded lithic clasts ranging in size from lapilli to blocks (Mellors and Sparks 1991; J.K. Russell, pers. comm.). The lithic clasts at Santorini are made up of basaltic to andesitic lavas, schist, limestone, tuffs and gabbroic nodules (Mellors and Sparks, 1991). Up to 20% of the lithic clasts were reported to be rounded and hydrothermally altered, with some of the rounded blocks (i.e. larger clasts) showing remnants of what was described as highly altered concentric spheroidal or "onion-skin" weathering rinds (Mellors and Sparks, 1991). The rounded nature of the lag breccia clasts was attributed by the authors to be the product of abrasion of the fragile altered outer margins of the lithic clasts during their eruption and subsequent transport (Mellors and Sparks, 1991). The co-ignimbrite lithic breccia unit of the Kos Plateau Tuff, in Greece, has also been observed to contain rounded lithic clasts (Allen and Cas, 1998). Larger lithic clasts, especially those > 20 cm in diameter, were observed to be generally well to moderately rounded, as opposed to the smaller lithic clasts, which tended to be more angular in shape (Allen and Cas, 1998). Therefore, the general trend from these three lithic-rich pyroclastic deposits is that lithic clasts typically display a wide range in overall roundness, but that larger clasts tend to be more rounded than smaller clasts.

While many studies have examined the componentry of accessory lithic clasts, and the overall evolution of this componentry throughout the course of an eruption, to date no studies specifically investigating the morphologies of accessory lithic clasts exist. In this study, I will address the question of how two specific types of accessory lithic clasts arrived at their final morphologies, and what processes might be recorded by these morphologies. Chapter 6 contains a discussion on the various mechanical and thermochemical processes which might have affected the shapes of these lithic clasts.

3. Field Area: Mount Meager Volcanic Complex

The Mount Meager Volcanic Complex (MMVC) is located in southwestern British Columbia, Canada, approximately 150 km north of Vancouver (Figure 1-1). The MMVC is part of the Garibaldi Volcanic Belt, the northernmost extension of the Cascade Volcanic Arc (Green et al., 1988; Read, 1990; Sherrod and Smith, 1990). This calc-alkaline stratovolcano complex is made up of a number of partially overlapping volcanoes, and consists of central overlapping piles of andesite lava flows, dacite domes and lava flows, pyroclastic units and rock avalanche deposits, as well as peripheral basaltic lava flows and volcaniclastic deposits (Read, 1977a, 1977b). The complex has been subdivided into various assemblages relating to past episodes of volcanism, including the Devastator, Pylon, Job, Capricorn, Plinth, and Mosaic Assemblages (Figure 3-1) (Read, 1977a, 1977b). The volcanic history of the MMVC extends from at least 2.2 Ma to Recent times; its most recent explosive eruption occurred at 2360 B.P. (Clague et al., 1995; Leonard, 1995; Read, 1977a). The deposits of this last eruption, the Pebble Creek Formation, have been extensively mapped and studied (Figure 3-2) (Hickson et al., 1999; Read, 1977a, 1977b, 1990; Stasiuk et al., 1996; Stewart et al., 2002, 2008).

The MMVC, which rises to an elevation of 2645 masl, has been subjected to high rates of erosion and mass wasting for most of its existence, partly due to the high regional uplift rates and glacial erosion (Farley et al., 2001). The base of the volcanic complex is currently situated at 1100 – 1200 masl, lying atop a basement composed of various plutonic and metamorphic lithologies (Read, 1977a, 1990) (Figure 3-1).
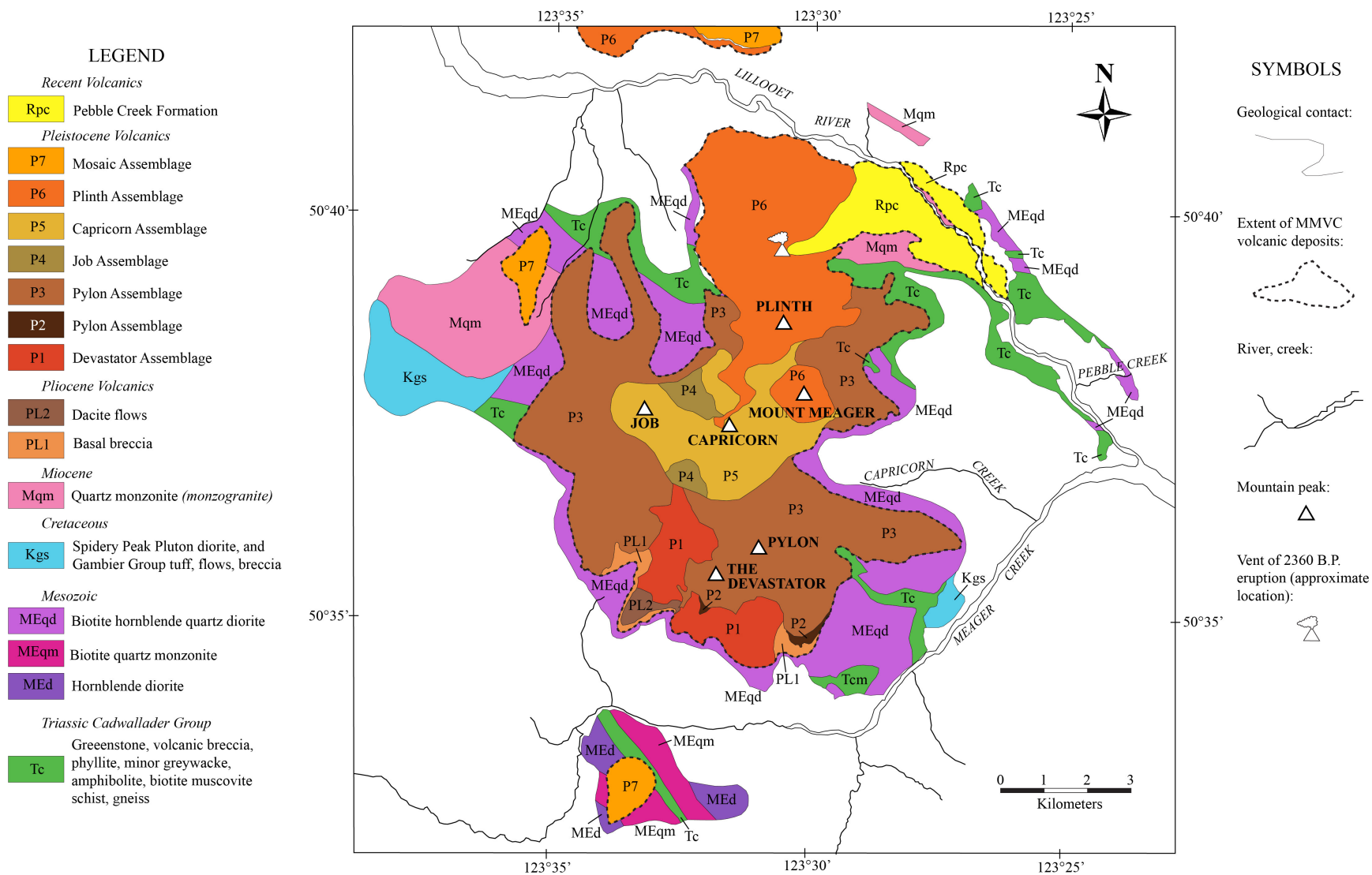
Figure 3-1. Map of the Mount Meager Volcanic Complex, modified from Read (1977b).

LEGEND

Recent Volcanics
- Rpc — Pebble Creek Formation

Pleistocene Volcanics
- P7 — Mosaic Assemblage
- P6 — Plinth Assemblage
- P5 — Capricorn Assemblage
- P4 — Job Assemblage
- P3 — Pylon Assemblage
- P2 — Pylon Assemblage
- P1 — Devastator Assemblage

Pliocene Volcanics
- PL2 — Dacite flows
- PL1 — Basal breccia

Miocene
- Mqm — Quartz monzonite *(monzogranite)*

Cretaceous
- Kgs — Spidery Peak Pluton diorite, and Gambier Group tuff, flows, breccia

Mesozoic
- MEqd — Biotite hornblende quartz diorite
- MEqm — Biotite quartz monzonite
- MEd — Hornblende diorite

Triassic Cadwallader Group
- Tc — Greeenstone, volcanic breccia, phyllite, minor greywacke, amphibolite, biotite muscovite schist, gneiss

SYMBOLS

Geological contact:

Extent of MMVC volcanic deposits:

River, creek:

Mountain peak:

Vent of 2360 B.P. eruption (approximate location):

25

Figure 3-2. Map of the Pebble Creek Formation, displaying locations of sampled outcrops. Modified from Stewart et al. (2008), with basement lithologies mapped by Read (1977b).

3.1 Basement Lithologies

Basement rocks in the immediate vicinity of Mount Meager are poorly exposed, but recent diamond drilling has provided additional useful information concerning the basement geology to the MMVC. A series of short diamond drill holes were drilled just east of the MMVC in 2010 by Innergex Renewable Energy Inc. I have constructed two geological cross-sections (Figures 3-3, 3-4) using the existing geological maps of the area (Hickson et al., 1999; Read, 1977b; Stasiuk et al., 1996; Stewart et al., 2008) and new data gathered from the core of these diamond drill holes. The first cross-section cuts through the Pebble Creek Formation deposits and underlying basement to the east of the MMVC (A-A'-A''; Figure 3-3). The second cross-section, which is more hypothetical due to the lack of drill hole data on the NE portion of the MMVC edifice, is oriented from the SW towards the NE and cuts through the inferred vent location of the 2360 B.P. eruption (B-B'; Figure 3-4).

The presumed location of the vent of the 2360 B.P. eruption is located on the NE flank of Plinth Peak, at an elevation of approximately 1500 – 1600 m (Read, 1977a) (Figure 3-2). The presumed vent location is underlain by a ~ 550 m thick sequence of Pleistocene-aged volcanic deposits belonging to the MMVC (Figure 3-4). This volcanic sequence is discussed in greater detail in the following section (Section 3.2). The basement to the MMVC comprises Miocene, late Mesozoic (Cretaceous/Jurassic), and Triassic aged rocks. The oldest observed rocks belong to the Triassic Cadwallader Formation (Tc), which comprises a variety of lithologies, including greenstone and volcanic breccia, gray phyllite and minor greywacke, streaky amphibolite, biotite muscovite schist and gneiss (Read, 1977b). Late Mesozoic (Cretaceous and/or Jurassic) lithologies include biotite quartz monzonite (Meqm), biotite hornblende quartz diorite (Meqd) and hornblende diorite (Med) bodies. Rare outcrops of aphanitic flows, tuffs and breccias thought to have been emplaced during the lower Cretaceous, and are ascribed to the Gambier Group (Read, 1977b), and the biotite hornblende quartz diorite of the Spidery Peak Pluton was emplaced during the upper Cretaceous (Kgs) (Read, 1977b). Finally, several felsic plutonic bodies were emplaced during the Miocene, including the Affliction Creek Stock to the west of the MMVC and the Fall Creek Stock exposed immediately to the east of the MMVC (Read, 1977b) (Figure 3-1). These felsic plutonic bodies were originally described as quartz monzonites by Read (1977b) although my analysis of their mineralogy suggests that they are technically monzogranites (see discussion in Section 4.4).
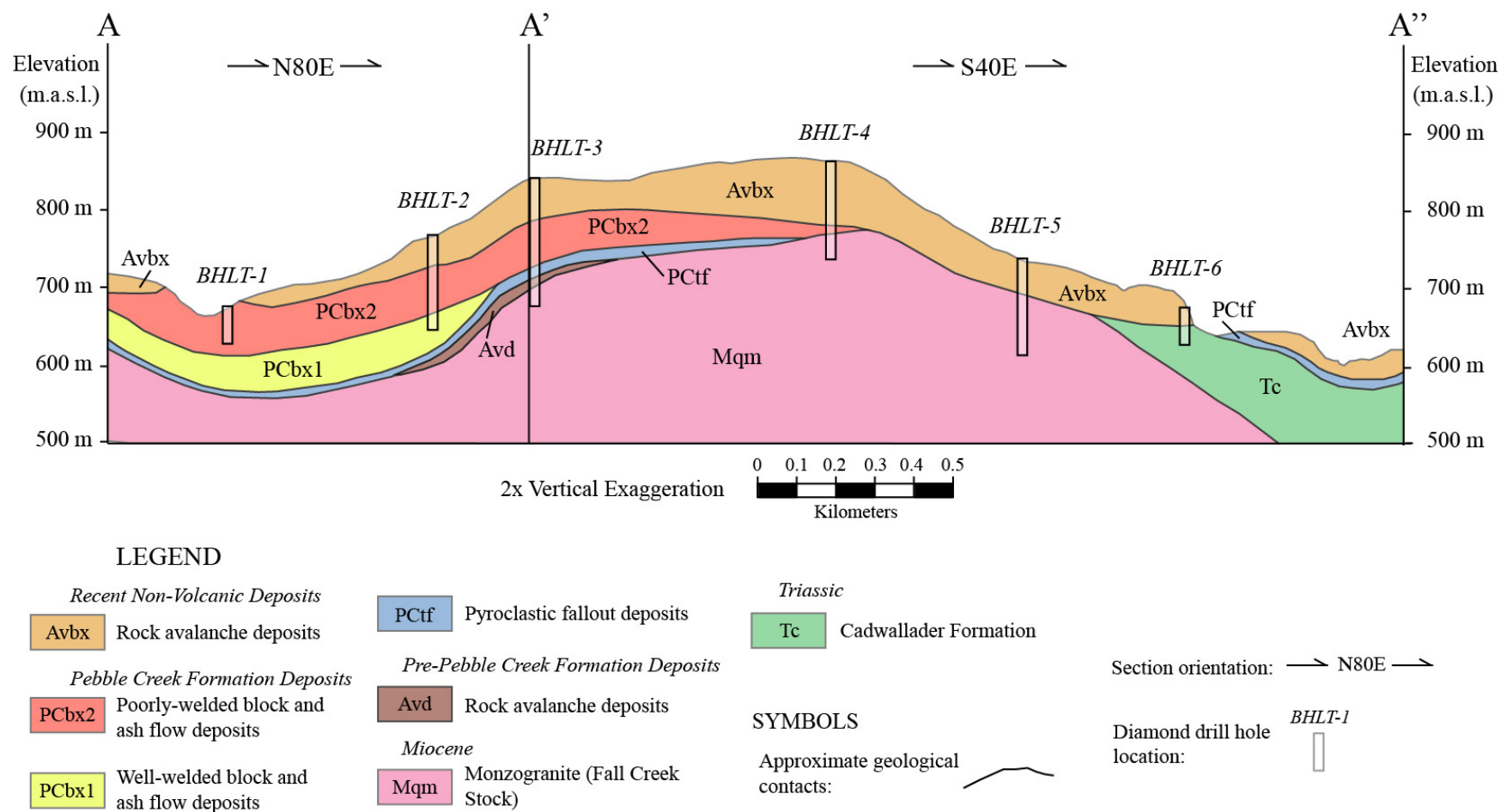
Figure 3-3. Cross-section through Quaternary deposits and basement lithologies east of the Mount Meager Volcanic Complex. The cross-section was constructed using the information from 6 diamond drill holes drilled by Innergex in 2010, as well as the maps by Stewart et al. (2008) and Read (1977b). Cross-section location is shown on Figure 3-2.
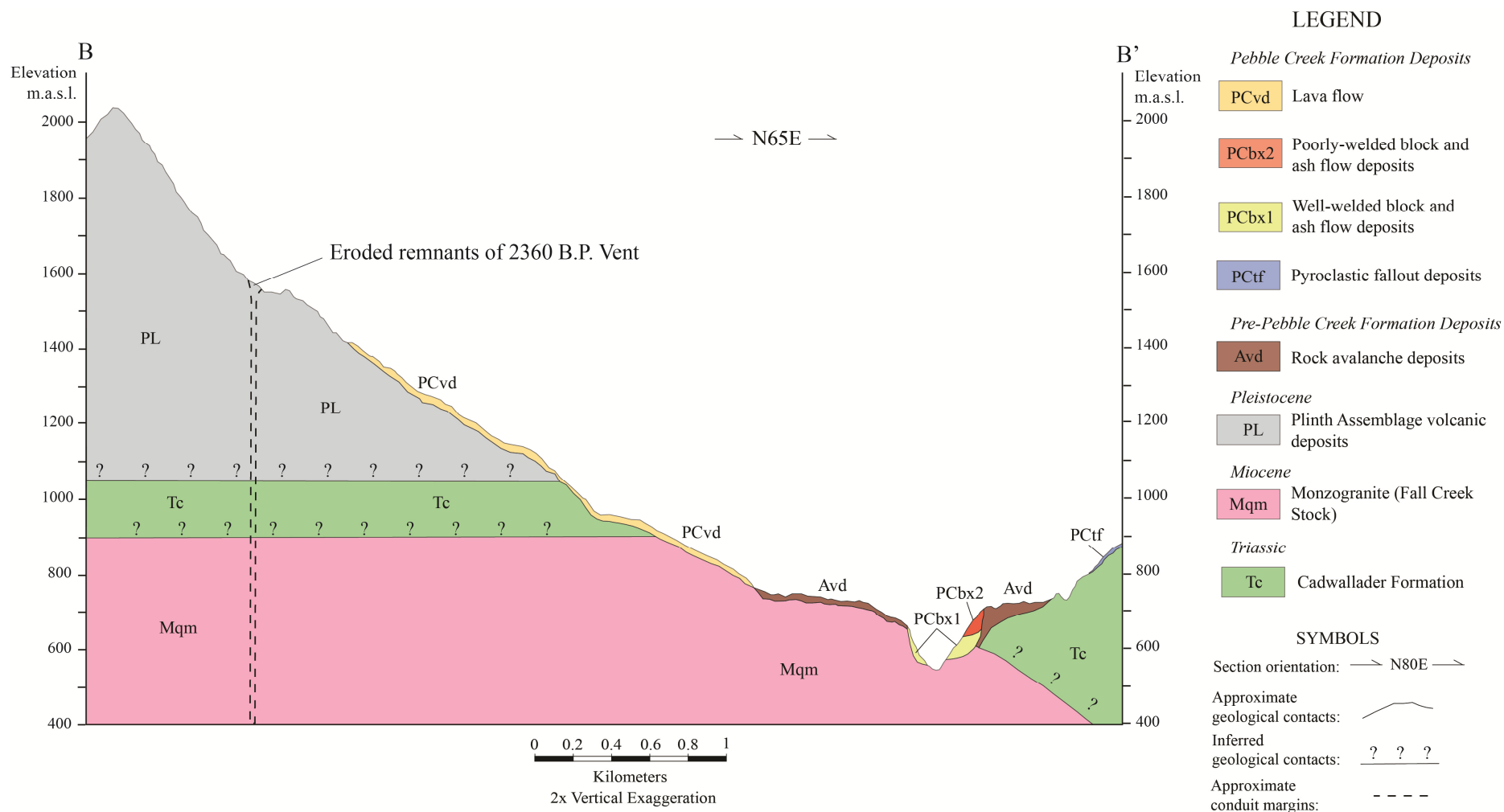
Figure 3-4. Cross-section through the approximate vent location of the 2360 B.P. Mount Meager Volcanic Complex eruption, showing inferred contacts between basement lithologies. The cross-section was constructed using the maps by Stewart et al. (2008) and Read (1977b). Cross-section location is shown on Figure 3-2.

3.2 Mount Meager Volcanic Complex Volcanic Deposits

The various volcanic assemblages that make up the MMVC have been extensively described in the literature (Read, 1977a, 1977b, 1990), and their spatial relationships are summarized in Figure 3-1. Here I briefly describe, in chronological order, each of the main assemblages present. The earliest known volcanic assemblages belonging to the MMVC, dating to the Pliocene, include a basal volcaniclastic breccia (PL1) and porphyritic dacite lava flows (PL2), which are both confined to the southern side of the MMVC. The next assemblage emplaced was the Devastator (P1), composed of highly altered felsic volcanic rocks and hypabyssal intrusions; these deposits are also restricted to the southern flanks of the MMVC (Read, 1990). The Pylon Assemblage was erupted next, and is composed of basal andesitic, aphanitic flows (P2) forming small lenses on the southern side of the MMVC, and an extensive porphyritic plagioclase andesite unit (P3) made up primarily of gently dipping flows, as well as basal and intercalated breccias and tephra lenses, plugs and dykes (Read, 1990). The P3 unit is thought to be the most extensive unit of the MMVC, underlying most of its southern, central and western sections (Read, 1990), and perhaps extending far enough to the north to underlie the inferred vent of the 2360 B.P. eruption. Next, the porphyritic hornblende, biotite and quartz rhyodacite flows of the Job Assemblage (P4), and the coarse-grained plagioclase, quartz- and biotite-phyric rhyodacite of the Capricorn Assemblage (P5) were emplaced in the centre of the MMVC complex (Read, 1990). The Plinth Assemblage (P6) was erupted at ~ 100 $\pm$ 20 Ka (K-Ar) and forms the uppermost 600 m of Mount Meager and the bulk of Plinth Peak (Read, 1990). The Plinth Assemblage, therefore, constitutes the bulk of the country rock immediately underlying the vent of the 2360 B.P. eruption (Hickson et al., 1999; Read, 1990). It consists of light gray, porphyritic, aphanitic, commonly vesicular rhyodacite or dacite (the chemical classification depends on whether certain minerals present are counted as phenocrysts or xenocrysts) (Read, 1990; Stasiuk and Russell, 1989). The mineralogy of this assemblage includes plagioclase, quartz, minor biotite and rare hornblende phenocrysts, and characteristic rounded fine-grained andesite inclusions are also observed (Read, 1990). Plinth Peak consists of columnar- or platy-jointed lava flows, dipping subparallel to local topography, as well as tephra dispersed on its northern side (Read, 1990). The Mosaic Assemblage (P7), composed of porphyritic basalt and trachybasalt, is present in four areas around the MMVC, each

of which likely has its own subjacent vent (Read, 1990). Finally, the Pebble Creek Formation was emplaced during the 2360 B.P. eruption of the MMVC.

In summary, the Plinth Assemblage rocks are the wall rocks directly underlying the vent of the 2360 B.P. eruption. The older Pylon Assemblage is the only other volcanic assemblage that could also underlie the vent, but it is not known if this assemblage extends that far north.

3.3 Pebble Creek Formation

The Pebble Creek Formation (PCF) encompasses the volcanic deposits and coeval rock-avalanche and debris-flow deposits resulting from the 2360 B.P. eruption of the MMVC (Hickson et al., 1999; Stewart et al., 2002). The diversity of lithofacies present within this formation reflects the dynamic interaction between an active volcanic system and the rugged terrain surrounding it. The area around the MMVC is characterized by mountainous topography and steep-sided river channels caused by high rates of uplift, mass wasting and glacial erosion over the past 4 Ma (Farley et al., 2001). The vent of this eruption has been highly eroded and is no longer exposed, but it is inferred to have been situated in a col upon the northeastern flank of Plinth Peak, surrounded by units of the Plinth Assemblage (PL) (Figure 3-2) (Read, 1977a, 1990). The eroded remains of the inferred vent are located at an elevation of ~ 1500 masl, approximately 1000 m above a narrow and deeply incised valley containing the Lillooet River, (Figure 3-2) (Hickson et al., 1999; Read, 1977a, 1977b). The deposits of the Pebble Creek Formation are predominantly dacitic to trachydacitic in composition, and their geology has already been described in detail (Hickson et al., 1999; Stasiuk et al., 1996; Stewart et al., 2002). In order of emplacement, the PCF deposits include: 1) pyroclastic fallout deposits (PCtf), 2) multiple pumiceous pyroclastic flow deposits (not shown on map), 3) unwelded to welded block and ash flow deposits, which accumulated in and eventually dammed the paleo-Lillooet River valley (PCbx1 and PCbx2), 4) a hot outburst flood deposit, caused by the failure of the dam of welded block and ash flow material (PCdf), 5) a lava flow extending from the presumed vent location down towards the Lillooet Valley (PCvd), and 6) post-eruption rock avalanche deposits (Avbx) (Hickson et al., 1999). The deposit of interest to this study is the first erupted unit of the Pebble Creek Formation: the pyroclastic fallout deposits.

3.3.1 Pyroclastic Fallout Deposit

The pyroclastic fallout deposits of the Pebble Creek Formation mantle the slopes of the mountainous terrain towards the northeast of the MMVC, extending from NNW of the inferred vent to east of the inferred vent. Proximal deposits of this tephra reach thicknesses of 80 m and thin (approximately 5 cm thick) distal layers of the same ash have been identified in Alberta, approximately 500 km to the NE of the vent (Hickson et al., 1999; Nasmith et al., 1967; Westgate and Dreimanis, 1967). The fallout tephra originally blanketed this whole area, but due to the unconsolidated nature of the deposit as well as the steepness of the regional topography, certain portions of the deposit have been significantly eroded or remobilized. Areas mapped as primary fallout deposits by Stewart et al. (2008) are classified as unit PCtf on Figure 3-2, while predominantly remobilized deposits, which are weakly sorted in crude, reversely graded beds and contain significantly more rounded pumice clasts than the primary deposits (Stewart et al., 2002), have been mapped as unit Qtf (Stewart et al., 2008). These remobilized sections lie at very steep angles (22°-37°) on the northeastern flanks of Plinth Peak, and contain thin interspersed lenses of avalanche deposits of the Plinth Assemblage (Stewart et al., 2002). Some outcrops of primary fallout deposits are also capped by a relatively thin band of subrounded to rounded, remobilized pumiceous fallout tephra, likely accumulated as pumice clasts were dislodged from unstable slopes and rolled downhill during the years following the eruption (e.g. Outcrop 8) (Figure 3-2). The fallout deposits within and along the margins of the Lillooet River valley were buried by subsequent pyroclastic flows, block and ash flows and rock avalanche deposits, as well as Quaternary colluvium and alluvium.

The primary pyroclastic fallout deposit is unconsolidated, well-sorted and clast-supported, and consists primarily of whitish juvenile pumice clasts. Other juvenile clasts include slightly gray pumice clasts and white-and-gray banded pumice clasts. Four main types of accessory lithics occur pervasively, albeit in minor amounts, within the fallout deposits: (1) dacite lava clasts, (2) monzogranite clasts, (3) clasts of various metamorphic and other (non-granitic) plutonic lithologies, and (4) welded volcanic breccia clasts. Section 4.1.3 contains detailed componentry of the fallout deposit, including descriptions and relative abundances of the main juvenile and accessory lithic clast types. The fallout deposit does not contain entrained accidental lithic clasts, but does occasionally contain charred wood clasts from the forest predating the 2360 B.P. eruption, ranging from small

carbonaceous fragments to full-size trees (Stasiuk et al., 1996). The age of the PCF was obtained by radiocarbon dating a sample of charred wood from one of these stumps (Read, 1990). Data and results obtained from the field work conducted on the fallout deposits over the course of this study, including stratigraphic logs, granulometry and detailed componentry data, are found in Chapter 4.

3.3.2   Characteristics of the 2360 B.P. Eruption

The 2360 B.P. eruption of the Mount Meager Volcanic Complex produced a sequence of volcanic deposits totalling > 0.55 km^3, but likely less than 1 km^3, in volume (Andrews et al., 2012). The eruption commenced with a subplinian phase which produced pyroclastic fallout deposits (~ 4.2 x 10^8 m^3), as well as the deposits of pyroclastic density currents generated by the partial collapse of the subplinian column (~ 1 x 10^7 m^3) (Andrews et al., 2012; Hickson et al., 1999; Stasiuk et al., 1996). Based upon field data, this initial subplinian phase had a Volcanic Explosivity Index (VEI) of 4, and a plume height of approximately 15-17 km (Hickson et al., 1999; Luty, 1994). Chapter 6 also contains calculations and estimates for many other parameters related to the PCF eruption.

It is difficult to derive the exact duration of this subplinian phase based upon forensic volcanological studies, but based upon estimates for VEI = 4 eruptions in general, the duration of this phase was likely > 12 hours, with a continuous blast duration of 6 – 12 hours (Newhall and Self, 1982). Andrews et al. (2012) estimated the duration of the subplinian phase to be approximately 1 – 2 days. Following the subplinian phase, the intensity of the eruption waned and volcanic activity progressed to an explosive Vulcanian phase, which produced a series of unwelded to welded block and ash flow deposits (Michol et al., 2008).

4. Field Volcanology

The field work for this project was undertaken during the summers of 2010 and 2011. The Mount Meager Volcanic Complex area was accessed via the Upper Lillooet Service Road, as well as a network of connected logging roads.

4.1 Pumice Fallout Deposits

A total of 8 outcrops of the pyroclastic fallout deposits from the 2360 B.P. eruption of the MMVC were analyzed for this study (Figure 4-1). Outcrop selection was based primarily upon quality of the exposure; consequently, selected outcrops were located at roadcuts, cliffs, or within a pumice quarry. Images of each outcrop analyzed are found in Appendix A1. Locations of the selected outcrops are shown in Figure 3-2, and a selection of parameters relating to the location and physical characteristics of each outcrop are found in Table 4-1. All of the selected outcrops, except for Outcrop 5, are located at distances of 3.4 to 4.7 km from the vent of the 2360 B.P. eruption, and are 2.5 to 5.2 m thick (Table 4-1). Outcrop 5 is slightly more proximal, at a distance of only 2.2 km from the vent, and is approximately 15 m thick.

Resedimented
Fallout Deposit

Primary
Fallout Deposit

(Base of Deposit
Not Exposed on
Photograph)
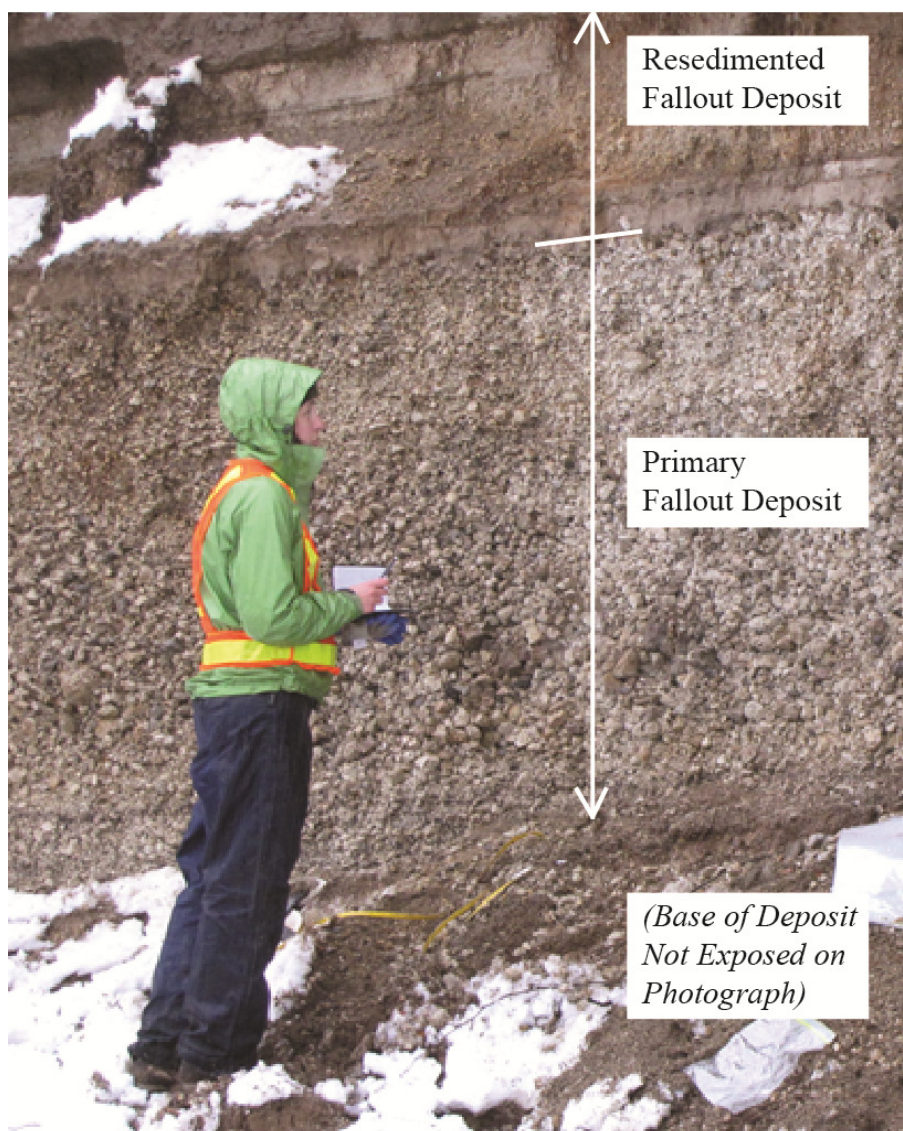
Figure 4-1. Photograph of the author logging stratigraphic relationships in a pumice fallout deposit (Outcrop 2).

Outcrop #	Northing (UTM)	Easting (UTM)	Elevation (masl)	Distance from Inferred Vent (km)	Bearing from Inferred Vent Location	Thickness (m)	Degree of Bedding	Units
1	5,613,316 N	467,882 E	745	4.0	N 72 E	3.0	Well-bedded	1-1, 1-2, 1-3, 1-4, 1-5
2	5,614,048 N	467,833 E	944	4.2	N 63 E	> 3.2	Well-bedded	2-1, 2-2, 2-3, 2-4, 2-5, 2-6
3	5,614,916 N	466,191 E	740	3.5	N 37 E	> 3.6	Crudely bedded	3-1
4	5,613,488 N	467,795 E	771	4.0	N 69 E	3.5	Well-bedded	4-1, 4-2, 4-3, 4-4, 4-5
5	5,614,283 N	464,682 E	770	2.2	N 15 E	~ 15	Crudely bedded	5-1
6	5,615,033 N	465,880 E	730	3.4	N 32 E	2.5	Poorly bedded	6-1, 6-2, 6-3
7	5,612,745 N	468,374 E	651	4.4	N 82 E	2.7	Crudely bedded	7-1
8	5,614,258 N	468,219 E	1023	4.7	N 63 E	5.2	Well-bedded	8-1, 8-2, 8-3, 8-4, 8-5, 8-6, 8-7

Table 4-1. Locations and parameters of the 8 outcrops studied for this project, from the fallout deposits of the 2360 B.P. eruption of the Mount Meager Volcanic Complex.

4.1.1 Stratigraphic Logs

Stratigraphic relationships were logged for each of the selected outcrops (Figure 4-1) and subdivided into distinct units based upon any distinguishable changes in grain size or componentry. Samples were collected for each unit within the 8 outcrops, and a graphic log was produced for each outcrop (e.g. Figure 4-2; all logs are found in Appendix A2). The graphic logs display the maximum recorded grain size (i.e. the diameter of the largest pumice clast observed) for each unit. Attempts were made to dig to the basal contact of each outcrop, to establish true thickness of the pumice fallout deposit at each location. However, due to difficulties in excavating the unconsolidated deposits, the basal contacts of several of the outcrops (Outcrops 2, 3, 5 and 8) were not uncovered. The locations of Outcrops 2, 5 and 8 fall within the remobilized fallout deposit zones mapped by Stewart et al. (2008) (Qtf; Figure 3-2). However, it appears that these outcrops are predominantly composed of primary fallout deposits, recognizable by the angular nature of the pumice clasts, and are only capped by remobilized or resedimented pumice fallout deposits, which are characterized by rounded pumice clasts and sediment-rich matrices. The remobilized units likely formed during the years following the eruption, as pumice clasts were dislodged and rolled down the steep flanks of the MMVC and surrounding mountains, or as pumice clasts were resedimented by flowing water.

All outcrops are primarily composed of unconsolidated, well-sorted, angular to subangular pumice clasts. The degree of bedding observed was variable. Outcrops 1, 2, 4 and 8 featured distinct bedding. Beds within these outcrops varied from 2 cm to 1.6 m thick, and contacts between individual beds, or units, were marked by significant and sudden changes in average grain size, sometimes accompanied by distinct changes in componentry. Conversely, outcrops 3, 5, 6 and 7 were only crudely bedded; individual beds could not easily be identified, and only a rough alignment of clasts with the paleotopographic surface could be distinguished. Outcrop 6 featured a slightly finer-grained middle unit sandwiched between two coarser-grained units (Appendix A2), but the upper and lower contacts of this middle unit were relatively poorly defined.

Outcrop #1
Graphic Log

Location: Mount Meager, British Columbia

Coordinates: 5613316 N 467882 E

Elevation: 745 M.A.S.L.

Logged by: Michelle Campbell August 2011

Max. Grain Size (mm)

Cumulative Granulometry Plots

Description

Recent Soil
Post-Pebble Creek Formation

Pebble Creek Formation Pumice Fallout Deposits (2360 B.P.)
Pumiceous, unconsolidated, well-sorted, clast-supported, matrix-free deposit, draping topography. Deposit at this location is moderately well-bedded, and units here are divided principally on the basis of consistent and obvious change in grain size.

Beds are dipping at: ~14° @ 110°

Unit 1-5 (Bed "E")

Unit 1-4 (Bed "D")
Unit 1-3 (Bed "C")
Unit 1-2 (Bed "B")

Unit 1-1 (Bed "A")

Legend
- Juvenile (pumice) clast
- Accessory lithic clast
- Sediment

Paleosol
Pre-Pebble Creek Formation. Partially charred and contains carbonized wood fragments.

Figure 4-2. Stratigraphic log of Outcrop 1, with cumulative granulometry plots of each unit.

38

The relatively well-bedded outcrops (1, 2, 4 and 8) are clustered within an area lying east-northeast of the 2360 B.P. vent, which I have termed the "relatively well-bedded zone" (Figure 4-3). Areas containing only crude bedding are located to the north and to the east of the vent, flanking the well-bedded zone on either side; I have termed these sections the "crudely bedded zone" (Figure 4-3). A comparison of the graphic logs produced for the well-bedded outcrops reveals a very similar pattern within the bedding. The pervasive bedding pattern is expressed as five units labelled here as A, B, C, D and E. In order of increasing stratigraphic height, these recurring beds are: (A) a lowermost coarse-grained unit; (B) a very coarse-grained unit; (C) a ~ 10 to 15 cm thick medium-grained unit; (D) a 2 to 3 cm thick, fine-grained unit with a high concentration of gray, porphyritic, dacitic accessory lithic clasts of the Plinth Assemblage; and (E) an upper coarse-grained unit. The locations of these five recurring beds are indicated on the stratigraphic logs of the bedded outcrops (Appendix A2). Bed "D", the thin, fine-grained, lithic-rich unit, serves as a type of marker horizon that is very easily distinguishable within the bedded outcrops. Outcrop 8 features an anomalously thick base; here the lowermost Bed "A" is made up of two units (Units 8-1 and 8-2), which are found beneath the distinctively coarse-grained Bed "B" (Unit 8-3) (Appendix A2). In Outcrop 8, Bed "A" measures a total of at least 3.4 m thick, whereas the equivalent Bed "A" in Outcrops 1 and 4 (Units 1-1 and 4-1, respectively) measure only ~ 1.5 m thick. The significantly greater thickness of this basal unit of Outcrop 8 may be due to its location in a steep-sided paleo-river valley, which could have allowed the accumulation of greater basal thicknesses through the incorporation of extra fallout tephra that rolled down from the valley sides and floated down the river, before the river was choked by the fallout deposits. Polymictic, poorly-sorted, rounded pebble- and cobble-bearing deposits underlie parts of the quarry where Outcrop 8 is located, evidence of a paleo-river bed. Outcrops 2 and 8 are also capped by remobilized volcaniclastic deposits. The remobilized section at the top of Outcrop 2 includes finely-bedded resedimented volcaniclastic material, with variable amounts of pumice, silt and sand, and lithic clasts; these beds were likely subaqueously remobilized. The remobilized unit (Unit 8-7) capping Outcrop 8 features predominantly rounded pumice clasts in a sediment-rich matrix. The rounded shape, lowered surface roughness and decreased shape complexity of these juvenile clasts suggests that this unit has been remobilized (Carey et al., 2000; Carey and Sigurdsson, 1978), likely formed by the gradual redeposition of the fallout deposits during the years following the eruption.
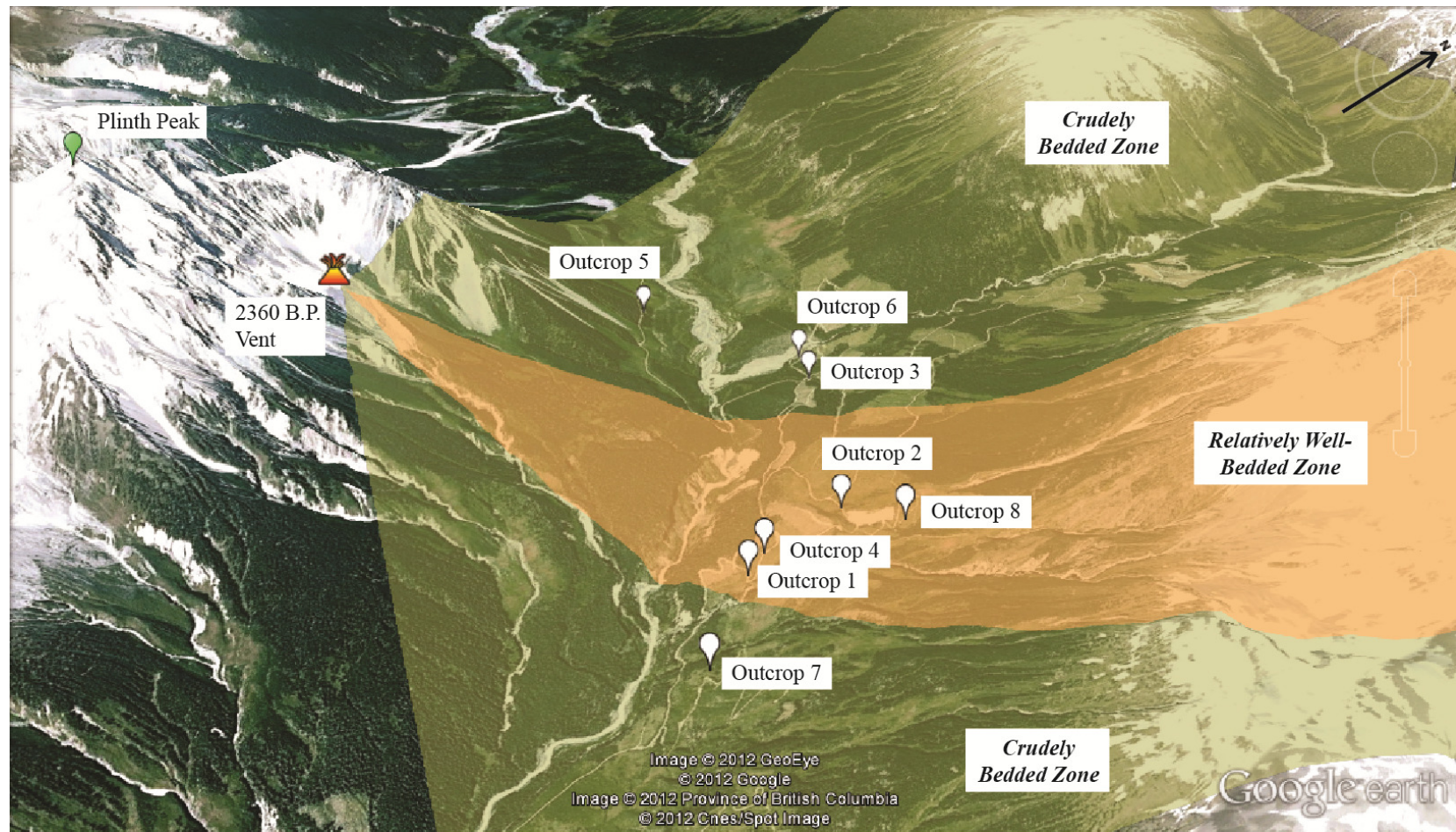
Figure 4-3. View of the 2360 B.P. vent and surrounding fallout deposits of the Pebble Creek Formation. The fallout deposits are subdivided into a central "relatively well-bedded" zone, where distinct beds are readily visible within the primary deposits, and a "crudely bedded" zone which flanks the relatively well-bedded zone on either side. The relatively well-bedded zone is located approximately due ENE of the 2360 B.P. vent. Imagery from Google Earth (© 2012 Google).

The significance of the central, relatively well-bedded zone within the fallout deposits (Figure 4-3) is unclear. Bed "D," the very thin, fine-grained, lithic-rich marker horizon (e.g. Figure 4-2), may represent deposition from a dilute pyroclastic surge, which would have been emplaced only within a narrow zone extending approximately northeast to east-northeast of the 2360 B.P. vent. It should also be noted that the plumes of explosive eruptions are hardly stationary during the course of an eruption. Changes in the wind speed, wind direction or in the intensity of the eruption (and consequently, the height of the column) can all affect the plume's positioning. Consequently, sections along the margins of the fallout deposit may not have experienced continuous clast deposition over the course of the eruption, due to changes in the orientation of the plume. The occurrence of the well-bedded zone may indicate that the plume was relatively narrow and oriented ENE during the phase of the subplinian eruption when the marker horizon and the subjacent unit were erupted, such that erupted material from this episode only accumulated in the bedded zone.

4.1.2   Granulometry

The samples collected for each unit of the pyroclastic fallout deposit were sieved by hand. Using the phi (φ) scale, where:

$$\varphi = -log_2(d) \qquad (4.1)$$

where d is the grain diameter (mm), the sieve sizes used range from -6 φ (64 mm) to 2 φ (0.2 mm). A normalized cumulative grain size distribution curve was graphed for each unit by fitting a shape-preserving interpolant to the normalized weight data points for each unit's sieved fractions (i.e. Piecewise Cubic Hermite Interpolation Polynomial function in Matlab®). These cumulative grain size plots are found beside their respective units in the stratigraphic logs of Appendix A2.

Inman parameters (Inman, 1952) of median grain diameter (Md_φ) and graphical standard deviation (σ_φ), were also calculated for each unit using the fitted curves:

$$Md_\varphi = \varphi_{50} \qquad (4.2)$$

$$\sigma_\varphi = \frac{\varphi_{84} - \varphi_{16}}{2} \qquad (4.3)$$

The values of these Inman parameters, which give quantitative estimates of each unit's central grain size tendency and overall sorting, respectively, are found in Table 4-2 (Inman, 1952). The five

recognizable beds recurring throughout the relatively well-bedded zone of the fallout deposits (beds "A", "B", "C", "D" and "E"), described in Section 4.1.1, are indicated beside the relevant units of the bedded outcrops. Averages of the Inman parameters of each of these five recurring beds were calculated from the results of the four bedded outcrops and are found in Table 4-3. The granulometry data for these five beds (Figure 4-4) mirrors the pattern visible in the stratigraphic logs, which were constructed using maximum apparent grain size, and implies that each of these beds does indeed represent a continuous and distinct stratum within the bedded zone.

The Md_φ values calculated vary from -5.6 φ (47 mm) to -1.9 φ (4 mm). The uppermost and lowermost units in all units analyzed have similar, relatively coarse Md_φ values, ranging from -4.3 φ (20 mm) to -5.4 φ (42 mm). The σ_φ values calculated vary little among the units, from 0.8 φ to 1.6 φ, excluding the 1.7 φ value obtained for the remobilized unit at the top of outcrop 8 (Unit 8-7). All of these values fall within the range of very well- to well-sorted for volcaniclastic deposits (Cas and Wright, 1987).

Unit	Bed Type	Median Clast Diameter $Md_\varphi = \varphi_{50}$	Median Clast Diameter (mm)	Standard Deviation $\sigma_\varphi = \dfrac{\varphi_{84} - \varphi_{16}}{2}$
1-1	*Bed "A"*	-4.52	23.0	1.11
1-2	*Bed "B"*	-5.56	47.2	1.40
1-3	*Bed "C"*	-3.25	9.49	1.55
1-4	*Bed "D"*	-1.88	3.67	1.25
1-5	*Bed "E"*	-4.75	26.8	0.87
2-1	*Bed "A"*	-4.74	26.7	1.04
2-2	*Bed "B"*	-5.21	36.9	0.91
2-3	*Bed "C"*	-4.13	17.5	0.97
2-4	*Bed "D"*	-2.95	7.75	0.98
2-5	*Bed "E"*	-4.98	31.6	0.86
2-6	*Remobilized*	-4.30	19.6	1.14
3-1	*No clear bedding*	-4.94	30.7	1.19

Unit	Bed Type	Median Clast Diameter $Md_\varphi = \varphi_{50}$	Median Clast Diameter (mm)	Standard Deviation $\sigma_\varphi = \dfrac{\varphi_{84} - \varphi_{16}}{2}$
4-1	*Bed "A"*	-4.86	29.0	0.98
4-2	*Bed "B"*	-5.45	43.6	0.82
4-3	*Bed "C"*	-4.37	20.7	1.45
4-4	*Bed "D"*	-2.57	5.94	1.18
4-5	*Bed "E"*	-4.95	30.9	0.77
5-1	*No clear bedding*	-4.94	30.6	1.19
6-1	*Crude bed*	-5.17	35.9	0.76
6-2	*Crude bed*	-3.76	13.6	1.13
6-3	*Crude bed*	-4.89	29.6	1.37
7-1	*No clear bedding*	-4.40	21.0	1.20
8-1	*Bed "A"*	-5.41	42.4	0.94
8-2	*Bed "A"*	-4.56	23.6	1.13
8-3	*Bed "B"*	-5.18	36.2	0.74
8-4	*Bed "C"*	-4.43	21.5	1.01
8-5	*Bed "D"*	-3.11	8.66	1.11
8-6	*Bed "E"*	-4.98	31.6	0.85
8-7	*Remobilized*	-4.80	27.81	1.71

Table 4-2. Granulometry results (Inman parameters) for all sampled units.

Recurring Beds	Average Md_φ (phi)	Average Md_φ (mm)	Average σ_φ
A	-4.67	25.6 ± 2.8	1.07
B	-5.35	41.0 ± 5.3	0.97
C	-4.05	17.3 ± 5.5	1.25
D	-2.63	6.51 ± 2.2	1.13
E	-4.92	30.2 ± 2.3	0.84

Table 4-3. Average Inman Parameters of the recurring beds in the "relatively well-bedded zone."
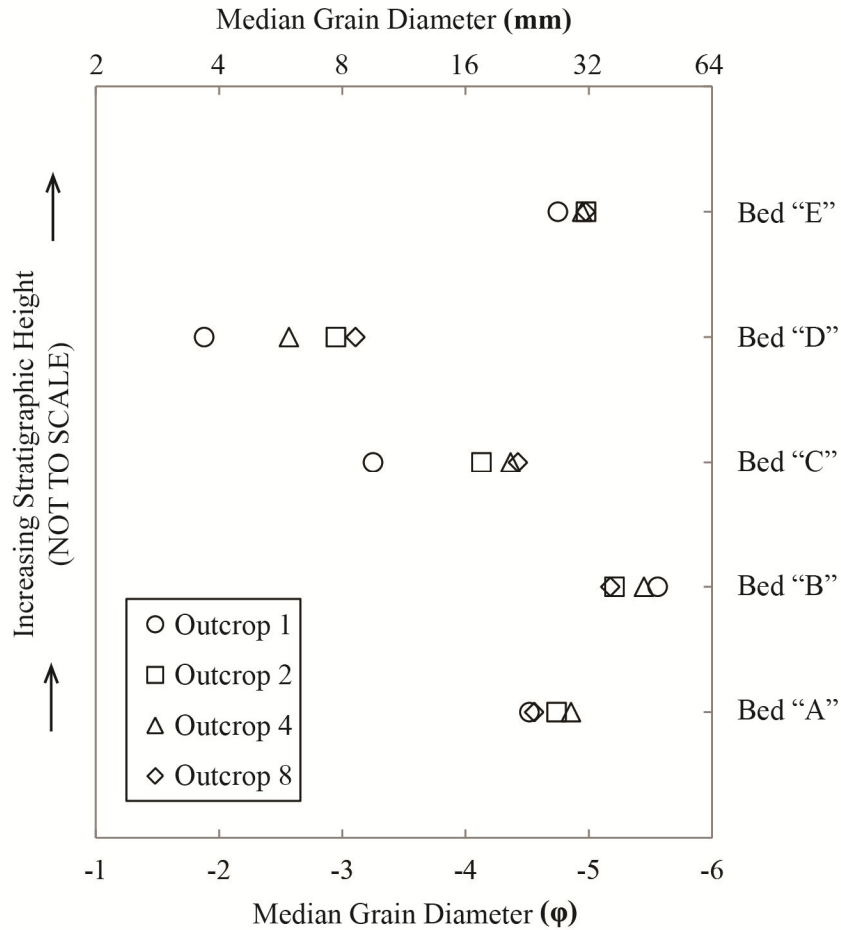
Figure 4-4. Granulometry summary of the relatively well-bedded zone of the pyroclastic fallout deposit of the Pebble Creek Formation. Median Grain Diameter (Md_φ) data are displayed for the 5 distinct beds present at each of the four bedded outcrops that were stratigraphically logged and sampled. Thicknesses of beds are not shown to scale.

4.1.3   Componentry

In order to determine the relative abundances of the various types of juvenile and accessory lithic clasts present in the fallout deposits, each of the five units of Outcrop 1 (Units 1-1, 1-2, 1-3, 1-4 and 1-5) was sorted in terms of clast componentry by hand. The following sieve fractions, from the granulometry work done on the Outcrop 1 samples, were sorted: 64 – 128 mm, 32 – 64 mm, 16 – 32 mm, 8 – 16 mm, and 4 – 8 mm. Clasts smaller than 4 mm were not sorted, as they were too difficult to accurately classify. These sieve fractions were sorted into one of six lithological categories: (1) pumice clasts; (2) gray, porphyritic, dacitic, extrusive volcanic clasts (typically 2 – 6 wt. %, but up to 21 wt. %

in some very thin units), most likely sourced from the Plinth Assemblage; (3) pale pink monzogranite clasts (0.2 – 4 wt. %), which likely originate from the Miocene Fall Creek Stock, exposed to the east of the vent; (4) clasts of various metamorphic and other (non-granitic) plutonic lithologies, typically greenstones, oxidized and fine-grained metasediments, and diorites (0.3 – 2 wt. %); these lithologies likely belong to the Triassic Cadwallader Formation; (5) welded volcanic breccia clasts containing pumiceous fragments within a reddish, fine-grained matrix (< 2 wt. %), which may originate from vent breccias predating the Pebble Creek Formation; and (6) clasts of other or undetermined lithology. Category 1 represents the juvenile material from the fallout deposits, while categories 2 to 5 represent the accessory lithic components of the fallout deposits. Descriptions for each of the lithological classes are found in Table 4-4, and images of the various types of juvenile and accessory lithic clasts are displayed in Figure 4-5. Componentry results for the five units of Outcrop 1 are found in Table 4-5, and displayed in Figure 4-6. The componentry results show that monzogranite and dacite clasts are present throughout the pyroclastic fallout deposits, but that their relative abundances change over the course of the eruption.

The juvenile pumice clast category was further subdivided for the sieve fractions larger than and including 8 – 16 mm, into: (1a) white pumice, and (1b) gray pumice and banded pumice. For the size fractions smaller than 8 – 16 mm, it becomes very difficult to properly differentiate the various pumice types. The relative proportions of white pumice, gray and banded pumice, and total accessory lithics, are compiled in Table 4-5 and displayed in Figure 4-7. The overall abundance of gray and banded pumice clasts increases steadily with increasing stratigraphic height (Figure 4-7). The banded pumices have compositional banding that is interpreted to represent magmatic mingling of lighter-coloured dacite with subordinate, dark-coloured basaltic andesite (Hickson et al., 1999; Stasiuk et al., 1996). Therefore, the increase in the amount of banded pumice with increasing stratigraphic height indicates an increase in the amount of mingled magma incorporated into the stream of erupting material as the eruption progressed. The significance of the gray and banded pumice within the pyroclastic fallout deposits is discussed in depth in Stasiuk et al. (1996).

	Lithological Category	Description
Juvenile Clasts	White Pumice	White to cream to pale gray, porphyritic, fibrous pumice. Larger clasts are often breadcrusted and commonly have pink, orange or reddish cores. Larger clasts generally have low competency and are pervasively fractured. The phenocryst assemblage is dominated by plagioclase, with minor amounts of orthopyroxene, amphibole and apatite, and glomerocrysts are common (Stasiuk et al., 1996). Range in size from < 1cm lapilli, to > 1m wide blocks in the proximal deposits, and are typically angular to subangular (although rounded in the remobilized zones of the fallout deposits).
	Gray and Banded Pumice	The gray pumice clasts are medium gray, relatively dense and often breadcrusted, and petrographically identical to the pumice clasts (Stasiuk et al., 1996).
		The banded pumices exhibit alternate white and gray banding on the cm scale (typically 0.5 – 2 cm thick). The compositional heterogeneity represented by the banding likely corresponds to magmatic mingling of volumetrically subordinate basaltic andesite (gray bands) with the dominant dacite (white bands) (Stasiuk et al., 1996).
Accessory Lithic Clasts	Dacite	Massive, light to dark gray, commonly weathering to a reddish colour, highly porphyritic, aphanitic, variably vesicular dacite lava from the Pleistocene Plinth Assemblage. The phenocryst assemblage is dominated by plagioclase, with lesser amounts of quartz, biotite, amphibole, clinopyroxene and oxides (Hickson et al., 1999). The groundmass is fine-grained and slightly glassy. Dacite clasts are typically angular to subangular, with very rough surfaces.
	Monzogranite	Massive, pale pink, crystalline, medium- to coarse-grained granitic rock most likely originating from the Miocene Fall Creek Stock. Mineralogy is dominated by plagioclase, K-spar and quartz, with minor biotite. Weathers to ochre or rusty coloration; many of the smaller clasts and a few of the larger clasts display significant weathering. Clasts are hard, dense and competent, but often contain partial fractures. Intact larger clasts are almost ubiquitously rounded and smooth-surfaced; smaller clasts display variable rounding and smoothing.
	Metamorphic / Non-Monzogranite Plutonic	Clasts of a variety of different lithologies, but primarily: (1) greenstone (greenish, porphyritic, moderately oxidized rocks, likely greenschist facies volcanics, usually blocky and subrounded, sometimes with flakey surface texture); (2) metasediments (olive green to dark brown, fine-grained, typically subangular to subrounded, probably greenschist facies); and (3) intermediate intrusives (salt-and-pepper, fine-grained to medium-grained plutonic rocks, typically quite rough and subangular). Clasts likely originate from basement rocks of the Triassic Cadwallader Group, and Jurassic/Cretaceous quartz diorites.
	Pumice Breccia	Welded breccias with a variety of different textural and lithological characteristics, but primarily: (1) breccias with a fine-grained reddish matrix and moderately flattened white pumice clasts, as well as minor lithics; (2) breccias with glassy, dark gray matrices and flattened white to gray pumice clasts, as well as minor amounts of angular monzogranite clasts; (3) rare clasts of black, highly glassy breccia (highly welded). Welded breccia clasts are typically rough and angular, and likely formed as vent or conduit infill prior to or concurrently with the emplacement of the Pebble Creek Formation (Stasiuk et al., 1996).

Table 4-4. Descriptions of the main juvenile and accessory lithic clast types present in the pyroclastic fallout deposits of Pebble Creek Formation.

Lithological Category	Unit 1-1 (Weight %)	Unit 1-2 (Weight %)	Unit 1-3 (Weight %)	Unit 1-4 (Weight %)	Unit 1-5 (Weight %)
White Pumice	94.4	90.9	87.0	62.8	67.4
Banded and Gray Pumice	1.4	3.5	7.1	12.4	19.9
Total Juvenile	*95.8*	*94.5*	*94.1*	*75.2*	*87.2*
Dacite	3.3	2.0	2.0	21.3	5.6
Monzogranite	0.2	0.8	1.8	1.8	4.3
Metamorphic / Other Plutonic	0.3	0.4	0.7	0.5	1.9
Breccia	0.2	2.2	0.8	0.0	0.1
Other Lithics	0.1	0.2	0.5	1.2	0.9
Total Lithics	*4.2*	*5.5*	*5.9*	*24.8*	*12.8*
Total Clasts	*100.0*	*100.0*	*100.0*	*100.0*	*100.0*

Table 4-5. Normalized abundances of all juvenile and accessory lithic clast types from the units of Outcrop 1. Descriptions of all clast types are found in Table 4-4.
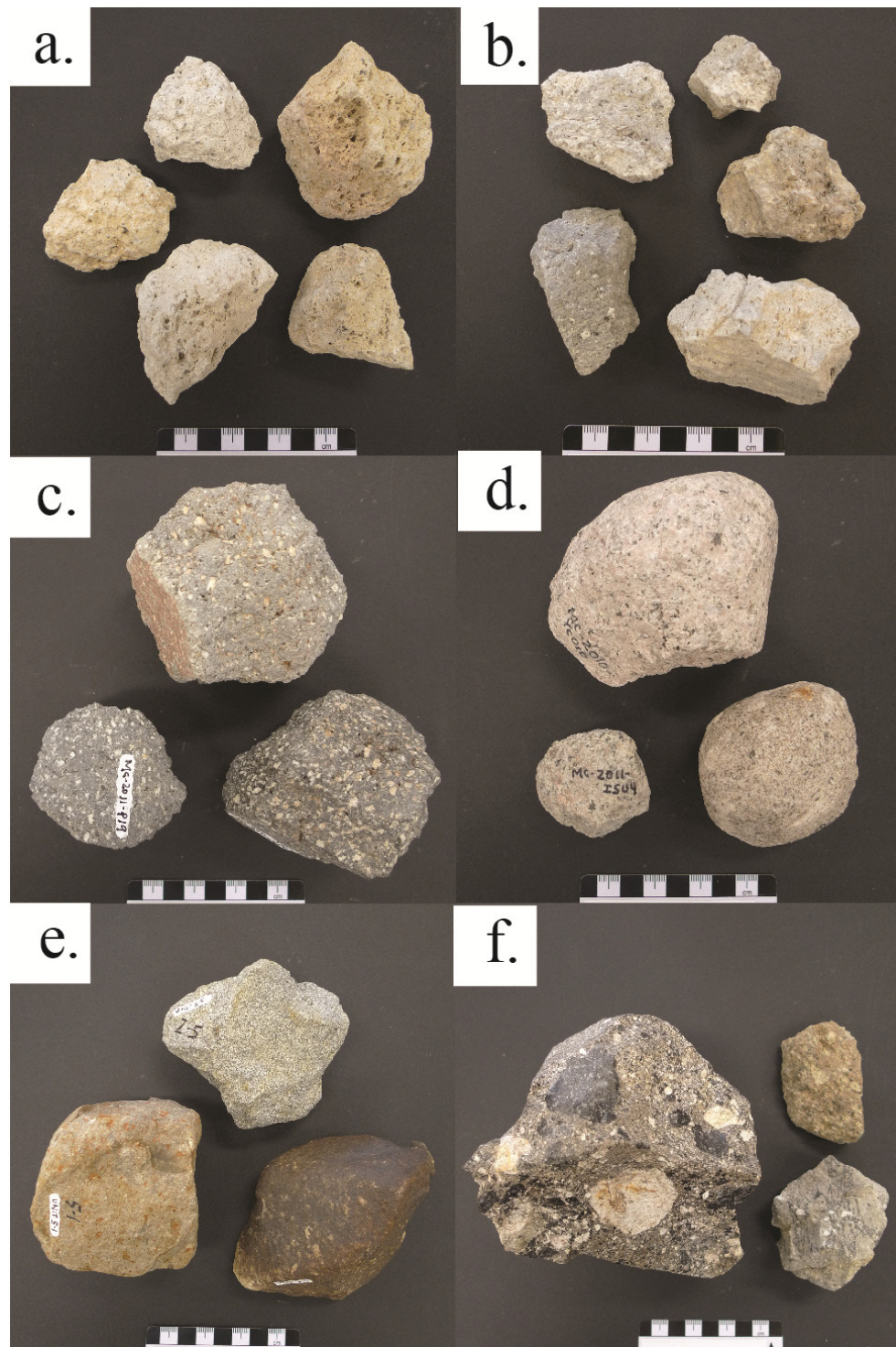
Figure 4-5. Main clast types present in the 2360 B.P. Pebble Creek Formation fallout deposits. a) white pumice; b) gray and banded pumice; c) dacite; d) monzogranite; e) metamorphic and plutonic clasts; f) pumice breccias.
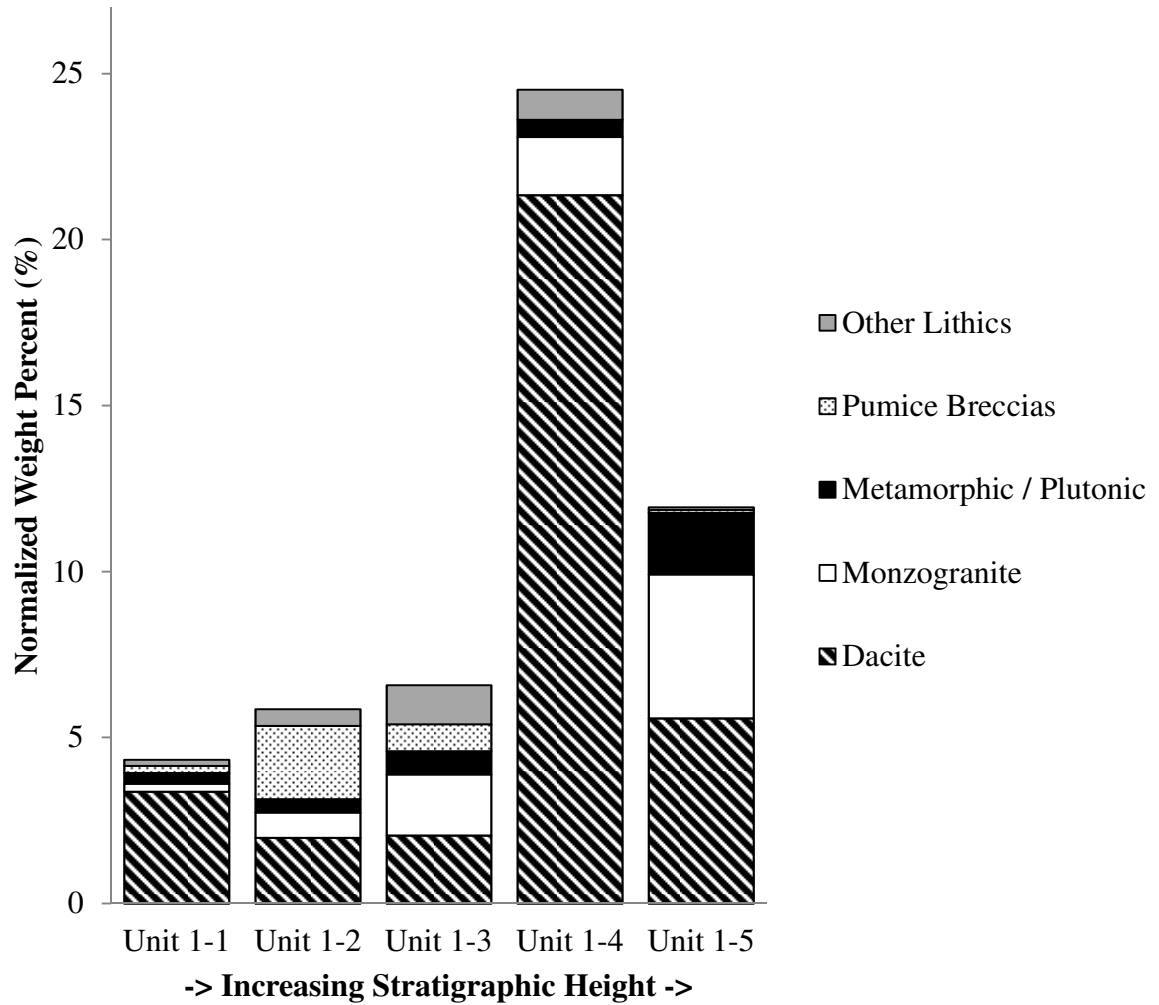
Figure 4-6. Accessory lithic componentry of the units of Outcrop 1. Abundances are shown as normalized weight percent values of the entire unit sampled. Accessory lithics are sorted into 5 lithological categories: (1) dacite clasts, (2) monzogranite clasts, (3) metamorphic and non-monzogranite plutonic clasts, (4) pumice breccias clasts, and (5) other lithic clasts, including unidentifiable clasts.
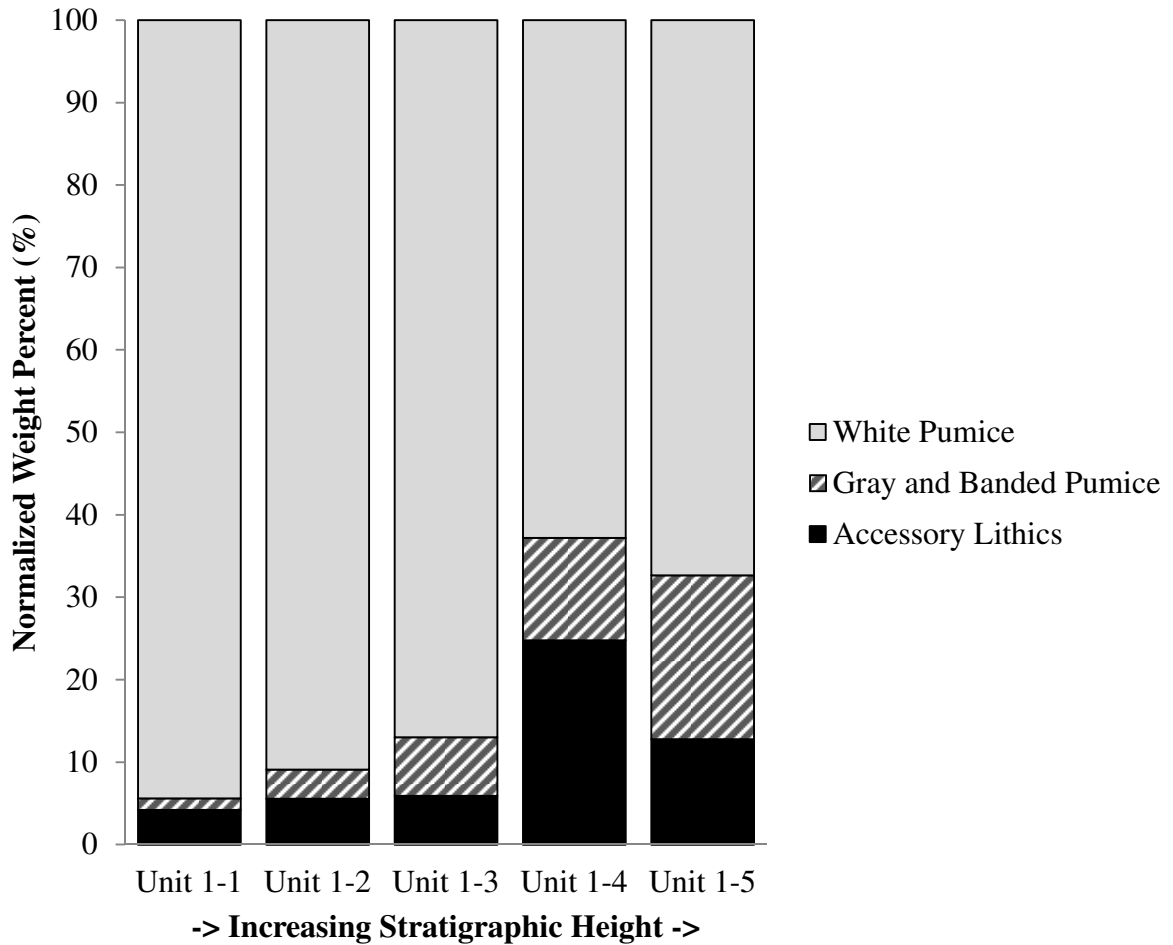
Figure 4-7. Juvenile and total accessory lithic componentry of the units of Outcrop 1. Clasts are subdivided into 3 categories: (1) white pumice, (2) gray pumice and banded pumice, and (3) accessory lithic clasts. Abundances are shown as normalized weight percent values of the unit sampled. Detailed componentry of the accessory lithics is found in Figure 4-6.

4.2 Accessory Lithic Sample Collection

Two types of accessory lithic were selected for further study: the monzogranite and the dacite clasts. These lithic clast types were chosen because they represent the two most abundant classes of accessory lithics within the PCF fallout deposits (Table 4-5), and because their characteristic morphologies differ significantly. The dacite clasts are typically blocky, angular and rough, while many of the monzogranite clasts are highly rounded and smooth. One of the main goals of this study is to examine how these two clast types differ morphologically (and how they are similar), and why.

4.2.1 Pumice Quarry Sample Collection

Many of the samples in this study were recovered from the sorting piles of the Great Pacific Pumice Quarry, located approximately 3 km north of the 2360 B.P. vent (Figure 3-2). The operators of this quarry separate the lighter, economically desirable pumice from the much denser accessory lithics, which are left in large piles around the quarry sorting yards. A total of 115 accessory lithic clasts were collected from these piles, including 96 monzogranite clasts and 19 dacite clasts. In order to minimize sampling bias, samples were chosen at random from a selected sorting pile until the desired number of samples was obtained. Samples were not collected from the sorting piles of a second pumice quarry operating near the MMVC, the Garibaldi Pumice quarry, which is located approximately 4.5 km ENE of the vent (Figure 3-2). These sorting piles were observed to contain large amounts of polymictic, subrounded to rounded, pebble- to cobble-sized clasts, resembling clasts from a fluvial deposit. The Garibaldi Pumice operators confirmed that parts of the pumice deposits at their quarry are underlain by these deposits, likely indicating that this quarry is located at the site of a paleo-river valley. Due to the abundance of clasts within these sorting piles that likely originated from the underlying paleo-river deposits, I decided not to collect or analyze any samples from this location.

4.2.2 In Situ Sample Collection

In order to verify that the monzogranite clasts were indeed originating from the fallout deposits, and not from some other adjacent or underlying source, a suite of in situ accessory lithics were also collected from the nearby proximal pumice deposits of Outcrop 5 (Unit 5-1). These in situ accessory lithics included 13 monzogranite clasts and 20 dacite clasts (e.g. Figure 4-8). The clasts collected in situ are identical in terms of lithology and typical morphology to their respective lithic counterparts collected from the sorting piles of the Great Pacific Pumice quarry.
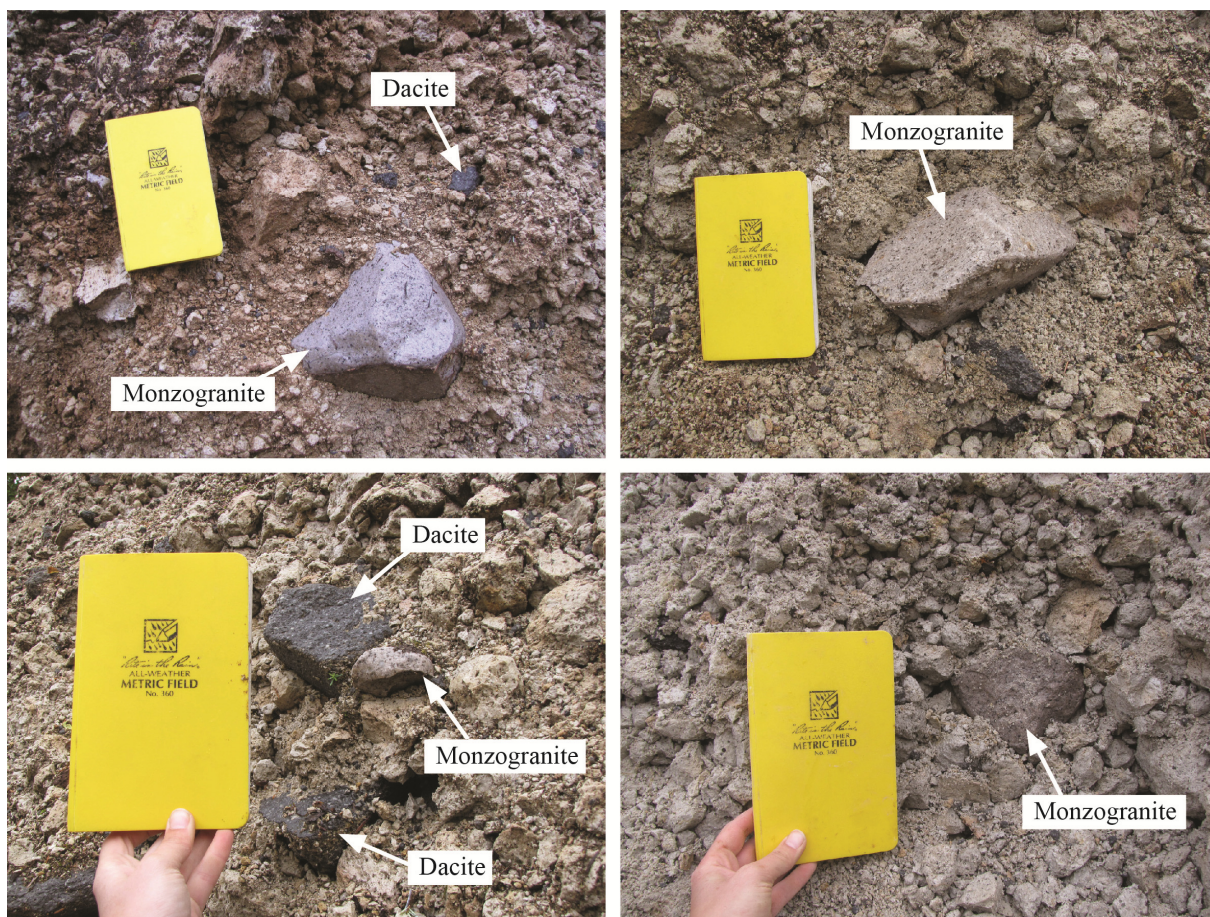
Figure 4-8. In situ monzogranite and dacite accessory lithics from Unit 5-1 (Outcrop 5). The field notebook included for scale measures approximately 12 cm x 19 cm.

4.3 Monzogranite Accessory Lithics

The monzogranite accessory lithic samples analyzed are massive, crystalline rocks with no visible foliation or other fabric, and are pale pink to beige in colour (Figure 4-9). The monzogranite varies in grain size from coarse-grained, with an average grain size of ~5 mm (Figure 4-9a), to medium-grained, with an average grain size of ~ 1 mm (Figure 4-9b). Samples display grain sizes ranging between these two end-members as well. Occasional monzogranite clasts display planar, oxidized fracture surfaces (Figure 4-10), which are likely joint surfaces predating the 2360 B.P. eruption. A few monzogranite clasts also contain fine-grained, medium gray, rounded enclaves of what is likely an intrusion of intermediate composition.
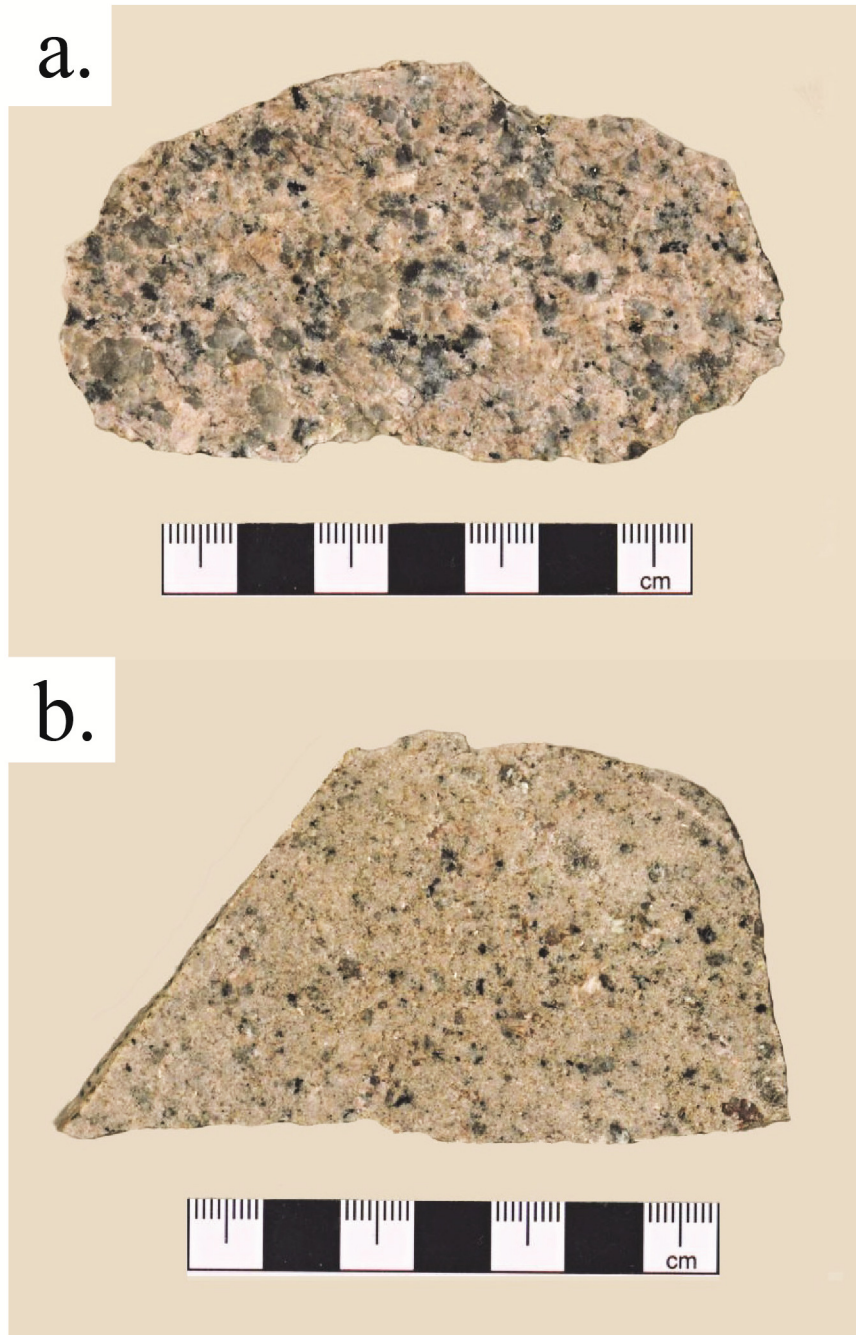
Figure 4-9. Cut monzogranite accessory lithic samples, from the Pebble Creek Formation Fallout deposits, displaying the typical massive texture. a) Example of coarse-grained monzogranite. b) Example of medium-grained monzogranite.
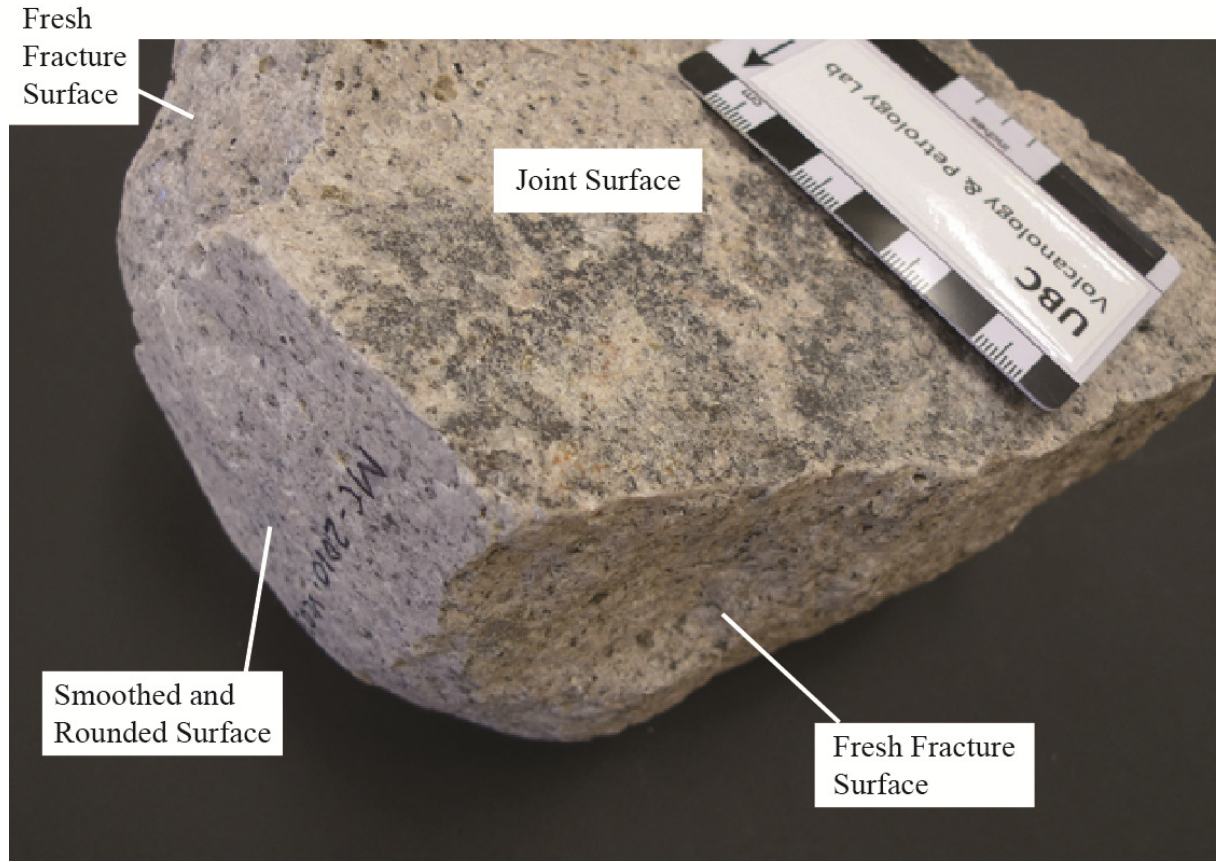
Figure 4-10. Primary, pre-fragmentation joint surface on a monzogranite accessory lithic clast. The upper, planar, slightly oxidized face of this sample is the exposed joint surface. The rough surfaces at the upper left and lower right of the sample are relatively fresh fracture surfaces. The lower left surface of the sample is smoothed and rounded.

4.3.1 Comparison to the Fall Creek Stock

As stated in Chapter 3, the monzogranite accessory lithic samples from the PCF Fallout deposits are lithologically indistinguishable from the Miocene Fall Creek Stock, a plutonic body exposed along Fall Creek and the Lillooet River (Figure 3-2). The Fall Creek Stock is a massive, crystalline, quartz- plagioclase and K-feldspar-rich, biotite-bearing, ochre-weathering plutonic body. Figure 4-11 shows an cut sample of the Fall Creek Stock collected from an outcrop along the banks of the Lillooet River (Figure 3-2); this sample is texturally and mineralogically identical to the coarse-grained monzogranite accessory lithic shown in Figure 4-9a, with the caveat that the Fall Creek Stock sample displays minor signs of weathering. Three of the six Innergex diamond drill holes (BHLT-3,

BHLT-4 and BHLT-5; Figure 3-2, Figure 3-3) also terminate in a pale pink, crystalline, coarse-grained, quartz- plagioclase- K-spar- and biotite-bearing felsic plutonic formation: the Fall Creek Stock. The Fall Creek Stock intersected by these drill holes is typically coarse-grained and equigranular, and is cross-cut by at least one medium-grained monzogranite dyke (Figure 4-12). The overall mineralogy and textures observed in the core closely resemble those observed in the Fall Creek Stock samples collected from the outcrop near the Lillooet river (Figure 4-11), as well as those from the monzogranite accessory lithic sample set (Figure 4-9). Therefore, based upon the lithological similitude and the location of the Fall Creek Stock at the base of the MMVC, the monzogranite accessory lithics are most likely sourced from the extension of the Fall Creek Stock beneath the vent of the 2360 B.P. eruption.

Figure 4-11. Cut monzogranite slab from an outcrop of the Fall Creek Stock near the Lillooet River (location shown on Figure 3-2).

Very little prior analytical work has been carried out on the Fall Creek Stock, or the other similar felsic plutonic bodies in the vicinity of the MMVC. The Fall Creek Stock was originally classified as a quartz monzonite, based upon field descriptions made by Read (1977a) as "an ochre-weathering, biotite leucoquartz monzonite." No known microanalytical work has been performed on the Fall Creek Stock, except for the calculation of a single radiometric biotite K-Ar date, which yielded an age of 10.1 ± 0.6 Ma (Read, 1977b).
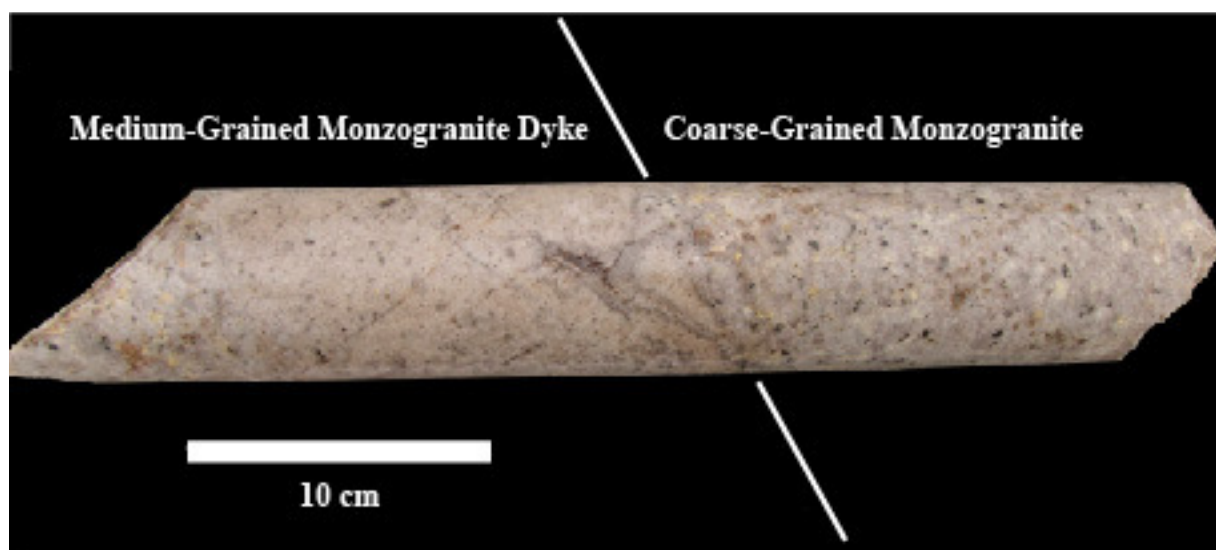
Figure 4-12. Diamond drill core showing contact between medium-grained and coarse-grained monzogranite, from Innergex diamond drill hole BHLT-4.

4.3.2   X-Ray Diffraction

In order to further characterize the mineralogy of the monzogranite, I have carried out X-Ray Diffraction (XRD) analyses on one typical coarse-grained and one typical medium-grained monzogranite sample (the samples shown in Figures 4-7a and 4-7b, respectively). Samples were first crushed and ground to < 0.5 mm grain size, and then reduced to < 10 μm grain size, the optimal grain size range for XRD analysis, by grinding under ethanol in a vibratory agate McCrone Micronizing Mill for 7 minutes. Smear mounts of the finely milled sample powders were analyzed using a Bruker D8 Focus Bragg-Brentano diffractometer in the Department of Earth and Ocean Sciences, at the University of British Columbia. Step-scan X-ray powder diffraction data were collected over a range of 3 – 80

°2θ, with a step size of 0.04°, using Cobalt-K-Alpha (CoKα) radiation. The long fine-focus Cobalt X-ray tube was operated at a voltage of 35 kV and a current of 40 mA. The X-ray diffractograms produced were analyzed using the PDF-4 International Centre for Diffraction Database, using Search-Match software by Bruker.

In order to determine the relative abundances of the various crystalline phases present within each sample, quantitative Rietveld phase analysis of the X-ray powder diffraction data from the samples was completed, using the Topas 4.2 software by Bruker. The final, refined Rietveld phase analysis plots for the coarse-grained and the medium-grained monzogranite samples are shown in Appendix B. The final modal mineralogical abundances of the major and minor crystalline phases for the coarse-grained and the medium-grained monzogranite samples are shown in Table 4-6.

The XRD results (Tables 4-6) show that the two monzogranite samples analyzed are essentially identical in terms of mineralogy. Both have normalized abundances of 37-38% quartz, 35-36% plagioclase, 26% orthoclase and 1% biotite. These modal abundances put these samples in the granite field, and in the monzogranite subfield, of the QAFP classification chart of plutonic rocks (Streckeisen, 1976) (Figure 4-13). Therefore, the original classification of the Fall Creek Stock body as a quartz monzonite (Read, 1977a, 1977b) is technically incorrect.

	Accessory Lithic Monzogranite Samples	
	Coarse-Grained Monzogranite (MC-2010-Ya033)	**Medium-Grained Monzogranite** (MC-2010-Ya011)
Mineral Phase Name	**Weight %**	**Weight %**
Quartz	36.7	37.8
Plagioclase	36.0	35.0
Orthoclase	26.5	26.2
Biotite	0.9	1.0
Total:	*100.0*	*100.0*

Table 4-6. X-Ray Diffraction results for two monzogranite accessory lithic samples from the Pebble Creek Formation fallout deposits: one typical coarse-grained sample, and one typical medium-grained sample. The XRD results show that the two samples have essentially identical mineralogies.
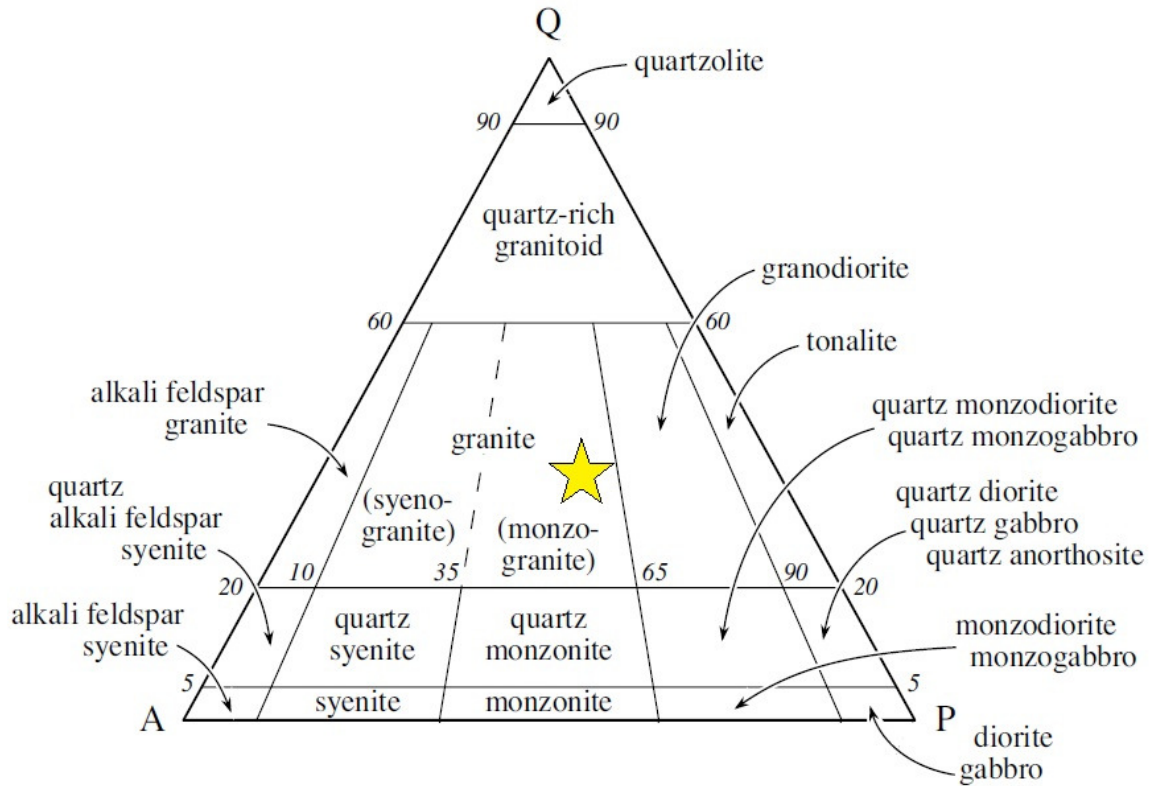
Figure 4-13. Upper part of the QAFP classification chart (modified from Le Maitre (2002), which is based on the figure from Streckeisen (1976)) showing where the monzogranite plots based on mineralogical abundances (star). The endmembers are: Q = quartz, A = alkali feldspar and P = plagioclase. This diagram is valid only for rocks in which the mafic mineral content is less than 90%.

4.4 Dacite Accessory Lithics

The dacite accessory lithic samples from the PCF Fallout deposits are medium to dark gray, reddish-weathering, vesicular, porphyritic, plagioclase- quartz- and biotite-phyric lavas with a fine-grained, hyalocrystalline groundmass (Figure 4-14). As stated earlier, these dacite lithics originate from lavas of the Plinth Assemblage, which make up the bulk of Plinth Peak (Figure 3-1). Columnar joint surfaces – approximately planar, slightly oxidized, and minimally rough – are commonly visible on the dacite lithic clasts (Figure 4-15); The Plinth Assemblage lavas exposed around Plinth Peak are also known to be extensively columnar jointed (Read, 1977a). The Plinth Assemblage dacite has been extensively described in the literature, in terms of lithology, mineralogy and geochemistry (Hickson et al., 1999; Read, 1977a, 1990).

Figure 4-14. Cut face of a dacite accessory lithic clast (Plinth Assemblage).

Figure 4-15. Columnar joint surfaces on a dacite accessory lithic clast (Plinth Assemblage). The lower and right faces of the photographed clast are relatively smooth and planar columnar joint surfaces, while the uppermost face is a relatively rough fractured surface.

5. Morphological Analysis of Lithic Samples

5.1 Mass, Density and Volume Measurements

Densities (g/cm^3) of all monzogranite and dacite accessory lithic samples (ρ_s) weighing less than 10 kg were measured using Archimedes' wet-dry principle, where:

$$\rho_s = \frac{M_{dry}}{M_{dry} - M_{wet}} \times \rho_w \qquad (5.1)$$

Sample density is computed from values of the density of the water (ρ_w), the dry mass of the sample (M_{dry}) and the mass of the sample suspended in water (M_{wet}). For each sample, M_{dry} was determined by averaging three separate measurements of the sample's dry mass. Similarly, the M_{wet} value for each sample was determined by averaging three separate measurements of the sample's mass while suspended from a scale and immersed in water. All samples were soaked overnight (> 12 hours) prior to the measurement of M_{wet}, ensuring that water had permeated all interconnected pore spaces or fractures within the samples. Values of ρ_{water} were corrected for temperature based on regular measurements of the water in the bucket. All samples masses and densities are reported in Appendix C1. The densities of the 7 largest accessory lithic samples (> 10 kg) were not measured directly although their dry masses were recorded (Appendix C1).

Measured values of density for all lithic samples are displayed in Figure 5-1, where they are plotted against their calculated volumes. Sample volume (V) is calculated from measured values of mass and density:

$$V = \frac{M_{dry}}{\rho_s} \qquad (5.2)$$

The approximate volumes of the 5 largest monzogranite samples and 2 largest dacite samples, weighing > 10 kg, were calculated using the average monzogranite and dacite densities, respectively. The calculated volumes of all samples are found in Appendix C1.

The measured densities of the monzogranite and dacite sample sets do not increase or decrease significantly with changing volume (Figure 5-1). The monzogranite samples show very little variation in density, ranging from a minimum of 2.54 g/cm^3 to a maximum of 2.62 g/cm^3, with a mean density of 2.59 g/cm^3 $\pm$ 0.01 g/cm^3 (Appendix C1). The dacite samples, however, show considerably more variability in density, ranging from 2.26 g/cm^3 to 2.65 g/cm^3, and averaging 2.47 g/cm^3 $\pm$ 0.10 g/cm^3

(Appendix C1). The high degree of variation in density among the dacite samples is mostly due to variations in vesicularity among clasts of this volcanic assemblage; in contrast, the intrusive monzogranite has virtually no porosity.
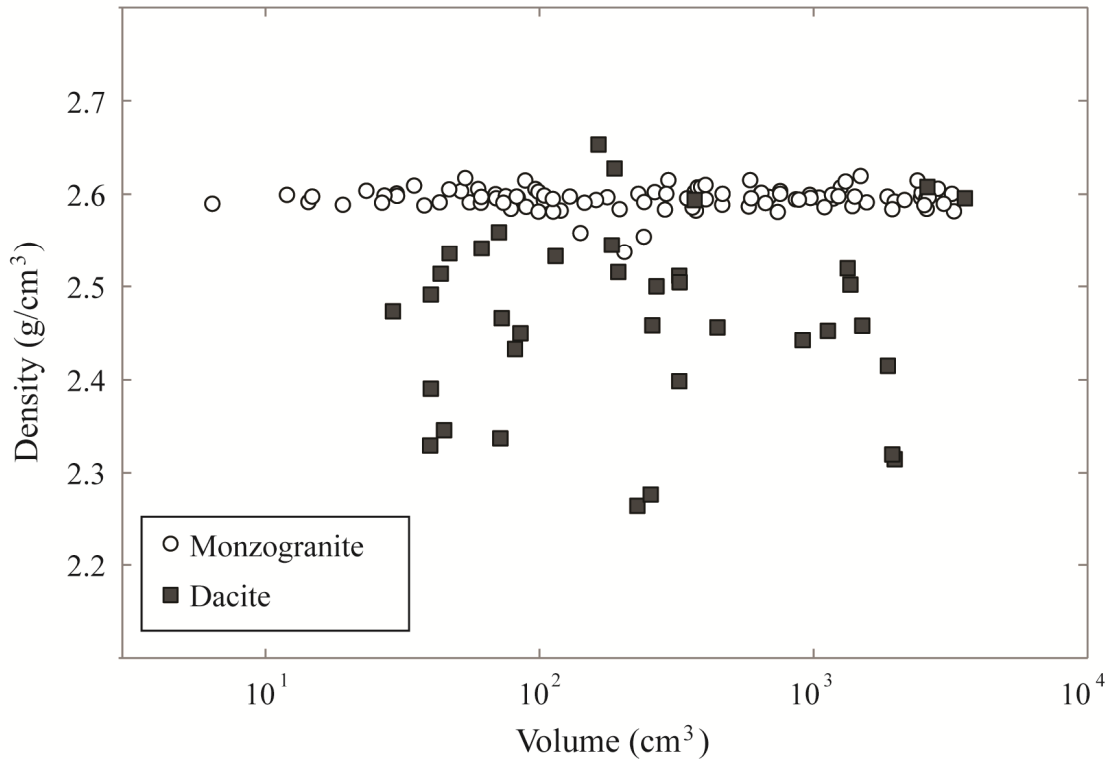
Figure 5-1. Density vs. volume of monzogranite and dacite accessory lithic samples as measured by the Archimedes wet-dry method. Volumes are calculated by dividing each sample's measured density with its dry sample mass.

5.2 Form Measurements

The quantification of form requires the accurate measurement of the length, width and height of a particle. These three measurements are usually referred to as the long, intermediate and short axes of a particle, and a variety of notations have been used to denote them, including a, b and c (Krumbein and Pettijohn, 1938; Zingg, 1935), L, I and S (Sneed and Folk, 1958) and D', D'' and D''' (Wentworth, 1922). Here, I will denote these axes as a (long axis), b (intermediate axis) and c (short axis). A number of different systems and methods have also been described in the literature to select and measure each of these three axes (see reviews in Barrett, 1980; Blott and Pye, 2008).
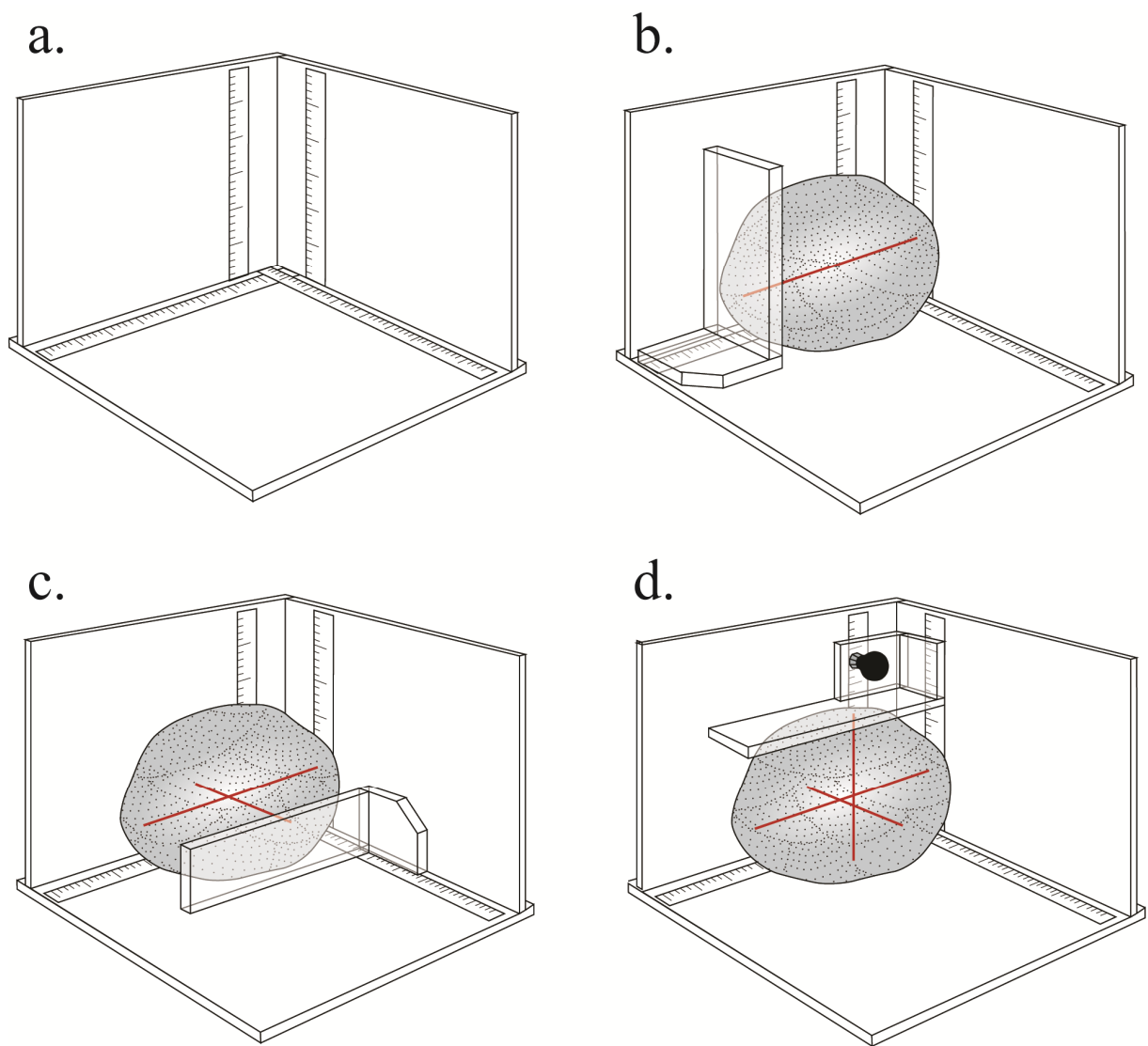
Figure 5-2. Measurement of the three principal orthogonal axes on lithic clast. a) Diagram of the 3-sided plexiglass box, with inlaid metal rulers, used as a measurement frame for the clasts. b) Measurement of the long axis ("a") of the clast. c) Measurement of the short axis ("c") of the clast, by rotating the clast about its long axis until the shortest orthogonal axis is found. d) Measurement of the intermediate axis ("b") of the clast, which is simply the axis orthogonal to both axis "a" and axis "b". Note that although all three axes are orthogonal to one another, they do not necessarily intersect, or pass through the centroid of the sample.

Here, I designed a 3-sided plexiglass box, measuring approximately 40 cm x 40 cm x 30 cm, with inlaid metal rulers, to serve as a measurement frame for the clasts (Figure 5-2a, Appendix D1). Samples were placed inside the frame and manually rotated until the long axis 'a' was identified and aligned parallel to both the base and one of the walls of the frame (Figure 5-2b). This axis was then measured by pushing an "L"-shaped plexiglass block up against the edge of the sample, and the length of this axis was read from one of the inlaid rulers (Figure 5-2b). The sample was then rotated about this long axis, until the short axis 'c,' defined here as the shortest dimension of the sample orthogonal to the long axis, was identified, aligned such that it was perpendicular to the base of the frame, and measured (Figure 5-2c). Lastly, the intermediate axis 'b' is measured as the third dimension, orthogonal to both 'a' and 'c' (Figure 5-2d). This method of axis measurement most closely resembles that described in Krumbein (1941), with the difference that Krumbein (1941) defined the intermediate axis 'b' as being the longest axis orthogonal to the long axis 'a,' and defined the short axis 'c' as being the remaining axis orthogonal to both 'a' and 'b.'

The three orthogonal axes were measured for the 109 monzogranite and 39 dacite accessory lithic samples collected (Appendix D2). The axes of five samples were measured three times, at intervals of a few hours to a few days, in order to test the reproducibility of the axis measurements (Appendix D3). In all cases, variation of no more than 5 mm (and no more than 4.9% of the average axis length measured) was recorded for the repeat measurements of each axis.

Sneed and Folk (1958) proposed the use of a triangular diagram in order to plot the axial data characterizing a particle's form (Figure 5-3). The three apices of this diagram represent: (1) compact (or "equant"), (2) elongated, and (3) platy particles. Data points are plotted in the Sneed and Folk Shape Classification diagram according to compactness, as measured by the ratio $\frac{a}{c}$, and according to the value of $\frac{a-b}{a-c}$, which classifies particles into platy, bladed and elongate forms (Figure 5-3). Data points plotted upon the Sneed and Folk diagram occur within one of 10 class subdivisions: Compact, Compact-Bladed, Compact-Elongate, Compact-Platy, Bladed, Elongate, Platy, Very-Bladed, Very-Elongate and Very-Platy. Arcuate lines on the diagram also show the value of each particle's Maximum Projection Sphericity (Ψ_p) (Sneed and Folk, 1958):

$$\Psi_p = \sqrt[3]{\frac{c^2}{a \times b}} \qquad\qquad (5.3)$$

This value provides an approximation of the particle's overall sphericity based only on the axes. It should be noted that even though this metric's name contains the term "sphericity," it is better thought of as a measure of equancy. Although it does yield a value of $\Psi_p \approx 1$ for spheroids, it will also yield a value of $\Psi_p = 1$ for a perfect cube, a shape that is highly equant but not very spherical.
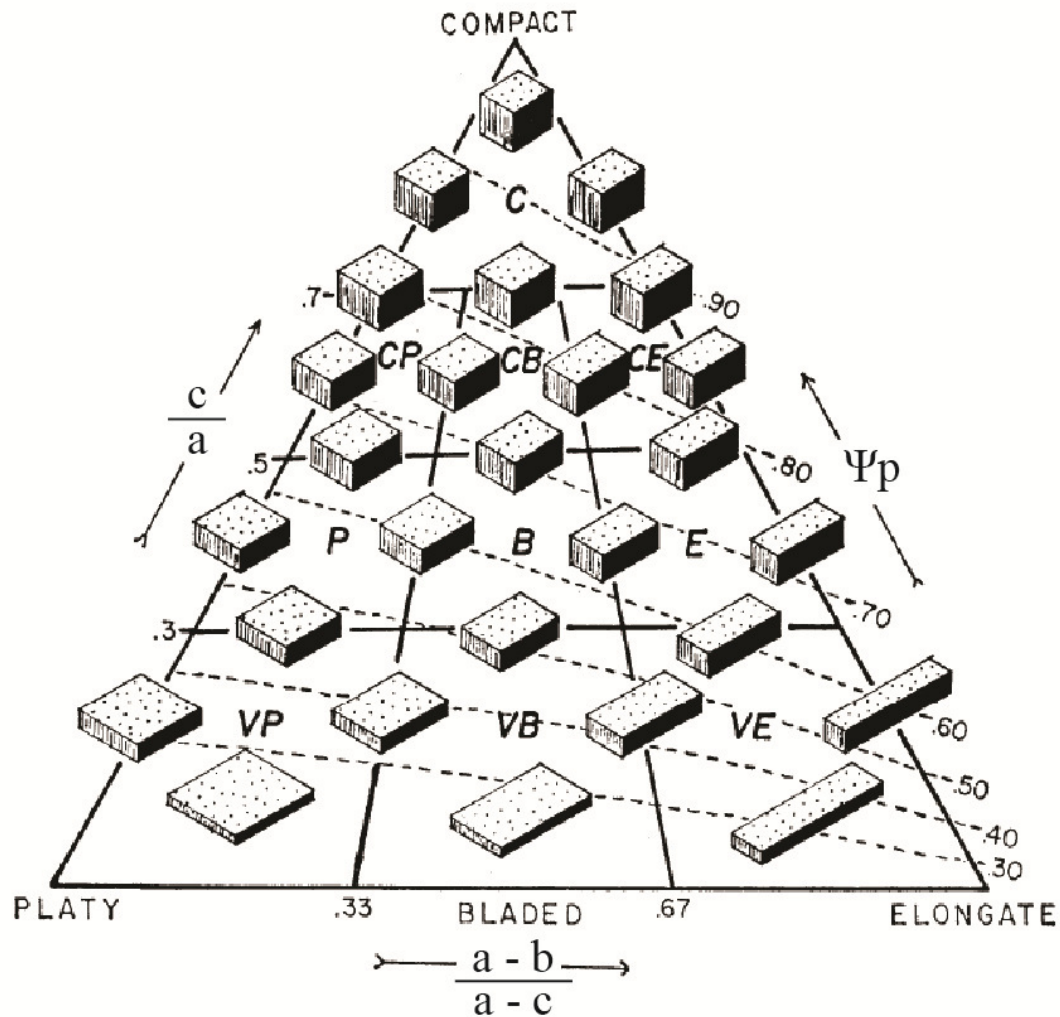
Figure 5-3. Shape classification diagram reproduced from Sneed and Folk (1958). Particles are plotted on this diagram according to the ratios $\frac{c}{a}$ and $\frac{a-b}{a-c}$ calculated from the particle's measured long axis (a), intermediate axis (b) and short axis (c). The third side of the diagram is a measure of equancy, measured as the particle's Maximum Projection Sphericity (Ψ_p) (see text). The 10 shape classes on this diagram are Compact (C), Compact-Platy (CP), Compact-Bladed (CB), Platy (P), Bladed (B), Elongate (E), Very Platy (VP), Very Bladed (VB) and Very Elongate (VE).

Figure 5-4 shows the axial data collected for the monzogranite and dacite accessory lithic samples. This axial data is plotted on Sneed and Folk Shape Classification diagrams, and displayed in histograms showing both the relative abundances of the clasts contained within each of the 10 main Sneed and Folk form class subdivisions and the Ψ_p values for the sample populations. Results were plotted on the Sneed and Folk diagram using the Excel spreadsheet developed by Graham and Midgley (2000). Figure 5-5 displays the Ψ_p values of the clasts plotted against clast volume.

Figures 5-4 and 5-5 also show results for a subdivision of the monzogranite sample set: intact monzogranite samples, which I define as samples with < 10% of their surfaces made up of freshly fractured surfaces (Figure 5-4b, Figure 5-5b, Figure 5-6a). The samples that have $\geq$ 10% of their total surface areas made up of freshly fractured surfaces will be termed the broken monzogranite samples (Figure 5-6b). The intact monzogranites are clasts with morphologies that were primarily generated by non-disruptive processes, such as abrasion by ash-sized particles (Figure 5-6a). The broken monzogranites are characterized by prominent, relatively recent fracture surfaces, which are typically quite planar and rough, and bear angular edges (Figure 5-6b). Most of the broken monzogranites show at least some signs of non-disruptive comminution (i.e. parts of their surfaces are quite smooth and rounded), indicating that these samples have been affected by both gradual abrasive processes and sudden, relatively recent breakages. Therefore, the two subdivisions of the monzogranite accessory lithic sample set were chosen to distinguish clasts which have been primarily affected by either non-disruptive comminution alone, or a combination of non-disruptive comminution and one or more disruptive collisions just prior to or during their ejection and emplacement. The types of fracture surfaces visible on the monzogranite clasts are discussed further in Section 5.6.1. A subdivision between intact and broken clasts was not possible for the dacite accessory lithic sample set, as the dacite clasts do not display fresh fracture surfaces that are easily distinguishable from surfaces shaped by non-disruptive processes.
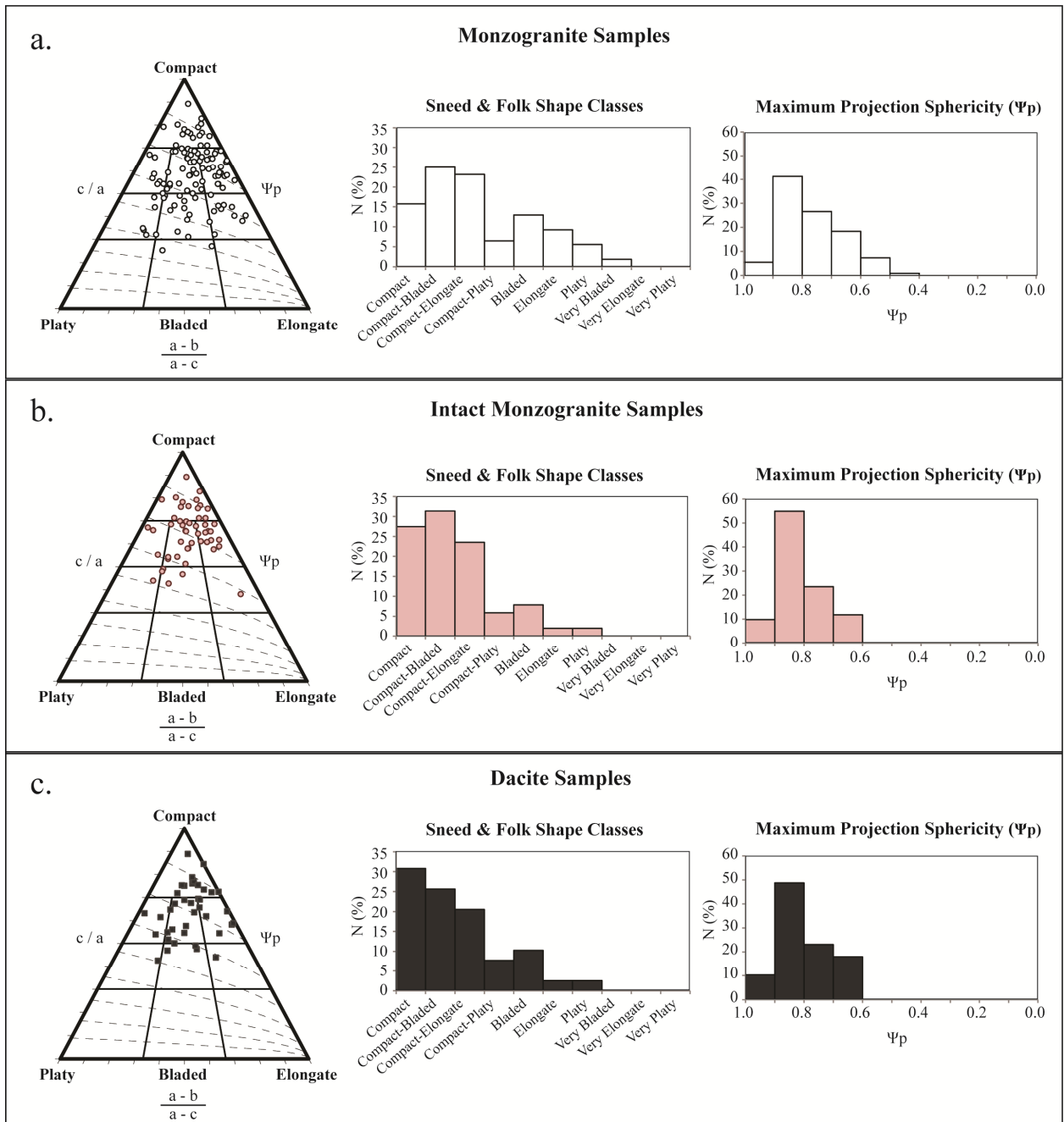
Figure 5-4. Form data for monzogranite and dacite accessory lithic samples, based on orthogonal axial measurements of each sample. Data is shown plotted on Sneed and Folk (1958) Shape Diagrams (left), in histograms showing the distribution of samples in each Sneed and Folk Shape class (middle), and in histograms displaying the distribution of the samples' calculated Maximum Projection Sphericity (right). Maximum Projection Sphericity (Ψ_p), a measure of equancy (see text). a) Form data for all 109 monzogranite accessory lithic samples. b) Form data for the 51 intact monzogranite accessory lithic samples. c) Form data for all 39 dacite accessory lithic samples.
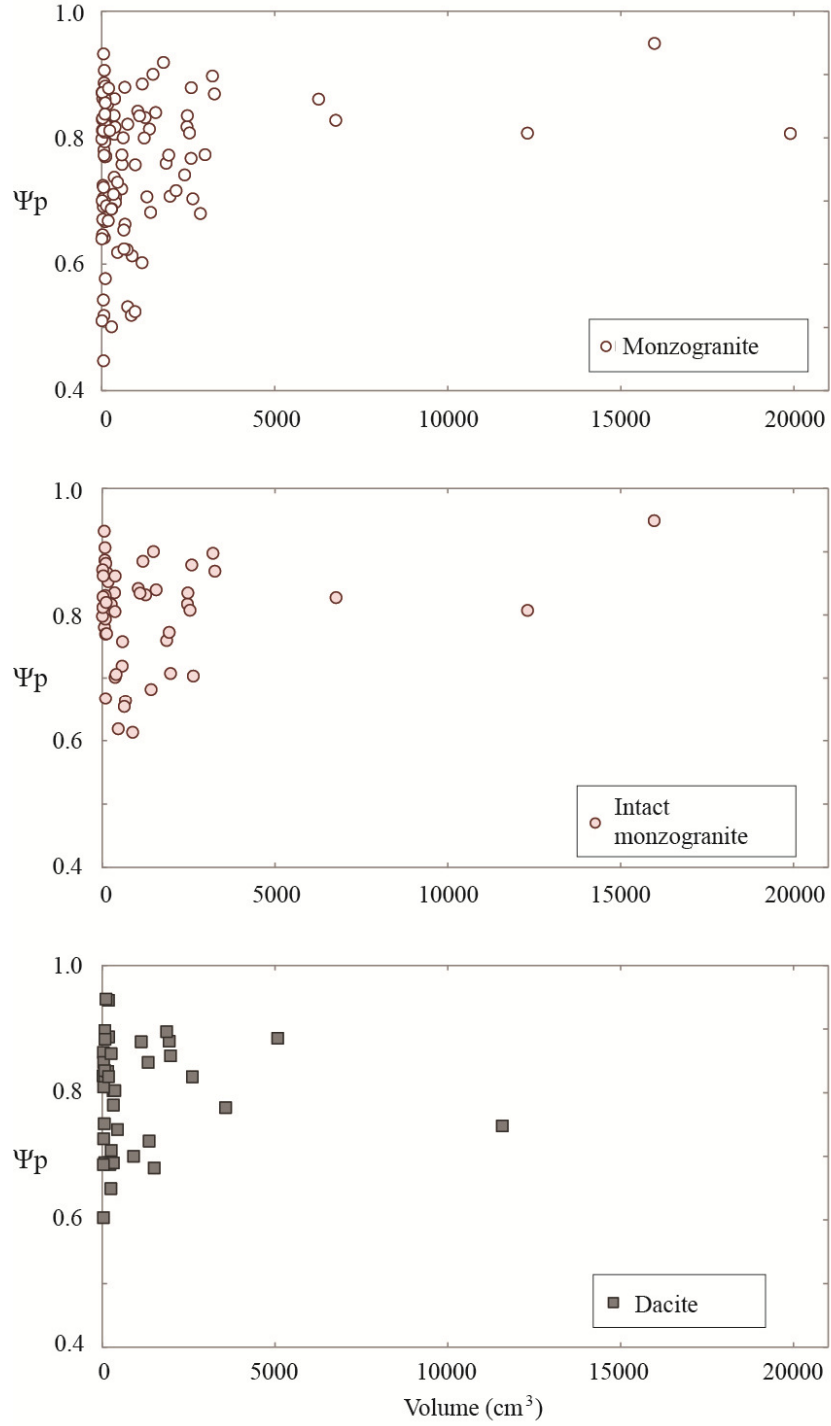
Figure 5-5. Maximum Projection Sphericity (Ψ_p) values for all monzogranite and dacite clasts. Ψ_p is a measure of the equancy of clasts (see text). a) Ψ_p data for all 109 monzogranite accessory lithic samples. b) Ψ_p data for the 51 intact monzogranite accessory lithic samples. c) Ψ_p data for all 39 dacite accessory lithic samples.
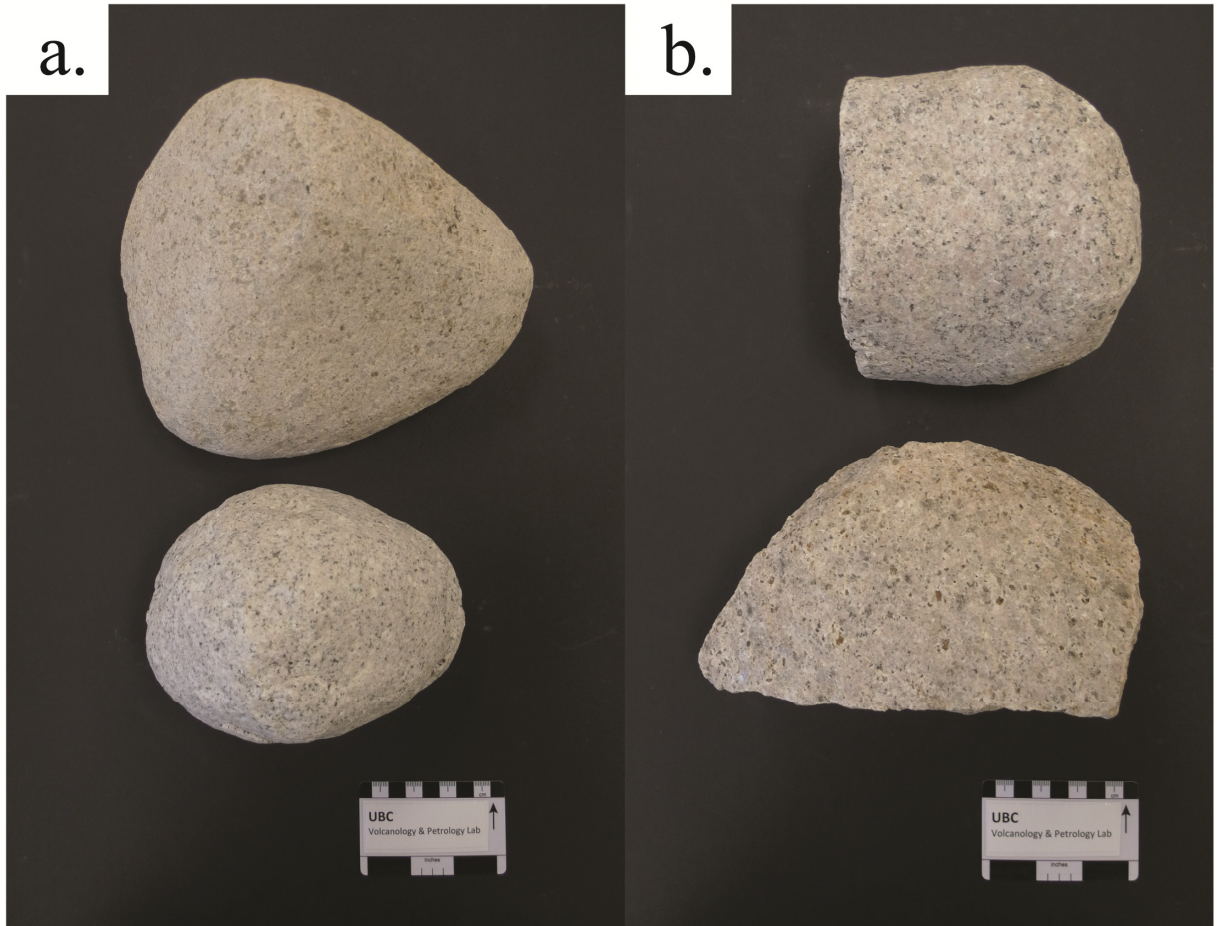
Figure 5-6. Intact versus broken monzogranite accessory lithic clasts. a) Examples of intact monzogranite clasts; note that nearly all of the surfaces of these samples are rounded and smoothed, indicating that no late disruptive collisions occurred to break these clasts. b) Examples of broken monzogranite clasts; note that while part of the clasts' surfaces display signs of smoothing and rounding, a significant portion of their surfaces are relatively rough and recent fracture surfaces.

Overall, the complete monzogranite dataset is scattered over 8 of the 10 Sneed and Folk shape classes, but is concentrated within the Compact-Bladed, Compact-Elongate, Compact and Bladed fields (Figure 5-4a). This dataset is similarly spread out in terms of Maximum Projection Sphericity (Ψ_p), with values ranging from $\Psi_p = 0.45$ to $\Psi_p = 0.95$, with a mean of $\Psi_p = 0.76 \pm 0.11$ (1σ) (Appendix D2). The two monzogranite population subsets, intact samples and broken samples, overlap but are centered in different parts of the Sneed and Folk diagram (Figure 5-4b). The intact samples cluster principally about the Compact, Compact-Bladed, and Compact-Elongate fields, and have Ψ_p values ranging from 0.61 to 0.95, with a mean of $\Psi_p = 0.80 \pm 0.08$ (Figure 5-4b; Appendix D2). Therefore, the intact monzogranite samples are overall more compact than the broken monzogranite samples, which display more variation in form. We may infer from this relationship that disruptive collisions (which affected the clasts from the broken monzogranite subset prior to their eruption) tend to diminish the compactness of the monzogranite clasts (Figure 5-7a). Conversely, the intact monzogranite samples, with morphologies only affected by gradual non-disruptive processes, have progressed towards the compactness endmember of the Sneed and Folk diagram. Therefore, it seems logical that the gradual non-disruptive comminution processes that have shaped the intact monzogranite sample subset will slowly drive particles towards compactness (Figure 5-7b).

The dacite samples cluster principally around the Compact, Compact-Bladed and Compact-Elongate fields, and have relatively high Ψ_p values, ranging from 0.60 to 0.95, with a mean of $\Psi_p = 0.80 \pm 0.09$ (Figure 5-4c; Appendix D2). The dacite sample set is therefore more compact than the complete monzogranite dataset. The dacite sample set is, however, statistically indistinguishable from the intact monzogranite subset in terms of range and mean of Maximum Projection Sphericity and distribution of samples belonging to the various Sneed and Folk Shape classes (Figure 5-4b, c).

Figure 5-5 shows that a certain covariance exists between Ψ_p and sample volume for the monzogranites. The monzogranite samples < 3000 cm^3 display a wide range in Ψ_p values, from 0.45 to 0.93 (Figure 5-5a). However, the monzogranite samples > 3000 cm^3 display a much narrower and higher range in Ψ_p values, from 0.81 to 0.95 (Figure 5-5a). The intact monzogranites (Figure 5-5b) and the dacites (Figure 5-5c) also display a similar, albeit less pronounced, increase in minimum Ψ_p with increasing size.

It should also be noted that none of the samples measured plot within the Very Platy or Very Elongate shape fields of the Sneed and Folk diagrams (Figure 5-4). Particles with very platy or very elongate forms would be quite fragile, and likely would not survive the volcanic eruption and emplacement processes without undergoing further breakages. Disruptive collisions affecting particles of these forms would most likely reduce the long axis of the particles, while affecting to a lesser degree the short and intermediate axes, forcing the particles in the direction towards compactness (Figure 5-7a).

Even though monzogranite and dacite have very different physical properties, the forms of the intact monzogranites, which did not undergo a major disruptive collision just prior to their eruption and emplacement, are nearly identical to the forms of the dacite accessory lithics (Figure 5-4). Because the dacite is relatively weak and friable, the effect on form of a disruptive collision affecting a dacite clast within the volcanic conduit may be rapidly undone by other minor collisions and abrasion. Perhaps the development of compact forms occurred much more rapidly and efficiently for the dacite, while broken monzogranites required longer timescales to regain their compact and rounded appearance. Many of the dacite clasts display one or more faces that appear to be old columnar joint surfaces. Therefore, while minor joints and fracture sets occur in the Fall Creek Stock monzogranite, pervasive columnar jointing likely exists within the Plinth Assemblage deposits. The spacing of the columnar joints may have an influence on the final form of the dacite samples, by controlling the dimensionality of the blocks being incorporated into the stream of erupting material.

It should be noted that measurements of the three orthogonal axes of a particle provide data solely about the form, or dimensionality, of the particle, irrespective of the particle's roundness or surface roughness. Therefore, axes measurements can only reveal part of the total morphological information carried by a clast.
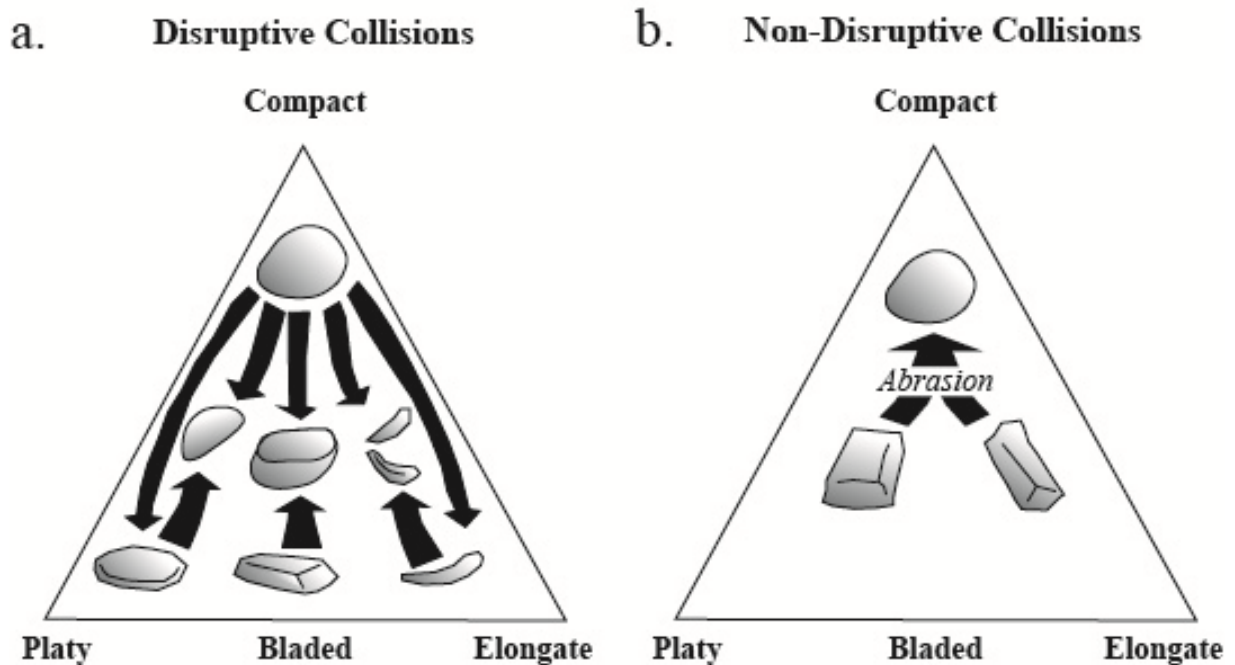
Figure 5-7. Schematic diagram of how disruptive and non-disruptive collisional events tend to affect the form of accessory lithic clasts. Figures are shown as simplified Sneed and Folk Shape Classification diagrams (Figure 5-3). a) Potential effect of disruptive collisions on particles of various morphologies; relatively compact particles that break will likely suffer a significant reduction in compactness, while relatively platy, bladed or elongate particles that break will likely increase their compactness. b) Effect of non-disruptive collisions (e.g. abrasion) on irregular or blocky particles; the rounding or corners and smoothing of any protrusions will gradually increase most particles' compactness.

5.3 Perimeter Measurements

Additional morphological information about the lithic clasts is embedded in the perimeters of each clast. A perimeter value of a clast is dependent on the form (i.e. dimensionality), roundness (i.e. angularity) and, to a certain extent, the surface roughness of the clast outline in question. The manual measurement of clast perimeters, using such implements as lengths of string or tape, is cumbersome and time consuming. However, the advent of digital photography and image analysis software in recent decades has made the quantification of 2D views of lithic clast outlines straightforward.
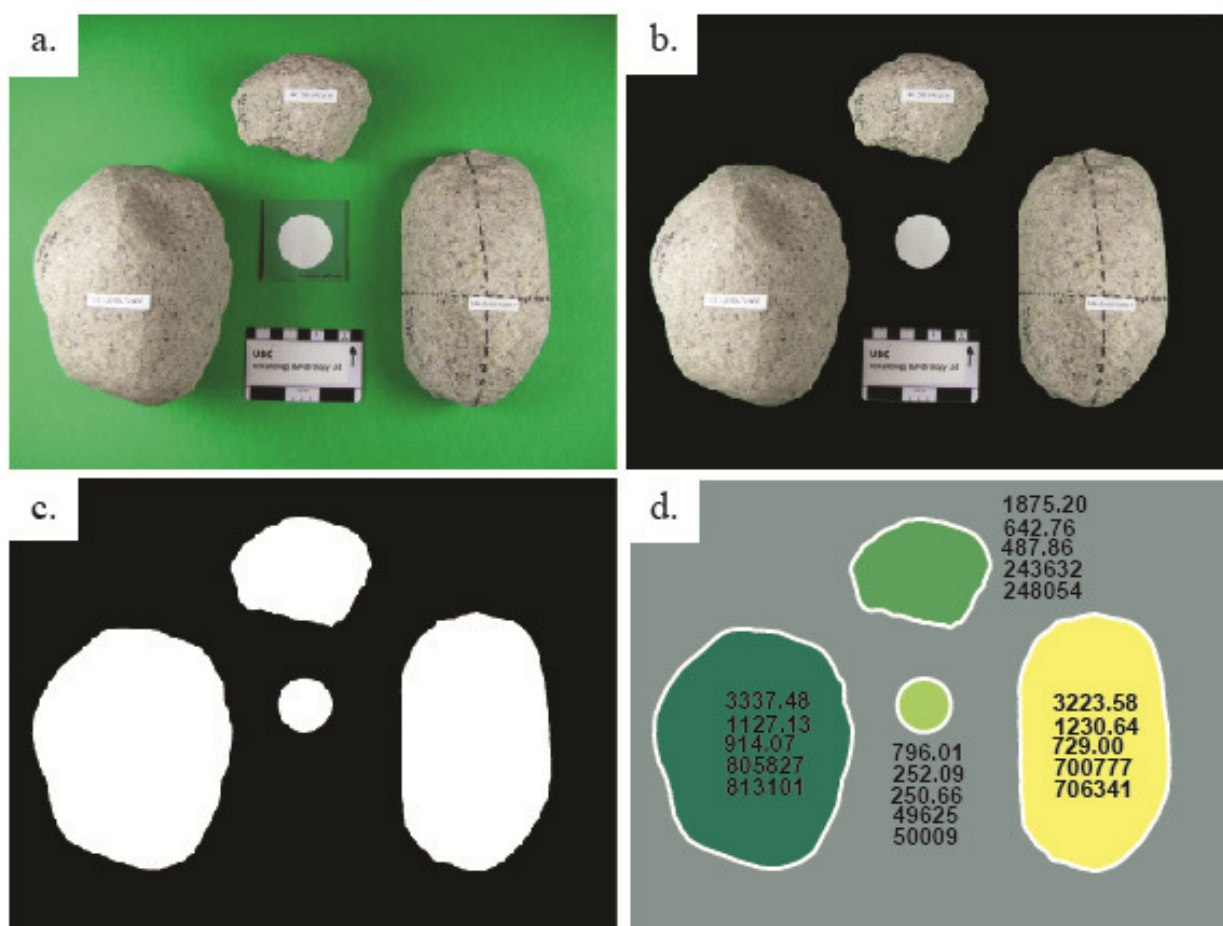
Figure 5-8: Image analysis methodology, showing the stages of image analysis of a single photograph. a) Original photograph taken of monzogranite accessory lithic clasts. b) The green background of the photograph is selected and turned to black in Adobe Photoshop. c) All remaining non-black regions of the photograph are converted to white in Adobe Photoshop, and the scale bar is erased. d) The black and white image is imported into Matlab®, where a script modified from Manga et al. (2011) contours all distinct white regions in the image, and calculates a suite of shape parameters relating to each detected particle. From top to bottom, the shape parameters listed for each contoured clast are, in unscaled pixel counts: perimeter (P_{image}), major axis (a_{image}), minor axis (b_{image}), area (A_{image}) and convex hull area (A_{convex}).

All of the clasts from the accessory lithic sample set analyzed in Subsections 5.2 and 5.3 (109 monzogranite and 39 dacite clasts) were photographed using a digital camera. Samples were photographed in well-lit conditions against a solid-coloured background (e.g. Figure 5-8a; all other photographs are found in Appendix E1). All samples were positioned such that their long and intermediate axes were approximately horizontal and their short axes were approximately vertical. Photographs were taken from directly above, looking down at the samples. A size standard, a white

72

circle measuring exactly 40.0 mm in diameter, was included in each of the photographs. Images were first processed in Adobe Photoshop CS5, where the solid background colour was converted to fully black (Figure 5-8b), and the clasts and standard circle were converted to white (Figure 5-8c). I then followed the image analysis protocol described in Manga et al. (2011), whereby the black and white images are imported into Matlab® and analyzed using a shape analysis script (Appendix E2). This Matlab® script, modified from that used in the electronic supplement of Manga et al. (2011), detects all discrete white shapes larger than a specified pixel threshold and computes the cross-sectional area (A_{image}), perimeter (P_{image}), major axis (a_{image}) and minor axis (b_{image}) and convex hull area (A_{convex}) of each shape via pixel counts (Figure 5-8d).
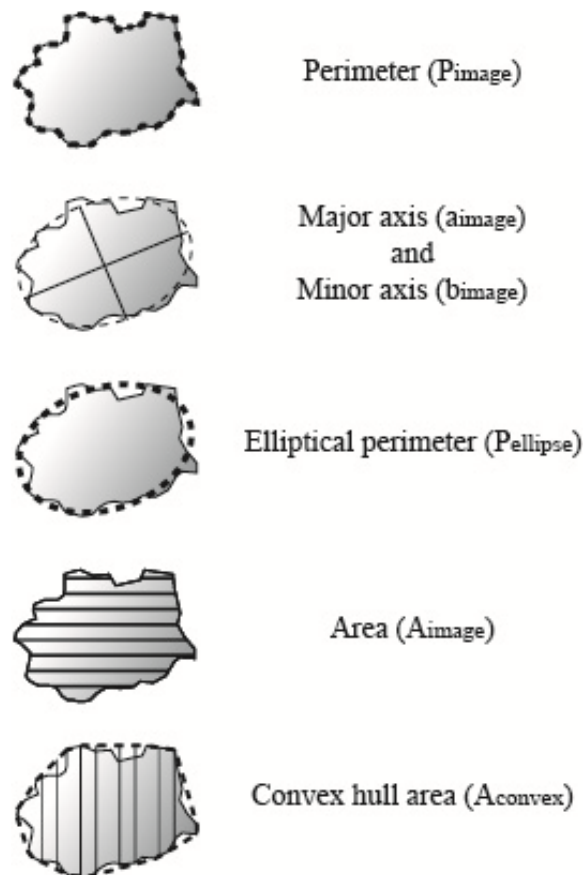
Figure 5-9. Visual representations of the shape parameters computed via image analysis.

Visual representations of the five computed shape parameters are shown in Figure 5-9. The major and minor axes computed in Matlab® are scalars that represent the lengths of the major and minor axis of the ellipse that has the same normalized second central moments as the clast shape (i.e. the major and minor axes of the best-fit ellipse to the clast's outline) (Figure 5-9). The convex hull area is the area of the smallest convex polygon that can encompass the clast outline (Figure 5-9). The five computed parameters may be converted into absolute values (e.g. in millimeters or centimeters) by using the computed values measured for the standard circle of fixed diameter contained within each photograph. However, I have chosen to analyze metrics which are unitless, and thus such conversions are unnecessary.

The first metric I analyzed is circularity (C), which is defined as:

$$C = \frac{\left(P_{image}\right)^2}{4\,\pi\,A_{image}} \qquad\qquad (5.4)$$

C = 1 for a perfect circle (or any image of a perfect sphere), and 0 < C < 1 for any other shape. Thus, values of C ≈ 1 denote nearly circular shape outlines, while values of C ≪ 1 denote either a very elongate, very angular, very irregular or very rough surfaced shape. This metric has previously been referred to as the Shape Factor (e.g. Shea et al., 2010) or Roundness "R" (e.g. Manga et al., 2011). I have chosen to discontinue the use of the name 'Roundness' for this metric, as it can counter intuitively yield very low values for very round shapes if they are quite elongate, for example a flattened ellipse. This metric does not indicate how "round" a shape is, strictly speaking, only how similar it is to a circle.

The second metric I employ is ellipticity (E), which I define as:

$$E = \frac{P_{ellipse}}{P_{image}} \qquad\qquad (5.5)$$

where P_{image} is the aforementioned clast perimeter measured by the Matlab® script. $P_{ellipse}$ is the perimeter of an ellipse with the major and minor axes equaling those measured on the image (a_{image} and b_{image}), calculated with Ramanujan's formula for the approximation of an ellipse based upon its major and minor axes:

$$P_{ellipse} = \pi \left(3\left(\frac{a_{image}}{2} + \frac{b_{image}}{2} \right) \right.$$

$$\left. - \sqrt{\left(\frac{3a_{image}}{2} + \frac{b_{image}}{2} \right)\left(\frac{a_{image}}{2} + \frac{3b_{image}}{2} \right)} \right) \qquad (5.6)$$

With this metric, as with circularity, E = 1 for all ideal ellipses (including circles), and $0 < E < 1$ for all other shapes. Image analysis results for the intact monzogranite and dacite accessory lithics are shown in Figure 5-10; circularity is plotted against sample volume in Figure 5-10a, and ellipticity is plotted against sample volume in Figure 5-10b.

The circularity values obtained for the intact monzogranite samples range from $0.75 \leq C \leq 0.95$, with an average of $C = 0.90 \pm 0.04$ (Appendix E3). The circularity values measured for the dacite samples range from $0.70 \leq C \leq 0.87$, with an average of $C = 0.78 \pm 0.04$ (Appendix E3). Although a clear distinction exists between the intact monzogranite and dacite sample populations, there is still significant overlap between the two sample sets (Figure 5-10a). Much of this overlap is attributable to the three intact monzogranite samples that have $C < 0.84$. These three samples are quite elongate, and the two smaller ones have somewhat rough surfaces.

The ellipticity values obtained for the intact monzogranite samples range from $0.94 \leq E \leq 0.98$, with an average of $E = 0.96 \pm 0.01$ (Appendix E3). The ellipticity values measured for the dacite samples range from $0.87 \leq E \leq 0.95$, with an average of $E = 0.92 \pm 0.02$ (Appendix E3). A very clear distinction occurs between the ellipticity values of the intact monzogranite and dacite sample sets, with almost no overlap occurring between the two populations (Figure 5-10b).

Circularity and ellipticity data for the monzogranite broken clasts are listed in Appendix E3. The broken monzogranite sample set displays a significant range of C ($0.52 \leq C \leq 0.92$) and E ($0.86 \leq E \leq 0.98$), and relatively low average C (0.81 ± 0.08) and E (0.94 ± 0.02) values, showing that overall the broken monzogranites are less circular and elliptical than the intact monzogranite sample set.
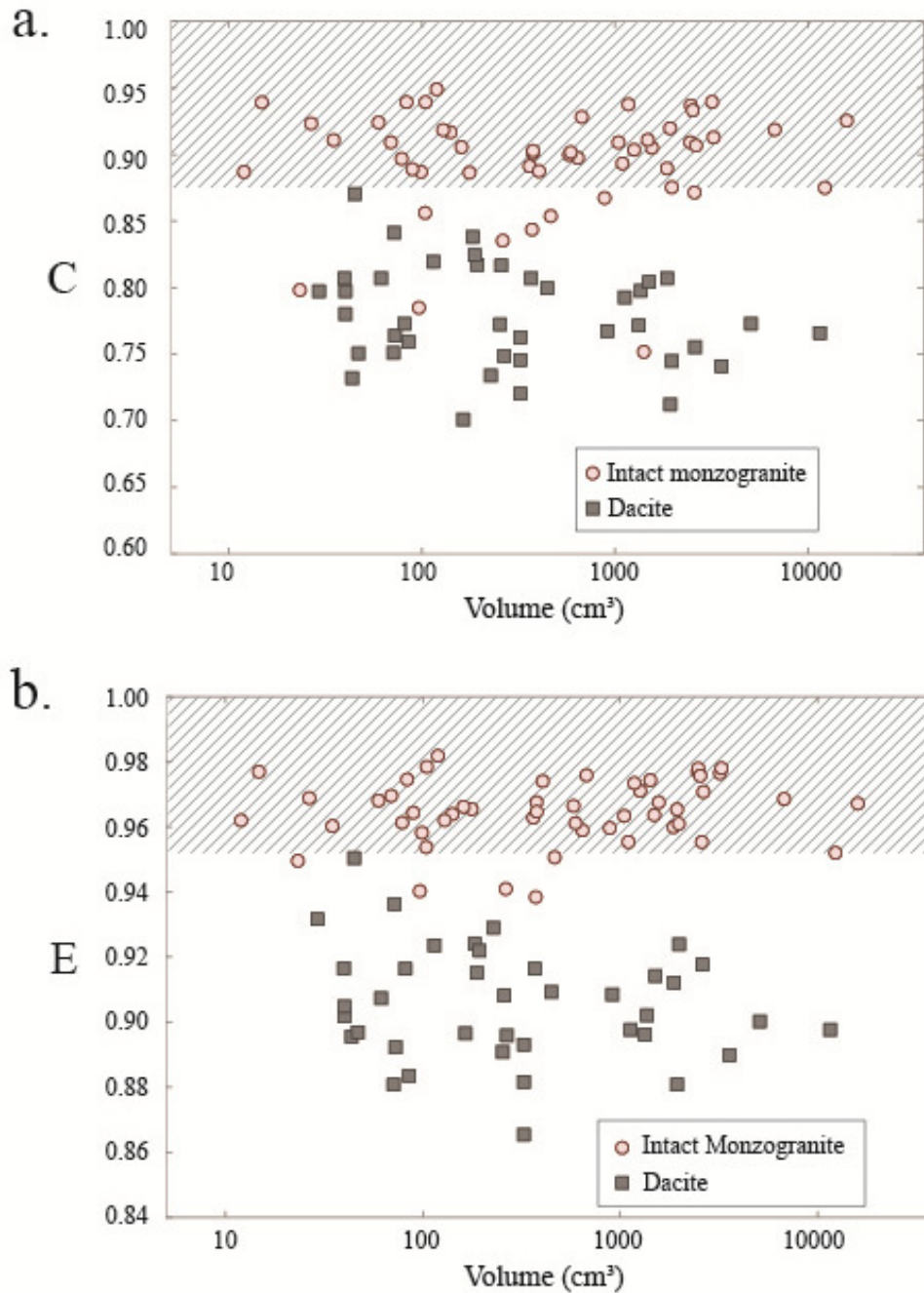
Figure 5-10. Circularity and ellipticity metrics for intact monzogranite samples and dacite samples from the Pebble Creek Formation fallout deposits. a) Computed circularity metric (C) values plotted against clast volume. b) Computed ellipticity metric (E) values plotted against clast volume. The hashed zones in a) and b) represent the dacite exclusion zone, where no dacite accessory lithics plot.

Overall, the metrics for ellipticity and circularity both separate the intact monzogranite and dacite samples sets into distinct clusters of data. Ellipticity provides a slightly better overall metric to differentiate between the intact monzogranite and dacite sample sets, as it does not feature as many outliers (e.g. values of C < 0.84). This is because ellipticity is less sensitive to form than circularity; an elongate clast, even if highly rounded and smoothed, will necessarily have a low circularity value. However, this same rounded elongate clast could have a relatively high ellipticity value. Circularity is a metric sensitive to equancy, roundness and surface roughness, while ellipticity is sensitive to roundness and surface roughness.

Figure 5-10 shows that there is little variation in the circularity or ellipticity of monzogranite samples with changing sample volume. However, it was observed during stratigraphic logging that small monzogranite clasts (< 10 cm^3) appeared to have rougher (i.e. less smoothed) surfaces than the larger clasts. In order to test the hypothesis that surface roughness is dependent on sample size, I have photographed and analyzed a supplementary set of 93 small monzogranite and dacite accessory lithic clasts, which were sampled in situ from Outcrop 1. In order to avoid sampling bias, all lithics identifiable as either monzogranite or dacite were collected from the outcrop, until a sufficient quantity (a total of 51 monzogranite and 42 dacite clasts) was obtained. Dry masses, densities and volumes for all 93 distal accessory lithic samples were obtained using the wet-dry method described in Section 5.1, and these results are displayed in Appendix C2. This set of small accessory lithic clasts, which I will refer to as the "supplementary small volume sample set," was also subdivided into intact clasts and broken clasts, as per the method described above. The supplementary small volume sample set was photographed in batches, and the images were processed according to the image analysis methodology described above (images for this supplementary sample set are found in Appendix E1).

The investigation of surface roughness required the use of a new metric, as circularity and ellipticity to a particles' roundness (and form, in the case of circularity) as well as its surface roughness. Surface roughness may be regarded as the distribution and magnitude of the peaks (convexities) and depressions (concavities) on the topography of an object's surface (e.g. Dinesh, 2008). I have therefore chosen to utilize particle convexity as a proxy for surface roughness, as rough surfaces necessarily contain abundant surficial depressions (concavities) which decrease the overall convexity of the sample (Figure 5-9). The convexity metric (C_{vx}) I will use is measured as:

77

$$C_{vx} = \frac{A_{image}}{A_{convex}} \qquad (5.7)$$

where A_{image} is the area within the object, and A_{convex} is the area of the convex hull encompassing the object. A visual depiction of the parameters of this metric is displayed in Figure 5-9. A perfectly convex (and therefore, perfectly smooth) surface will have $C_{vx} = 1$, and all other surfaces will have $0 < C_{vx} < 1$ (with decreasing C_{vx} as surface roughness increases). C_{vx} provides a proxy for the smoothness of an object's surface, so long as that object does not have large sections of continuous concavity. For example, a scythe-shaped object will be characterized by a low C_{vx} value, even if it has a very smooth surface. However, only two of the clasts in my sample set, both broken monzogranites, display large segments of continuous concavity (MC-2010-Yb015 and MC-2010-Yc029; see images of these clasts in Appendix E1). As the outlines of the clasts from the remainder of the sample set do not display long segments of continuous concavity, the variations in convexity observed must be attributed to variations in surface smoothness.

Computed image analysis results for all analyzed accessory lithic clasts are found in Appendix E3 and displayed in Figure 5-11. The convexity values of the two clasts featuring continuously concave zones ($C_{vx} = 0.87$ for MC-2010-Yc029 and $C_{vx} = 0.90$ for MC-2010-Yb015) were excluded from these graphs. The results show a weak correlation between convexity and sample size for the entire monzogranite sample set (Figure 5-11a). However, the results for the intact monzogranites show a clear positive correlation between convexity and sample volume (Figure 5-11b). In contrast, the dacite samples show no variation in convexity with increasing sample size (Figure 5-11c). Using convexity as a proxy for surface smoothness, these results show that the smoothness of the intact monzogranites increases significantly with increasing sample size, whereas there is no correlation between surface smoothness and sample size for the dacite samples.
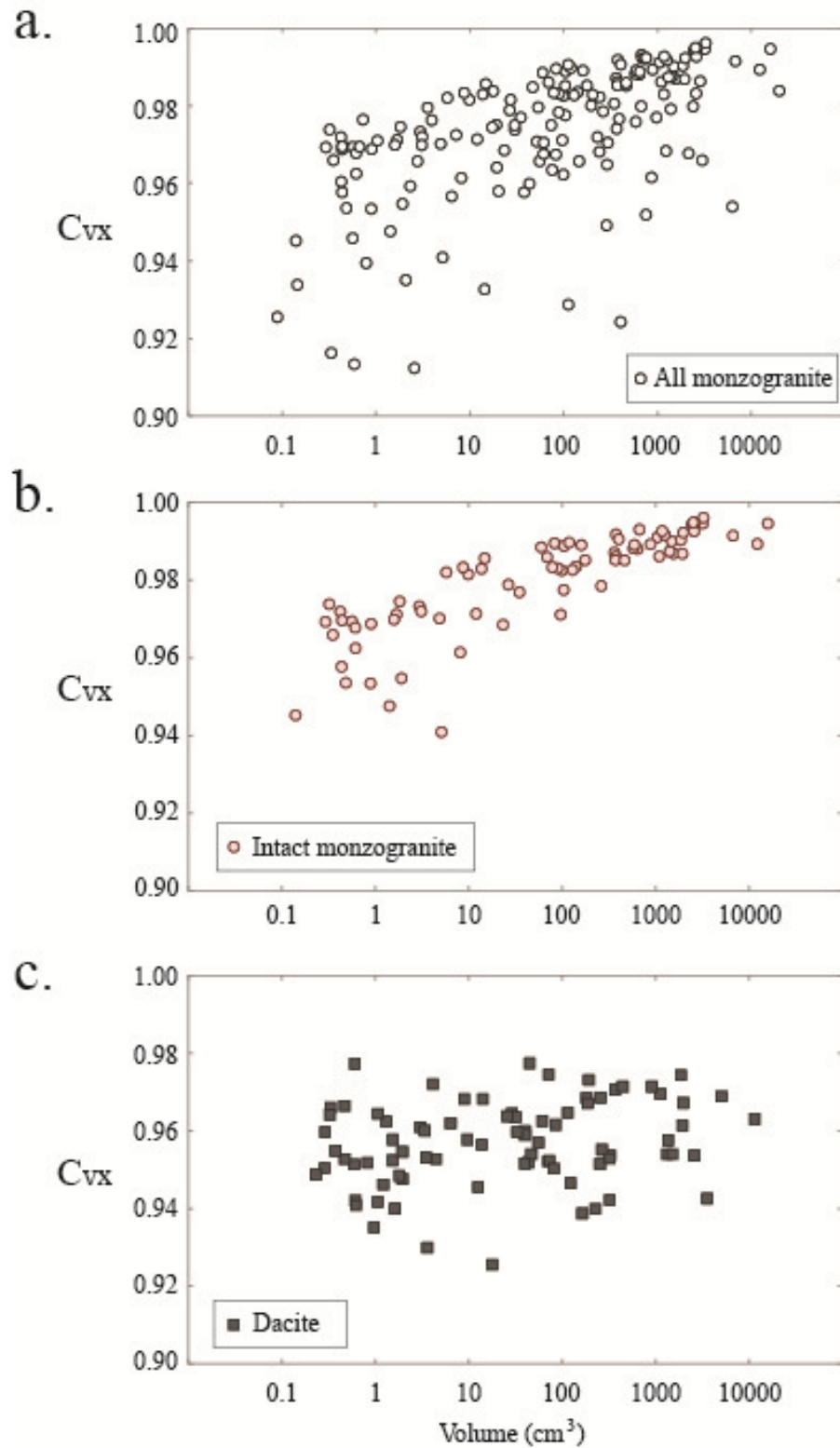
Figure 5-11. Convexity metric (C_{vx}) results for all accessory lithics analyzed, including the supplementary small volume sample set (see text). a) Convexity values for all monzogranite clasts, except for the two samples with large concavities (see text). b) Convexity values for all intact monzogranite clasts. c) Convexity values for all dacite clasts.

5.4 Whole Rock 3-D Scan Measurements

The surface area of a particle is a fundamental morphological characteristic that is surprisingly difficult to accurately measure. However, the commercial availability of 3-dimensional laser scanners in recent years has now made it possible to rapidly scan, and digitally recreate and analyze, the outer surfaces of clastic particles. To date however, only a few examples of the use of this technology exist in the geological literature (Anochie-Boateng et al., 2011; Hayakawa and Oguchi, 2005).

Here, I present the first 3-D scan data set of accessory lithic clasts from a volcaniclastic deposit. A NextEngine™ 3-D laser scanner (Figure 5-12) was used to scan the outer surfaces of a selection of accessory lithic samples. Samples were scanned and processed using the NextEngine™ ScanStudio HD PRO software (Figure 5-13). A complete 3-D scan of an object takes approximately one hour to complete, and requires the scanning of all faces of the object. Samples may be placed on a rotating pad that automatically rotates the sample by set increments, with a scan made after each successive rotation. Between 14 and 24 individual scans were required to adequately image the outer surfaces of each sample, depending on the sample's complexity and irregularity (Figure 5-13a). These individual scans were then trimmed of any non-sample surfaces (e.g. parts of the sample holder apparatus) (Figure 5-13b) and aligned with respect to one another using a combination of automatic and manual alignment (Figure 5-13c). Finally, all scans are fused together to form a complete triangulated mesh, a process which also fills any small holes in the mesh (Figure 5-13d). The ScanStudio HD PRO software may then be used to calculate the surface area of this finalized mesh, a 3-D replica of the complete outer surface of the scanned sample. I determined the volumes of the 3-D scans by exporting the final fused mesh as a .STL file, and computing the volume of the shape file in Matlab®.

Figure 5-12. NextEngine[TM] 3-D laser scanner workstation. A personal computer and monitor are connected via USB to the NextEngine[TM] 3-D scanner (back right). The scanner connects to the AutoDrive sample platform (front right) upon which the sample is positioned, held in place by a movable part gripper.

A total of 9 monzogranite and 9 dacite samples were 3-D scanned using the NextEngine[TM] scanner. The samples were selected based upon their volumes, which range from 40 cm^3 to 1048 cm^3. The 7 monzogranite and 7 dacite samples with volumes of < 900 cm^3 were scanned in Macro mode at a resolution of $\sim 28,400$ points/cm^2 (see Appendix F for discussion of the choice of scan modes and resolutions). The 4 larger samples (> 900 cm^3), which needed to be scanned using the Wide mode, were scanned at a resolution of 7,100 points/cm^2. The results for the 18 3-D scanned samples are found in Table 5-1. The measured surface areas for the 18 accessory lithic samples scanned are shown in Figure 5-14, plotted against the wet-dry measured volumes of these samples.
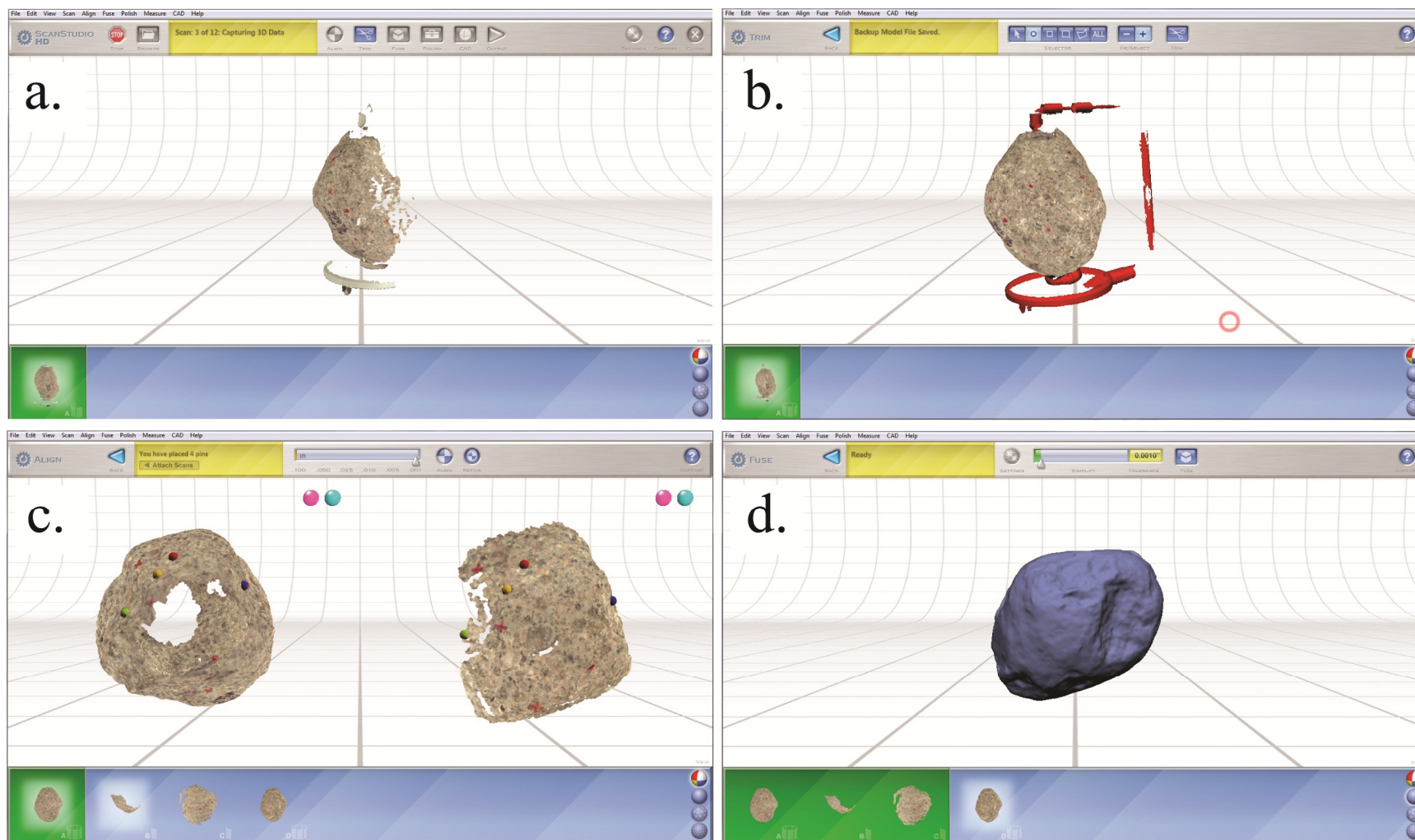
Figure 5-13. Whole rock 3-D scan methodology. a) Single sample scan, one of between 14 and 24 that will be merged to digitally recreate the whole external surface of the sample. b) Trimming away the partially scanned sample holder apparatus. c) Manually aligning the top and bottom scan sets. d) Final fused sample.

Sample #	Scan Resolution (points/cm^2)	Volume, from Wet-Dry Technique (cm^3)	Volume, from 3-D Scan (cm^3)	Surface Area (cm^2)	Sphericity (Ψ_t)
Monzogranite Samples					
MC-2011-IS04	28387	34.9	35.6	56.5	1.26
MC-2010-Yb002	28387	69.3	70.2	87.2	1.19
MC-2010-Yb005	28387	129.3	130.6	133.2	1.23
MC-2010-Ya014	28387	176.9	179.2	164.0	1.21
MC-2010-Yb009	28387	263.4	265.5	227.1	1.47
MC-2010-Yc006	28387	378.0	381.5	276.2	1.28
MC-2010-Ya004	28387	675.1	685.4	408.6	1.28
MC-2010-Ya003	7097	1047.9	1057.6	534.8	1.21
MC-2010-Yc004	7097	1262.1	1277.3	605.8	1.21
Dacite Samples					
MC-2010-PP02	28387	40.1	43.6	73.6	1.85
MC-2011-P19	28387	85.4	93.7	120.8	2.45
MC-2010-PP04	28387	114.7	117.1	137.1	2.04
MC-2011-P10	28387	164.4	174.9	203.7	2.39
MC-2011-P07	28387	254.6	264.9	266.7	1.77
MC-2010-PP08	28387	369.0	386.9	325.4	1.63
MC-2011-P04	28387	447.3	467.8	342.7	1.98
MC-2011-P03	7097	913.9	957.0	589.4	1.69
MC-2010-PP14	7097	1130.9	1177.5	642.9	1.66

Table 5-1. Data from whole rock 3-D scans of 18 accessory lithic samples.
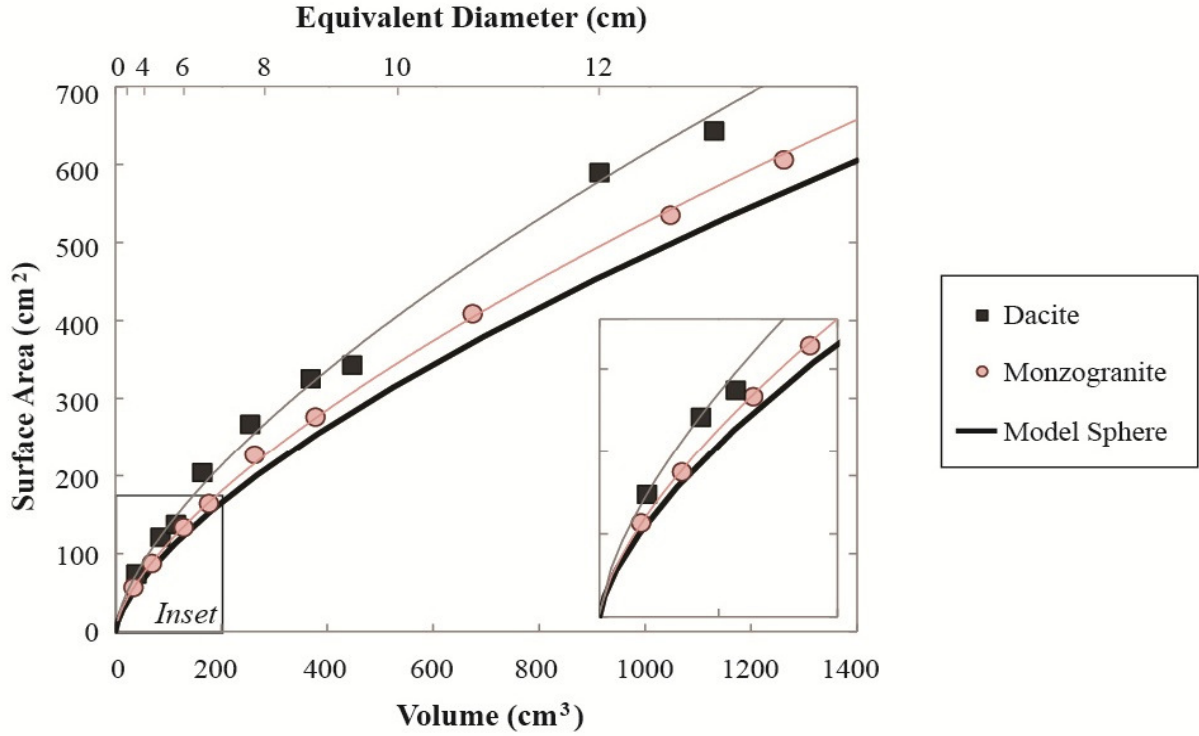
Figure 5-14. Surface area (A_{surf}) results for the 18 3-D scanned samples, plotted against sample volume (V; measured via the wet-dry technique). Equivalent diameter is the diameter of a sphere with the corresponding volume on the lower horizontal axis. The formula for the dacite trendline is $A_{surf} = 6.5701V^{0.6569}$ ($R^2 = 0.9948$), and the formula for the monzogranite trendline is $A_{surf} = 5.2834V^{0.6659}$ ($R^2 = 0.9993$). The relationship between A_{surf} and V for a model sphere is $A_{surf} = 4.836V^{0.6667}$ ($R^2 = 1$).

The results in Figure 5-14 show that the relationships between surface area and volume for the set of monzogranite samples and the set of dacite samples may both be well fitted by a power law trendline. This is to be expected, to certain extent, as $V_{sphere} \propto r_{sphere}^3$ and $A_{sphere} \propto r_{sphere}^2$ for a sphere of any size. In order to eliminate this power law effect, I have calculated a unitless metric of true sphericity (Ψ_t) for all of the scanned samples, which I define as:

$$\Psi_t = \frac{A_{surf}^3}{36\,\pi\,V^2} \qquad (5.8)$$

$\Psi_t = 1$ for only spheres, and $\Psi_t > 1$ for particles of any other morphology, with Ψ_t increasing as the particle shape increasingly deviates from sphericity. Ψ_t results for the 18 scanned samples are shown in Figure 5-15. A clear difference is apparent between the Ψ_t values for the monzogranite and the dacite

sample sets. The monzogranite samples range from $1.22 \leq \Psi_t \leq 1.49$, with an average of $\Psi_t = 1.29 \pm$ 0.08. The dacite samples range from $1.73 \leq \Psi_t \leq 2.77$, with an average of $\Psi_t = 2.16 \pm 0.35$. Therefore, the monzogranites are considerably, and quantifiably, more spherical than the dacite samples. Furthermore, there is no apparent covariance between Ψ_t and sample size for either the monzogranite or dacite sample sets.
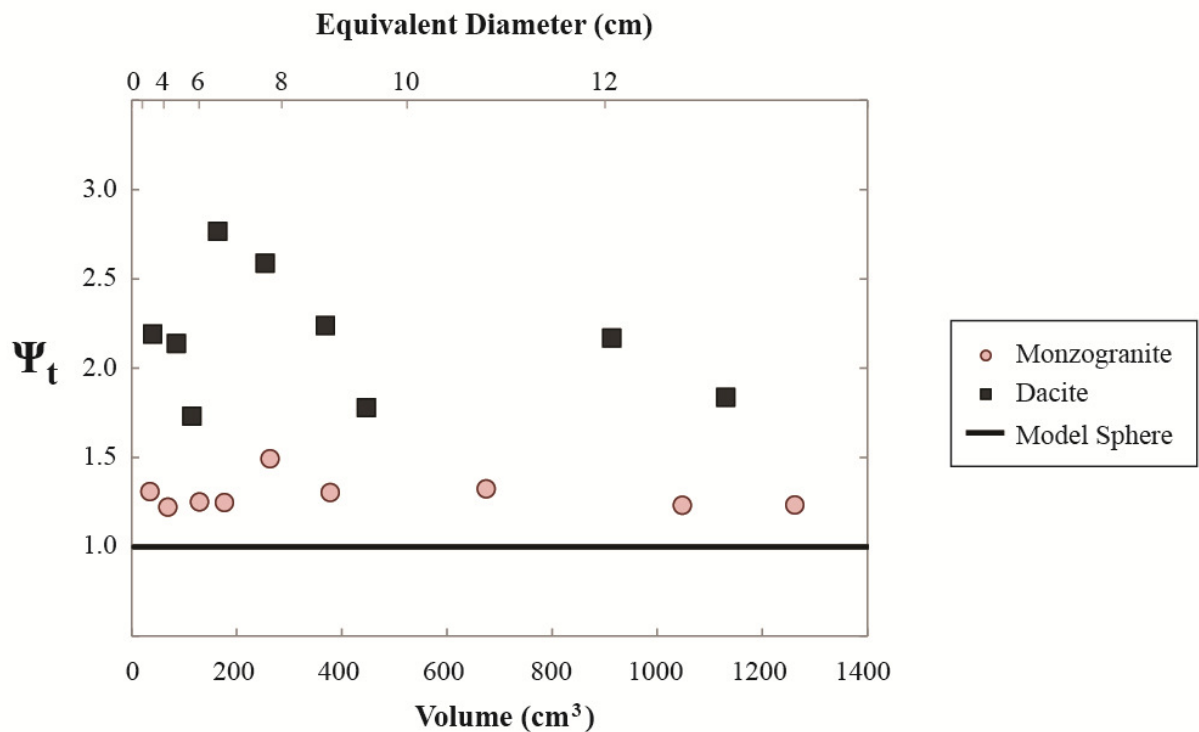
Figure 5-15. True sphericity metric (Ψ_t) vs. sample volume (measured via the wet-dry technique) of the 3-D scanned accessory lithic samples. Equivalent diameter is the diameter of a sphere with the corresponding volume on the lower horizontal axis.

5.5 Surface Roughness

In order to quantify the surface roughness of the accessory lithic samples, square patches of the surfaces of a selection of accessory lithic clasts were scanned using the NextEngine[TM] 3-D laser scanner. The size of these square regions vary depending on the size of the sample being scanned: a 15 x 15 mm region was scanned for samples < 70 cm^3; a 20 x 20 mm region was scanned for samples ranging from 70 – 250 cm^3; a 30 x 30 mm region was scanned for samples ranging from 250 – 600 cm^3; and a 40 x 40 mm region was scanned for samples > 600 cm^3. For every sample, the area with lowest apparent surface roughness was selected for scanning. Therefore, the square surface patches represent the maximum smoothness attained by the clast. In the case of the dacite clasts, care was also taken not to scan columnar joint surfaces.

Square regions of the surfaces of a total of 20 intact monzogranite and 17 dacite accessory lithic clasts were scanned. Samples from a range of volumes were selected in order to investigate whether maximum clast smoothness varies with sample volume. The accessory lithic clasts selected range in volume from 15 to 12,307 cm^3 for the monzogranite, and from 29 to 11,577 cm^3 for the dacite. Methodology for the surface region scanning is shown in Figure 5-16. Squares delimitating the area to be scanned were inked onto the samples prior to scanning. Patches were all scanned using the Single scan mode of the ScanStudio HD PRO software, at a resolution of 258,000 points/cm^2 (Figure 5-16a). Any holes present within the mesh were filled using the Hole Fill tool in ScanStudio (Figure 5-16b). Excess scanned material was trimmed from the square-shaped patch, if necessary, using the Trim tool in ScanStudio. The final product is a high resolution, square-shaped, continuous triangulated mesh (Figure 5-16c). Figure 5-16d shows a close-up view of the final mesh, emphasizing the detail of the surface roughness captured by the scan at this resolution. The surface areas of the final scanned regions (A_{meas}) are also generated by ScanStudio.
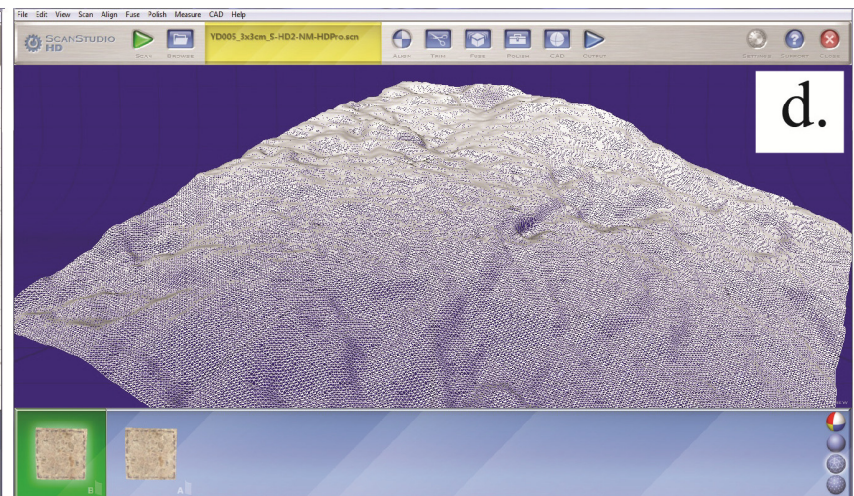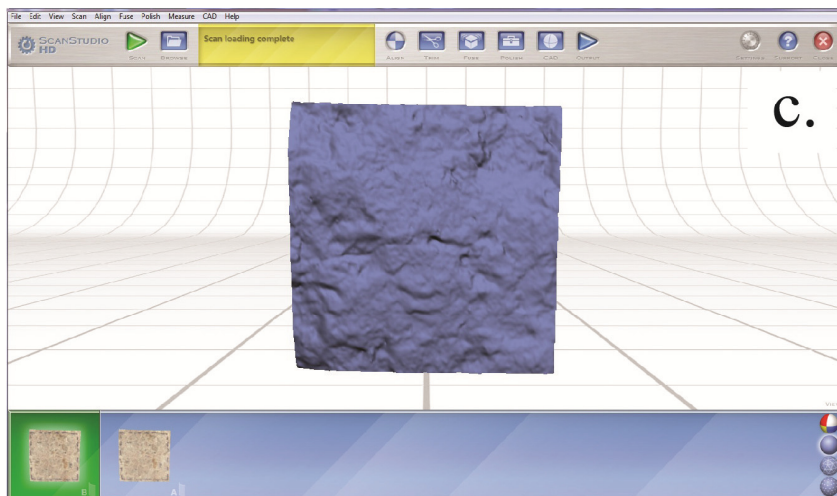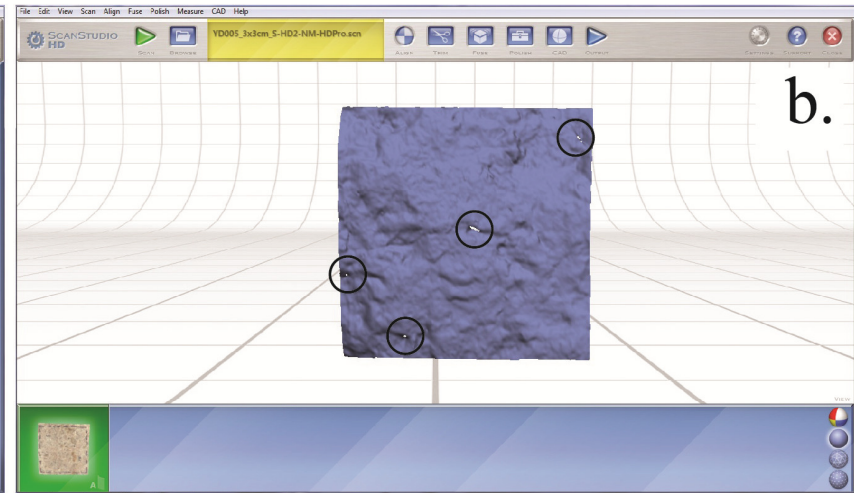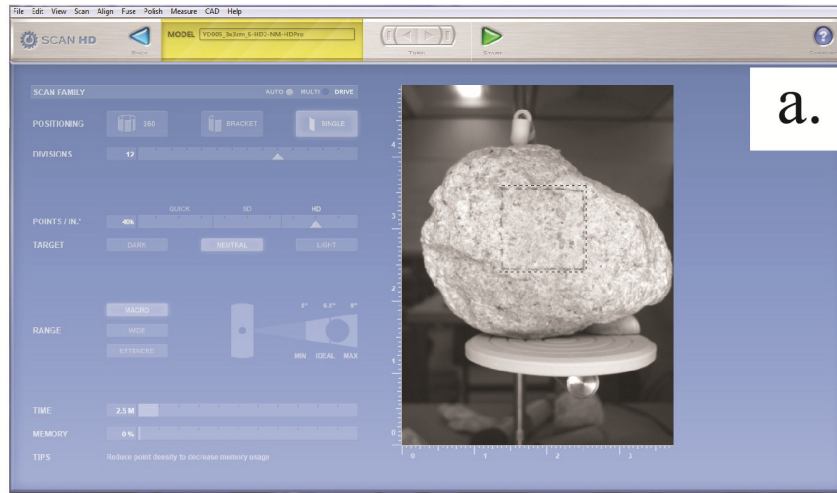
Figure 5-16. 3-D patch scan methodology. a) Selection of appropriate scan settings. b) Filling any holes present in the mesh. c) Final complete mesh, trimmed to a square shape. d) Close-up view of the final mesh.

In order to be able to compare the relative roughness of the various scanned surface regions, square patches of varying sizes, a simple surface smoothness metric was calculated for all of the scanned regions:

$$S_{max} = \frac{A_{proj}}{A_{meas}} \qquad (5.9)$$

Where S_{max} is the surface smoothness metric being calculated (for the region on the sample estimated to have maximum smoothness), and A_{proj} is the projected surface area of the square region, computed using data generated in ScanStudio (Figure 5-17). Dividing A_{proj} by A_{meas} creates a unitless metric, which is not dependant on the size of the square region originally scanned. $S_{max} = 1$ for a perfectly planar surface and $0 < S_{max} < 1$ for all other surfaces, with the value of S_{max} decreasing with increasing surface roughness. The computed S_{max} values for the square scanned regions of all 37 samples are compiled in Appendix F and displayed in Figure 5-18, where they are plotted against sample volume.
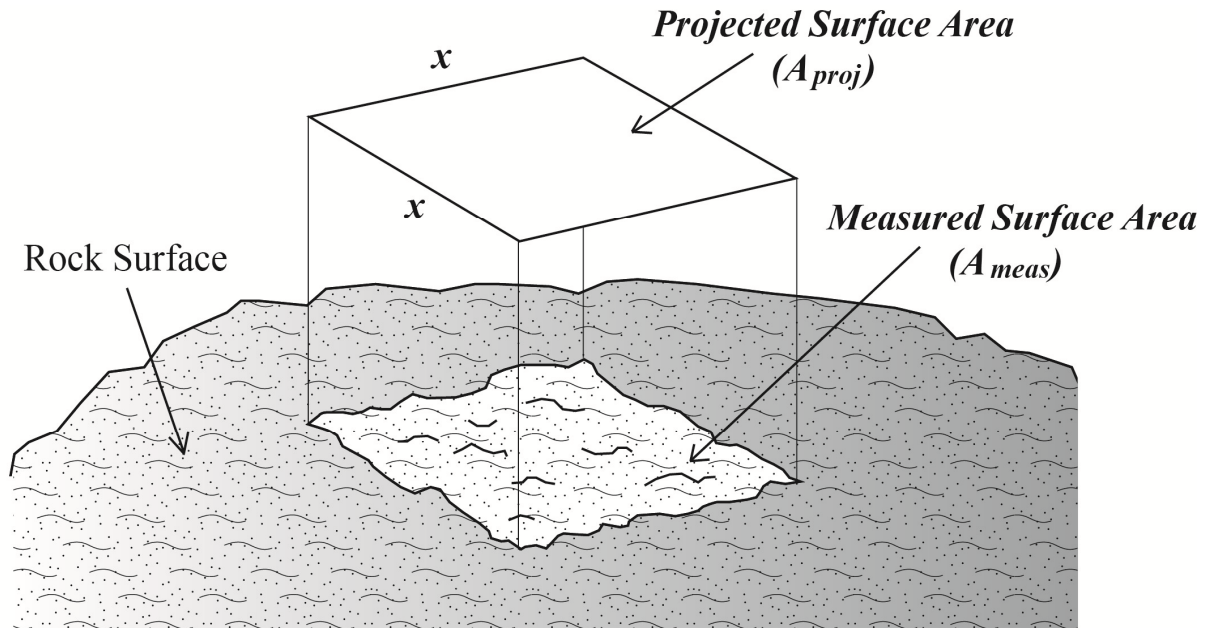
Figure 5-17. Visual explanation of projected surface area (A_{proj}) vs. measured surface area (A_{meas}).

The results for the monzogranite samples show a large range in maximum smoothness values for the smaller samples, and trend towards an increasingly narrow range of high smoothness values with increasingly sample size (Figure 5-18). The monzogranites smaller than 400 cm^3 have S_{max} values ranging from 0.89 – 0.98, indicating that some of the smaller clasts remained quite rough, while others achieved high levels of smoothness. The monzogranites larger than 400 cm^3 all have S_{max} values of 0.97 – 0.98, indicating that all of the larger samples became quite smooth. This latter range represents the maximum smoothness attainable by the monzogranite clasts from the rounding processes to which they were subjected, as there is no significant increase in S_{max} past this range. The topography images of the monzogranite samples display rare pits, likely from the plucking of individual grains from the monzogranite surface. Overall however, the monzogranite topographies are relatively smooth and featureless (Figure 5-19a).

The results for the dacite samples do not show a correlation between maximum smoothness and sample volume (Figure 5-18). Furthermore, the dacites have significantly lower S_{max} values, ranging from 0.81 – 0.90, than the monzogranite sample population (Figure 5-18). The topographies of the dacite sample regions (e.g. Figure 5-19b) also typically have much higher relief and more surface irregularities than the monzogranites (e.g. Figure 5-19a). The topographies of certain scanned dacite samples display rectangular pits from eroded plagioclase phenocrysts. The preferential erosion of these crystals is one of the factors increasing the overall surface roughness of the dacite samples.
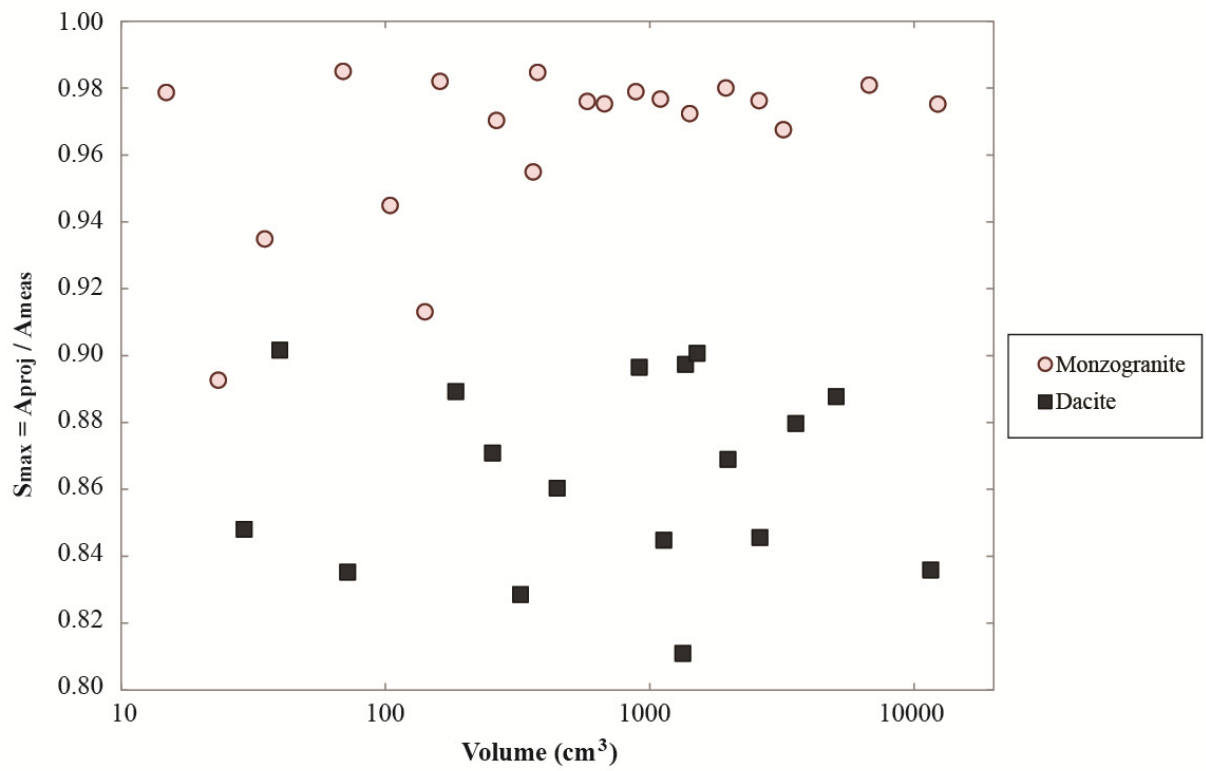
Figure 5-18. Maximum surface smoothness results for scanned surface regions on intact monzogranite and dacite accessory lithic clasts.

a)
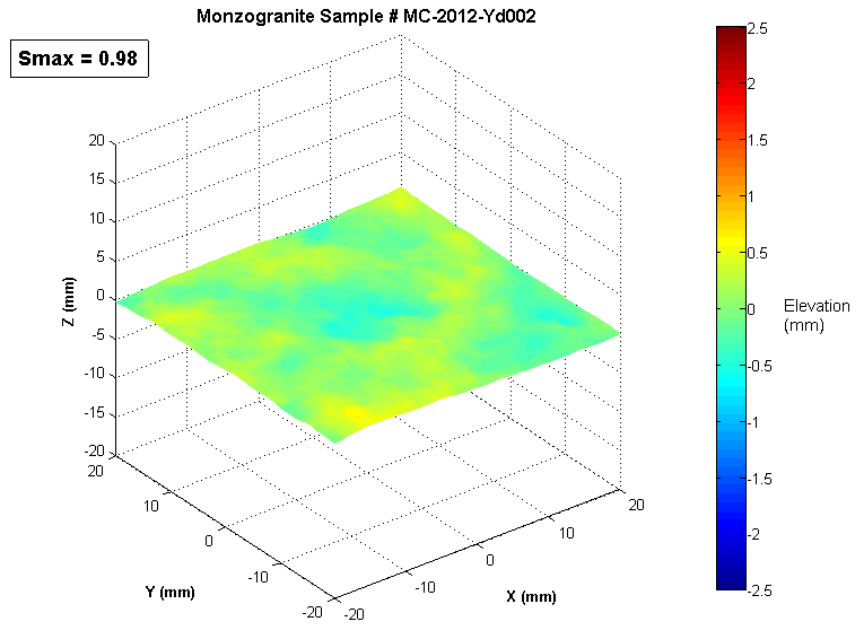
b)
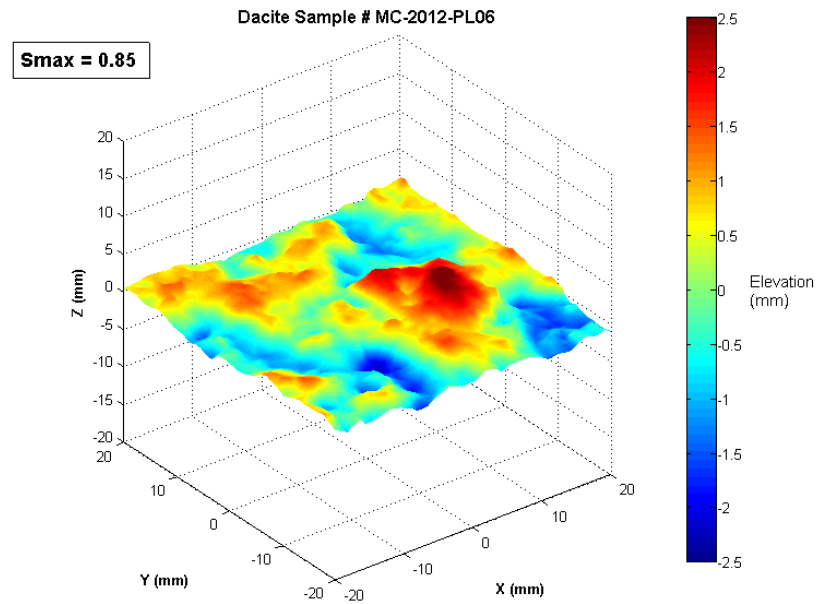
Figure 5-19. Colourmapped topographies of two 3-D scanned surface patches of accessory lithic clasts, produced in Matlab®. The colour bar on the right of each figure denotes the vertical elevation at each point on the surface. a) Surface region of intact monzogranite clast MC-2012-Yd002, with S_{max} = 0.98. b) Surface region of dacite clast MC-2012-PL06, with S_{max} = 0.85.

5.6 Surface Textures

The morphological characterization of the accessory lithic clasts has thus far focussed on the quantification of various parameters relating to the overall shape of the particles. Here, I will describe, in a more qualitative fashion, the surface textures visible upon the accessory lithic clasts. First, I describe the important macroscopic surface textures, easily visible with the naked eye. Secondly, I describe microscopic textures visible on the surfaces of the clasts using a Scanning Electron Microscope.

5.6.1   Macroscopic Surface Textures

One of the most notable macroscopic surface features present on many of the monzogranite clasts are 0.5 – 3 mm thick, partial concentric spalls on the sample surfaces (Figure 5-20). These spalls sometimes terminate abruptly (e.g. Figure 5-20a) and sometimes taper at their edges. Occasionally spalls appear to be partially overlapping (e.g. Figure 5-20b). It was also observed that very thin, small flakes could also be easily detached from the surfaces of many of the monzogranite clasts by the application and removal of masking tape. These spalls and flakes are observed on monzogranite clasts of all grain sizes, and on clasts as small as 6 cm^3 (sample #1-1-M4). Finally, it should be noted that these macroscopic surficial spalls do not characterize monzogranite samples rounded via any natural processes, as they do not occur on river-rounded monzogranite clasts sampled from the Lillooet River, or on the surfaces of weathered monzogranite outcrops of the Fall Creek Stock.

There are no observed instances of macroscopic scratches, gouges, striations, or percussion marks on the monzogranite clasts. However, occasional monzogranite clasts do have large concave chips missing from their surfaces (e.g. Figure 5-21). Fine cracks and microfractures are also commonly observed running through the monzogranite clasts.
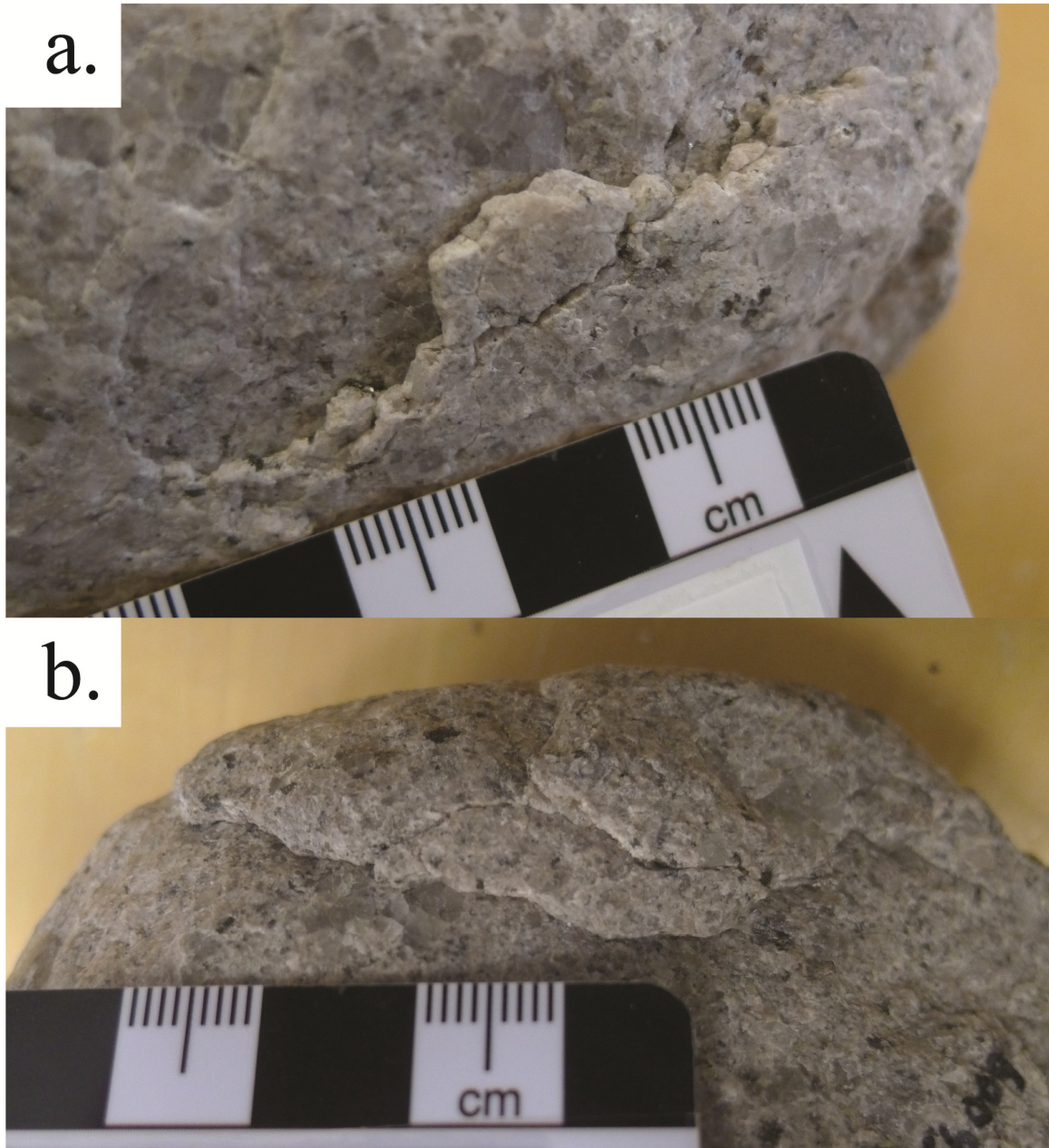
Figure 5-20. Close-up photographs of spalls on the surfaces of monzogranite clasts. a) Single partially attached spall layer (sample # MC-2010-YC007). b) Slightly overlapping spall layers (sample # MC-2010-YB009).
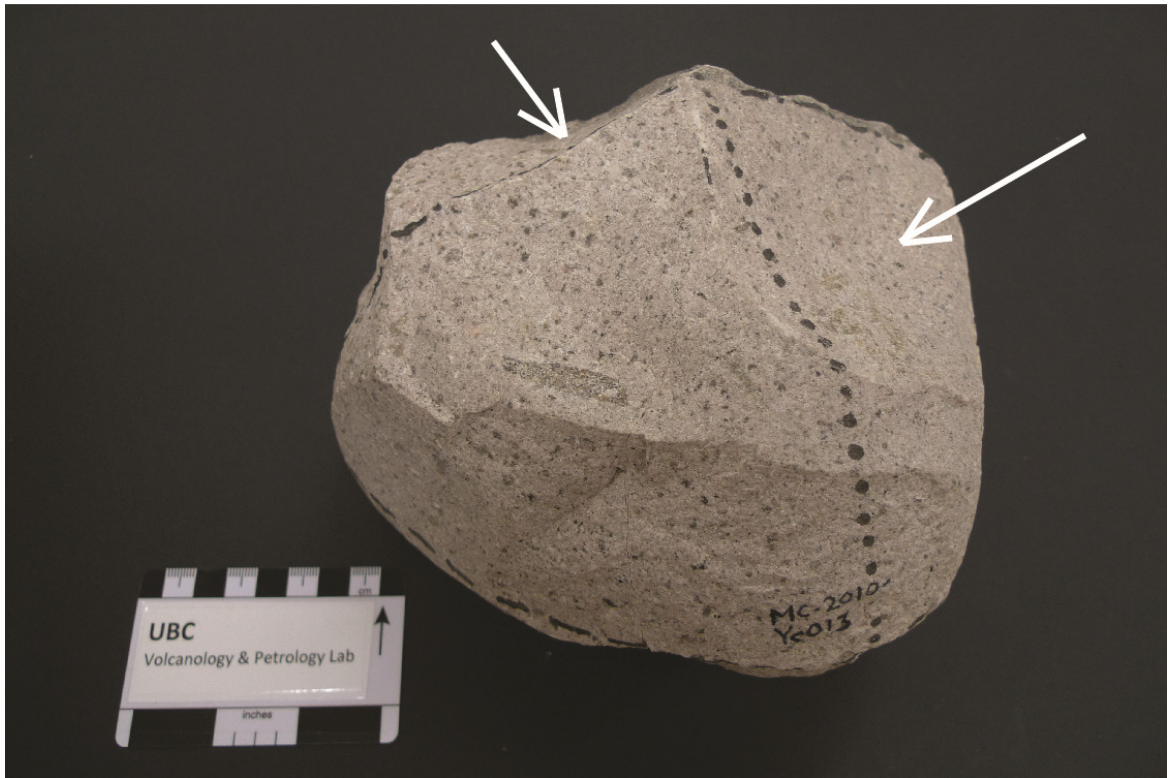
Figure 5-21. Monzogranite lithic clast displaying two large concave fracture surfaces (white arrows).

Significant degrees of clasts rounding are observed on monzogranite clasts of all sizes, including on some of the smallest (0.3 cm^3; Figure 5-22a) and largest clasts sampled (16,000 cm^3) (Figure 5-22e). The degree of rounding of the edges and corners of monzogranite samples is variable (Figure 5-23). As previously discussed in Section 5.2, many monzogranite clasts are "broken," indicating that they have undergone disruptive collisions. Such clasts feature relatively rough, freshly broken surface regions covering > 10% of their total surface areas. Usually these rough areas are delimitated by angular edges (e.g. Figure 5-6; Figure 5-23d). In contrast, many of the intact monzogranite clasts have either very well-rounded edges (Figure 5-23b), or are so well-rounded that they do not display any discernible edges (Figure 5-23a). Furthermore, many clasts have edges with degrees of rounding falling between these two extremes: slightly to moderately rounded edges are also observed (Figure 5-23c). Some clasts also display multiple fracture surfaces with different degrees of edge angularity (Figure 5-23c). A discussion of the implications of the slightly to moderately rounded edges and the differentially rounded edges is found in Section 6.3.

As with the monzogranite clasts, the dacite accessory lithic clasts do not display visible gouge marks or striations, but do commonly feature thin fractures. The surfaces of the dacite clasts are typically rough and irregular, and often feature protrusions and pits. The relatively low competency of the dacite allows small fragments of the clasts to readily break off. The plagioclase phenocrysts exposed at the surfaces of the clasts are typically broken, and have often been plucked from the surface. The columnar joint surfaces commonly observed on the dacite clasts (Figure 4-15) are typically smoother than the fractured surfaces. Finally, no spalls or other signs of exfoliation have been observed on any of the dacite clasts.
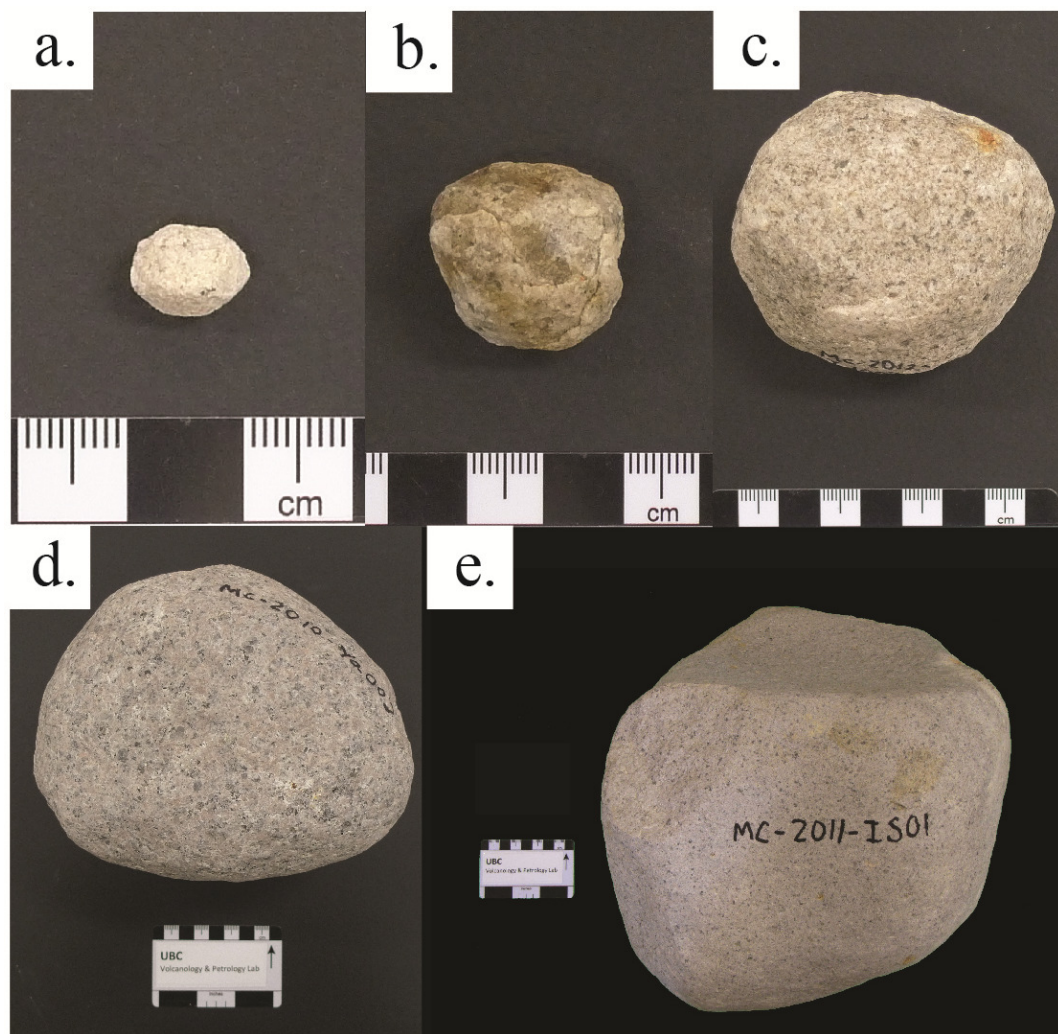
Figure 5-22. Examples of rounded monzogranite accessory lithic clasts from every size range sampled. a) 0.3 cm^3 clast (sample # 1-5-M36); b) 6 cm^3 clast (sample # 1-1-M4); c) 120 cm^3 clast (sample # MC-2012-Yd009), d) 2,500 cm^3 clast (sample # MC-2010-Ya003); e) 16,000 cm^3 clast (sample # MC-2011-IS01).
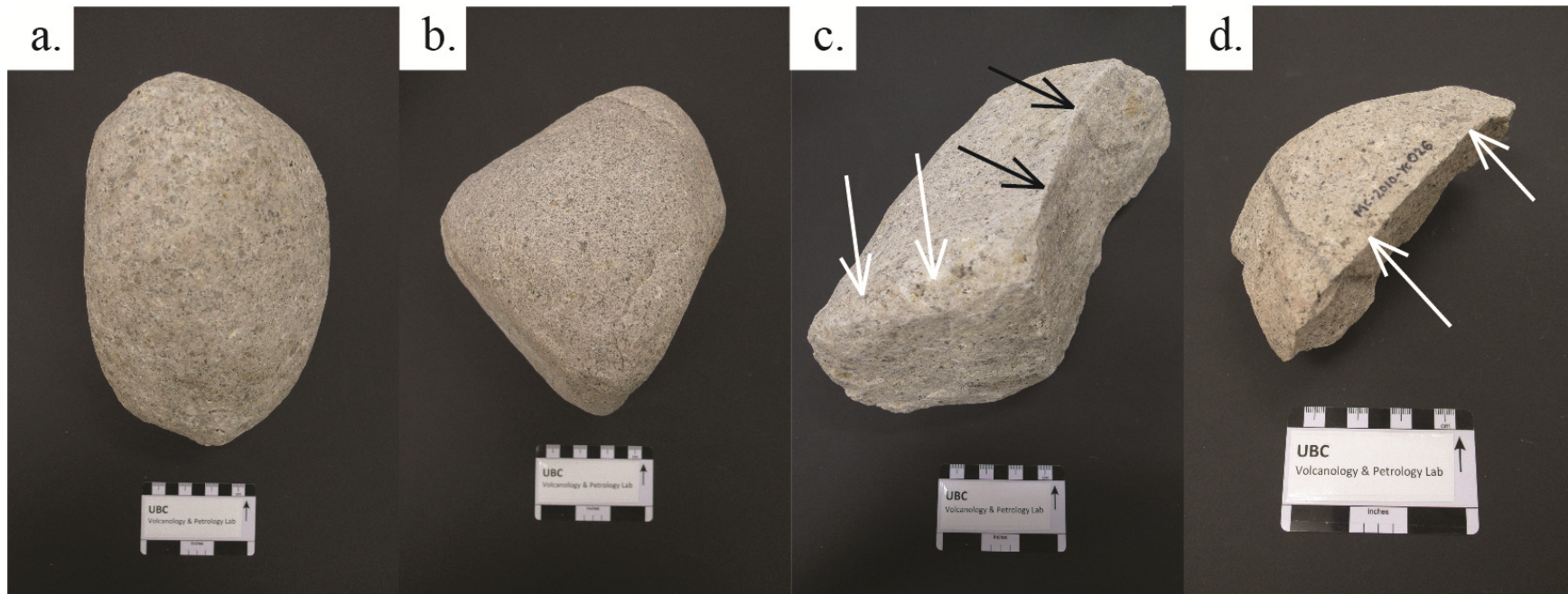
Figure 5-23. Variability in rounding of edges observed in monzogranite clasts. a) This clast is so well-rounded that edges are no longer distinguishable. b) Very well-rounded clast edges. c) Moderately rounded edge (indicated by white arrows) and angular edge (black arrows) on a clast. d) Very angular edge (indicated by arrows) on a clast.

5.6.2   Microscopic Surface Textures

Scanning Electron Microscope (SEM) imaging of rock surfaces was conducted on a collection of clasts (Table 5-2). In order to examine these surfaces with the SEM, small (~ 1 cm x 1 cm wide, and ~ 0.5 cm thick) blocks were cut from the surfaces of the desired samples using a circular rock saw. These blocks were then mounted, carbon coated, and imaged using a Philips XL30 Scanning Electron Microscope at the University of British Columbia. Terminology from Table 2-2 is used to describe some of the surface textures observed.

SEM images from the surfaces of accessory lithic monzogranite clasts are displayed in Figures 5-24, 5-25 and 5-26. Images of the surfaces of the two smaller, intact, accessory lithic clasts (MC-2010-Yb004 and MC-2010-Yb008) are displayed in Figure 5-24. These clasts display moderate relief, occasional conchoidal fractures (Figure 5-24a) and rare concave depressions which may represent impact pits (Figure 5-24b), but the main surface textures observed are thin, flaky breakage planes lying parallel to the clast surface. This flaky surface texture is also pervasive on the surface of the larger intact monzogranite accessory lithic clast imaged, which has relatively low relief (MC-2010-Ya004; Figure 5-25). Two surfaces were examined on the broken sample MC-2010-Yc012: a smoothed, rounded surface, and a relatively fresh fracture surface. The smoothed, rounded surface is predominantly characterized by the same flaky surface texture visible on the other clasts examined, with occasional small conchoidal fractures observed (Figure 5-26a). The relatively fresh fracture surface, however, has a completely different appearance, characterized by very high relief, angular and blocky grains, and impact pits (Figure 5-26b). The flaky surface texture is not observed on this surface.

Sample #	Volume	Grain Size	Surface Type	Surface Texture Summary
Monzogranite Accessory Lithic Clasts				
MC-2010-Yb008	105 cm^3	Coarse-grained	Surface of intact clast	Flaky breakage planes, moderate relief
MC-2010-Yb004	161 cm^3	Medium-grained	Surface of intact clast	Flaky breakage planes, moderate relief
MC-2010-Ya004	675 cm^3	Coarse-grained	Surface of intact clast	Flaky breakage planes, low relief
MC-2010-Yc012	688 cm^3	Medium-grained	Smoothed surface	Flaky breakage planes, low relief
MC-2010-Yc012	688 cm^3	Medium-grained	Relatively fresh fracture surface	Angular, broken crystals, high relief, conchoidal fractures, impact pits, scratches, no flaky breakage planes
Monzogranite River-Rounded Clast				
MC-2011-LB10	204 cm^3	Medium-grained	Surface of intact clast	Uniformly rough, moderate relief, no flaky breakage planes
Dacite Accessory Lithic Clast				
MC-2011-P17	1511 cm^3	Porphyritic	Typical surface (non-columnar jointed)	Rough, irregular, high relief, large pits, microvesicular groundmass, highly fractured crystals, no flaky breakage planes

Table 5-2. Properties of the samples examined with the SEM.
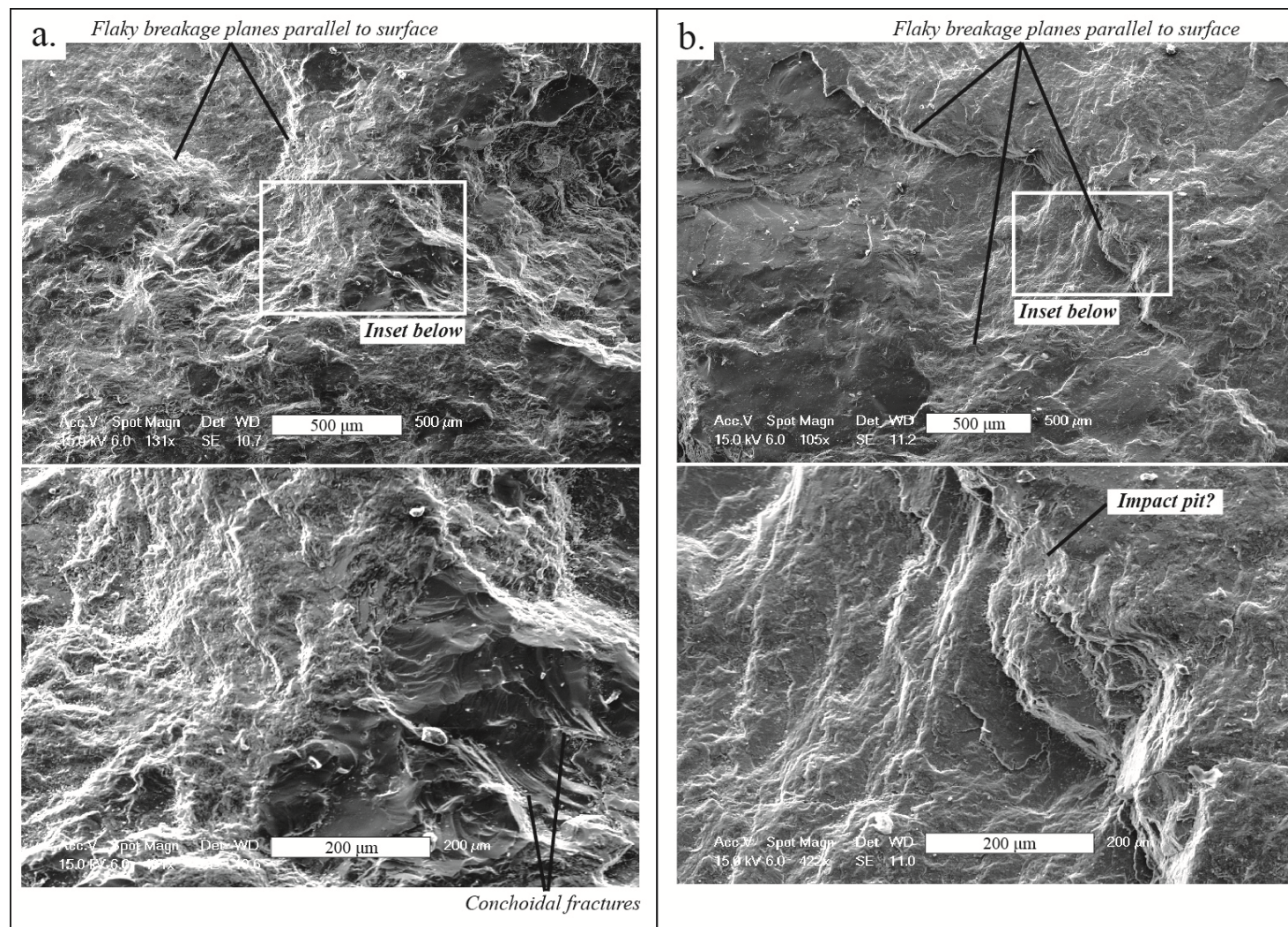
Figure 5-24. SEM images of the surfaces of small, intact monzogranite accessory lithic samples. a) Images from the surface of sample # MC-2010-Yb004. b) Images from the surface of sample # MC-2010-Yb008. The surfaces of both samples display thin, flaky breakage planes parallel to the surface, and minor conchoidal fractures are visible in the inset of a).
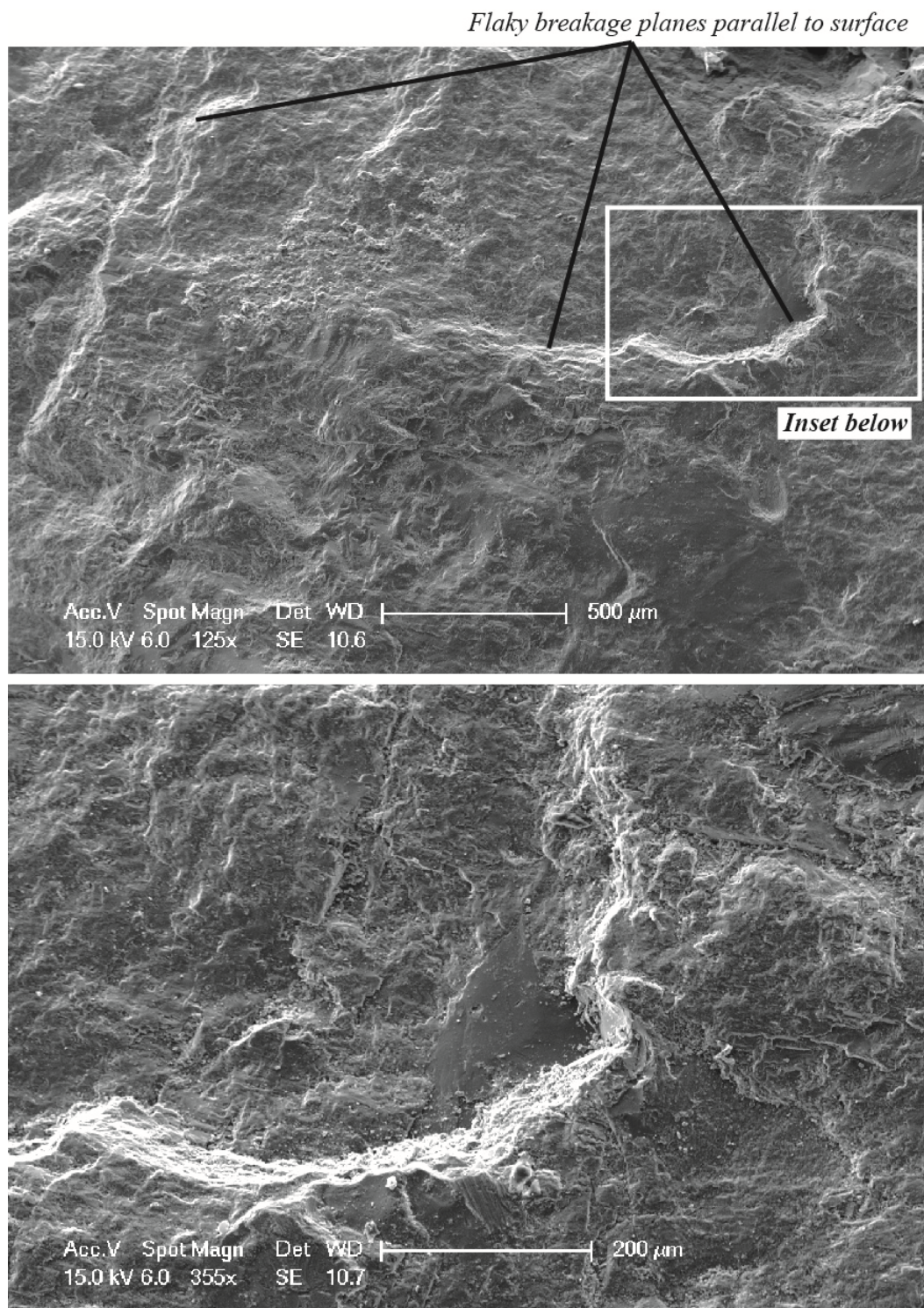
Figure 5-25. SEM images of the surface of a relatively large intact monzogranite accessory lithic sample (# MC-2010-Ya004). Note the pervasive flaky surface texture.
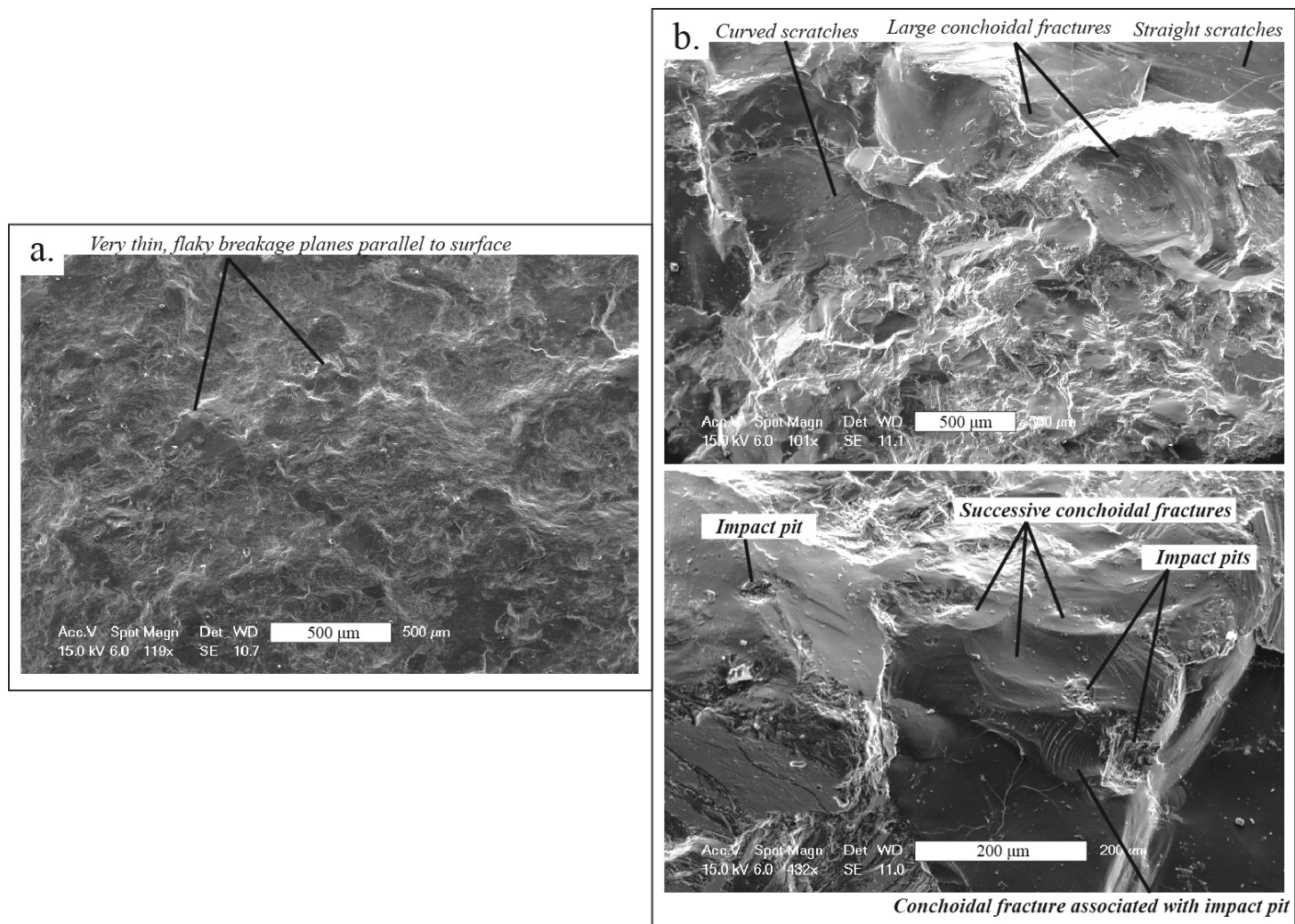
Figure 5-26. SEM images of two surfaces of a relatively large broken monzogranite accessory lithic sample (# MC-2010-Yc012). a) Smoothed and rounded surface, displaying low relief and characteristic flaky breakage planes throughout. b) Relatively fresh fracture surface, displaying a variety of mechanical impact features, including numerous conchoidal fractures, scratches and impact pits.

A block cut from the surface of a river-rounded monzogranite clast sampled from the Lillooet River was also imaged using the SEM, in order to compare its microscopic surface features to those of the monzogranite accessory lithic clasts. The surface of this river-rounded clast differs markedly from the accessory lithic monzogranites; flaky breakage planes are absent, and the surface is instead uniformly rough in appearance (Figure 5-27). Therefore, SEM results indicate a difference in the primary smoothing mechanism of these two sample types.
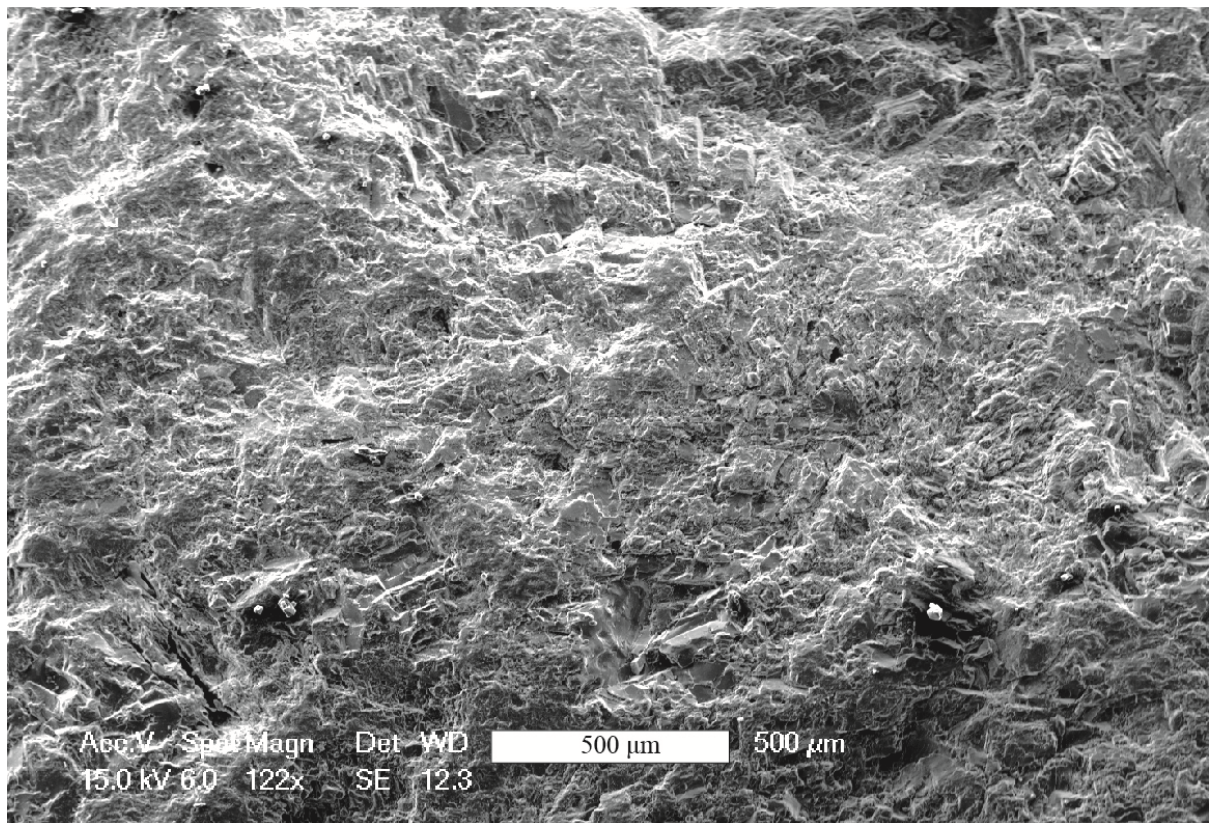
Figure 5-27. SEM image of the typical surface texture of a river-rounded monzogranite clast (#MC-2011-LB10).

The surface of the dacite clast analyzed also displays surface textures quite different from those of the monzogranite accessory lithic clasts. The dacite has high relief, a rough and irregular surface, many large pits (vesicles and plucked crystals), large plagioclase phenocrysts that are highly fractured along cleavage planes, and a microvesicular groundmass (Figure 5-28). No flaky breakage planes are observed.
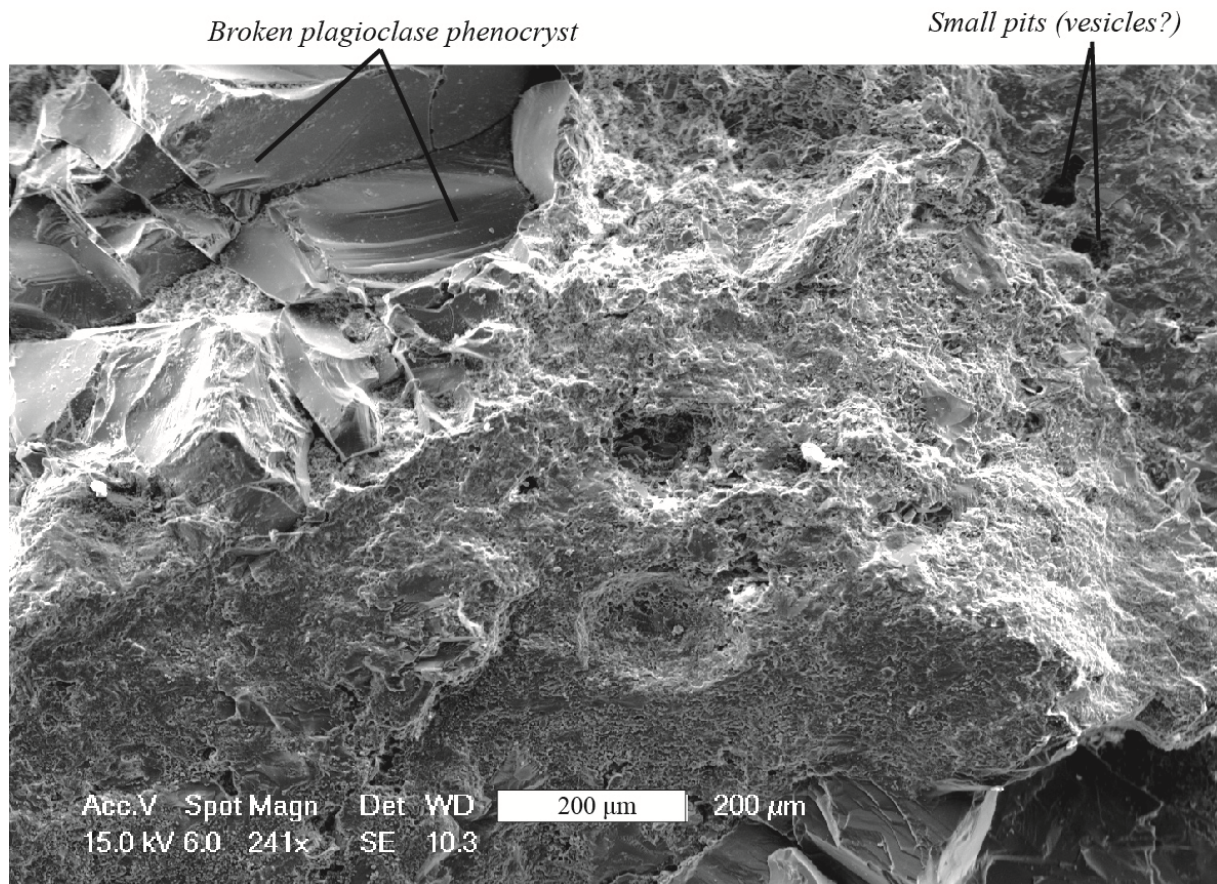
Figure 5-28. SEM image of the typically rough and irregular surface of a dacite accessory lithic clast (#MC-2011-P17). The large plagioclase phenocrysts are usually highly fractured, and the groundmass is rough and microvesicular.

In summary, the primary microscopic surface features of the smoothed and rounded surfaces of the monzogranite accessory lithic clasts are thin, flaky breakage planes parallel to the surface; this flakiness is likely the microscopic equivalent of the partially attached surficial spalls observed macroscopically on these samples (Figure 5-20). The flaky texture is more pervasive on the larger monzogranite clasts. These surfaces also display occasional signs of mechanical abrasion (e.g. small conchoidal fractures, impact pits). The relatively fresh fracture surface of the broken monzogranite clast analyzed did not display this flaky texture, and was instead dominated by angular, broken grains, small and large conchoidal fractures, scratches and impact pits. Finally, the dacite accessory lithic clast and the river-rounded monzogranite clast display their own distinct microscopic surface textures.

5.7 Thermal Spalling

The dominant surface textures visible on the smoothed and rounded faces of the monzogranite accessory lithic clasts, namely the concentric spalls (Section 5.6.1) and the pervasive flaky surface texture (Section 5.6.2), resemble the descriptions of thermally spalled rock surfaces in the literature (Section 2.2.2.1; Thirumalai, 1969). The thermally spalled surfaces are a result of exfoliation induced by thermal gradients. In order to investigate the extent to which the surfaces of the monzogranite lithics are controlled by heating, I cut a monzogranite clast into six cubes measuring approximately 4 x 4 x 4 cm using a circular rock saw. I split one face of each sample with a rock splitter to create a freshly fractured face. I then used a propane blowtorch to expose a circular area approximately 16 mm in diameter on a freshly split face to a temperature of 900°C. A temperature of 900°C was chosen for these experiments as it a likely maximum temperature of the subplinian phase of the PCF eruption. The cubes were exposed to a blowtorch flame for specific durations ranging from 30 seconds to 16 minutes. Following their exposure to the heat of the blowtorch, the rough faces of each of the six cubes underwent thermal spalling, whereby very thin flakes, or spalls, were suddenly and violently expelled from the surface of the samples. The flakes typically measure < 1mm in thickness and < 5 mm in length, although a few spalls up to 2 mm thick and 10 mm long were also formed.

Almost all of the visible spalling occurred during the first minute of exposure to the flame. Many of the samples formed very thin cracks propagating away from the heated area of the surface,

likely due to the thermal expansion of the heated area. The post-spalling surfaces of the samples typically took on a whitish, somewhat bleached colour, and gritty surface texture. Oftentimes, partially detached flakes could be observed on the sample surfaces.

In order to compare the surface textures produced via thermal spalling, I examined the surfaces of the thermally spalled samples with the SEM, using the sample preparation procedure described in Section 5.6.2. The samples chosen for SEM analysis were TS02, heated for a total of 30 seconds, and TS03, heated for a total of 8 minutes. The microscopic surface textures of both of these samples were characterized by small, platy flakes covering much of their surfaces (Figure 5-29a, 5-29b). These flakes tend to typically appear partially detached and uplifted around the edges. The flaky breakage planes visible on the surfaces of the smoothed and rounded portions of the monzogranite accessory lithics, however, always lie parallel to the surface, and do not have the same partially uplifted appearance. TS03 also displayed certain zones characterized by highly pitted surfaces, which appear somewhat porous (Figure 5-29b). The cause of this texture is unclear, but it is not observed on any of the other monzogranite samples analyzed, and is possibly a melting feature related to the prolonged exposure of sample TS03 to the heat of the blowtorch.

Two dacite blocks were also prepared using the method described above, and exposed to the flame of the propane blowtorch using the same experimental conditions employed for the monzogranite. However, neither dacite sample displayed any signs of thermal spalling, even after 16 minutes of exposure to the heat. The only apparent post-heating effect on the dacite surfaces was slight oxidation.
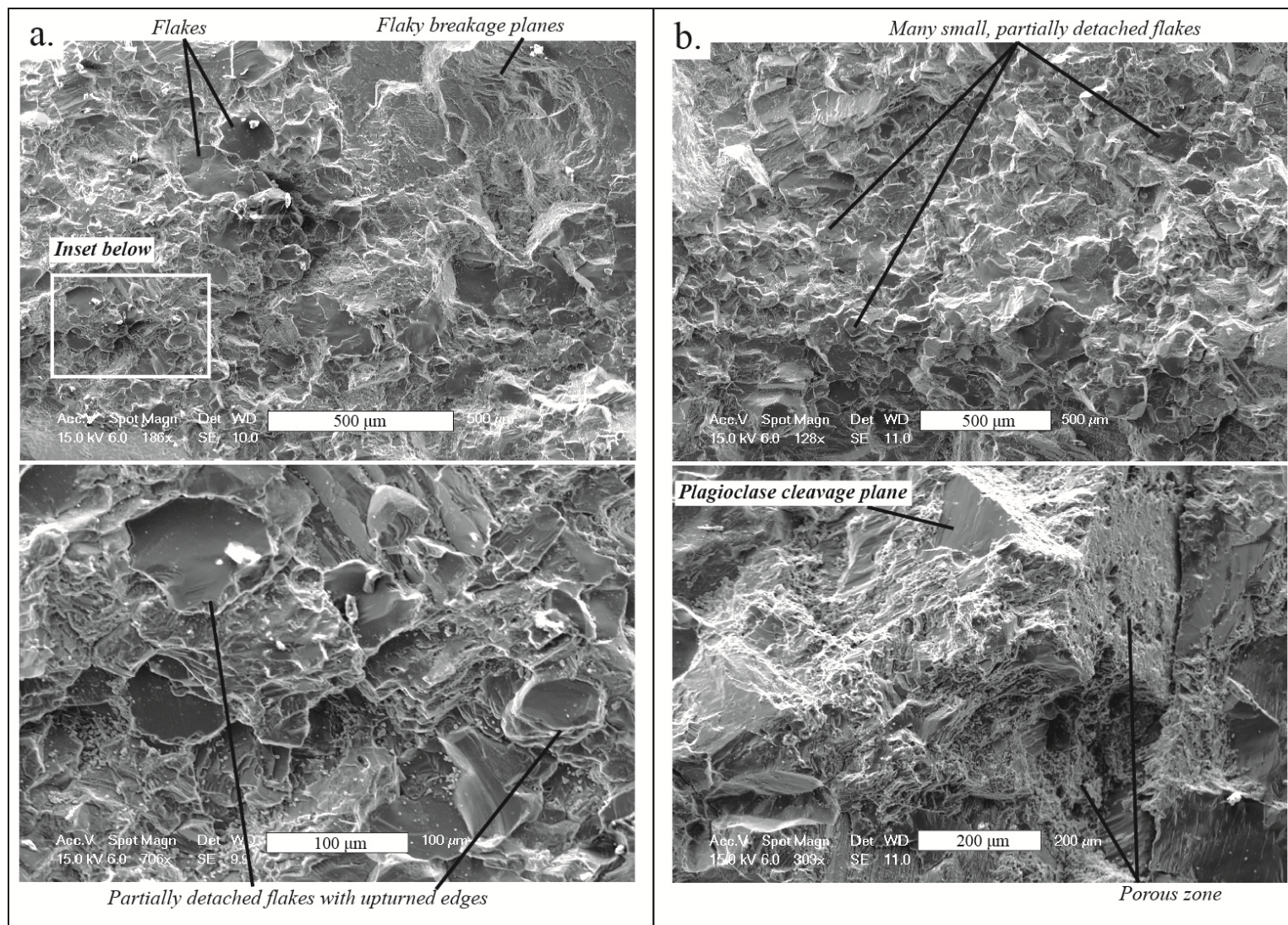
Figure 5-29. SEM image of the surfaces of two thermally spalled monzogranite samples. a) Sample #TS02, heated at 900°C for 30 seconds. b) Sample #TS03, heated at 900°C for 8 minutes.

In order for thermal spalling to occur, a steep thermal gradient is needed between the outer and inner parts of a clast. Figure 5-30 displays temperature profiles through a 15 cm diameter spherical lithic clast, which were generated using a Matlab® code for heat conduction by Recktenwald (2006). The input parameters values used for the model were clast radius (7.5 cm), ambient temperature (900°C), thermal conductivity of the clast (2.5 W/m K), thermal diffusivity (10^{-6} m^2/s) and heat transfer coefficient (100 W/m^2 K). Thermal profiles from the center to the outer surface of the clast are shown for six different durations of heating (i.e. residence times of the clast within the volcanic conduit): 0.2 minutes, 1 minute, 2 minutes, 5 minutes, 10 minutes and 20 minutes. The slope of the thermal profile indicates the steepness of the thermal gradient within the clast. Figure 5-30 shows that the steepest thermal gradients exist during the earliest stages of heating of the clast; this explain why the bulk of the thermal spalling of the monzogranite sample cubes occurred during the first minute of exposure to the heat from the blowtorch. Figure 5-30 also shows that a considerable amount of time (>> 20 minutes) is necessary to thermally equilibrate a clast of this size within the conduit.
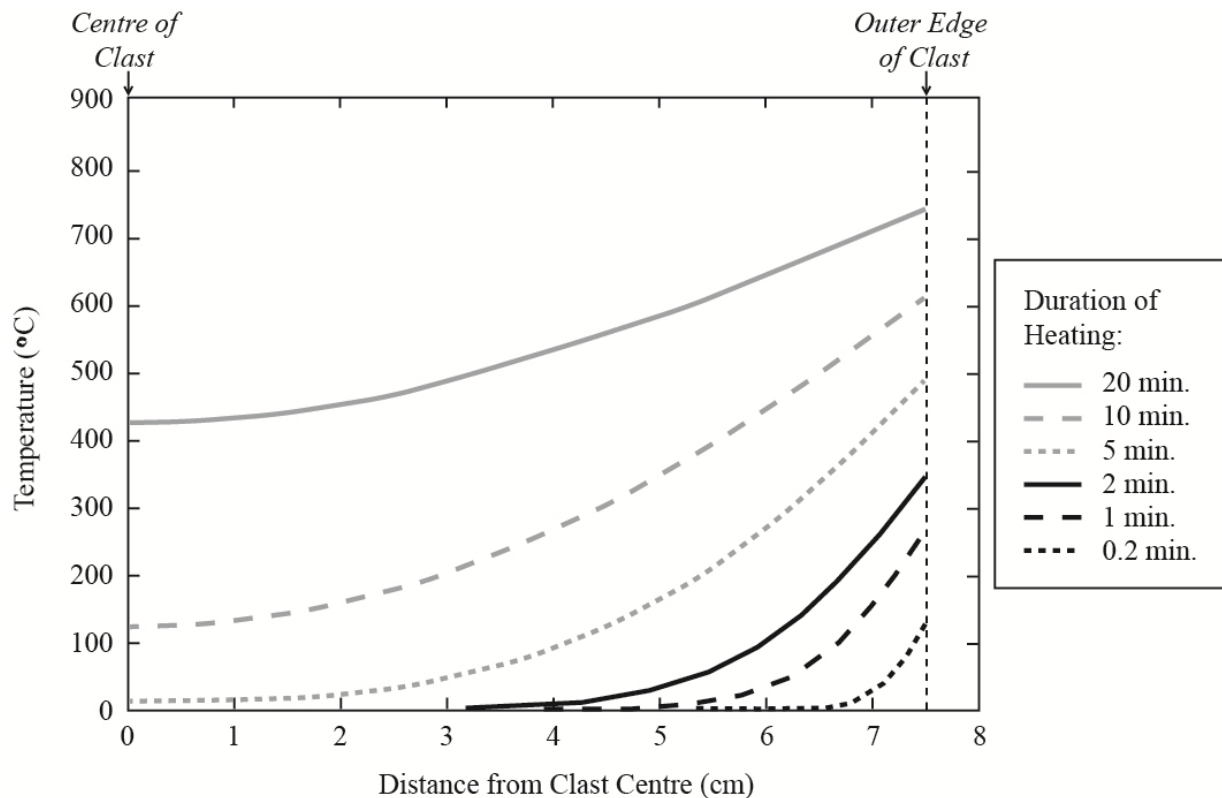
Figure 5-30. Temperature profiles through a 15 cm diameter spherical lithic clast, according to duration of heating (i.e. residence time of the clast in the 900°C volcanic conduit).

6. Discussion

6.1 Covariance of Size, Shape and Roughness of Lithics

The results presented in the previous chapter show that the monzogranite and the dacite accessory lithic sample sets have distinct morphological characteristics. In this section, I summarize the morphological data gathered for the monzogranites and the dacites, and explore important instances of covariance noted within the dataset.

Both the dacite and the intact monzogranite sample sets display similar shape distributions on Sneed and Folk Form diagrams (Figure 5-4). More than 75% of the samples from both sample sets fall within either the Compact, Compact-Bladed or Compact-Elongate Sneed and Folk Shape Classification fields (Figure 5-4), and all clasts from the two sample suites have Maximum Projection Sphericity (Ψ_p) values > 0.6. Neither suite contains particularly elongate or platy samples, nor do they contain highly equidimensional samples. A certain degree of correlation is also observed between Maximum Projection Sphericity and size for the monzogranite samples (Figure 5-5), as the smaller clasts (< 3000 cm^3) display a wider range and lower average of Maximum Projection Sphericity values than the larger clasts (> 3000 cm^3). Therefore, only some of the smaller monzogranite clasts are quite equant, while all of the larger clasts are quite equant.

Image analysis of the monzogranite and dacite clasts revealed that the monzogranites have significantly higher degrees of ellipticity and circularity than the dacites (Figure 5-10). The analysis of clast convexity also revealed significant differences between the monzogranite and dacite sample sets (Figure 5-11). At relatively small clast sizes (< 100 cm^3), the monzogranites and the dacites display similar convexity values, but at larger clast sizes (> 100 cm^3), the convexity values of the monzogranite sample set gradually increase to become considerably higher than those of the dacite clasts within the same size range (Figure 5-11). There is also a notable correlation between sample volume and convexity for the intact monzogranite clasts (Figure 5-11b). Using convexity as a proxy for surface roughness and irregularity (see discussion in Section 5.3), this data set shows that the intact monzogranites are relatively rough and irregular at small volumes, and become gradually smoother with increasing sample size. Importantly, the dacite sample set displays no such correlation between convexity and volume.

The 3-D scan analyses performed on accessory lithic samples revealed that the intact monzogranites and dacites have very different characteristic values of true sphericity (Ψ_t), with the monzogranites characterized by much higher Ψ_t values (Figure 5-15). The 3-D analysis of discrete surface patches on a selection of the accessory lithic clasts also revealed very different characteristic maximum smoothness values for the monzogranite and dacite clasts (Figure 5-18). A correlation between sample size and maximum surface smoothness was also found for the monzogranite clasts, whereby the smaller clasts (< 400 cm^3) display a large range in values of maximum smoothness ($S_{max} =$ 0.89 – 0.98; Figure 5-18), while the larger clasts (> 400 cm^3) all display very high maximum smoothness values ($S_{max} = 0.97 – 0.98$; Figure 5-18).

Sneed and Folk (1958) identified 6 main parameters that may influence the final morphology of a lithic clast: (1) its original morphology when liberated from the parent rock; (2) intrinsic properties of the clast (e.g. hardness, anisotropies, pre-existing fractures, etc.); (3) particle size; (4) distance or effectiveness of transport; (5) agent of transport; and (6) the many other factors which might be termed "chance." This comprehensive suite of parameters must therefore explain the differences and similarities identified within the two suite of accessory lithic clasts analyzed in this study. The high degree of similarity in form, or dimensionality, between both the dacite and the intact monzogranite sample sets might be attributable to similarities in the forms of these clasts when they were first liberated from the conduit walls during the eruption, and incorporated into the stream of erupting material. An important parameter controlling the form of the initial particles includes the spacing of the joint sets within the host rock bodies; if the columnar joints within the dacite body and the joints within the monzogranite body had similar spacing, the dimensions of the blocks fractured from the conduit wall rocks might be quite similar. In all other aspects of morphology analyzed, however, the monzogranites and the dacites display significant differences. Certainly part of these differences are due to dissimilarities in the intrinsic rock properties of these two clast types. For instance, the monzogranites are much harder, are more competent, and are much less porous than the dacites. The plagioclase phenocrysts within the porphyritic dacites also appear to be quite weak, as they are readily plucked or broken; the loss of these weak crystals from the surfaces of the dacite clasts certainly increases their overall surface roughness. Furthermore, it was observed that, when heated to eruption

temperatures ($\sim 900^{\circ}$C), monzogranite will exhibit violent thermal spalling, while the dacite does not. These properties could have important implications for the reshaping effectiveness of these clast types.

Although the monzogranites and the dacites are both accessory lithics from the same volcanic deposits, and were therefore emplaced by the same overall volcanic process, the duration of transport and the specific conditions encountered for each of these clast types may differ. Importantly, the source to the dacite accessory lithic clasts is the Plinth Assemblage, which is located at a much higher elevation than the intrusive body (the Fall Creek Stock) which sourced the monzogranite accessory lithic clasts (Figure 3-4). Thus, in order to exit the conduit, the monzogranite clasts must have travelled a greater distance than the dacite clasts. The differences in density between the two accessory lithic types may influence their effective transportation velocities within the conduit, a parameter which could influence the abrasion rates (via ash-blasting) encountered by these clast types. Furthermore, the density and velocity of the dusty gas phase within the conduit does not remain constant as the particle-laden erupting gas stream rises to the surface: it continually increases in velocity (up to a certain extent) and decreases in density as it rises upward. Thus, the comminution conditions encountered by the monzogranite clasts at depth, when they are first ripped from the conduit walls, will not be the same as those encountered by the dacite clasts when they are incorporated from their parent rock situated much higher up within the conduit.

In the following two sections, I will investigate how the transport conditions within the volcanic conduit may have differed for the monzogranite and the dacite clasts. In Section 6.2, I will present calculations of the likely velocity conditions within the conduit. In Section 6.3, I will discuss the main comminution processes operating within the volcanic conduit, and will utilize the quantitative and qualitative morphological data gathered to generate a mechanistic model of how the accessory lithic clasts were reshaped during the 2360 B.P. MMVC eruption.

6.2 Lithic Velocities and Residence Times in the Conduit

Above the fragmentation front (Figure 2-2), all of the clasts within the volcanic conduit are subject to two competing forces: the drag from the rapidly ascending particle-laden stream of erupting gas, and gravity. For a clast of spherical shape, the following equilibrium relationships exist between gravity and drag (Wilson et al., 1980):

$$\frac{\pi d^3 g (\rho_c - \rho_g)}{6} = \frac{\pi C_D d^2 \rho_g (U_T)^2}{8} \qquad (6.1)$$

$$[Gravity] \qquad\qquad [Drag]$$

where d is the diameter of the clast, ρ_c is the density of the clast, ρ_g is the density of the particle-laden gas, g is the acceleration due to gravity (9.81 m/s^2) and C_D is the drag coefficient. I will use a drag coefficient of $C_D = 1.2$ (Table 6-1), as this is an appropriate value for lithic clasts settling in a subplinian to plinian eruption column (Walker, 1971). The drag force of the rising gas pushes the clasts upwards, while gravity inevitably pulls the clast downwards. Whether or not the clast will rise or fall within the conduit, relative to a fixed reference frame, depends on the velocity of the particle-laden gas stream as well as the terminal velocity (U_T) of the clast in the dusty gas. For a spherical clast, equation 6.1 may be rearranged to yield the terminal velocity of a clast within the conduit:

$$U_T = \sqrt{\frac{4 d g (\rho_c - \rho_g)}{3 C_D \rho_g}} \qquad (6.2)$$

Equation 6.1 shows that larger clasts and denser clasts will have greater terminal velocities, while an increase in the density of the gas within the conduit will decrease the terminal velocity of the clast. The velocity of the clast relative to a fixed reference frame may then be defined as:

$$U_R = U_G - U_T \qquad (6.3)$$

where U_G is the velocity of the gas jet, and U_R is the velocity of the clast relative to a fixed reference frame (e.g. the Earth's surface). If $U_R > 0$, the clast will be lofted in the conduit (i.e. have a net upward velocity), and if $U_R < 0$, the clast will sink (i.e. have a net downward velocity). In the special case that $U_R = 0$, the clast will remain stationary relative to the surface, tumbling around at a fixed depth in the conduit.

Eruption Parameter	Value Used for this Study
Estimated Parameters	
Plume Height (H)	16 km
Depth to fragmentation front (km)	< 2 km
Drag coefficient (C_D)	1.2
Magma density (ρ_m)	2500 kg/m^3
Exsolved weight fraction of gas (n_f)	0.03
Molar weight of gas phase (m)	18.0153 g/mol
Temperature (T)	1173 K
Calculated Parameters	
Mass flux (M_f)	2.1·10^7 kg/s
Conduit diameter (D)	40 – 50 m

Table 6-1. Parameters used to model the 2360 B.P. Pebble Creek Formation eruption.

In order to determine U_T and U_R values for clasts within the conduit of the 2360 B.P. MMVC eruption, we must first determine ρ_g and U_G (the density and velocity of the dusty gas stream, respectively). Because the pressure of the dusty gas phase within the conduit is approximately lithostatic pressure, the pressure of the gas phase will decrease significantly as it rises up through the crust. As the pressure decreases, the volume of the gas will increase considerably, and therefore its density will decrease. The density of the gas at a given depth within the conduit is given by Wilson et al. (1980):

$$\rho_g = \frac{P\ m}{Q\ T} \qquad (6.4)$$

where *P* is the lithostatic pressure (Pa) at the given depth, *m* is the molecular weight of the gas (kg/mol), *Q* is the Universal Gas Constant (8.31 J/[K·mol), and *T* is the temperature of the gas phase (K) (Table 6-1). Assuming that the gas is mostly made up of $H_2O_{(g)}$, m will be approximately $1.80153 \cdot 10^{-2}$ kg/mol. I will also assume that the temperature of the gas was fixed at 900°C (1173 K) for the duration of the eruption, and throughout the conduit. The calculated values of ρ_g, using these values, therefore range from 102 kg/m^3 at 2 km depth to 5 kg/m^3 at 0.1 km depth (Table 6-2).

Depth Below Surface (km)	Lithostatic Pressure, P (MPa)	Gas Density, ρ_g (kg/m^3)	Bulk Density, ρ_B (kg/m^3)
0.1	2.75	5	159
0.2	5.5	10	299
0.4	11.0	20	537
0.6	16.5	30	729
0.8	22.0	41	888
1.0	27.5	51	1022
1.2	33.0	61	1137
1.4	38.5	71	1235
1.6	44.0	81	1321
1.8	49.5	91	1397
2.0	55.0	102	1464

Table 6-2. Variation in gas density and bulk density relative to depth below the surface.

Now that the velocity profile of the gas phase within the conduit has been constrained, we may calculate the terminal velocities of clasts settling within the conduit using equation 6.2. Terminal velocity profiles for monzogranite and dacite clasts, using their respective mean densities (2590 kg/m^3 and 2470 kg/m^3, respectively), are shown in Figures 6-1a and 6-1b. Note that the terminal velocity profiles of both clast types are essentially identical, as the only intrinsic clast properties contained in equation 6.2 are clast size (diameter) and density, and the mean densities of the monzogranite and dacite clasts are quite similar. In reality, factors such as particle form and surface roughness will also affect clast terminal velocities. However, such calculations are beyond the scope of this work, and here we assume that all clasts are approximately spherical. The maximum depth of 2 km shown on the graphs of Figure 6-1 and subsequent figures in this chapter was chosen as a likely maximum depth to the fragmentation front (e.g. Melnik and Sparks, 2006).

a)

Monzogranite Clasts

b)
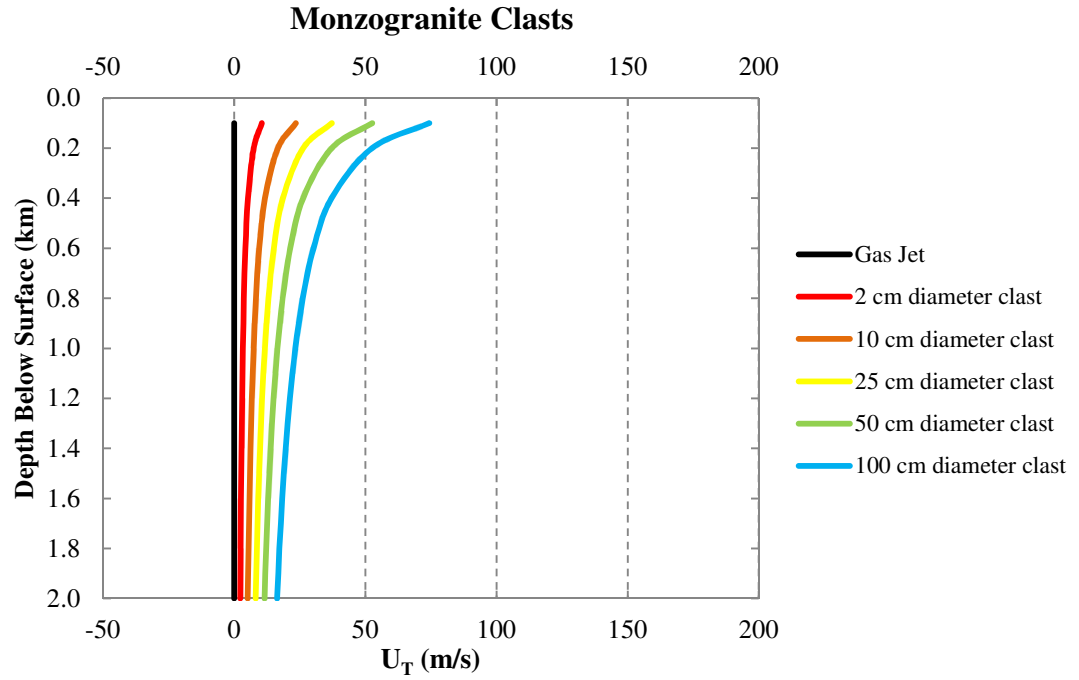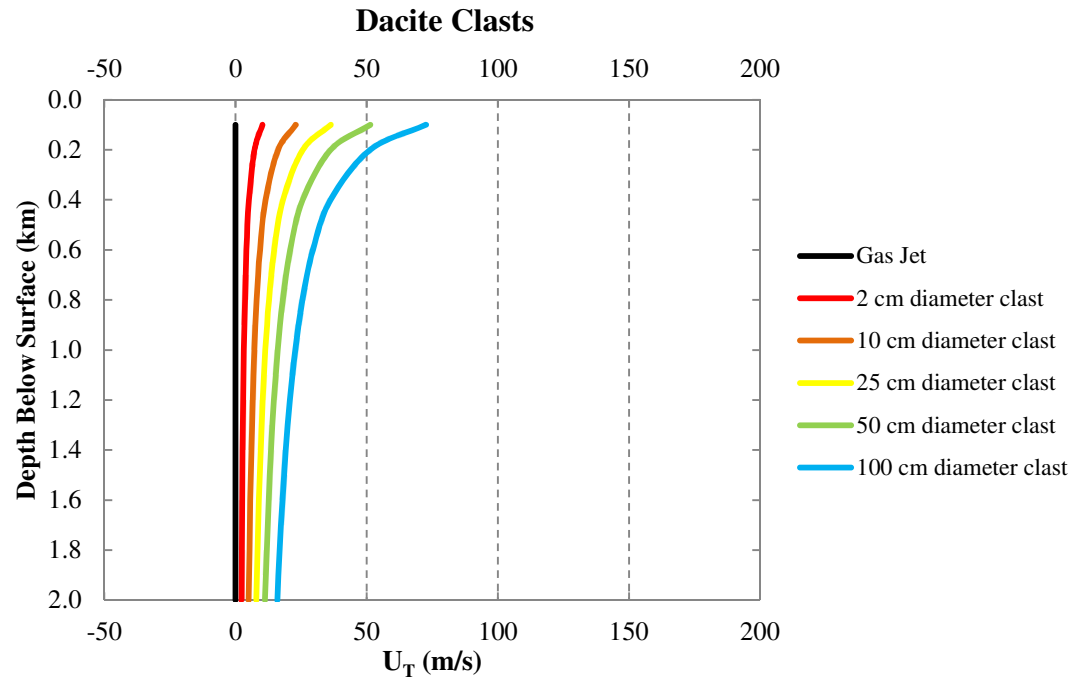
Dacite Clasts

Figure 6-1. Terminal settling velocities (U_T) for accessory lithic clasts, according to position below the surface. a) Terminal settling velocities of monzogranite clasts, using mean monzogranite density (2590 kg/m^3). b) Terminal settling velocities of dacite clasts, using mean dacite density (2470 kg/m^3). The small difference in mean density between the two clast types has a negligible influence on the terminal settling velocity profiles.

The second parameter relating to the gas phase, velocity (U_g), is somewhat more difficult to quantify as it depends on both the mass flux (M_f) of the eruption as well as the diameter of the conduit. The mass flux, measured in units of kg/s, is assumed to stay constant throughout the conduit, as the rate of the mass entering at the base of the magmatic plumbing system must equal the rate of mass exiting the system through the vent, if no magmatic material is being lost along the way. I will also assume that the mass flux will remain constant throughout the course of the eruption. The mass flux of the eruption may be approximated from the height of the volcanic plume of the eruption (H), according to the following relationship for subplinian and plinian eruptions from Wilson et al. (1980):

$$H = 0.236 \sqrt[4]{M_f} \qquad (6.5)$$

The plume height of the subplinian phase of the 2360 B.P. MMVC eruption has been estimated at 15-17 km (Hickson et al., 1999; Luty, 1994). Therefore, using an average value of 16 km for H, $M_f = 2.1 \cdot 10^7$ kg/s. M_f may in turn be related to the velocity of the gas phase (Ug) using the following relationship:

$$M_f = \pi \left(\frac{D}{2}\right)^2 \rho_B \, U_g \qquad (6.6)$$

where D is the radius of the volcanic conduit (assuming a perfectly cylindrical conduit), and ρ_B is the bulk density of the erupting particle-gas mixture (Wilson et al., 1980). In turn, ρ_B is given by:

$$\frac{1}{\rho_B} = \frac{n_f}{\rho_g} + \frac{\left(1 - n_f\right)}{\rho_m} \qquad (6.7)$$

where n_f is the exsolved weight fraction of gas, and ρ_m is the density of the magmatic liquid (Wilson et al., 1980). I will use values of $n_f = 0.03$, and $\rho_m = 2500$ kg/m^3 as best approximations for the conditions within the conduit of the 2360 B.P. MMVC eruption. Computed bulk densities, according to depth below the surface, are found in Table 6-2.

Finally, in order to determine the gas velocity profile (U_g) within the conduit using equation 6.6, one last variable must be constrained: the diameter (D) of the conduit. The expected range of conduit diameters for a subplinian to plinian eruption is 10 – 100 m, and the expected range for an eruption with $M_f = 2.1 \cdot 10^7$ kg/s is on the order of 20 m to 60 m (Wilson et al., 1980). Figure 6-2 shows the calculated gas velocity profiles for conduit diameters of 20, 30, 40, 50 and 60 m. Figure 6-2

clearly shows the significant effect of conduit diameter on gas velocities; the narrower the conduit, the higher the gas velocities must be in order to maintain constant M_f.

We may now compute U_R, the relative (i.e. net upward) velocities of clasts, using equation 6.2. Computed U_R profiles for monzogranite clasts (2590 kg/m^3) of a selection of different sizes: 2 cm, 10 cm, 25 cm, 50 cm and 100 cm diameter are shown in Figure 6-3. These results show that conduit diameter has a significant impact on the relative velocities of clasts.
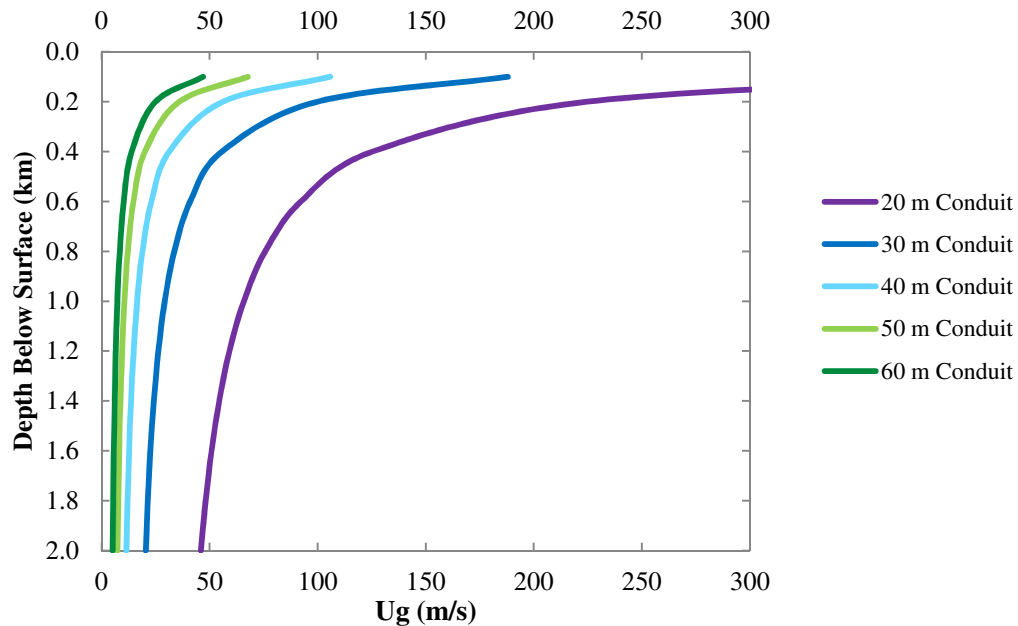
Figure 6-2. Gas velocity profiles for varying conduit diameters, using the parameters found in Tables 6-1 and 6-2.

The largest monzogranite accessory lithic clast collected from the fallout deposits (sample # MC-2010-Yc040) weighs 51.7 kg and has a volume of approximately 19,900 cm^3. The equivalent diameter of this clast (i.e. the diameter of a sphere with equivalent volume) is 33.6 cm (the 3 measured orthogonal axes of this clast are 44.7, 34.9 and 28.6 cm). Therefore, the conditions within the conduit should be capable of lofting a particle of this size. The U_R results for the conduit diameter of 60 m show that clasts > 10 cm in diameter cannot be lofted within the conduit (Figure 6-3e). Therefore, the conduit of the 2360 B.P. eruption must have had diameter D < 60 m. Furthermore, the U_R results for the conduit diameters of 20 m and 30 m show that even extremely large monzogranite clasts (over 100

cm in diameter) could easily be lofted out of the conduit (Figures 6-3a, 6-3b). Due to the scarcity of accessory lithic clasts of this size within the proximal fallout deposits, it is unlikely that these values represent the conditions of the 2360 B.P. eruption, and so it is probable that D > 30 m. The computed U_R results for conduit diameters of 40 m and 50 m, however, appear to recreate realistic conditions within the conduit (Figures 6-3c, 6-3d).

The shaded areas in the graphs of Figure 6-3 denote regions of clast sinking ($U_R < 0$), while the white areas represent zones of clast lofting ($U_R > 0$), relative to the Earth's surface. In order to better explain the significance of these velocity zones, the U_R versus depth profile of a single clast size (25 cm diameter) within a 50 m diameter conduit (Figure 6-3d) is displayed in Figure 6-4. Figure 6-4 shows that above 0.6 km depth, 25 cm diameter clasts will be lofted in the conduit and eventually be ejected from the vent ($U_R > 0$). However, below 0.6 km depth, clasts of this size will sink down into the conduit ($U_R < 0$). Therefore, the depth at which a clast is incorporated into the stream of erupting material can affect whether or not a clast will ultimately be ejected from the vent. Based on the estimated stratigraphy beneath the vent of the 2360 B.P. vent (Figure 3-4), the dacite clasts were incorporated from the Plinth Assemblage deposits at depths of 0 to 550 m below the surface, while monzogranite clasts were incorporated from the Fall Creek Stock at depths of > 700 m below the surface. Therefore, using the example in Figure 6-4 (50 m diameter conduit), a 25 cm dacite clast suddenly ripped from the Plinth Assemblage conduit walls (at < 550 m depth) would be lofted in the conduit and erupted, while a 25 cm monzogranite clast suddenly ripped from the Fall Creek Stock monzogranite walls (at > 700 m depth) could not be erupted, and would slowly descend deeper into the conduit.
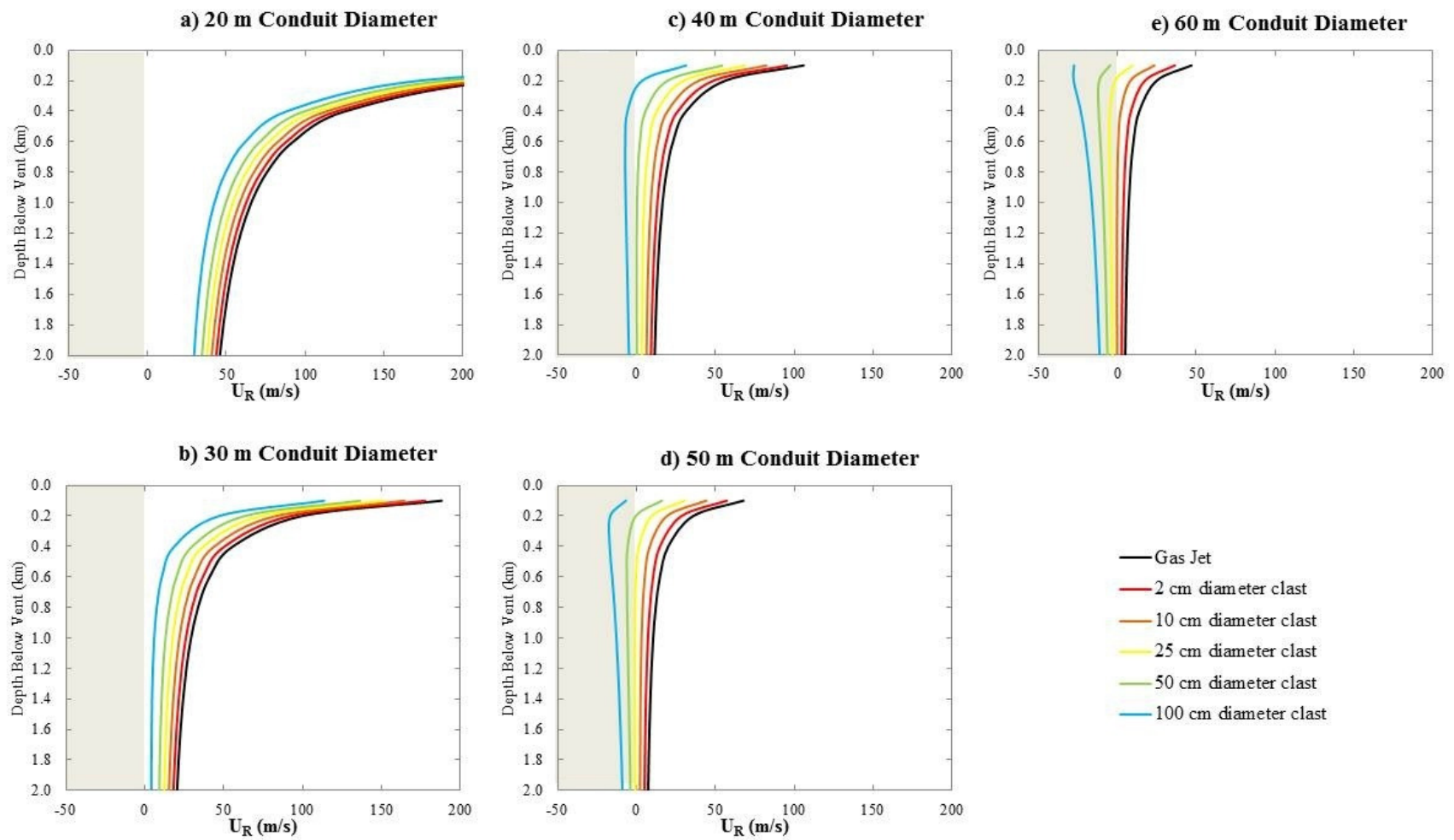
Figure 6-3. Relative velocity profiles of a selection of monzogranite clast sizes at the conditions described in Tables 6-1 and 6-2, for varying conduit diameters. Gray areas ($U_R < 0$) indicate zones of clast sinking, while white areas are zones of clast lofting ($U_R > 0$).
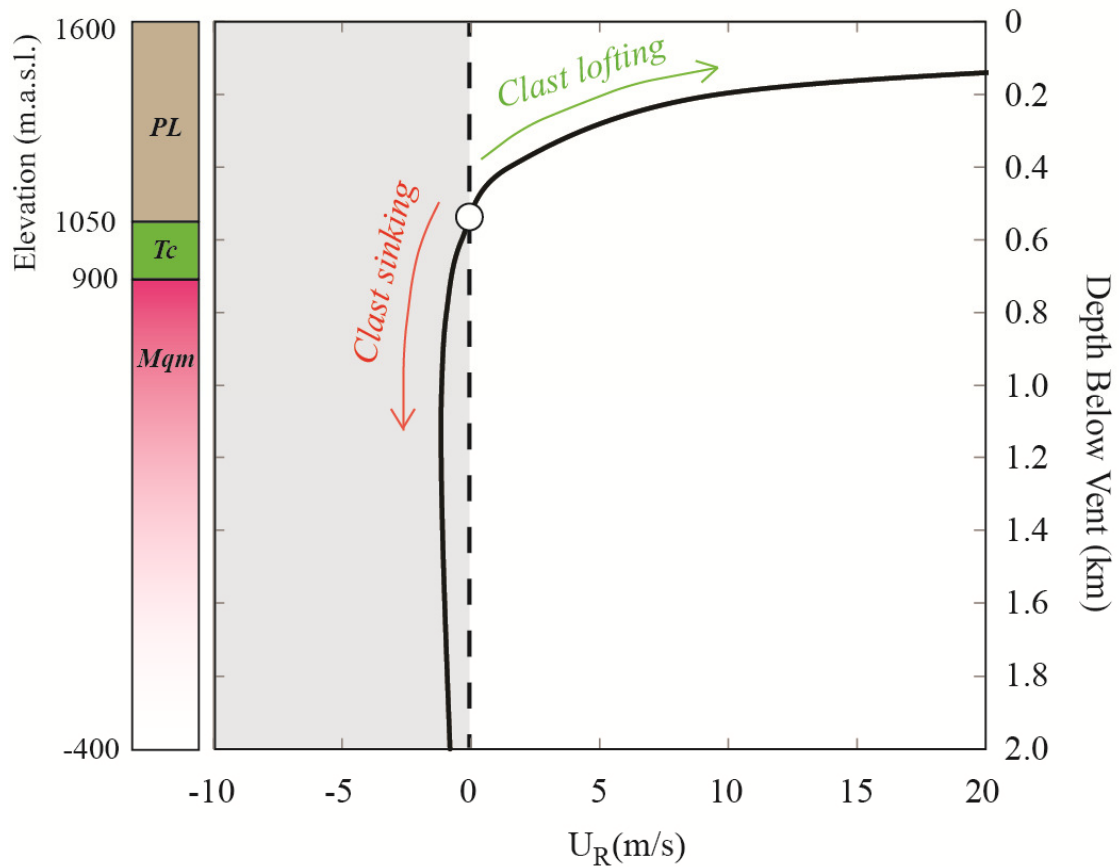
Figure 6-4. Relative velocity (U_R) profile of a 25 cm diameter clast settling in a 50 m diameter conduit. The shaded area represents the zone of clast sinking ($U_R < 0$), while the unshaded area represents the zone of clast lofting ($U_R > 0$). The white circle, at $U_R = 0$, marks the depth of neutral buoyancy of the clast. The vertical bar at the left denotes the approximate depths of the three main lithologies beneath the vent of the 2360 B.P. eruption: the Plinth Assemblage dacite (PL), the Cadwallader Formation (Tc) and the Fall Creek Stock monzogranite (Mqm) (Figure 3-4).

Another important parameter which may be obtained from the relative velocity profiles is the residence time of clasts within the conduit. I define the "residence time" of a clast as the total time spent in the volcanic conduit, from the moment that the clast is first incorporated into the dusty gas stream (i.e. broken loose of the conduit walls) to the moment that the clast is ejected from the vent. Residence time is an important parameter to consider in the study of clast reshaping, as increased residence times will correspond to increased amounts of total clast comminution. Residence time is somewhat difficult to calculate, as the relative velocities of clasts depend on their position within the

conduit as well as their size (Figure 6-3). However, smaller clasts will tend to have higher relative velocities, and therefore shorter residence times, than larger clasts. In order to estimate residence time, I fit power-law trendlines to the U_R versus depth profiles of clasts of different sizes in Microsoft® Excel, producing trendlines of the following format:

$$Z = a \cdot (U_R)^b \qquad (6.8)$$

where Z is the depth (negative number) in meters below the surface (e.g. Z = -2000 m at 2 km depth), and "a" and "b" are constants. The "a" and "b" values computed for the trendlines of the relative velocity profiles of various clast sizes, and for conduits of 40 m and 50 m diameter, are displayed in Table 6-3. Furthermore, because U_R is the relative velocity in m/s, U_R may be expressed as the change in depth with time (t) of the clast:

$$U_R = \frac{dZ}{dt} = \left(\frac{Z}{a}\right)^{1/b} \qquad (6.9)$$

Therefore, dt may be expressed as:

$$dt = \frac{a^{(1/b)} \, dZ}{Z^{(1/b)}} \qquad (6.10)$$

In order to determine the residence time of a clast, we must determine the time between incorporation of the clast into the gas jet (at depth Z_0) and the moment that the clast is ejected from the vent (at depth Z_f). The residence time (Δt) of a clast may be expressed as:

$$\Delta t = \int_{Z_0}^{Z_f} \frac{a^{\left(\frac{1}{b}\right)} \, dZ}{Z^{\left(\frac{1}{b}\right)}} = \left[\frac{b \cdot \left(a^{(1/b)}\right)}{b-1}\right] \cdot \left[Z_f^{\left(\frac{b-1}{b}\right)} - Z_0^{\left(\frac{b-1}{b}\right)}\right] \qquad (6.11)$$

Since we are considering the case where the final depth of the clast is the surface ($Z_f = 0$), equation 6.11 may be rewritten as:

$$\Delta t = \left[\frac{b \cdot \left(a^{(1/b)}\right)}{b-1}\right] \cdot \left[1 - Z_0^{\left(\frac{b-1}{b}\right)}\right] \qquad (6.12)$$

The Δt values for a selection of clast sizes were computed for four depths of incorporation into the gas stream (Z_0): 2000 m, 1500 m, 1000 m and 500 m (Table 6-3). Furthermore, in order to investigate the effect of conduit diameter on the residence times of clasts, Δt values were computed for two conduit diameters: 40 m and 50 m (Table 6-3). These residence time results are presented in Figure 6-5, where clast residence time is plotted against clast size.

Clast diameter (cm)	"a" value	"b" value	Clast residence time Δt (min) for source depth:			
			2000 m	1500 m	1000 m	500 m
40 m diameter conduit						
0	50144	-1.376	1.9	1.1	0.6	0.2
5	22077	-1.248	2.7	1.6	0.8	0.2
10	14552	-1.176	3.3	2.0	0.9	0.3
15	10122	-1.109	4.1	2.4	1.1	0.3
20	7178	-1.042	5.0	2.8	1.3	0.3
25	5109	-0.971	6.3	3.5	1.5	0.4
30	3611	-0.894	8.1	4.4	1.9	0.4
35	2503	-0.807	11.3	5.9	2.4	0.5
40	1669	-0.700	17.8	8.8	3.3	0.6
45	1262	-0.620	26.8	12.6	4.4	0.7
50	977	-0.558	∞	∞	6.2	0.9
60	516	-0.378	∞	∞	∞	2.1
62	416	-0.302	∞	∞	∞	3.6
63	---	---	∞	∞	∞	∞
50 m diameter conduit						
0	27129	-1.376	2.9	1.8	0.9	0.3
2	12778	-1.250	4.2	2.5	1.2	0.3
5	7404	-1.146	5.7	3.3	1.6	0.4
10	3434	-0.980	9.5	5.3	2.3	0.6
15	1562	-0.775	20.0	10.4	4.1	0.8
18	880	-0.586	50.0	22.9	7.7	1.2
19	685	-0.478	101.4	41.7	11.9	1.4
20	551	-0.386	∞	∞	21.7	1.8
25	401	-0.344	∞	∞	∞	4.1
26	---	---	∞	∞	∞	∞

Table 6-3. Residence times of lithic clasts, based on clast size and depth of incorporation into the volcanic conduit for two different conduit diameters: 40 m and 50 m. Infinite values ("∞") are assigned to clasts with negative relative velocities ($U_R < 0$), as they will not be lofted in the conduit or erupted under these conditions. Note that the values for a clast size of "0 cm diameter" refer to the residence time of the gas jet (and of any extremely small particles coupled to the gas jet).

a) 40 m Diameter Conduit
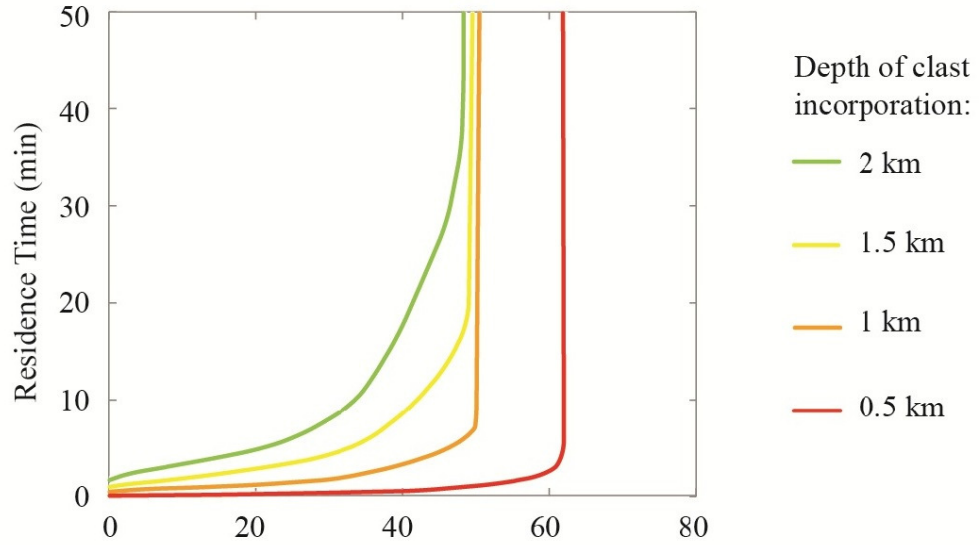
b) 50 m Diameter Conduit
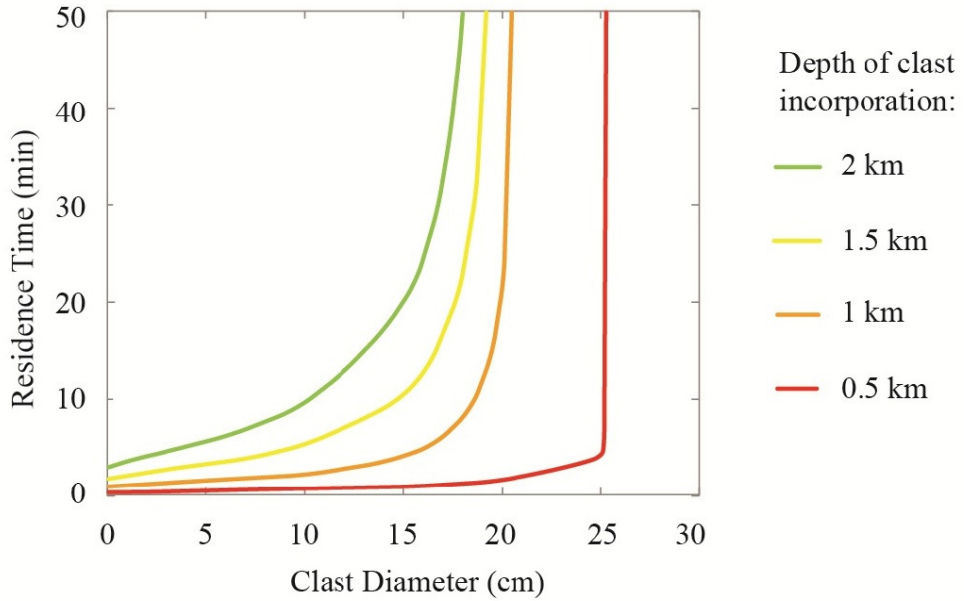
Figure 6-5. Residence time (Δt) of lithic clasts within the conduit, as a function of the size and the depth of incorporation of the clast. a) Residence times of clasts within a 40 m diameter conduit. b) Residence times of clasts within a 50 m diameter conduit. Residence times go to infinity for clasts of a size for which $U_R = 0$ m/s (i.e. when a clast is suspended indefinitely).

A number of important trends are visible in Figure 6-5. First, as previously stated, the choice of conduit diameter affects the maximum lithic size that may be erupted. Much larger clasts may be erupted from the 40 m diameter conduit (Figure 6-5a) than the 50 m diameter conduit (Figure 6-5b). Secondly, the depth of incorporation has a very important effect on both residence time and maximum lithic size that may be erupted. In the case of the 50 m diameter conduit (Figure 6-5b), a 18 cm clast incorporated at 1 km depth will have a residence time of 7.7 minutes, while a clast of the same size incorporated at 0.5 km depth will have a residence time of only 1.2 minutes (Table 6-3). Furthermore, a 23 cm diameter clast incorporated at 0.5 km depth will have a residence time of ~ 3 minutes, while a clast of the same size that is incorporated at 1 km depth will not be lofted, or erupted ($U_R < 0$ at 1 km depth, and so the clast's residence time is measured as infinite).

It should be noted that up to this point, all eruption parameters, including mass flux, volatile content and temperature, have been modeled as static and unchanging (Table 6-1). However, over the course of a real eruption, short-term fluctuations or sustained trends will affect many of the parameters. For example, the mass flux (M_f) may fluctuate over the course of the eruption, affecting the relative velocities of the both the gas phase and particles. The effective conduit diameter may also change over the course of the eruption, as gradual erosion widens the conduit, or if a section of the wall rocks suddenly fails and creates a blockage within the conduit. Therefore, the results computed in this section are best viewed as proxies for the typical conditions within the conduit of the 2360 B.P MMVC eruption. These proxies are necessary in order to show the influence of specific parameters (e.g. depth of incorporation, or clast size) on the behaviour of accessory lithics in the conduit.

It should also be emphasized that the accessory lithic clasts themselves are also in a state of constant change within the conduit. Clasts will be gradually abraded by ash-blasting, and will occasionally undergo more energetic collisions resulting in disruptive fragmentation. For example, the effective drag on a monzogranite clast will decrease as the clast gradually becomes smoother and rounder due to volcanic ash-blasting. Let us also consider a scenario where a large clast sustains an impact that causes it to break into multiple small fragments. The relative velocities of these small fragments will be significantly higher than the relative velocities of the larger intact clast, and therefore the fragments will rise at a faster pace within the conduit (e.g. Figure 6-3). The implications of this scenario will be examined further in the next section (Section 6.3).

6.3 Mechanistic Model for Reshaping These Lithics in the Flux

To set the scene for a comprehensive model of how the accessory lithic clasts were reshaped in the volcanic conduit, the specific processes that affected their morphologies must be discussed. First, potential non-volcanic causes of the rounding of the monzogranite clasts, such as the possibility that they represent glacially faceted clasts from a paleo-till deposit that had overlain the vent, or that the monzogranite clasts are corestones from spheroidally weathered basement rocks, can be discounted. The rounded monzogranite clasts cannot be sourced from a surficial till deposit because they occur throughout all phases of the fallout deposits (Table 4-5). The contents of a surficial deposit overlying the vent, which the eruption would have blasted through in the early stages of the eruption, should be concentrated within the lowermost (i.e. earliest) parts of the fallout deposits. Furthermore, glacial till typically contains rounded pebbles and cobbles of many different lithologies, whereas few rounded lithics of lithologies other than monzogranite have been noted in the PCF fallout deposits. Spheroidal weathering may be discounted as the source of the monzogranite rounding, due to the paucity of clasts resembling altered monzogranite rind material in the fallout deposits, and because of the presence of fresh, planar joint surfaces on many monzogranite clasts (spheroidal weathering would have produced alteration along these joints). Therefore, the source of the rounding of the monzogranite accessory lithic clasts is almost certainly attributable to volcanic reshaping.

Three main volcanic processes have been identified which likely contributed to the reshaping of accessory lithic clasts: 1) solid impingement erosion, via ash-blasting; 2) thermal effects; and 3) disruptive fragmentation, caused by energetic collisions. The two accessory lithics studied here, the monzogranite and the dacite clasts, were both affected by the three aforementioned volcanic processes, but were erupted with significantly different final morphologies. In order to understand why these differences in final morphology exist between the monzogranite and dacite clasts, I will examine each of the three aforementioned processes and discuss the different influence that each of them may have had on the two clast types.

6.3.1   Solid Impingement Erosion (Ash-Blasting)

During an eruption, ash-sized (i.e. < 2 mm) particles with negligible terminal velocities will travel upward through the conduit at velocities approximately coupled to that of the gas phase. Larger

clasts do not ascend the conduit as rapidly as the gas phase, and the differential velocity between the ash-laden gas jet and the clast is given by the terminal settling velocity of the clast. Lithic clasts will therefore be bombarded by the particles contained within the ash-laden gas jet as it flows upwards past them. This bombardment is a form of solid impingement which I will refer to as ash-blasting.

Volcanic ash-blasting of lithic clasts is, to date, an unstudied process. Therefore, in order to understand the likely parameters involved in ash-blasting, the analogous solid impingement erosion process of sandblasting was investigated. Solid impingement erosion via sandblasting has significant material removal capability, and is used for such industrial applications as drilling operations and cleaning stone walls (Momber, 2004). The study of sandblasting is also of interest to sedimentologists studying the effects of wind abrasion (e.g. Kuenen, 1960; Suzuki and Takahashi, 1981). The effectiveness of the sandblasting process is a function of the strength of the target rock, the strength of the abradant particles, the abradant mass flow rate, the velocity of the abradant particles, the angle of impact, and various other intrinsic properties of the abradant particles (e.g. angularity, size distribution) and of the target rock (e.g. grain size, anisotropies such as foliation) (Momber, 2004; Suzuki and Takahashi, 1981; Verhoef et al., 1984). Sandblasting produces multiple failure mechanisms in the surface of the target rock, including breakages along pre-existing flaws in the rock surface, along grain boundaries and within individual mineral grains (Verhoef et al., 1984). However, Momber (2004) noted that in the case of sandblasted granite, the primary fracture mechanism was the cleavage or fracture of minerals, as the bond forces between individual mineral grains appeared to be higher than the cohesion forces within the minerals. Verhoef et al. (1984) studied the microstructure of sandblasted rocks of various lithologies, and observed that many fractures were induced sub-parallel to the surface of the targeted rock. These sub-parallel fractures likely result from failure in tension due to elastic rebound following impact (Verhoef et al., 1984). Other fractures approximately perpendicular to the surface of the targeted sample, as well as conchoidal fractures in quartz, were interpreted to result from compressive failure during impact (Verhoef et al., 1984). The abrasion rates associated with sandblasting have been shown to be inversely proportional to the tensile strength (e.g. Verhoef et al., 1984), the fracture toughness (e.g. Momber, 2004), and the compressive strength (e.g. Suzuki and Takahashi, 1981) of the targeted rocks; therefore, weaker rocks will abrade faster than stronger rocks under fixed sandblasting conditions.

It should be noted that the tensile strength (Figure 6-6; Bauer and Johnson, 1979), fracture toughness (Figure 6-7; Atkinson et al., 1984; Meredith and Atkinson, 1985) and compressive strength (e.g. Tullis and Yund, 1977) of granite have all been experimentally shown to decrease significantly with increasing temperature. Even though the cores of accessory lithic clasts will take a long time to completely thermally equilibrate within the conduit (e.g. Figure 5-30), ash-blasting will only affect the outer surface of the clasts, which may be heated quite rapidly. Therefore, the thermal conditions within the conduit could significantly enhance the expected ash-blasting erosion rates of the monzogranite clasts.
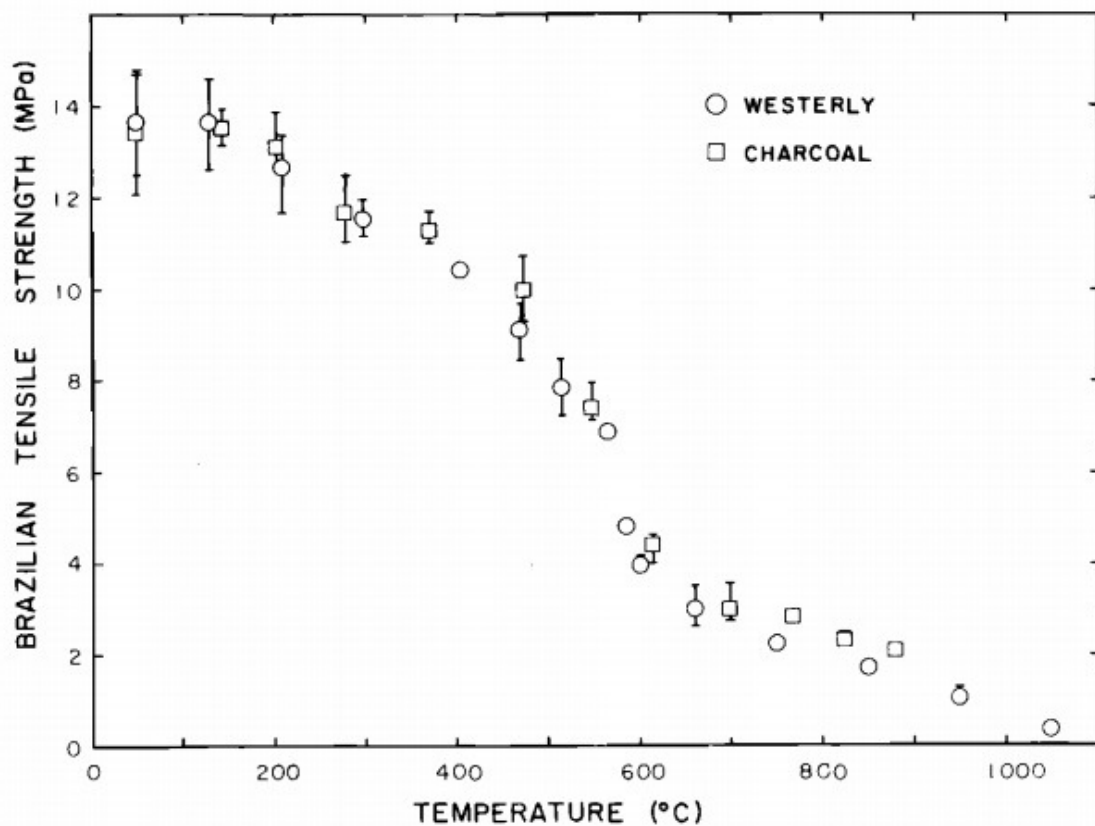
Figure 6-6. Brazilian tensile strength of Westerly granite and Charcoal granite versus maximum thermal cycle temperature. Vertical bars represent the range of results obtained at each temperature. Figure from Bauer and Johnson (1979).
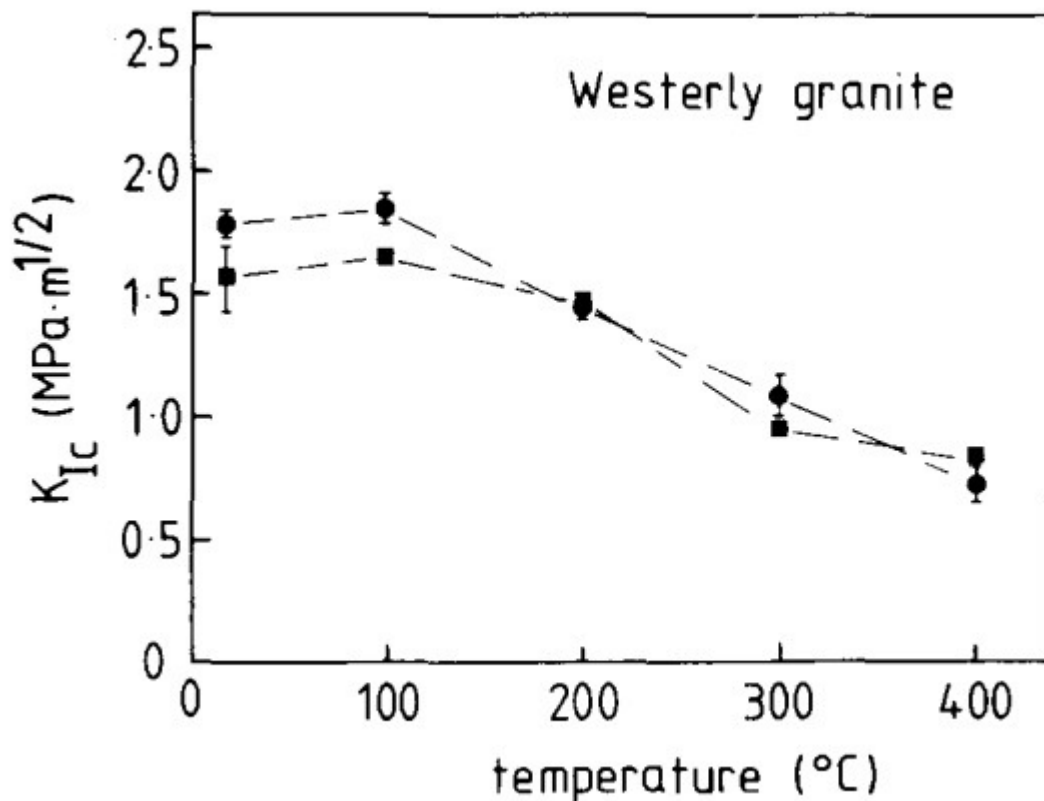
Figure 6-7. Temperature dependence of fracture toughness (Klc) for double torsion specimens of Westerly granite. Circles represent data from Meredith and Atkinson (1985) for samples tested in a vacuum at the temperature indicated. Squares represent data from Atkinson et al. (1984) for samples heat-treated to the temperature indicated but tested in ambient conditions after cooling. Figure from Meredith and Atkinson (1985).

In volcanology, the term ash refers to any clastic particle smaller than 2 mm produced by a volcanic eruption. In the volcanic conduit of a subplinian eruption, ash-sized particles will primarily be comprised of juvenile material, including broken glassy shards (bubble walls of the highly vesiculated magma), tiny pumice clasts and loose crystals. These abradant particles likely do not have the same abrasive effectiveness as the typical particles used in sandblasting, which are predominantly made up of individual quartz and feldspar grains (e.g. Suzuki and Takahashi, 1981). To date, there are no literature estimates of the abrasion rates expected for the solid impingement erosion of granitic or dacite clasts with volcanic ash. Therefore, the expected abrasion rate for volcanic ash-blasting on clasts of different lithologies would need to be experimentally determined. However, from the literature we do know that abrasion rates will increase with increasing velocity of the abradant particles.

127

Because larger clasts have greater terminal settling velocities than smaller clasts (Figure 6-1), the velocity differential between larger clasts and the ash-laden gas will be greater. In other words, larger clasts will be ash-blasted at higher overall velocities than smaller clasts. Furthermore, the residence times of larger clasts within the volcanic conduit are longer than those of smaller clasts (Figure 6-5), and so larger clasts will be exposed to ash-blasting for an even longer period of time. Furthermore, clasts incorporated into the conduit at greater depths will have longer residence times than clasts incorporated at shallower depths (Figure 6-5). Therefore, the total abrasion of a clast (i.e. mass lost) due to ash-blasting will increase with increasing clast size and with increasing depth of incorporation. The monzogranite surface smoothness (S_{max}) results presented in Figure 5-18 offer morphological evidence of these relationships. The larger clasts (> 400 cm^3) all display very high S_{max} values, indicating that all of these large clasts have been exposed to ash-blasting at a sufficient intensity, and for a sufficiently long period of time, to achieve a high degree of surface smoothness. The smaller clasts (< 400 cm^3), however, display variable degrees of S_{max}. This variability might correspond to variations in the depth of incorporation of these monzogranite clasts. Small clasts incorporated at great depth, perhaps within the lower reaches of the Fall Creek Stock, may have had sufficiently long residence times to become quite smooth. However, small clasts incorporated at relatively shallow depths, near the top of the Fall Creek Stock (~ 700 m depth; Figure 3-4), may not have had residence times that were sufficiently long to achieve a smoothed surface. The larger clasts do not show much variability in S_{max}, because even those large clast incorporated at shallow depths have achieved the maximum smoothness (S_{max} ~ 0.98) that may be imparted to monzogranite clasts by ash-blasting. A large monzogranite clast incorporated at greater depth will undergo more total abrasion during its transit to the surface, but cannot become any smoother than S_{max} ~ 0.98.

The dacite clasts were all incorporated at shallower depth than the monzogranite clasts, as the Plinth Assemblage dacite overlies the Fall Creek Stock monzogranite (Figure 3-4). Thus, the dacite clasts had shorter residence times within the conduit than monzogranite clasts of a similar size, and so were exposed to ash-blasting for shorter periods of time. This may be one factor behind the relatively rough surfaces of the dacite clasts (Figure 5-18). The common occurrence of visible columnar joint surfaces on dacite clasts (Figure 4-15) also indicates that these clasts could not have been significantly affected by solid impingement erosion, as any appreciable erosion would have removed the joint

surfaces. The intrinsic properties of the dacite are also not conducive to smoothing. First, the plagioclase phenocrysts of the dacite appear to be particularly friable, and so ash-blasting may preferentially erode or pluck these crystals from the clast's surface, leaving behind small pits. Second, the dacite clasts are much less competent than the monzogranite clasts, and it was not uncommon for minute pieces of the dacite clasts to break off during sample analysis, even with gentle handling. This low competency may allow the dacite clasts to be easily comminuted but not achieve high degree of smoothness, which requires that minute amounts of the surface be removed incrementally.

6.3.2   Thermal Effects

The partial spalls on the surfaces of many monzogranite clasts (Figure 5-20) and the pervasive flakiness observed microscopically on the smoothed surfaces of the monzogranite clasts (Figures 5-24, 5-25) likely share a thermal origin. The thermal spalling experiments performed on monzogranite cubes (Section 5.7) revealed that the exposure of a monzogranite surface to sudden, intense heat produces violent spalling, and leaves behind a surface covered in microscopic, partially detached flakes (Figure 5-29). The experimentally thermally spalled surfaces are, however, still quite rough and display relatively high relief. Thermal spalling alone therefore does not appear to contribute significantly to the smoothing of clasts. However, thermal spalling may enhance the abradability of monzogranite clasts, as the partially detached flakes formed via thermal spalling could easily be removed via ash-blasting. Therefore, thermal spalling may enhance the abrasion rates caused by ash-blasting, by weakening the surfaces of clasts. As noted in Section 5.7, the dacite clasts do not undergo thermal spalling, and so the ash-blasting of dacite clasts would not be enhanced by this process.

The temperature within the volcanic conduit should also be sufficient to melt granitic clasts. The lack of melted outer rinds on the monzogranite clasts, however, indicates that this did not take place. The residence times of the clasts within the conduit may have been insufficient to allow partial melting of the clast surfaces. Alternatively, melted outer rinds could have been progressively removed by ash-blasting erosion.

Finally, it is possible that the sudden exposure of entire clasts to intense heat could enhance clast rounding by the formation of heat stress fractures along concentric isothermal planes within the

clasts, as observed by Norton (1925). This hypothesis would have to be tested experimentally, by placing whole samples of various sizes in a high-temperature oven, and observing the results.

6.3.3   Disruptive Collisions

Many of the monzogranite clasts, the broken clasts, display clear evidence of disruptive collisions. Many of these clasts display multiple fracture surfaces, which resulted from multiple collisions (e.g. Figure 5-21). Some clasts have fracture surfaces from disruptive events that occurred at different times, as evidenced by differences in the angularity of the edges around each fracture surface (e.g. Figure 5-23c). Some of the fresh fracture surfaces may be due to the impact of the lithic clasts with the ground, as they are deposited following their eruption. However, in situ lithic clasts that were broken into two or more pieces were rarely observed. Therefore, many or most of the relatively fresh fracture surfaces on the accessory lithic clasts were likely caused prior to their ejection and deposition.

Energetic collisions are necessary in order to break hard, dense accessory lithic clasts. The dacite clasts have relatively low competency, and their friable nature indicates that they would likely break quite easily. The monzogranite clasts, however, appear to be significantly stronger than the dacites. Even though, as previously stated, the fracture toughness and tensile strength of a heated granite will be somewhat reduced (Figures 6-6, 6-7), the collision of a monzogranite clast with a pumice clast is likely to result in the fragmentation of only the pumice, and not of the monzogranite clast. Most of the disruptive collisions of lithics within the conduit are likely the result of collisions between two lithic clasts, or between a lithic clast and the conduit wall, if conditions within the conduit were sufficiently turbulent. However, accessory lithics only make up a small proportion of the total clasts within the conduit, and so one might expect the odds of two lithic clasts colliding within the conduit to be quite small.

One possible scenario that could augment the frequency of disruptive lithic collisions within the conduit is the accumulation of lithic clasts at certain depths. As discussed in Section 6.2, very large lithic clasts oftentimes cannot be lofted within the conduit (Figure 6-3). These large clasts, potentially including slabs of failed wall rocks, will sink further down into the conduit. However, these clasts will not simply disappear as they descend, and when enough large clasts accumulate in the lower reaches of the conduit, these clasts may eventually form a blockage: a lithic-rich raft of clastic material "choking"

the conduit. The conduit would not be blocked indefinitely, however. Pressure will build beneath the lithic-rich blockage until such a time that overpressurization suddenly and explosively clears the lithic-rich blockage. Lithic clasts could then be easily fractured during the clearing event. The blockage clearing hypothesis could also explain the common occurrence of relatively fresh fracture surfaces on monzogranite clasts, with rough (and thus poorly abraded) surfaces and angular edges. For fresh fracture surfaces to survive the ascent of the conduit without become abraded and smoothed, the fractured clast must ascend very quickly (i.e. have a short residence time). The clearing of the conduit blockage via overpressurization would result in a temporary increase in the mass flux propagating upwards through the conduit, resulting in temporarily elevated relative velocities of the gas jet and entrained clasts. Furthermore, the fragmentation of large lithics into smaller pieces will result in dramatically increasing relative velocities for the individual lithic fragments, compared to the relative velocity of the larger intact lithic (Figure 6-3).

The blockage clearing scenario should also result in the production of lithic-rich lenses within the fallout deposits. Some lithic-rich lenses have been noted in the Great Pacific Pumice quarry, within the proximal fallout deposits, but it is difficult to say whether these lenses are primary features, resulting from in situ deposition, or secondary features, formed through the remobilization of clasts on the steep slopes of the MMVC. The occurrence of proximal, lithic-rich lenses are however common in the fallout deposits of other volcanoes. These deposits, termed lag breccias, were introduced in Section 2.3.1.3. The fundamental characteristics of lag breccias, notably their intermittent occurrence within the pyroclastic deposits of explosive eruptions, their lithic-rich nature, and the fact that they commonly feature rounded lithic clasts, all fit well with the conduit blockage clearing hypothesis. For example, in their study of the lag breccias interbedded with the Kaingaroa Ignimbrites (Taupo Volcanic Zone, New Zealand), Nairn et al. (1994) noted that the largest lithic clasts in the deposit were typically the most rounded, and postulated that this rounding might be due to repeated fall back and milling in the vent. Furthermore, Nairn et al. (1994) observed that many of the lithic clasts appeared spheroidally heat spalled and/or reddened. Therefore, the volcanic lithic reshaping process described here has likely occurred within other volcanic systems as well. The detailed morphological data presented here simply provides evidence for how this process occurs, and how it may affect clasts of different lithologies in different ways.

7. Conclusions

Accessory lithic clasts are a fundamental yet little studied component of many volcaniclastic deposits. Much is still poorly understood about the processes governing the entrainment and the transport of these clasts within the volcanic conduit. There is especially little study of the processes operating on and modifying these clasts prior to their eventual eruption. The final shapes and surficial textures of accessory lithic clasts reflect the various volcanic processes which have affected them, following their incorporation into the conduit. Thus, the characteristic morphological features imprinted on the clasts contain hard information on the fluid-particle dynamics operating within near surface (< 2 km) volcanic conduits during explosive eruptions. This work represents the very first study of accessory lithic clast morphologies in volcanic fallout deposits with the intent to: i) identify and understand the processes that shape the clasts during volcanic eruption, and to ii) constrain the nature, intensity and dynamics of the explosive volcanic eruption.

Herein, I have described a variety of different methods, including axis measurements, image analysis and 3-D laser scanning, which were used to quantify the morphologies of monzogranite and dacite accessory lithic sample set from the 2360 B.P. Pebble Creek Formation, at the Mount Meager Volcanic Complex. Through the morphological data generated via these methods, I have shown quantitatively that the overall form (i.e. dimensionality) data of the dacite and intact monzogranite sample sets are very similar. I have also shown that the monzogranite clasts are significantly rounder than the dacite clasts, as evidenced by the roundness metrics of circularity (C), ellipticity (E) and sphericity (Ψ_t). A major result of this study for the monzogranite accessory lithics was the discovery of a strong covariance between sample size and smoothness as established by 3-D laser scanning. The implication of these data is that the processes operating to modify particle shape and smoothness operate longer on large clasts than on smaller clasts. Notably, the dacite sample set displayed no such trend, as no covariance was observed between smoothness and volume for the dacite clasts.

My analysis showed that the morphologies of the accessory lithic clasts are the products of three main processes that operated within the conduit during the eruption: 1) ash-blasting involving the continuous high velocity impact of volcanic ash on clasts suspended within the eruption flux, 2) spalling or flaking of exterior surfaces of lithics driven by steep thermal gradients resulting from rapid

heating of the entrained clast, and 3) disruptive fragmentation caused by energetic collisions between the clast and the conduit wall or with another lithic clast. The first two processes are ultimately responsible for the rounding and smoothing of the monzogranite clasts, while disruptive fragmentation causes substantial size reduction but increases the angularity and roughness of the lithics (Dufek et al., 2012). Based on the typical properties of monzogranite accessory lithic clasts, a review of the literature, estimated properties of the particle-laden gas jet and my results from thermal spalling experiments, I have ranked the relative efficiency of these 3 processes. This relative efficiency is an estimate of the average rate of attrition (mass or volume loss) suffered by the accessory lithics prior to being ejected. The most important process for governing final roundness and smoothness is the ash-blasting; it is continuous and involves high differential velocities and high particle densities. Thermal spalling is most efficient when new, relatively cool surfaces are exposed to and rapidly heated by the surrounding eruption stream. The heating of the outside surface is nearly instantaneous and produces a large thermal gradient in the outer rind of the sample, causing the formation and violent emission of flakes from the sample's surface. This thermal spalling proceeds for a duration on the timescale of minutes. As the sample continues to heat, thermal gradients within the sample diminish and thermal spalling becomes less important.

Disruptive fragmentation of pumices during volcanic eruptions has been well explored by Dufek et al. (2012). Here I envisage this third process, disruptive fragmentation, as playing a less frequent but important role in lithic size reduction and reshaping. The total volume fraction of accessory lithic clasts within the stream of erupting material in the conduit likely never exceeds 3 vol. % (gas fraction ≈ 70 vol. %), and the population of monzogranite clasts spans a size range of < 1 cm to > 50 cm in long axis length. Disruptive fragmentation requires high energies that result from kinetic energy transfers between two particles or between a particle and a fixed solid.

Because they are isotropic and have high fracture toughness, compressive strength and tensile strength (e.g. Bauer and Johnson, 1979; Meredith and Atkinson, 1985; Tullis and Yund, 1977), granite lithics are very difficult to break, thus requiring very high kinetic energy events to cause disruptive fragmentation. However, as these lithics are heated (> 600°C) and thermal spalling becomes less effective, the tensile strength of granite is reduced by more than two thirds. This may explain why

disruptive fragmentation of granitic lithics occurs at all. When disruptive fragmentation events occur, the ash-blasting process begins to operate immediately to smooth the sharp surfaces and potentially erase evidence of the disruptive event. Several lithic samples were recovered that show the partial smoothing of large (> 10 cm^2) fresh fracture surfaces. If the disruptive fragmentation event operates on a relatively cool sample, thermal spalling will also play a substantial role in the post-collisional smoothing.

I have also estimated the minimum residence times of accessory lithic clasts within the volcanic conduit prior to being evacuated. These minimum times provide an additional assessment of the timescales on which the thermal-mechanical shaping processes operate. The model uses a previous estimate of the peak height of the eruption column ($15 - 17$ km) to estimate eruption mass flux (Q), a parameter which constrains the exit velocity of the eruption stream and conduit cross-sectional area. My modelling ascribes a unique velocity-depth profile to each clast that reflects clast size, density and source (e.g. depth of incorporation and entrainment within the conduit). The velocity-depth profiles are then integrated to provide a minimum residence time within the volcanic conduit.

The largest milled monzogranite lithics recovered from the proximal fallout deposits are > 30 cm in diameter (equivalent diameter). The calculated terminal settling velocities data indicate that, in order to loft monzogranite clasts of this size, gas stream velocities of > 15 m/s are necessary at 700 m depth (the minimum depth of incorporation of these clasts), which then limits the conduit diameter to $\leq$ 46 m. This is a unique situation where I have been able to use the accessory lithics forensically to recover a fundamental property of an explosive eruption: conduit diameter. The calculated residence times for lithic clasts within the volcanic conduit are on the order of a few minutes (for small clasts, or those originating at shallow depths) to about an hour (for large clasts originating at great depths). Lithic milling in the volcanic conduit therefore occurs at much shorter timescales than other natural rounding processes, such as fluvial or glacial rounding.

The clast's residence time within the conduit controls the duration of milling and, thus, the extent of mass lost and the extent of rounding and smoothing. Firstly, residence time increases with increasing clast size, explaining the correlation between clast volume and clast smoothness for the monzogranites. Clast residence time also increases with increasing depth of incorporation. Based upon my reconstruction of the subsurface geology beneath the vent of the PCF eruption, the monzogranite

clasts originated at significantly greater depths (> 700 m) than the dacite clasts (< 550 m). Consequently, the transit time of a monzogranite clast through the volcanic conduit was significantly longer than that of a dacite clast of the same size. This longer residence time translates to a longer exposure to ash-blasting within the conduit, and a greater amount of abrasion and rounding. The shorter residence times of the more shallowly-sourced dacite clasts may have been insufficient to allow significant smoothing to occur. Indeed, the common occurrence of columnar joint surfaces on dacite clasts reveals how little mass loss many of these clasts have undergone; any significant abrasion would have removed these surficial features. Thus, the answer to the question of why the monzogranite and dacite lithics have such different final morphologies, even though they were emplaced during the same event, likely lies primarily in the different depths of incorporation of these clast types. Differences in the intrinsic properties (intrusive vs. extrusive) of these clasts may have also played a subordinate role in how they were reshaped by the volcanic processes. It is common to use the lithic clasts to reconstruct the basement underlying volcanic vents. Here, however, I have used independent knowledge of the basement underlying the vent to reconstruct the milling history of accessory lithic clasts.

The study of the fracture surfaces caused by disruptive collisions of the lithic clasts within the conduit has revealed some important implications for conduit dynamics. The occurrence of fracture surfaces smoothed and rounded to different degrees on a single lithic clast implies that these clasts were involved in multiple collisions spread over their sojourn within the conduit: earlier fracture surfaces are quite smoothed, with rounded edges, while later fracture surfaces are quite rough and have angular edges. However, the common occurrence of fresh fracture surfaces on many of the monzogranite clasts has led to the hypothesis that the breakage of these clasts occurred during highly explosive conduit clearing events, following overpressurization of the conduit caused by choking due to an accumulation of dense lithic clasts.

The set of morphological characteristics documented in this study are textural fingerprints left behind by the volcanic reshaping processes. These characteristic imprints vary for clasts of different lithologies, and differ according to the total duration of clast's exposure to these processes. Accessory lithic suites with morphological similarities to the monzogranites from the Pebble Creek Formation fallout deposits have been documented in pyroclastic deposits of other volcanic systems (e.g. lag

breccias; Mellors and Sparks, 1991; Nairn et al., 1994), indicating that the volcanic rounding process described here is probably not unique to the Mount Meager Volcanic Complex. Furthermore, the findings of this study could allow for the reinterpretation of the source of rounded lithic clasts found in other pyroclastic deposits, which have in some cases been attributed to the entrainment of river-rounded clasts (e.g. Cole et al., 1998), to rounding caused by downslope resedimentation (e.g. Adams et al., 2001) or to rounding caused during transportation in a pyroclastic density current (Perrotta and Scarpati, 1994). The further study of accessory lithic clast morphology could also shed light of the fragmentation processes that occur during the breakup and incorporation of wall rocks lining the conduit, which to date are still poorly understood (Macedonio et al., 1994). The granulometry and componentry results for the PCF fallout deposits presented in this study have shown that multiple phases can be distinguished within the deposits of the 2360 B.P. subplinian event. Accessory lithic clast morphology could potentially be used as a new method to distinguish different phases of an eruption, with changes in lithic roundness or smoothness possibly ascribable to changing clast residence times, due to fluctuations in such factors as mass flux, conduit diameter, or depth of fragmentation.

In summary, accessory lithic clast morphology is, to date, an underutilized source of information about volcanic eruptions. Accessory lithic morphologies have important implications for volcanic eruption processes and conduit dynamics, including estimates for minimum clast residence times, constraints on the effective conduit diameter and depth of the fragmentation front, and estimates for the frequency of clast collisions within the conduit. The application of the methods developed in this study to the lithic clasts of other volcaniclastic deposits will likely reveal an abundance of new information about the conduit processes that operate during different volcanic eruptions.

References

Adams, N.K., de Silva, S.L., Self, S., Salas, G., Schubring, S., Permenter, J.L., Arbesman, K., 2001. The physical volcanology of the 1600 eruption of Huaynaputina, southern Peru. Bulletin of Volcanology 62, 493-518.

Allen, S.R., Cas, R.A.F., 1998. Lateral variations within coarse co-ignimbrite lithic breccias of the Kos Plateau Tuff, Greece. Bulletin of Volcanology 59, 356-377.

Andrews, G.D.M., Russell, J.K., Stewart, M.L., 2012. The rise and fall of a welded pyroclastic dam: the 2,360 BP eruption of Mount Meager, British Columbia, Canada. Bulletin of Volcanology In Review.

Anochie-Boateng, J.K., Komba, J.J., Mvelase, G.M., 2011. Advanced and automated laser-based technique to evaluate aggregates. IRF International Road Congress – Innovations in Road Infrastructure, Moscow, Russia, 22-24 November 2011, 11 pp.

Arribas, J., Critelli, S., Johnsson, M.J., 2007. Sedimentary provenance and petrogenesis: perspectives from petrography and geochemistry. Geological Society of America, Boulder, Colorado.

ASTM Standard, G., 2010. G40-10b: Standard terminology relating to wear and erosion. ASTM International, West Conshohocken, PA.

Atkinson, B.K., MacDonald, D., Meredith, P.G., 1984. Acoustic response and fracture mechanics of granite subjected to thermal and stress cycling experiments, in: Hardy, H.R., Leighton, F.W. (Eds.), Proceedings of the 3rd International Conference on Acoustic Emission/Microseismic Activity in Geological Structures and Materials. Trans-Tech Publications, Clausthal, Germany, pp. 5-18.

Attal, M., Lavé, J., 2009. Pebble abrasion during fluvial transport: Experimental results and implications for the evolution of the sediment load along rivers. Journal of Geophysical Research 114, 1-22.

Barrett, P.J., 1980. The shape of rock particles, a critical review. Sedimentology 27, 291-303.

Bauer, S.J., Johnson, B., 1979. Effects of slow uniform heating on the physical properties of the Westerly and Charcoal granites, 20th U.S. Symposium on Rock Mechanics, Austin, Texas.

Blackwelder, E., 1926. Fire as an agent in rock weathering. Journal of Geology 35, 134-140.

Bloss, D., Gibbs, G.V., 1963. Cleavage in quartz. American Mineralogist 48, 821-838.

Blott, S.J., Pye, K., 2008. Particle shape: a review and new methods of characterization and classification. Sedimentology 55, 31-63.

Bowman, E.T., Soga, K., Drummond, T.W., 2001. Particle shape characterisation using Fourier Analysis. Geotechnique 51, 1-20.

Brett, R.D., Russell, J.K., Moss, S., 2009. Origin of olivine in kimberlite: phenocryst or impostor? Lithos 112S, 201-212.

Brown, J.E., 1973. Depositional histories of sand grains from surface textures. Nature 242, 396-398.

Brown, R.J., Kavanagh, J., Sparks, R.S.J., Tait, M., Field, M., 2007. Mechanically disrupted and chemically weakened zones in segmented dike systems cause vent localization: Evidence from kimberlite volcanic systems. Geology 35, 815-818.

Bull, P.A., 1981. Environmental reconstruction by electron microscopy. Progress in Physical Geography 5, 368-397.

Bull, P.A., Goudie, A.S., Price Williams, D., Watson, A., 1987. Colluvium: a scanning electron microscope analysis of a neglected sediment type, in: Marshall, J.R. (Ed.), Clastic particles: scanning electron microscopy and shape analysis of sedimentary and volcanic clasts, pp. 16-35.

Büttner, R., Dellino, P., Raue, H., Sonder, I, Zimanowski, B., 2006. Stress-induced brittle fragmentation of magmatic melts: Theory and experiments. Journal of Geophysical Research 111, 1-10.

Caballero, L., Capra, L., 2011. Textural evidence of particles from El Zaguán debris avalanche deposit, Nevado de Toluca volcano, Mexico: Evidence of flow behavior during emplacement. Journal of Volcanology and Geothermal Research 200, 75-82.

Calder, E.S., Sparks, R.S.J., Gardeweg, M.C., 2000. Erosion, transport and segregation of pumice and lithic clasts in pyroclastic flows inferred from ignimbrite at Lascar Volcano, Chile. Journal of Volcanology and Geothermal Research 104, 201-235.

Carey, S., Maria, A., Sigurdsson, H., 2000. Use of fractal analysis for discrimination of particles from primary and reworked jökulhlaup deposits in SE Iceland. Journal of Volcanology and Geothermal Research 104, 65-80.

Carey, S.N., Sigurdsson, H., 1978. Deep-sea evidence for distribution of tephra from the mixed magma eruption of the Soufrière on St. Vincent, 1902: ash turbidites and air fall. Geology 6, 271-274.

Carracedo Sánchez, M., Sarrionandia, F., Arostegui, J., Larrondo, E., Gil Ibarguchi, J.I., 2009. Development of spheroidal composite bombs by welding of juvenile spinning and isotropic droplets inside a mafic eruption column. Journal of Volcanology and Geothermal Research 186, 265-279.

Cas, R.A.F., Wright, J.V., 1987. Volcanic successions, modern and ancient. A geological approach to processes, products and successions. Chapman & Hall, London.

Clague, J.J., Evans, S.G., Rampton, V.N., Woodsworth, G.J., 1995. Improved age estimates for the White River and Bridge River tephras, western Canada. Canadian Journal of Earth Sciences 32, 1172-1179.

Cole, J.W., Brown, S.J.A., Burt, R.M., Beresford, S.W., Wilson, C.J.N., 1998. Lithic types in ignimbrites as a guide to the evolution of a caldera complex, Taupo volcanic centre, New Zealand. Journal of Volcanology and Geothermal Research 80, 217-237.

Culver, S.J., Bull, P.A., Campbell, S., Shakesby, R.A., Whalley, W.B., 1983. Environmental discrimination based on quartz grain surface textures: a statistical investigation. Sedimentology 30, 129-136.

Dawson, J.B., Powell, D.G., Reid, A.M., 1970. Ultrabasic xenoliths and lava from the Lashaine volcano, northern Tanzania. Journal of Petrology 11, 519-548.

de Vries Klein, G., 1963. Boulder surface markings in Quaco Formation (Upper Triassic), St. Martin's, New Brunswick, Canada. Journal of Sedimentary Petrology 33, 49-52.

Develi, K., Babadagli, T., Comlekci, C., 2001. A new computer-controlled surface-scanning device for measurement of fracture surface roughness. Computers & Geosciences 27, 265-277.

Diepenbroek, M., Bartholomä, A., Ibbeken, H., 1992. How round is round? A new approach to the topic 'roundness' by Fourier grain shape analysis. Sedimentology 39, 411-422.

Dinesh, S., 2008. Computation of surface roughness of mountains extracted from Digital Elevation Models. Journal of Applied Sciences 8, 262-270.

Dorn, R.I., 2003. Boulder weathering and erosion associated with a wildfire, Sierra Ancha Mountains, Arizona. Geomorphology 55, 155-171.

Druitt, T.H., 1985. Vent evolution and lag breccia formation during the Cape Riva eruption of Santorini, Greece. The Journal of Geology 93, 439-454.

Druitt, T.H., Sparks, R.S.J., 1984. On the formation of calderas during ignimbrite eruptions. Nature 310, 679-681.

Dufek, J., Manga, M., 2008. In situ production of ash in pyroclastic flows. Journal of Geophysical Research 113, 1-17.

Dufek, J., Manga, M., Patel, A., 2012. Granular disruption during explosive volcanic eruptions. Nature Geoscience 5, 561-564.

Durian, D.J., Bideaud, H., Duringer, P., Schroder, A.P., Marques, C.M., 2007. Shape and erosion of pebbles. Physical Review E 75, 1-9.

Ehlmann, B.L., Viles, H.A., Bourke, M.C., 2008. Quantitative morphologic analysis of boulder shape and surface texture to infer environmental history: A case study of rock breakdown at the Ephrata Fan, Channeled Scabland, Washington. Journal of Geophysical Research 113, 20 pp.

Farley, K.A., Rusmore, M.E., Bogue, S.W., 2001. Post-10 Ma uplift and exhumation of the northern Coast Mountains, British Columbia. Geology 29, 99-102.

Glover, P.W.J., Baud, P., Darot, M., Meredith, P.G., Boon, S.A., LeRavalec, M., Zoussi, S., Reuschlé, T., 1995. α/β phase transition in quartz monitored using acoustic emissions. Geophysical Journal International 120, 775-782.

Graham, D.J., Midgley, N.G., 2000. Graphical representation of particle shape using triangular diagrams: an Excel spreadsheet method. Earth Surface Processes and Landforms 25, 1473-1477.

Green, N.L., Armstrong, R.L., Harakal, J.E., Souther, J.G., Read, P.B., 1988. Eruptive history and K-Ar geochronology of the Late Cenozoic-Garibaldi Volcanic Belt, southwestern British Columbia. Geological Society of America Bulletin 100, 563-579.

Guest, J.E., Spudis, P.D., Greeley, R., Taylor, G.J., Baloga, S.M., 1995. Emplacement of xenolith nodules in the Kaupulehu lava flow, Hualalai Volcano, Hawaii. Bulletin of Volcanology 57, 179-184.

Hayakawa, Y., Oguchi, T., 2005. Evaluation of gravel sphericity and roundness based on surface-area measurement with a laser scanner. Computers & Geosciences 31, 735-741.

Heiken, G., 1972. Morphology and petrography of volcanic ashes. Geological Society of America Bulletin 83, 1961-1988.

Heiken, G., Wohletz, K., 1985. Volcanic Ash. University of California Press, Berkeley.

Hettema, M.H.H., Wolf, K.H.A.A., de Pater, C.J., 1998. The influence of steam pressure on thermal spalling of sedimentary rock: theory and experiments. International Journal of Rock Mechanics and Mineral Sciences 35, 3-15.

Hickson, C.J., Russell, J.K., Stasiuk, M.V., 1999. Volcanology of the 2350 B.P. Eruption of Mount Meager Volcanic Complex, British Columbia, Canada: implications for Hazards from Eruptions in Topographically Complex Terrain, pp. 489-507.

Hu, J., Stroeven, P., 2006. Shape characterization of concrete aggregate. Image Analysis and Stereology 25, 45-53.

Inman, D.L., 1952. Measures for describing the size distribution of sediments. Journal of Sedimentary Research 22, 125-145.

Judson, S., Barks, R.E., 1961. Microstriations on polished pebbles. American Journal of Science 259, 371-381.

Krinsley, D.H., Donahue, J., 1968. Pebble surface textures. Geological Magazine 105, 521-525.

Krinsley, D.H., Doornkamp, J.C., 1973. Atlas of quartz sand surface textures. Cambridge University Press, Cambridge.

Krumbein, W.C., 1941. Measurement and geological significance of shape and roundness of sedimentary particles. Journal of Sedimentary Petrology 11, 64-72.

Krumbein, W.C., Pettijohn, F.J., 1938. Manual of Sedimentary Petrography. Appleton-Century Crofts, Inc., New York.

Kuenen, P.H., 1956. Experimental abrasion of pebbles: 2. Rolling by current. Journal of Geology 64, 336-368.

Kuenen, P.H., 1960. Experimental abrasion 4: Eolian action. The Journal of Geology 68, 427-449.

Le Maitre, R.W., 2002. Igneous Rocks: A Classification and Glossary of Terms: Recommendations of the International Union of Geological Sciences Subcommission on the Systematics of Igneous Rocks. Cambridge University Press, Cambridge.

Lee, H.S., Ahn, K.W., 2004. A prototype of digital photogrammetric algorithm for estimating roughness of rock surface. Geosciences Journal 8, 333-341.

Leonard, E.M., 1995. A varve-based calibration of the Bridge River tephra fall. Canadian Journal of Earth Sciences 32, 2098-2102.

Luty, J.R., 1994. Eruption characteristics and industrial application potential of the Bridge River airfall pumice deposit, Mount Meager, southwestern British Columbia. University of British Columbia, Vancouver, B.C., pp. 1-41.

Mabbutt, J.A., 1961. "Basal surface" or "weathering front". Proceedings of the Geologists' Association of London 72, 357-358.

Macedonio, G., Dobran, F., Neri, A., 1994. Erosion processes in volcanic conduits and application to the AD 79 eruption of Vesuvius. Earth and Planetary Science Letters 121, 137-152.

Mahaney, W.C., 2002. Atlas of sand grain surface textures and applications. Oxford University Press, Oxford.

Mahaney, W.C., Stewart, A., Kalm, V., 2001. Quantification of SEM microtextures useful in sedimentary environmental discrimination. Boreas 30, 165-171.

Manga, M., Patel, A., Dufek, J., 2011. Rounding of pumice clasts during transport: field measurements and laboratory studies. Bulletin of Volcanology 73, 321-333.

Margolis, S.V., Kennett, J.P., 1971. Cenozoic paleoglacial history of Antarctica recorded in subantarctic deep-sea cores. American Journal of Science 271, 1-36.

Margolis, S.V., Krinsley, D.H., 1974. Processes of formation and environmental occurrence of microfeatures on detrital quartz grains. American Journal of Science 274, 449-464.

Marsland, P.S., Woodruff, J.G., 1937. A study of the effects of wind transportation on grains of several minerals. Journal of Sedimentary Petrology 7, 18-30.

Mastin, L.G., 2002. Insights into volcanic flow from an open-source numerical model. Geochemistry Geophysics Geosystems 3, 1-18.

Mellors, R.A., Sparks, R.S.J., 1991. Spatter-rich pyroclastic flow deposits on Santorini, Greece. Bulletin of Volcanology 53, 327-342.

Melnik, O., Sparks, S., 2006. Transient models of conduit flows during volcanic eruptions, in: Mader, H.M., Coles, S.G., Connor, C.B., Connor, L.J. (Eds.), Statistics in Volcanology. Geological Society of London, pp. 201-213.

Meredith, P.G., Atkinson, B.K., 1985. Fracture toughness and subcritical crack growth during high-temperature tensile deformation of Westerly granite and Black gabbro. Physics of the Earth and Planetary Interiors 39, 33-51.

Michol, K.A., Russell, J.K., Andrews, G.D.M., 2008. Welded block and ash flow deposits from Mount Meager, British Columbia, Canada. Journal of Volcanology and Geothermal Research 169, 121-144.

Momber, A.W., 2004. Damage to rocks and cementitious materials from solid impact. Rock Mechanics and Rock Engineering 37, 57-82.

Nairn, I.A., Wood, C.P., Bailey, R.A., 1994. The Reporoa Caldera, Taupo Volcanic Zone: source of the Kaingaroa Ignimbrites. Bulletin of Volcanology 56, 529-537.

Nasmith, H., Mathews, W.H., Rouse, G.E., 1967. Bridge River ash and some other recent ash beds in British Columbia. Canadian Journal of Earth Sciences 4, 163-170.

Neuendorf, K.K.E., Mehl, J.P., Jackson, J.A., 2011. Glossary of Geology. American Geosciences Institute, Alexandria, Virginia.

Newhall, C.G., Self, S., 1982. The Volcanic Explosivity Index (VEI): an estimate of explosive magnitude for historical volcanism. Journal of Geophysical Research 87, 1231-1238.

Norton, F.H., 1925. A general theory of spalling. Journal of the American Ceramic Society 8, 29-39.

Ollier, C.D., 1967. Spheroidal weathering, exfoliation and constant volume alteration. Zeitschrift für Geomorphologie 11, 103-108.

Ollier, C.D., 1971. Causes of spheroidal weathering. Earth-Science Reviews 7, 127-141.

Parfitt, E.A., Wilson, L., 2008. Fundamentals of physical volcanology. Blackwell Publishing, Oxford.

Pearce, T.H., 1971. Short distance fluvial rounding of volcanic detritus. Journal of Sedimentary Petrology 41, 1069-1072.

Perrotta, A., Scarpati, C., 1994. The dynamics of the Breccia Museo eruption (Campi Flegrei, Italy) and the significance of spatter clasts associated with lithic breccias. Journal of Volcanology and Geothermal Research 59, 335-355.

Pittari, A., Cas, R.A.F., Wolff, J.A., Nichols, H.J., Larson, P.B., Martí, J., 2008. Chapter 3: The Use of Lithic Clast Distributions in Pyroclastic Deposits to Understand Pre- and Syn-Caldera Collapse Processes: A Case Study of the Abrigo Ignimbrite, Tenerife, Canary Islands, Developments in Volcanology. Elsevier, pp. 97-142.

Porritt, L.A., Cas, R.A.F., 2009. Reconstruction of a kimberlite eruption, using an integrated volcanological, geochemical and numerical approach: A case study of the Fox Kimberlite, NWT, Canada. Journal of Volcanology and Geothermal Research 179, 241-264.

Porritt, L.A., Russell, J.K., Quane, S.L., 2012. Pele's tears and spheres: Examples from Kilauea Iki. Earth and Planetary Science Letters 333-334, 171-180.

Powers, M.C., 1953. A new roundness scale for sedimentary particles. Journal of Sedimentary Petrology 23, 117-119.

Preston, F.W., White, H.E., 1934. Observations on spalling. Journal of the American Ceramic Society 17, 137-144.

Rauenzahn, R.M., Tester, J.W., 1989. Rock failure mechanisms of flame-jet thermal spallation drilling - Theory and experimental testing. International Journal of Rock Mechanics and Mineral Sciences & Geomechanics Abstracts 26, 381-399.

Read, P.B., 1977a. Meager Creek volcanic complex, southwestern British Columbia. Report of Activities, Part A: Geological Survey of Canada Paper 77-1A, 277-281.

Read, P.B., 1977b. Geology of Meager Creek geothermal area, British Columbia: Geological Survey of Canada Open File 603, Scale 1:20 000.

Read, P.B., 1990. Mount Meager Complex, Garibaldi Belt, Southwestern British Columbia. Geoscience Canada 17, 167-170.

Recktenwald, G., 2006. Transient, one-dimensional heat conduction in a convectively cooled sphere, Portland State University, Department of Mechanical and Materials Engineering, accessed 10 October 2012 at http://web.cecs.pdx.edu/~gerry/epub/pdf/transientConductionSphere.pdf.

Riley, C.M., Rose, W.I., Bluth, G.J.S., 2003. Quantitative shape measurements of distal volcanic ash. Journal of Geophysical Research 108, 1-15.

Rose, W.I., Bonis, S., Stoiber, R.E., Keller, M., Bickford, T., 1973. Studies of volcanic ash from two recent Central American eruptions. Bulletin of Volcanology 37, 338-364.

Roussillon, T., Piégay, H., Sivignon, I., Tougne, L., Lavigne, F., 2009. Automatic computation of pebble roundness using digital imagery and discrete geometry. Computers & Geosciences 35, 1992-2000.

Rust, A.C., Cashman, K.V., 2007. Multiple origins of obsidian pyroclasts and implications for changes in the dynamics of the 1300 B.P. eruption of Newberry Volcano, USA. Bulletin of Volcanology 69, 825-845.

Shamberger, P.J., Hammer, J.E., 2006. Leucocratic and gabbroic xenoliths from Hualalai volcano, Hawai'i. Journal of Petrology 47, 1785-1808.

Shea, T., Houghton, B.F., Gurioli, L., Cashman, K.V., Hammer, J.E., Hobden, B.J., 2010. Textural studies of vesicles in volcanic rocks: An integrated methodology. Journal of Volcanology and Geothermal Research 190, 271-289.

Sherrod, D.R., Smith, J.G., 1990. Quaternary Extrusion Rates of the Cascade Range, Northwestern United States and Southern British Columbia. Journal of Geophysical Research 95, 19,465-419,474.

Sneed, E.D., Folk, R.L., 1958. Pebbles in the Lower Colorado River, Texas: a study in particle morphogenesis. The Journal of Geology 66, 114-150.

Stasiuk, M.V., Russell, J.K., 1989. Petrography and chemistry of the Meager Mountain volcanic complex, southwestern British Columbia. Geological Survey of Canada, Paper 89-1E, 189-196.

Stasiuk, M.V., Russell, J.K., Hickson, C.J., 1996. Distribution, nature, and origins of the 2400 B.P. eruption products of Mount Meager, British Columbia: linkages between magma chemistry and eruption behaviour. Geological Survey of Canada Bulletin 486.

Stewart, M.L., Russell, J.K., Hickson, C.J., 2002. Revised stratigraphy of the Pebble Creek Formation, British Columbia: evidence for interplay between volcanism and mountainous terrain. Geological Survey of Canada, Current Research 2002-E3, 1-7.

Stewart, M.L., Russell, J.K., Hickson, C.J., 2008. Geology, Pebble Creek Formation, British Columbia: Geological Survey of Canada Open File 5533, Scale 1:10 000.

Streckeisen, A., 1976. To each plutonic rock its proper name. Earth-Science Reviews 12, 1-33.

Suzuki-Kamata, K., Kamata, H., Bacon, C.R., 1993. Evolution of the Caldera-Forming Eruption at Crater Lake, Oregon, Indicated by Component Analysis of Lithic Fragments. Journal of Geophysical Research 98, 14059-14074.

Suzuki, T., Takahashi, K., 1981. An experimental study of wind abrasion. The Journal of Geology 89, 509-522.

Thirumalai, K., 1969. Process of thermal spalling behavious in rocks - an exploratory study. The 11th U.S. Symposium on Rock Mechanics (USRMS), Berkeley, CA, 705-727.

Tullis, J., Yund, R.A., 1977. Experimental deformation of dry Westerly granite. Journal of Geophysical Research 82, 5705-5718.

Van Hoesen, J.G., Orndorff, R.L., 2004. A comparative SEM study on the micromorphology of glacial and nonglacial clasts with varying age and lithology. Canadian Journal of Earth Sciences 41, 1123-1139.

Varekamp, J.C., 1993. Some remarks on volcanic vent evolution during plinian eruptions. Journal of Volcanology and Geothermal Research 54, 309-318.

Verhoef, P.N.W., Kuipers, T.J., Verwaal, W., 1984. The use of the sand-blast test to determine rock durability. Bulletin of the International Association of Engineering Geology 29, 457-461.

Wadell, H., 1932. Volume, shape and roundness of rock particles. The Journal of Geology 40, 443-451.

Walker, G.P.L., 1971. Explosive volcanic eruptions - 1. The rate of fall of pyroclasts. Geophysical Journal of the Royal Astronomical Society 22, 377-383.

Walker, G.P.L., 1981. Generation and dispersal of fine ash and dust by volcanic eruptions. Journal of Volcanology and Geothermal Research 11, 81-92.

Walker, G.P.L., Croasdale, R., 1971. Characteristics of some basaltic pyroclastics. Bulletin of Volcanology 35, 303-317.

Wentworth, C.K., 1919. A laboratory and field study of cobble abrasion. The Journal of Geology 27, 507-521.

Wentworth, C.K., 1922. The shapes of beach pebbles. Professional Papers of the U.S. Geological Survey 131C, 75-83.

Westgate, J.A., Dreimanis, A., 1967. Volcanic ash layers of Recent age at Banff National Park, Alberta, Canada. Canadian Journal of Earth Sciences 4, 155-161.

Wilson, C.J.L., Hildreth, W., 1998. Hybrid fall deposits in the Bishop Tuff, California: a novel pyroclastic depositional mechanism. Geology 16, 7-10.

Wilson, L., Sparks, R.S.J., Walker, G.P.L., 1980. Explosive volcanic eruptions - IV. The control of magma properties and conduit geometry on eruption column behaviour. Geophysical Journal of the Royal Astronomical Society 63, 117-148.

Winkelmolen, A.M., 1982. Critical remarks on grain parameters, with special emphasis on shape. Sedimentology 29, 255-265.

Wohletz, K.H., Sheridan, M.F., Brown, W.K., 1989. Particle-size distributions and the sequential fragmentation-theory applied to volcanic ash. Journal of Geophysical Research 94, 15703-15721.

Wright, J.V., Smith, A.L., Self, S., 1980. A working terminology of pyroclastic deposits. Journal of Volcanology and Geothermal Research 8, 315-336.

Zingg, T., 1935. Beitrage zur Schotteranalyse. Schweizerische Mineralogische und Petrographische Mitteilungen 15, 38-140.

Appendix A: Field Volcanology

Appendix A1: Outcrop Photographs
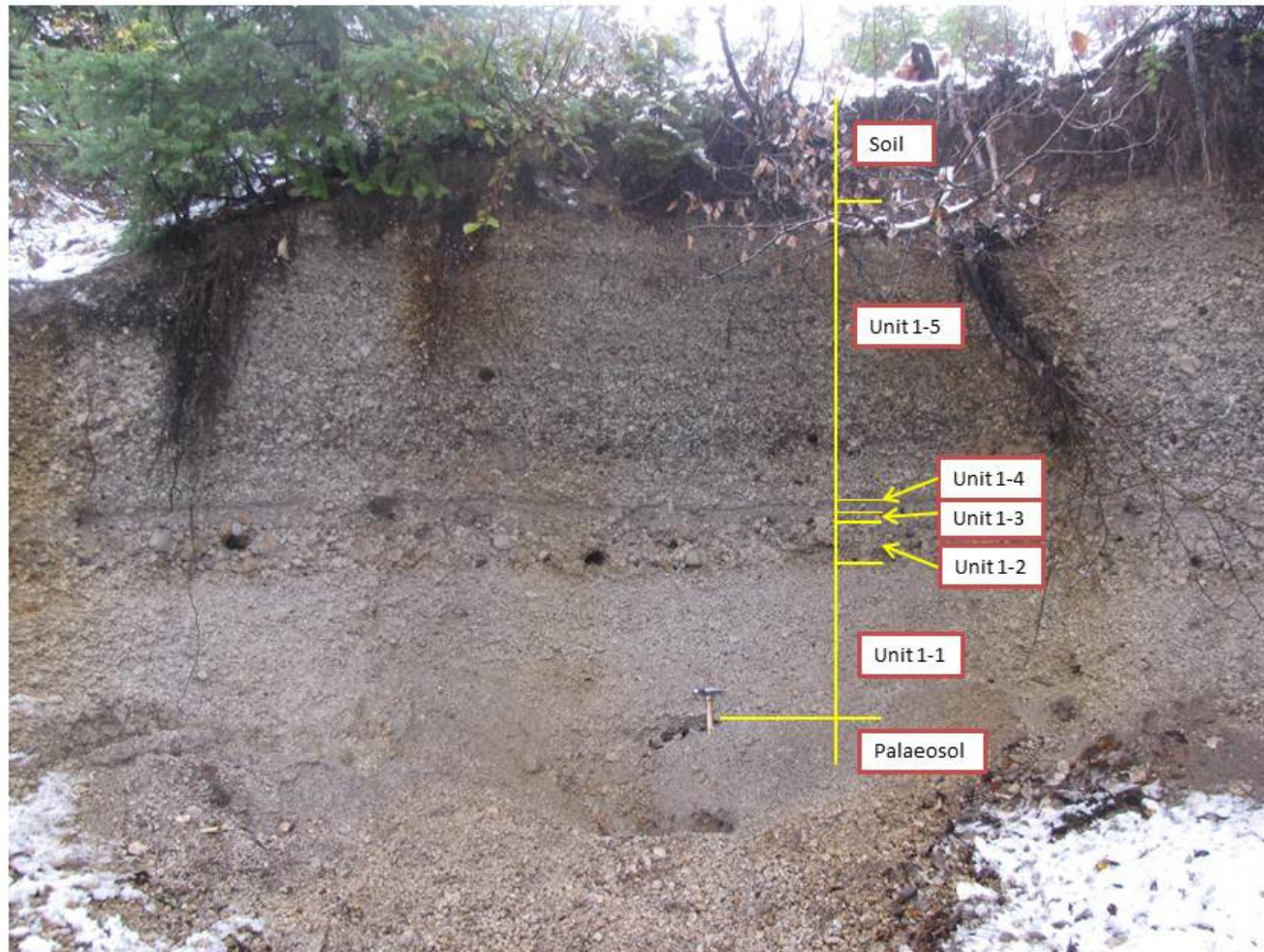
Figure A1-1. Photograph of Outcrop 1.
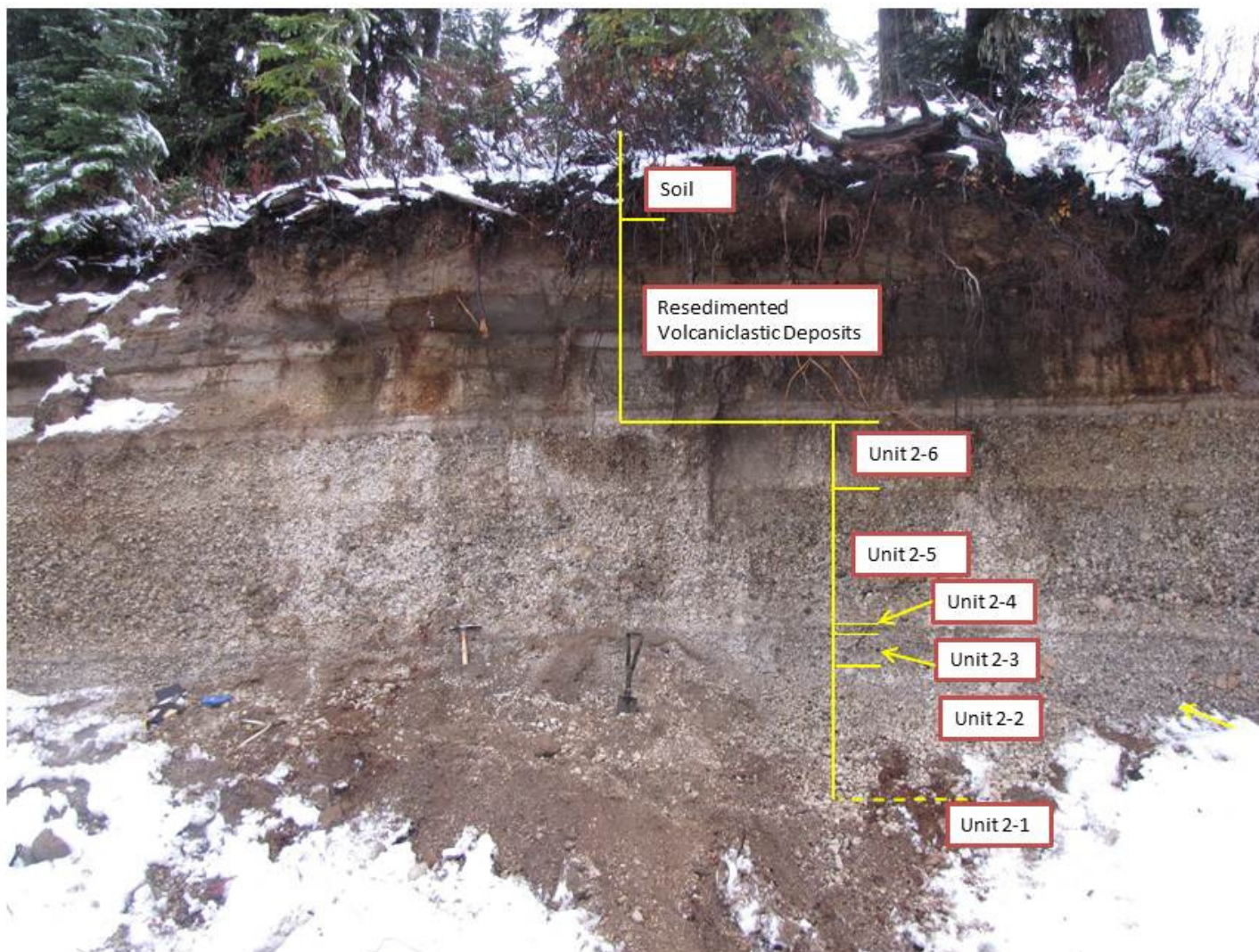
Figure A1-2. Photograph of Outcrop 2.
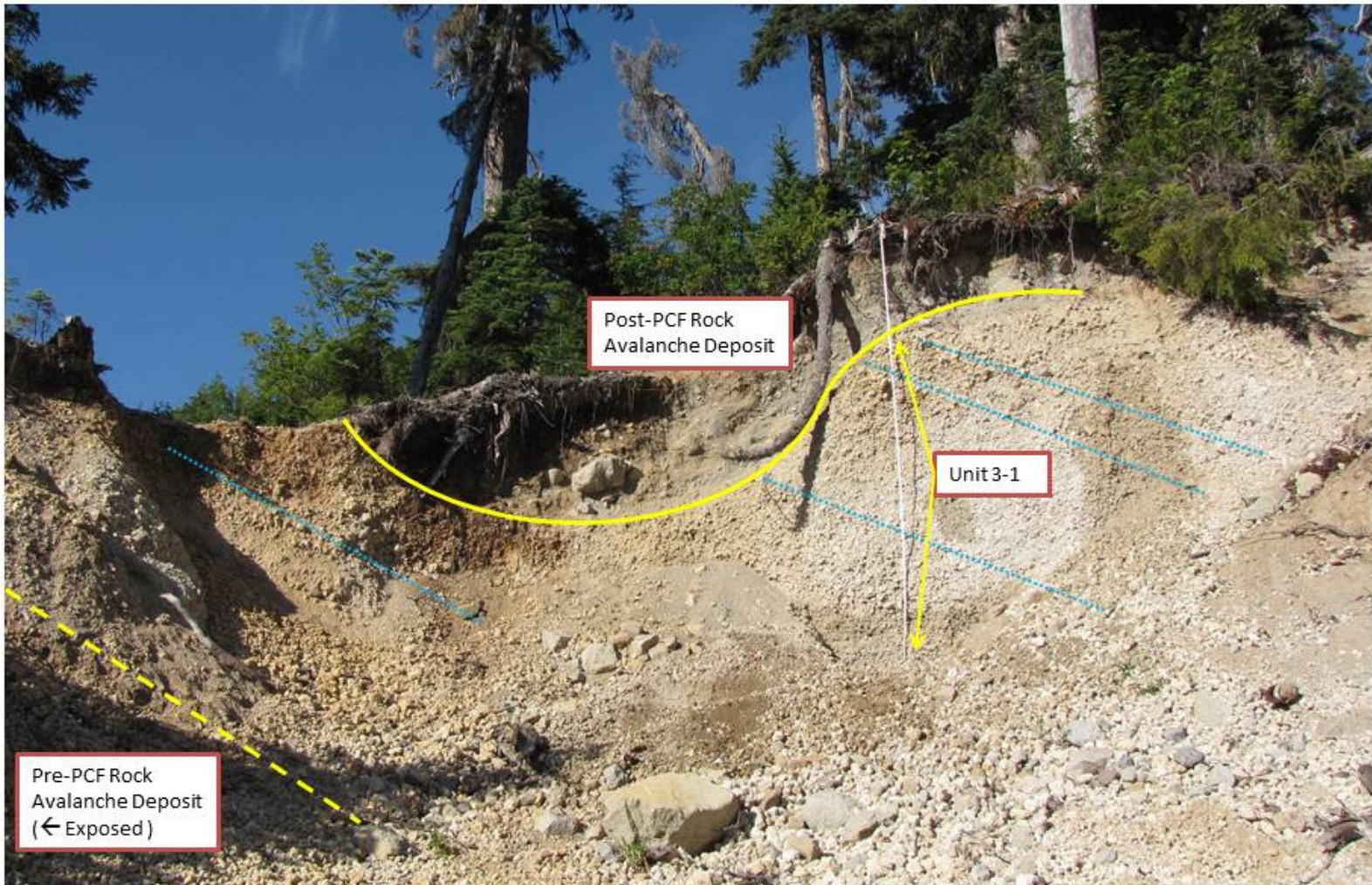
Figure A1-3. Photograph of Outcrop 3.
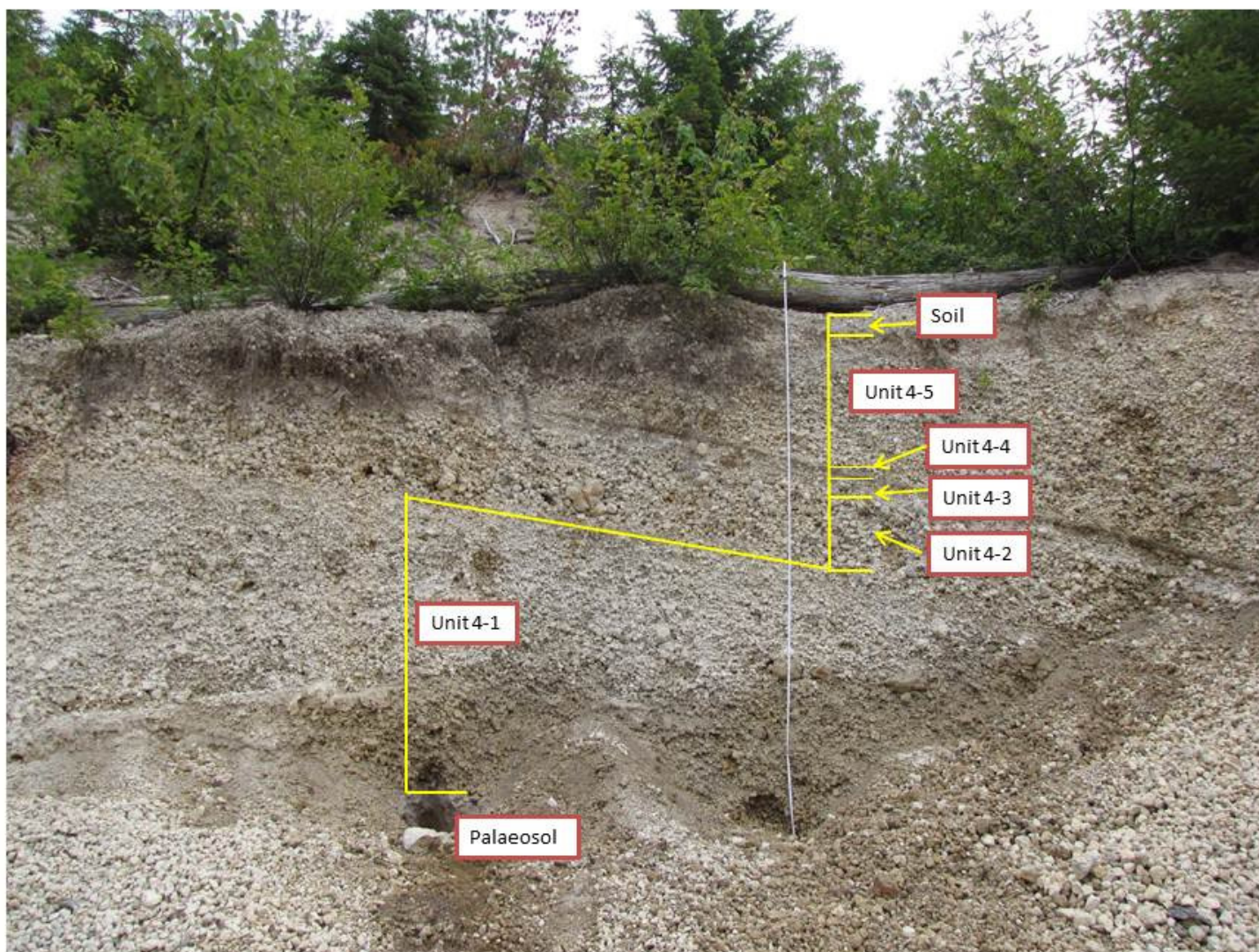
Figure A1-4. Photograph of Outcrop 4.

Figure A1-5. Photograph of Outcrop 5.
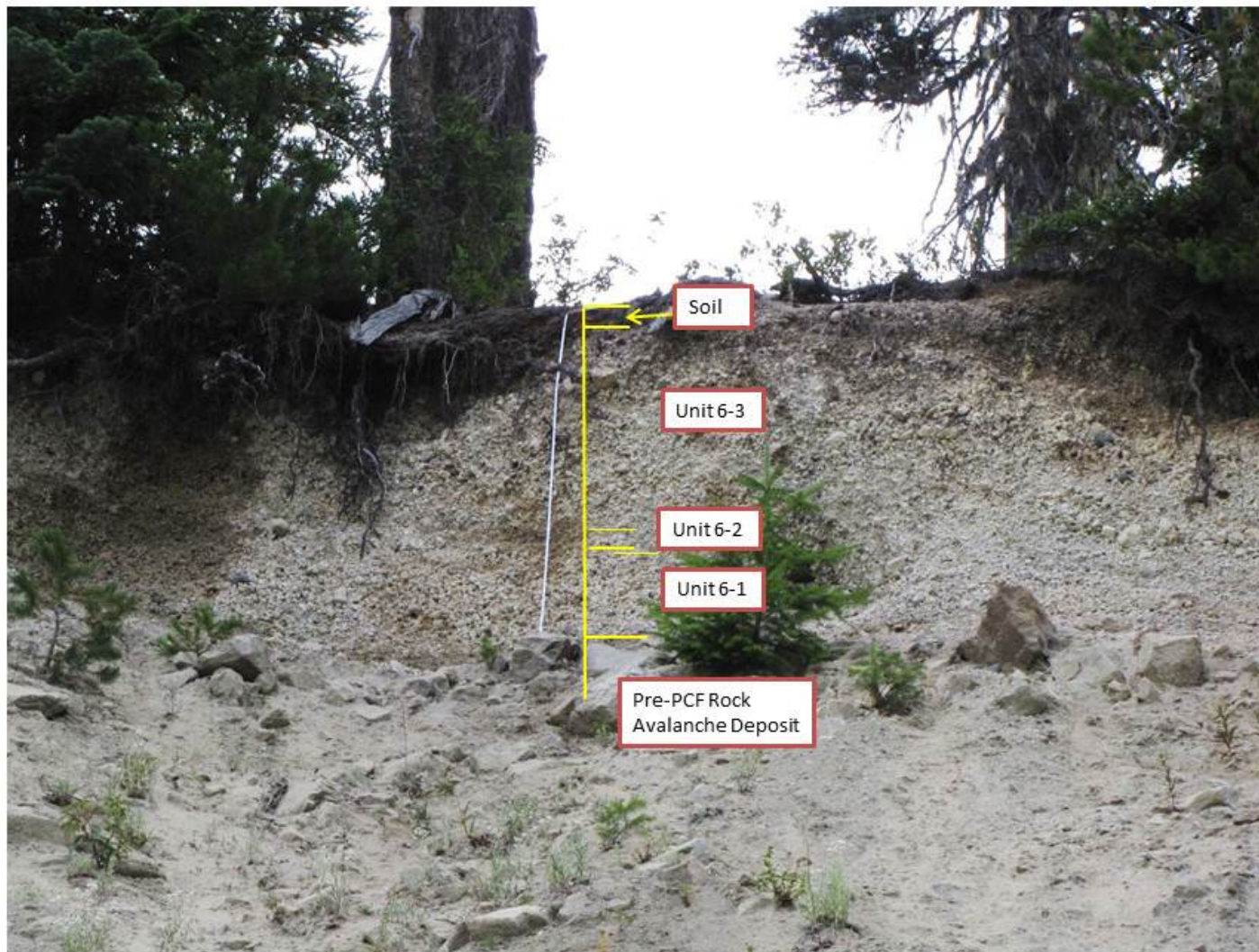
Figure A1-6. Photograph of Outcrop 6.
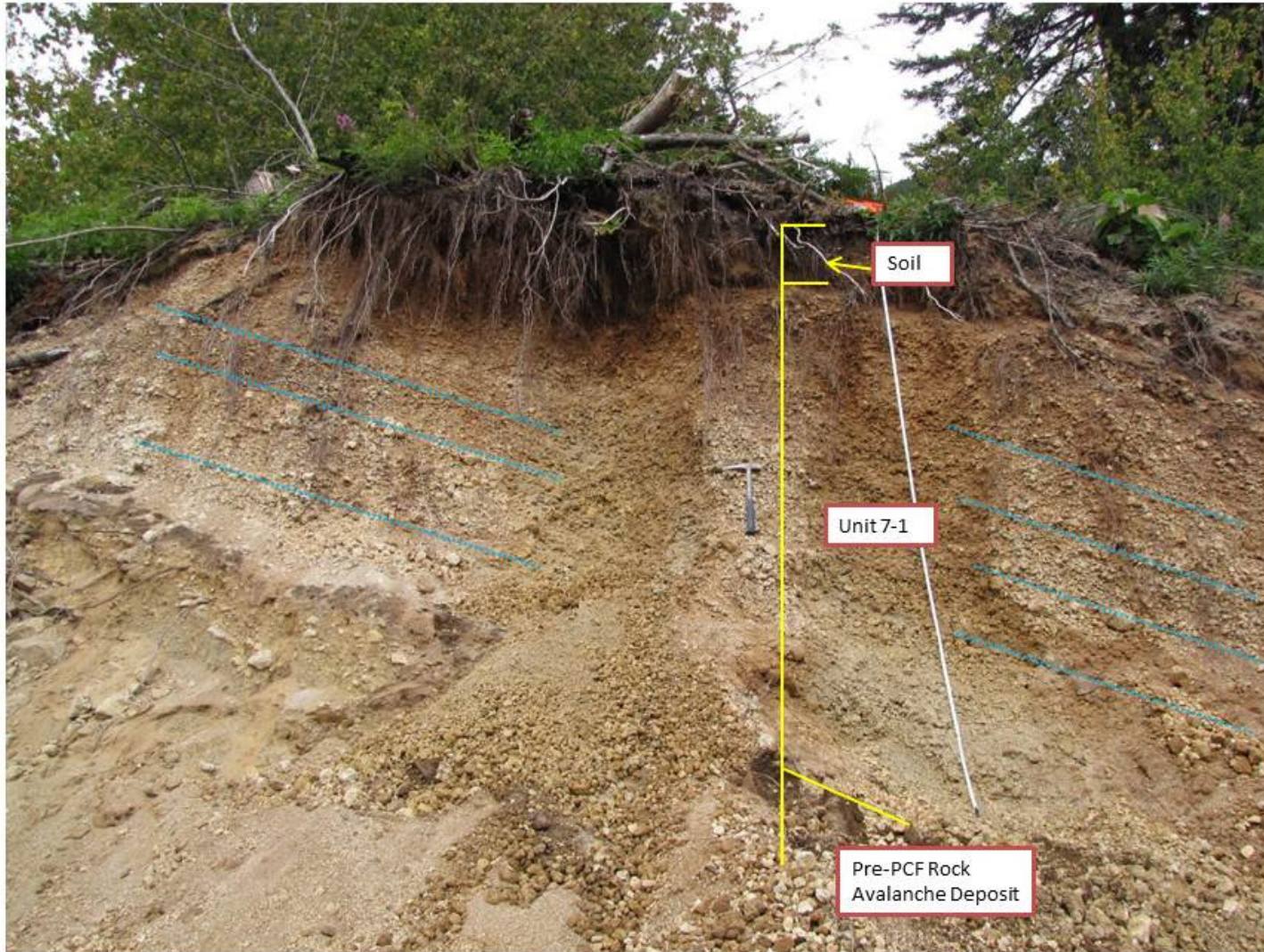
Figure A1-7. Photograph of Outcrop 7.
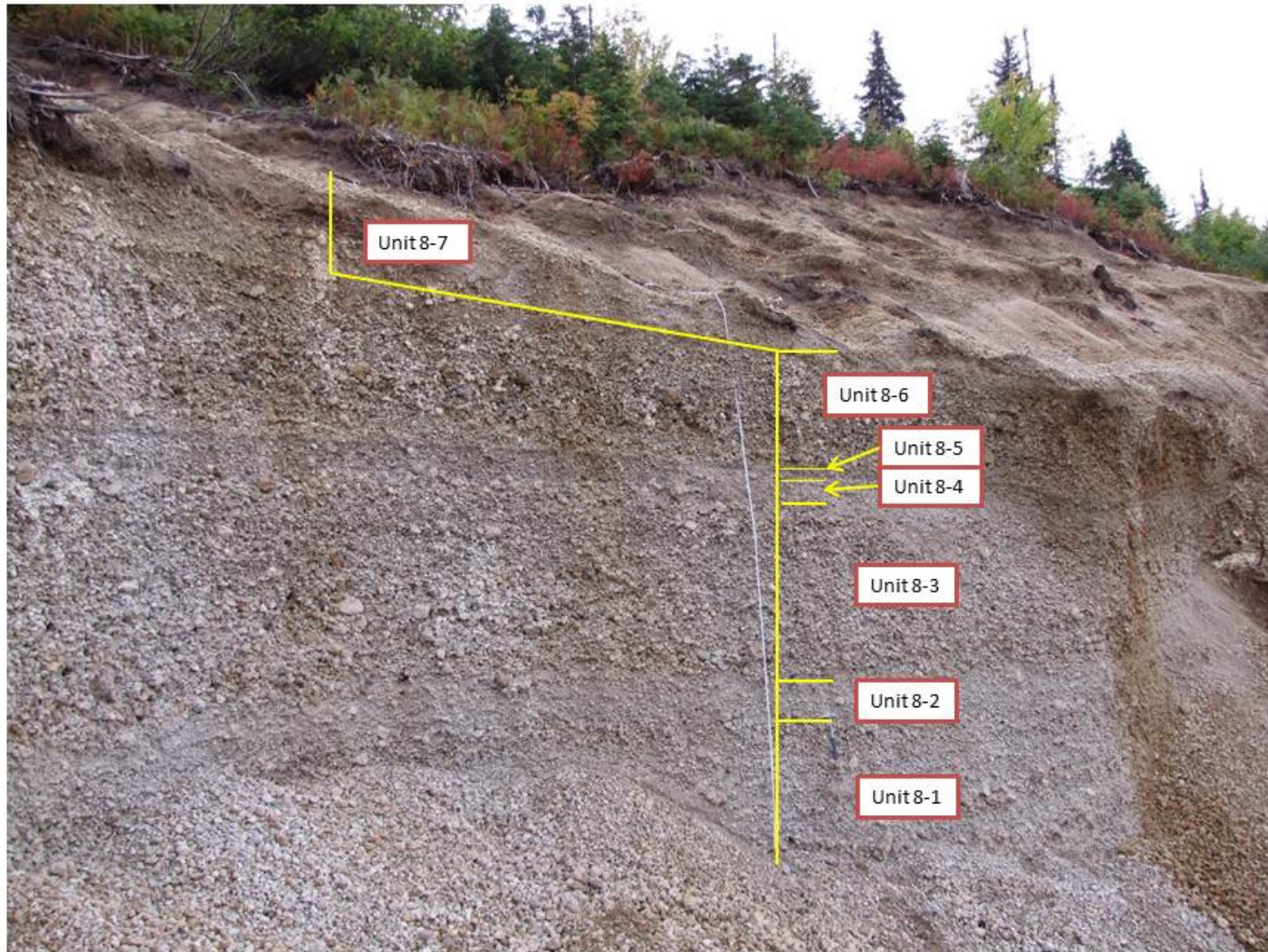
Figure A1-8. Photograph of Outcrop 8.

Appendix A2: Stratigraphic Logs.

Outcrop #1 Graphic Log	Location: Mount Meager, British Columbia	Coordinates: 5613316 N 467882 E	Elevation: 745 M.A.S.L.	Logged by: Michelle Campbell August 2011
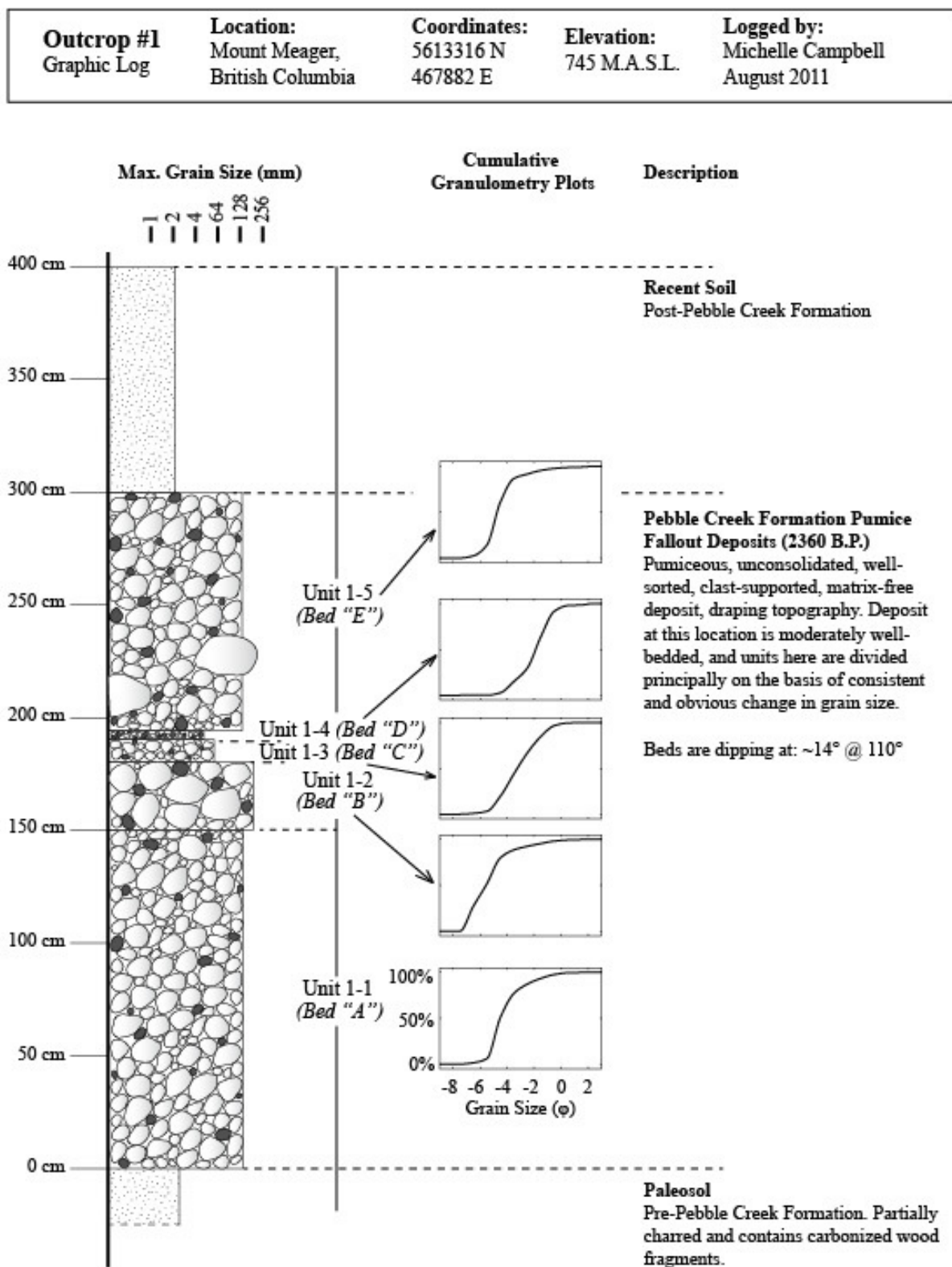
Figure A2-1. Graphic log of Outcrop 1.

154
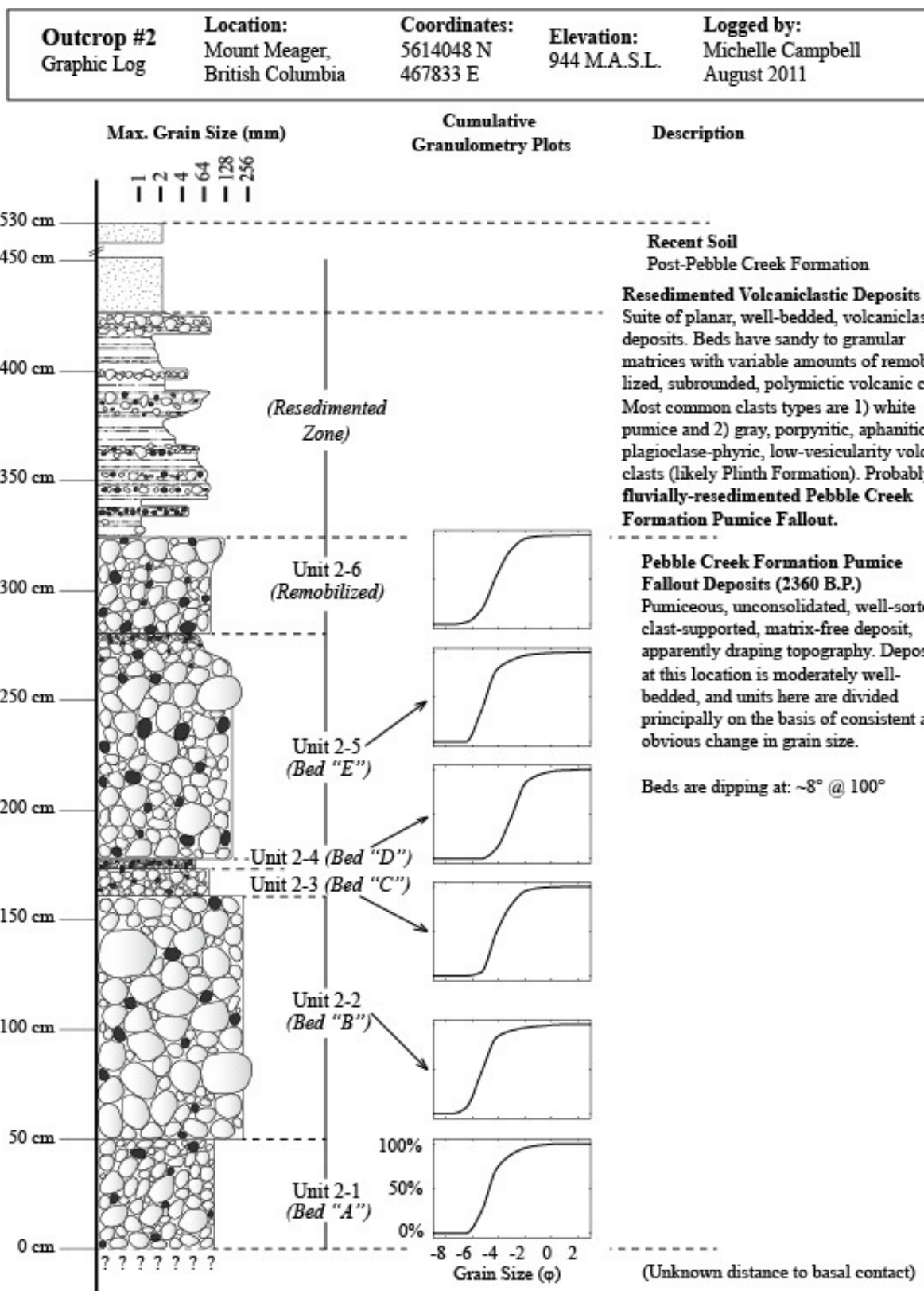
Figure A2-2. Graphic log of Outcrop 2.

Outcrop #3 Graphic Log	Location: Mount Meager, British Columbia	Coordinates: 5614916 N 466191 E	Elevation: 740 M.A.S.L.	Logged by: Michelle Campbell August 2011

Max. Grain Size (mm)

1 2 4 64 128 256

Cumulative Granulometry Plots

Description

470 cm

Recent Soil
Post-Pebble Creek Formation

450 cm

Rock Avalanche Deposit
Volcaniclastic, poorly-sorted, matrix-supported deposit with gray, subangular, monomictic, porphyritic, plagioclase-phyric, poorly-vesicular dacite clasts (likely Plinth Formation). Post-Pebble Creek Formation.

400 cm

350 cm

Pebble Creek Formation Pumice Fallout Deposits (2360 B.P.)
Pumiceous, unconsolidated, well-sorted, clast-supported, matrix-free deposit. No clear units or subdivisions of the deposit, having distinct and continuous characteristic grain size or componentry, are apparent in the outcrop at this location. Crude bedding is, however, visible as weak alignment of clasts, apparently draping topography.

300 cm

250 cm

Crude bedding is dipping at: ~30° @ 032°

Unit 3-1

200 cm

150 cm

100%

50%

0%

-8 -6 -4 -2   0   2
Grain Size (φ)

100 cm

50 cm

0 cm

? ? ? ? ? ? ?

(Unknown distance to basal contact)

Figure A2-3. Graphic log of Outcrop 3.

Outcrop #4
Graphic Log

Location:
Mount Meager,
British Columbia

Coordinates:
5613489 N
467789 E

Elevation:
771 M.A.S.L.

Logged by:
Michelle Campbell
August 2011

Max. Grain Size (mm)

Cumulative Granulometry Plots

Description

Unit 4-5
(Bed "E")

Unit 4-4 (Bed "D")
Unit 4-3 (Bed "C")

Unit 4-2
(Bed "B")

Unit 4-1
(Bed "A")

Grain Size (φ)

Pebble Creek Formation Pumice Fallout Deposits (2360 B.P.) Pumiceous, unconsolidated, well-sorted, clast-supported, matrix-free deposit, draping topography. Deposit at this location is moderately well-bedded, and units here are divided principally on the basis of consistent and obvious change in grain size.

Beds are dipping at: ~28° @ 150°

Paleosol
Pre-Pebble Creek Formation

Figure A2-4. Graphic log of Outcrop 4.

157

Outcrop #5 Graphic Log	Location: Mount Meager, British Columbia	Coordinates: 5614283 N 464682 E	Elevation: 770 M.A.S.L.	Logged by: Michelle Campbell August 2011

Max. Grain Size (mm)

Cumulative Granulometry Plots

Description

~ 12.5 m

~12 m

10 m

8 m

6 m

4 m

2 m

0 cm

? ? ? ? ? ? ?

[Inaccessible for detailed logging and sampling]

Unit 5-1

100%

50%

0%

-8 -6 -4 -2 0 2

Grain Size (φ)

Recent Soil
Post-Pebble Creek Formation

Pebble Creek Formation Pumice Fallout Deposits (2360 B.P.)
Pumiceous, unconsolidated, well-sorted, clast-supported, matrix-free deposit. Particularly thick (~12 m thick) and coarse-grained deposit, with pumice clasts up to 30 cm and accessory lithic clasts up to ~50 cm in diameter. The face of the outcrop is particularly steep and unstable, so the area above ~3 m could not be accessed for proper stratigraphic logging or sampling. The uppermost few meters of the deposit may be crudely bedded or remobilized. No clear units or subdivisions of the deposit, having distinct and continuous characteristic grain size or componentry, are apparent in the outcrop at this location.

(Unknown distance to basal contact)

Figure A2-5. Graphic log of Outcrop 5.

Outcrop #6 Graphic Log	Location: Mount Meager, British Columbia	Coordinates: 5615033 N 465880 E	Elevation: 730 M.A.S.L.	Logged by: Michelle Campbell August 2011

Max. Grain Size (mm)

Cumulative Granulometry Plots

Description

Recent Soil
Post-Pebble Creek Formation

Pebble Creek Formation Pumice Fallout Deposits (2360 B.P.)
Pumiceous, unconsolidated, well-sorted, clast-supported, matrix-free deposit, apparently draping topography. Deposit at this location is crudely bedded, with the middle unit (Unit 6-2) being subtly finer-grained than the units above and below.

Crude bedding is dipping at: ~22° @ 006°

Rock Avalanche Deposit
Polymictic, poorly-sorted, clast-supported deposit with subrounded, cobble- to boulder-sized clasts. Pre-Pebble Creek Formation.

Unit 6-3

Unit 6-2

Unit 6-1

Figure A2-6. Graphic log of Outcrop 6.

159

Outcrop #7 Graphic Log	Location: Mount Meager, British Columbia	Coordinates: 5612745 N 468374 E	Elevation: 651 M.A.S.L.	Logged by: Michelle Campbell August 2011

Max. Grain Size (mm)

Cumulative Granulometry Plots

Description

350 cm

300 cm

Recent Soil
Post-Pebble Creek Formation

250 cm

Pebble Creek Formation Pumice Fallout Deposits (2360 B.P.)
Pumiceous, unconsolidated, well-sorted, clast-supported, matrix-free deposit, apparently draping topography. No distinct units, or subdivisions of the deposit having distinct and continuous characteristic grain size or componentry, apparent in outcrop at this location.

200 cm

Basal contact with rock avalanche deposit dipping ~18° @ 040°

150 cm

Unit 7-1

100%
50%
0%
-8 -6 -4 -2 0 2
Grain Size (φ)

100 cm

50 cm

0 cm

Rock Avalanche Deposit
Polymictic, poorly-sorted, clast-supported deposit with subangular to subrounded clasts up to 50 cm in diameter, in sandy light brown matrix. Top 10 cm is charred and dark brown. Pre-Pebble Creek Formation.

Figure A2-7. Graphic log of Outcrop 7.

Figure A2-8. Graphic log of Outcrop 8.

Appendix B: X-Ray Diffraction Rietveld Analysis Plots

Sample MC-2010-Ya033 (Coarse-Grained Monzogranite)

Quartz	36.66 %
Albite low	20.74 %
Biotite 1M	0.87 %
Orthoclase	26.51 %
Albite low, calcian	15.12 %
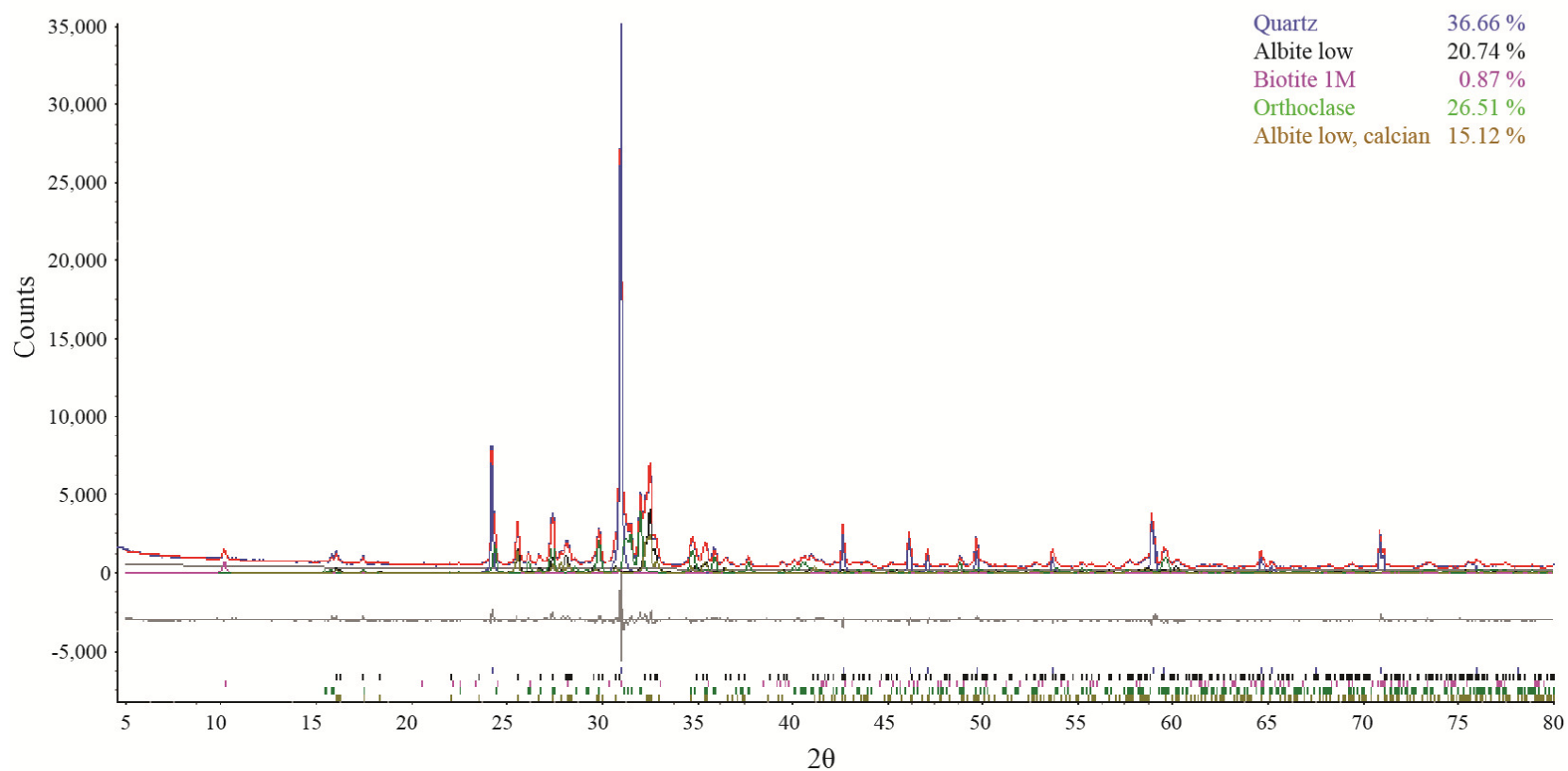
Figure B-1. Rietveld refinement plot of sample # MC-2010-Ya033: coarse-grained monzogranite. Blue line: observed intensity at each step. Red line: calculated intensity pattern from mineral abundance estimates. Coloured lines: individual diffraction patterns of all selected mineral phases. Gray line: difference between observed and calculated intensities. Vertical bars: positions of all Bragg reflections.

Sample MC-2010-Ya011 (Medium-Grained Monzogranite)

Quartz	37.83 %
Albite low	29.22 %
Biotite 1M	0.96 %
Orthoclase	26.19 %
Albite low, calcian	5.79 %
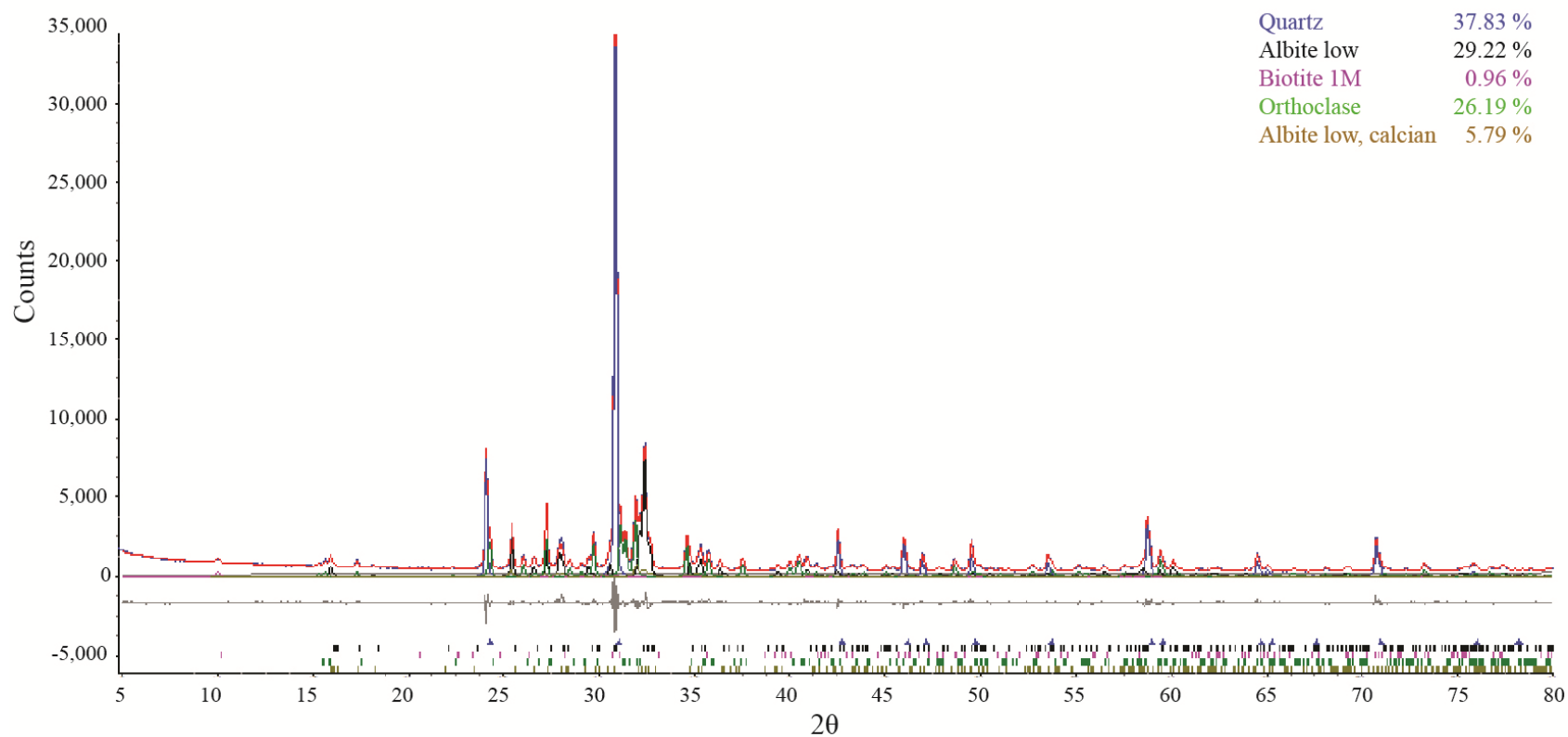
Figure B-2. Rietveld refinement plot of sample # MC-2010-Ya011: medium-grained monzogranite. Blue line: observed intensity at each step. Red line: calculated intensity pattern from mineral abundance estimates. Coloured lines: individual diffraction patterns of all selected mineral phases. Gray line: difference between observed and calculated intensities. Vertical bars: positions of all Bragg reflections.

Appendix C: Mass, Density and Volume Data for Accessory Lithic Clasts

Appendix C1: Main Accessory Lithic Sample Set

Table C1-1. Mass, density and volume data for monzogranite accessory lithic clasts (main sample set)

Sample #	Average Dry Weight (g)	Density (g/cm³)	Volume (cm³)	Sample #	Average Dry Weight (g)	Density (g/cm³)	Volume (cm³)
Monzogranite Samples: Great Pacific Pumice Quarry				MC-2010-Yb022	134.8	2.603	51.8
				MC-2010-Yb023	78.4	2.601	30.1
MC-2010-Ya001	6413.9	2.596	2470.5	MC-2010-Yb024	38.5	2.597	14.8
MC-2010-Ya003	6459.4	2.601	2483.3	MC-2010-Yb025	78.5	2.598	30.2
MC-2010-Ya004	1751.4	2.594	675.1	MC-2010-Yb026	49.6	2.588	19.2
MC-2010-Ya008	1676.3	2.601	644.4	MC-2010-Yb027	16.6	2.590	6.4
MC-2010-Ya009	4847.5	2.597	1866.4	MC-2010-Yb028	379.1	2.591	146.3
MC-2010-Ya010	977.6	2.594	376.9	MC-2010-Yb029	195.9	2.597	75.4
MC-2010-Ya014	459.3	2.596	176.9	MC-2010-Yb030	158.7	2.590	61.3
MC-2010-Yb001	216.5	2.596	83.4	MC-2010-Yb031	122.1	2.605	46.9
MC-2010-Yb002	180.1	2.600	69.3	MC-2010-Yb032	140.2	2.617	53.6
MC-2010-Yb003	155.7	2.605	59.8	MC-2010-Yb033	70.7	2.598	27.2
MC-2010-Yb004	417.6	2.594	161.0	MC-2010-Yb034	31.2	2.599	12.0
MC-2010-Yb005	335.8	2.597	129.3	MC-2010-Yb035	60.8	2.603	23.3
MC-2010-Yb006	231.7	2.586	89.6	MC-2010-Yb036	112.2	2.591	43.3
MC-2010-Yb007	203.2	2.584	78.7	MC-2010-Yb037	742.0	2.583	287.2
MC-2010-Yb008	271.3	2.589	104.8	MC-2010-Yb038	613.9	2.554	240.4
MC-2010-Yb009	685.4	2.602	263.4	MC-2010-Yb039	258.3	2.602	99.3
MC-2010-Yb010	232.1	2.615	88.8	MC-2010-Yc001	4055.4	2.591	1565.2
MC-2010-Yb011	251.8	2.605	96.6	MC-2010-Yc002	3897.5	2.619	1488.0
MC-2010-Yb011	251.8	2.605	96.6	MC-2010-Yc003	2720.3	2.596	1047.9
MC-2010-Yb013	958.1	2.602	368.3	MC-2010-Yc004	3290.5	2.607	1262.1
MC-2010-Yb015	180.6	2.595	69.6	MC-2010-Yc005	3062.8	2.595	1180.4
MC-2010-Yb016	269.8	2.593	104.1	MC-2010-Yc006	985.5	2.607	378.0
MC-2010-Yb017	37.2	2.591	14.4	MC-2010-Yc007	1502.8	2.586	581.1
MC-2010-Yb019	98.4	2.588	38.0	MC-2010-Yc008	2841.7	2.586	1099.0
MC-2010-Yb020	144.2	2.591	55.7	MC-2010-Yc009	3424.2	2.613	1310.3
MC-2010-Yb021	597.2	2.600	229.7	MC-2010-Yc010	625.8	2.591	241.5

Sample #	Average Dry Weight (g)	Density (g/cm^3)	Volume (cm^3)
MC-2010-Yc012	1787.3	2.597	688.2
MC-2010-Yc013	5131.3	2.592	1980.0
MC-2010-Yc014	1912.7	2.581	741.2
MC-2010-Yc015	3042.0	2.599	1170.4
MC-2010-Yc016	3205.4	2.598	1234.0
MC-2010-Yc017	1016.6	2.607	389.9
MC-2010-Yc018	1203.9	2.588	465.1
MC-2010-Yc019	1682.6	2.601	646.9
MC-2010-Yc020	1968.5	2.603	756.2
MC-2010-Yc021	1540.1	2.595	593.4
MC-2010-Yc022	1537.4	2.615	588.0
MC-2010-Yc023	507.7	2.584	196.5
MC-2010-Yc024	773.5	2.615	295.8
MC-2010-Yc025	964.1	2.582	373.4
MC-2010-Yc026	1055.7	2.610	404.5
MC-2010-Yc027	1734.1	2.590	669.5
MC-2010-Yc028	756.4	2.600	290.9
MC-2010-Yc029	2523.7	2.599	971.1
MC-2010-Yc030	8336.0	2.600	3205.8
MC-2010-Yc031	7439.2	2.606	2855.0
MC-2010-Yc032	6716.6	2.595	2588.0
MC-2010-Yc033	2237.7	2.594	862.6
MC-2010-Yc034	5581.9	2.593	2152.3
MC-2010-Yc035	3590.4	2.587	1387.9
MC-2010-Yc036	2533.4	2.596	976.0
MC-2010-Yc037	6279.6	2.615	2401.8
MC-2010-Yc038	6854.3	2.596	2639.9
MC-2012-Yd001	8426.2	2.581	3264.1
MC-2012-Yd002	6706.9	2.584	2595.5
MC-2012-Yd003	6578.2	2.588	2541.9
MC-2012-Yd004	5013.4	2.584	1940.5
MC-2012-Yd005	937.3	2.585	362.5
MC-2012-Yd006	256.3	2.581	99.3
MC-2012-Yd007	360.8	2.558	141.0
MC-2012-Yd008	69.1	2.590	26.7

Sample #	Average Dry Weight (g)	Density (g/cm^3)	Volume (cm^3)
MC-2012-Yd009	308.5	2.582	119.5
MC-2012-Yd010	2299.1	2.594	886.3
MC-2012-Yd011	1051.8	2.594	405.5
MC-2012-Yd012	1211.7	2.600	466.0
Average Density:		**2.595**	

Monzogranite Samples: In Situ Accessory Lithics (Unit 5-1)

Sample #	Average Dry Weight (g)	Density (g/cm^3)	Volume (cm^3)
MC-2011-IS02	159.5	2.597	61.4
MC-2011-IS03A	7746.5	2.589	2991.6
MC-2011-IS03B	289.7	2.581	112.2
MC-2011-IS04	91.1	2.609	34.9
MC-2011-IS05	214.5	2.597	82.6
MC-2011-IS06	191.5	2.591	73.9
MC-2011-IS07	270.6	2.598	104.2
MC-2011-IS08	898.2	2.595	346.1
MC-2011-IS09	3682.3	2.597	1417.8
MC-2011-IS10	1968.8	2.600	757.2
MC-2011-IS11	517.9	2.537	204.1
MC-2011-IS12	290.5	2.595	111.9
Average Density:		**2.591**	

Sample #	Average Dry Weight (g)	Approx. Density (g/cm^3)	Approx. Volume (cm^3)
Monzogranite Oversize Samples: > 10 kg Accessory Lithics			
MC-2011-IS01	41496.6	~ 2.595	~ 15992
MC-2010-Ya002	17584.8	~ 2.595	~ 6777
MC-2010-Yc039	16298.9	~ 2.595	~ 6281
MC-2010-Yc040	51700.7	~ 2.595	~ 19924
MC-2012-Yd013	31972.8	~ 2.595	~ 12321

Table C1-2. Mass, density and volume data for dacite accessory lithic clasts (main sample set)

Sample #	Average Dry Weight (g)	Density (g/cm^3)	Volume (cm^3)
Dacite Samples: Great Pacific Pumice Quarry			
MC-2010-PP01	777.1	2.398	324.0
MC-2010-PP02	100.0	2.491	40.1
MC-2010-PP03	468.0	2.545	183.9
MC-2010-PP04	290.5	2.532	114.7
MC-2010-PP05	814.6	2.504	325.3
MC-2010-PP06	109.8	2.513	43.7
MC-2010-PP07	168.2	2.337	72.0
MC-2010-PP08	957.0	2.594	369.0
MC-2010-PP09	156.4	2.541	61.6
MC-2010-PP10	4500.2	2.320	1940.0
MC-2010-PP11	668.6	2.500	267.5
MC-2010-PP12	72.3	2.473	29.2
MC-2010-PP13	119.1	2.536	47.0
MC-2010-PP14	2773.2	2.452	1130.9
MC-2012-PL03	9277.8	2.595	3575.1
MC-2012-PL04	4512.6	2.415	1868.9
MC-2012-PL06	6804.6	2.607	2609.8
MC-2010-PP01	777.1	2.398	324.0
MC-2010-PP02	100.0	2.491	40.1
MC-2010-PP03	468.0	2.545	183.9
MC-2010-PP04	290.5	2.532	114.7
MC-2010-PP05	814.6	2.504	325.3
MC-2010-PP06	109.8	2.513	43.7
MC-2010-PP07	168.2	2.337	72.0
MC-2010-PP08	957.0	2.594	369.0
MC-2010-PP09	156.4	2.541	61.6
MC-2010-PP10	4500.2	2.320	1940.0
MC-2010-PP11	668.6	2.500	267.5
MC-2010-PP12	72.3	2.473	29.2
MC-2010-PP13	119.1	2.536	47.0
MC-2010-PP14	2773.2	2.452	1130.9
MC-2012-PL03	9277.8	2.595	3575.1
MC-2012-PL04	4512.6	2.415	1868.9

Sample #	Average Dry Weight (g)	Density (g/cm^3)	Volume (cm^3)
MC-2012-PL06	6804.6	2.607	2609.8
Average Density:		**2.481**	
Dacite Samples: In Situ Accessory Lithics (Unit 5-1)			
MC-2011-P01	3363.8	2.519	1335.2
MC-2011-P02	515.4	2.265	227.6
MC-2011-P03	2232.0	2.442	913.9
MC-2011-P04	1098.5	2.456	447.3
MC-2011-P05	4581.6	2.315	1979.4
MC-2011-P06	487.6	2.515	193.9
MC-2011-P07	579.7	2.277	254.6
MC-2011-P08	814.2	2.511	324.2
MC-2011-P09	182.3	2.559	71.3
MC-2011-P10	436.2	2.653	164.4
MC-2011-P11	179.9	2.466	73.0
MC-2011-P12	494.3	2.627	188.2
MC-2011-P13	3413.8	2.502	1364.5
MC-2011-P14	635.5	2.458	258.6
MC-2011-P15	96.1	2.390	40.2
MC-2011-P16	92.9	2.329	39.9
MC-2011-P17	3713.3	2.458	1510.9
MC-2011-P18	198.0	2.433	81.4
MC-2011-P19	209.1	2.450	85.4
MC-2011-P20	105.3	2.346	44.9
Average Density:		**2.460**	

Sample #	Average Dry Weight (g)	Approx. Density (g/cm^3)	Approx. Volume (cm^3)
Dacite Oversize Samples: > 10 kg Accessory Lithics			
MC-2010-PL01	28571.4	~ 2.468	~ 11576
MC-2012-PL02	12535.9	~ 2.468	~ 5079

Appendix C2: Supplementary Small Volume Accessory Lithic Sample Set

Table C2-1. Mass, density and volume data for monzogranite accessory lithic clasts (supplementary sample set)

Sample #	Average Dry Weight (g)	Density (g/cm³)	Volume (cm³)	Sample #	Average Dry Weight (g)	Density (g/cm³)	Volume (cm³)
Monzogranite Samples: Outcrop 1				1-5-M14	4.3	2.540	1.7
				1-5-M15	4.0	2.528	1.6
1-1-M1	52.6	2.595	20.3	1-5-M16	2.7	2.640	1.0
1-1-M2	25.8	2.606	9.9	1-5-M17	3.6	2.543	1.4
1-1-M3	13.2	2.575	5.1	1-5-M18	2.3	2.612	0.9
1-1-M4	15.0	2.593	5.8	1-5-M19	2.2	2.478	0.9
1-1-M5	7.8	2.620	3.0	1-5-M20	1.9	2.436	0.8
1-1-M6	5.2	2.522	2.1	1-5-M21	1.9	2.554	0.7
1-1-M7	1.5	2.516	0.6	1-5-M22	1.4	2.538	0.6
1-1-M8	1.1	2.537	0.4	1-5-M23	1.6	2.392	0.7
1-1-M9	0.3	2.378	0.1	1-5-M24	1.4	2.363	0.6
1-2-M1	22.6	2.601	8.7	1-5-M25	1.6	2.577	0.6
1-2-M2	12.6	2.577	4.9	1-5-M26	1.2	2.443	0.5
1-2-M3	8.0	2.614	3.1	1-5-M27	1.4	2.476	0.6
1-2-M4	7.1	2.556	2.8	1-5-M28	1.1	2.482	0.4
1-5-M1	45.0	2.597	17.3	1-5-M29	1.1	2.577	0.4
1-5-M2	50.4	2.592	19.4	1-5-M30	1.2	2.661	0.4
1-5-M3	46.1	2.592	17.8	1-5-M31	1.1	2.527	0.4
1-5-M4	35.4	2.577	13.7	1-5-M32	0.9	2.693	0.3
1-5-M5	18.5	2.578	7.2	1-5-M33	0.8	2.591	0.3
1-5-M6	21.1	2.595	8.1	1-5-M34	0.9	2.422	0.4
1-5-M7	10.2	2.587	3.9	1-5-M35	1.1	2.528	0.4
1-5-M8	9.1	2.568	3.5	1-5-M36	0.8	2.452	0.3
1-5-M9	7.9	2.538	3.1	1-5-M37	0.3	2.425	0.1
1-5-M10	6.7	2.598	2.6	1-5-M38	0.2	2.495	0.1
1-5-M11	6.0	2.579	2.3	**Average Density:**		**2.544**	
1-5-M12	4.8	2.533	1.9				
1-5-M13	4.6	2.531	1.8				

Table C1-1. Mass, density and volume data for dacite accessory lithic clasts (supplementary sample set)

Sample #	Average Dry Weight (g)	Density (g/cm³)	Volume (cm³)
Dacite Samples: Outcrop 1			
1-1-P1	36.6	2.589	14.1
1-1-P2	33.5	2.420	13.9
1-1-P3	23.6	2.632	9.0
1-1-P4	16.2	2.530	6.4
1-1-P5	7.4	2.456	3.0
1-1-P6	3.7	2.424	1.5
1-1-P7	4.0	2.474	1.6
1-1-P8	2.4	2.445	1.0
1-1-P9	1.4	2.351	0.6
1-1-P10	1.5	2.434	0.6
1-1-P11	0.8	2.405	0.3
1-1-P12	0.7	2.494	0.3
1-2-P1	325.3	2.638	123.3
1-2-P2	78.5	2.471	31.8
1-2-P3	30.7	2.434	12.6
1-2-P4	10.1	2.448	4.1
1-2-P5	8.8	2.611	3.4
1-2-P6	3.9	2.542	1.5
1-5-P1	137.7	2.480	55.5
1-5-P2	83.8	2.531	33.1
1-5-P3	63.3	2.450	25.9
1-5-P4	44.6	2.494	17.9
1-5-P5	24.2	2.503	9.7
1-5-P6	10.5	2.353	4.5
1-5-P7	8.8	2.436	3.6
1-5-P8	8.6	2.446	3.5
1-5-P9	4.7	2.397	2.0
1-5-P10	4.5	2.299	1.9

Sample #	Average Dry Weight (g)	Density (g/cm³)	Volume (cm³)
1-5-P11	4.3	2.394	1.8
1-5-P12	3.1	2.499	1.2
1-5-P13	3.2	2.423	1.3
1-5-P14	1.9	2.323	0.8
1-5-P15	2.6	2.434	1.1
1-5-P16	2.6	2.441	1.1
1-5-P17	1.5	2.442	0.6
1-5-P18	1.4	2.290	0.6
1-5-P19	1.2	2.487	0.5
1-5-P20	1.1	2.280	0.5
1-5-P21	0.9	2.424	0.4
1-5-P22	0.7	2.226	0.3
1-5-P23	0.7	2.388	0.3
1-5-P24	0.5	2.300	0.2
Average Density:		**2.441**	

Appendix D: Form Measurements

Appendix D1: Axis Measurement Frame

Figure D1-1. Photograph of axis measurement frame used in this study (3-sided plexiglass box, with inlaid rulers).

Appendix D2: Axis Measurements

Table D2-1. Axis measurements of monzogranite and dacite samples.

Sample #	Long Axis "a" (cm)	Intermediate Axis "b" (cm)	Short Axis "c" (cm)	Maximum Projection Sphericity (Ψ_p)
Intact Monzogranite Accessory Lithic Clasts				
MC-2010-Ya001	23.1	16.0	14.2	0.82
MC-2010-Ya002	29.1	25.0	20.3	0.83
MC-2010-Ya003	20.4	17.0	14.2	0.83
MC-2010-Ya004	14.7	12.1	7.2	0.66
MC-2010-Ya008	14.6	12.0	7.0	0.65
MC-2010-Ya009	21.4	16.4	12.4	0.76
MC-2010-Ya010	12.0	9.9	6.4	0.70
MC-2010-Ya014	8.8	6.6	6.0	0.85
MC-2010-Yb001	6.2	5.2	4.9	0.91
MC-2010-Yb002	6.8	5.2	4.1	0.78
MC-2010-Yb003	5.8	4.9	4.8	0.93
MC-2010-Yb004	8.7	7.1	5.7	0.81
MC-2010-Yb005	7.6	7.2	5.0	0.77
MC-2010-Yb006	7.1	5.2	4.6	0.83
MC-2010-Yb007	6.5	5.3	4.9	0.89
MC-2010-Yb008	7.3	6.5	5.7	0.88
MC-2010-Yb009	11.2	8.5	7.2	0.82
MC-2010-Yb011	8.0	5.3	4.6	0.79
MC-2010-Yb024	3.8	2.9	2.7	0.87
MC-2010-Yb034	4.1	3.0	2.5	0.80
MC-2010-Yb035	5.1	3.3	3.0	0.81
MC-2010-Yc001	18.8	13.6	12.3	0.84
MC-2010-Yc002	17.3	13.4	13	0.90
MC-2010-Yc003	16.4	11.7	10.7	0.84
MC-2010-Yc004	18.0	11.9	11.1	0.83
MC-2010-Yc005	15.1	14.0	12.1	0.88
MC-2010-Yc006	11.4	9.0	8.1	0.86
MC-2010-Yc007	14.0	11.1	7.6	0.72
MC-2010-Yc008	16.4	13.4	11.3	0.83
MC-2010-Yc013	21.6	17.9	11.7	0.71
MC-2010-Yc021	14.7	11.3	8.5	0.76
MC-2010-Yc025	12.2	8.6	7.4	0.81
MC-2010-Yc030	21.8	17.7	16.7	0.90
MC-2010-Yc038	23.2	20.3	12.8	0.70
MC-2012-Yd001	23.8	17.0	16.3	0.87
MC-2012-Yd002	21.1	18.1	16.1	0.88
MC-2012-Yd003	21.5	19.1	14.7	0.81
MC-2012-Yd004	19.7	19.2	13.2	0.77
MC-2012-Yd005	11.1	8.7	7.5	0.84
MC-2012-Yd006	7.4	6.0	4.5	0.77
MC-2012-Yd007	7.9	7.0	6.0	0.87
MC-2012-Yd008	4.5	4.0	3.2	0.83
MC-2012-Yd009	7.5	6.3	5.1	0.82
MC-2012-Yd010	17.3	14.5	7.6	0.61
MC-2012-Yd011	12.9	9.6	6.6	0.71
MC-2012-Yd012	14.3	11.0	6.1	0.62
MC-2012-Yd013	35.8	29.1	23.4	0.81

Sample #	Long Axis "a" (cm)	Intermediate Axis "b" (cm)	Short Axis "c" (cm)	Maximum Projection Sphericity (Ψ_p)
MC-2011-IS01	36.0	33.5	32.1	0.95
MC-2011-IS04	4.8	4.7	3.8	0.86
MC-2011-IS07	9.0	6.6	4.2	0.67
MC-2011-IS09	26.3	12.0	10.0	0.68
			Average:	**0.80**

Broken Monzogranite Accessory Lithic Clasts

Sample #	Long Axis "a" (cm)	Intermediate Axis "b" (cm)	Short Axis "c" (cm)	Maximum Projection Sphericity (Ψ_p)
MC-2010-Yb010	8.0	5.0	4.6	0.81
MC-2010-Yb013	13.0	9.4	7.0	0.74
MC-2010-Yb015	12.2	6.4	3.3	0.52
MC-2010-Yb016	7.7	5.5	5.2	0.86
MC-2010-Yb017	5.3	4.1	1.7	0.51
MC-2010-Yb019	7.1	4.2	3.0	0.67
MC-2010-Yb020	7.4	5.3	3.7	0.70
MC-2010-Yb021	12.9	7.3	5.8	0.71
MC-2010-Yb022	7.4	4.2	3.2	0.69
MC-2010-Yb023	5.8	5.0	2.8	0.65
MC-2010-Yb025	5.0	3.8	3.3	0.83
MC-2010-Yb026	4.8	4.1	2.6	0.70
MC-2010-Yb027	3.8	2.9	1.7	0.64
MC-2010-Yb028	10.2	7.1	4.9	0.69
MC-2010-Yb029	7.4	4.7	4.0	0.77
MC-2010-Yb030	9.1	6.5	2.3	0.45
MC-2010-Yb031	5.7	5.0	3.9	0.81
MC-2010-Yb032	7.5	5.2	2.5	0.54
MC-2010-Yb033	4.3	3.6	3.2	0.87
MC-2010-Yb036	7.5	4.8	3.7	0.72
MC-2010-Yb037	15.4	7.7	6.2	0.69
MC-2010-Yb038	11.0	7.2	6.5	0.81
MC-2010-Yb039	8.6	6.9	5.9	0.84
MC-2010-Yc009	18.0	16.4	10.2	0.71
MC-2010-Yc010	10.2	8.1	6.5	0.80
MC-2010-Yc012	13.3	11.1	10.7	0.92
MC-2010-Yc014	18.6	10.9	7.0	0.62
MC-2010-Yc015	21.0	14.3	8.1	0.60
MC-2010-Yc016	20.1	13.1	11.6	0.80
MC-2010-Yc017	13.1	8.1	7.6	0.82
MC-2010-Yc018	14.5	10.0	7.5	0.73
MC-2010-Yc019	16.7	11.4	6.8	0.62
MC-2010-Yc020	22.2	14.2	6.9	0.53
MC-2010-Yc022	14.5	10.8	8.5	0.77
MC-2010-Yc023	10.4	8.7	5.2	0.67
MC-2010-Yc024	12.9	10.7	6.7	0.69
MC-2010-Yc026	15.7	9.2	7.0	0.70
MC-2010-Yc027	13.9	12.1	10.7	0.88
MC-2010-Yc028	14.4	11.7	4.6	0.50
MC-2010-Yc029	19.5	16.4	6.8	0.52
MC-2010-Yc031	24.5	18.7	12.0	0.68
MC-2010-Yc032	27.5	16.7	14.4	0.77
MC-2010-Yc033	20.5	17.1	7.0	0.52
MC-2010-Yc034	29.5	15.6	13.0	0.72
MC-2010-Yc035	21	12.1	11.7	0.81
MC-2010-Yc036	17.2	12.1	9.5	0.76
MC-2010-Yc037	22.3	19.2	13.2	0.74

Sample #	Long Axis "a" (cm)	Intermediate Axis "b" (cm)	Short Axis "c" (cm)	Maximum Projection Sphericity (Ψ_p)
MC-2010-Yc039	32.6	21.2	21.0	0.86
MC-2010-Yc040	44.7	34.9	28.6	0.81
MC-2011-IS02	7.0	6.4	4.1	0.72
MC-2011-IS03A	29.2	18.5	15.8	0.77
MC-2011-IS03B	14.3	7.7	4.6	0.58
MC-2011-IS05	8.5	6.1	3.7	0.64
MC-2011-IS06	7.4	6.5	4.0	0.69
MC-2011-IS08	15.6	7.1	6.3	0.71
MC-2011-IS10	15.1	12.2	10.1	0.82
MC-2011-IS11	10.2	7.1	7.0	0.88
MC-2011-IS12	8.0	5.2	5.1	0.86
			Average:	**0.71**

Dacite Accessory Lithic Clasts

Sample #	Long Axis "a" (cm)	Intermediate Axis "b" (cm)	Short Axis "c" (cm)	Maximum Projection Sphericity (Ψ_p)
MC-2010-PP01	11.9	10.4	8.0	0.80
MC-2010-PP02	5.6	4.9	4.2	0.86
MC-2010-PP03	9.0	7.6	7.6	0.95
MC-2010-PP04	7.2	6.7	6.4	0.95
MC-2010-PP05	11.6	10.2	7.5	0.78
MC-2010-PP06	6.2	4.9	4.3	0.85
MC-2010-PP07	8.0	5.5	3.8	0.69
MC-2010-PP08	12.6	9.8	8.0	0.80
MC-2010-PP09	7.3	5.7	4.2	0.75
MC-2010-PP10	20.3	16.0	14.9	0.88
MC-2010-PP11	12.6	10.6	6.9	0.71
MC-2010-PP12	5.5	3.3	3.2	0.83
MC-2010-PP13	6.8	4.9	4.2	0.81
MC-2010-PP14	17.1	14.5	13.0	0.88
MC-2011-P01	18.4	14.4	12.7	0.85
MC-2011-P02	13	7.7	5.7	0.69
MC-2011-P03	20.0	14.0	9.8	0.70
MC-2011-P04	12.2	11.9	7.7	0.74
MC-2011-P05	24.7	16.0	15.8	0.86
MC-2011-P06	9.1	7.7	7.0	0.89
MC-2011-P07	12.6	10.1	5.9	0.65
MC-2011-P08	13.0	11.5	7.0	0.69
MC-2011-P09	7.4	6.0	5.0	0.83
MC-2011-P10	11.4	6.8	6.7	0.83
MC-2011-P11	7.1	6.3	5.1	0.83
MC-2011-P12	9	7.6	6.2	0.83
MC-2011-P13	19.8	16.4	11.1	0.72
MC-2011-P14	10.5	9.3	7.9	0.86
MC-2011-P15	6.2	5.1	3.2	0.69
MC-2011-P16	6.6	5.4	2.8	0.60
MC-2011-P17	21.4	16.9	10.7	0.68
MC-2011-P18	7.6	5.5	5.5	0.90
MC-2011-P19	7.3	6	5.5	0.88
MC-2011-P20	6.6	5.1	3.6	0.73
MC-2012-PL01	38.1	34.4	23.4	0.75
MC-2012-PL02	31.3	23.5	22.6	0.89
MC-2012-PL03	30.9	19.5	16.8	0.78
MC-2012-PL04	18.8	16.2	14.8	0.90
MC-2012-PL06	25.3	19.4	16.6	0.82
			Average:	**0.80**

Appendix D3: Repeat Axis Measurements

Table D3-1. Repeat axis measurements on select lithic samples.

Sample #	Repeat #	Long Axis "a" (cm)	Intermediate Axis "b" (cm)	Short Axis "c" (cm)
MC-2010-Yb005	1	7.6	7.2	5.0
MC-2010-Yb005	2	7.6	7.1	5.0
MC-2010-Yb005	3	7.6	7.1	5.0
Max. Variance of Repeats (cm):		*0.0*	*0.1*	*0.0*
Max. Variance of Repeats (%):		*0.0*	*1.4*	*0.0*
MC-2010-Yb037	1	15.4	7.7	6.2
MC-2010-Yb037	2	15.4	7.7	6.3
MC-2010-Yb037	3	15.4	7.7	6.3
Max. Variance of Repeats (cm):		*0.0*	*0.0*	*0.1*
Max. Variance of Repeats (%):		*0.0*	*0.0*	*1.6*
MC-2010-Yc003	1	16.3	12.1	10.3
MC-2010-Yc003	2	16.4	11.7	10.7
MC-2010-Yc003	3	16.4	12.0	10.6
Max. Variance of Repeats (cm):		*0.1*	*0.4*	*0.4*
Max. Variance of Repeats (%):		*0.6*	*3.4*	*3.8*
MC-2010-Yc004	1	17.9	11.9	11.5
MC-2010-Yc004	2	17.7	11.9	11.1
MC-2010-Yc004	3	18.0	11.9	11.1
Max. Variance of Repeats (cm):		*0.3*	*0.0*	*0.4*
Max. Variance of Repeats (%):		*1.7*	*0.0*	*3.6*
MC-2010-Yc009	1	17.9	16.2	10.1
MC-2010-Yc009	2	17.9	16.3	10.6
MC-2010-Yc009	3	17.9	16.2	10.1
Max. Variance of Repeats (cm):		*0.0*	*0.1*	*0.5*
Max. Variance of Repeats (%):		*0.0*	*0.6*	*4.9*

Appendix E: Image Analysis

Appendix E1: Image Analysis Photographs

Monzogranite Accessory Lithics

Figure E1-1. Monzogranite accessory lithic samples aligned such that their short axes are vertical. Photos on the left are the originals, while photos on the right are the sample outlines in black and white, created using Adobe Photoshop. The circle in the middle of each photo is a 40 mm diameter standard.

a) IMG_0708.jpg. CW from bottom left: MC-2011-IS06, MC-2011-IS07, MC-2011-IS08, MC-2011-IS02, MC-2011-IS04, MC-2011-IS05.
b) IMG_0709.jpg. CW from bottom left: MC-2011-IS10, MC-2011-IS11, MC-2011-IS12, MC-2011-IS09.
c) IMG_0710.jpg. CW from bottom left: MC-2010-Yb005, MC-2010-Yb006, MC-2010-Yb007, MC-2010-Yb008, MC-2010-Yb001, MC-2010-Yb002, MC-2010-Yb003, MC-2010-Yb004.
d) IMG_0711.jpg. CW from bottom left: MC-2010-Yb015, MC-2010-Yb016, MC-2010-Yb017, MC-2010-Yb019, MC-2010-Yb009, MC-2010-Yb010, MC-2010-Yb013.

Figure E1-2. Monzogranite accessory lithic samples aligned such that their short axes are vertical. Photos on the left are the originals, while photos on the right are the sample outlines in black and white, created using Adobe Photoshop. The circle in the middle of each photo is a 40 mm diameter standard.

a) IMG_0712.jpg. CW from bottom left: MC-2010-Yb025, MC-2010-Yb026, MC-2010-Yb027, MC-2010-Yb029, MC-2010-Yb020, MC-2010-Yb022, MC-2010-Yb023.

b) IMG_0713.jpg. CW from bottom left: MC-2010-Yb033, MC-2010-Yb024, MC-2010-Yb035, MC-2010-Yb039, MC-2010-Yb024, MC-2010-Yb030, MC-2010-Yb031, MC-2010-Yb032.

c) IMG_0719.jpg. CW from bottom left: MC-2010-Yc012, MC-2010-Yc026, MC-2010-Yc025, MC-2010-Yc018.

d) IMG_0720.jpg. Left to right: MC-2010-Yc019, MC-2010-Yc008.

Figure E1-3. Monzogranite accessory lithic samples aligned such that their short axes are vertical. Photos on the left are the originals, while photos on the right are the sample outlines in black and white, created using Adobe Photoshop. The circle in the middle of each photo is a 40 mm diameter standard.

a) IMG_0721.jpg. CW from bottom left: MC-2010-Yc003, MC-2010-Yc010, MC-2010-Yc014.
b) IMG_0722.jpg. CW from bottom left: MC-2010-Yc027, MC-2010-Yc021, MC-2010-Yc002.
c) IMG_0723.jpg. CW from bottom left: MC-2010-Yc007, MC-2010-Yc006, MC-2010-Yc001.
d) IMG_0724.jpg. CW from bottom left: MC-2010-Yc022, MC-2010-Yc023, MC-2010-Yc009.
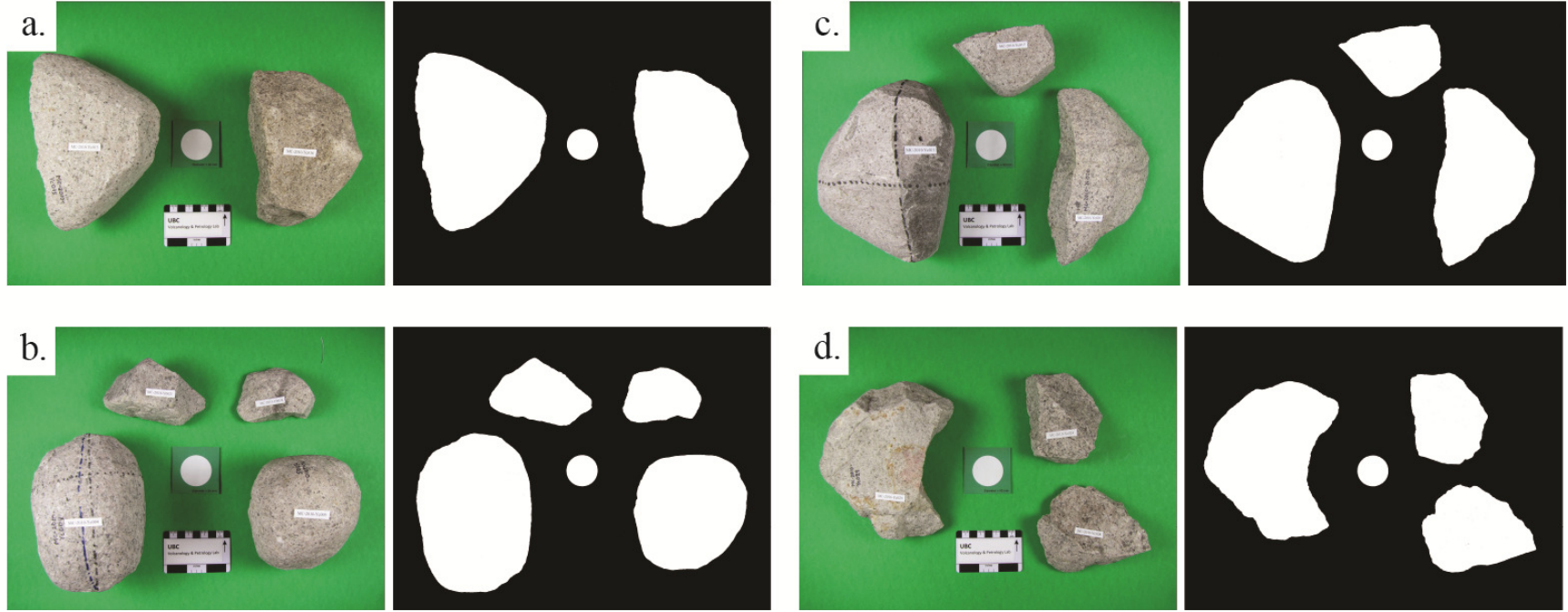
Figure E1-4. Monzogranite accessory lithic samples aligned such that their short axes are vertical. Photos on the left are the originals, while photos on the right are the sample outlines in black and white, created using Adobe Photoshop. The circle in the middle of each photo is a 40 mm diameter standard.

a) IMG_0725.jpg. Left to right: MC-2010-Yc015, MC-2010-Yc016.
b) IMG_0726.jpg. CW from bottom left: MC-2010-Yc004, MC-2010-Yb021, MC-2010-Yb028, MC-2010-Yc005.
c) IMG_0727.jpg. CW from bottom left: MC-2010-Yc013, MC-2010-Yc017, MC-2010-Yc020.
d) IMG_0728.jpg. CW from bottom left: MC-2010-Yc029, MC-2010-Yc024, MC-2010-Yc028.
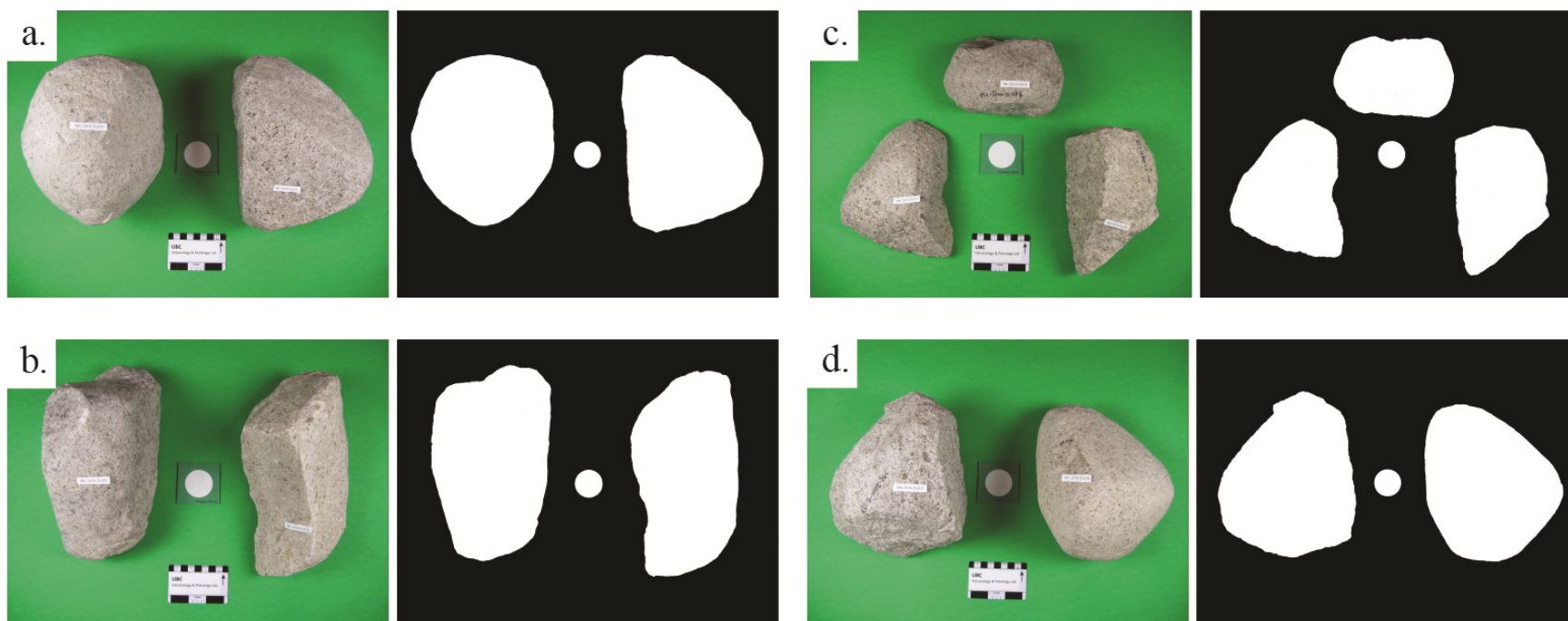
Figure E1-5. Monzogranite accessory lithic samples aligned such that their short axes are vertical. Photos on the left are the originals, while photos on the right are the sample outlines in black and white, created using Adobe Photoshop. The circle in the middle of each photo is a 40 mm diameter standard.

a) IMG_0729.jpg. Left to right: MC-2010-Yc030, MC-2010-Yc031.
b) IMG_0730.jpg. CW from bottom left: MC-2010-Yc032, MC-2010-Yc034.
c) IMG_0731.jpg. Left to right: MC-2010-Yc033, MC-2010-Yc036, MC-2010-Yc035.
d) IMG_0732.jpg. Left to right: MC-2010-Yc037; MC-2010-Yc038.
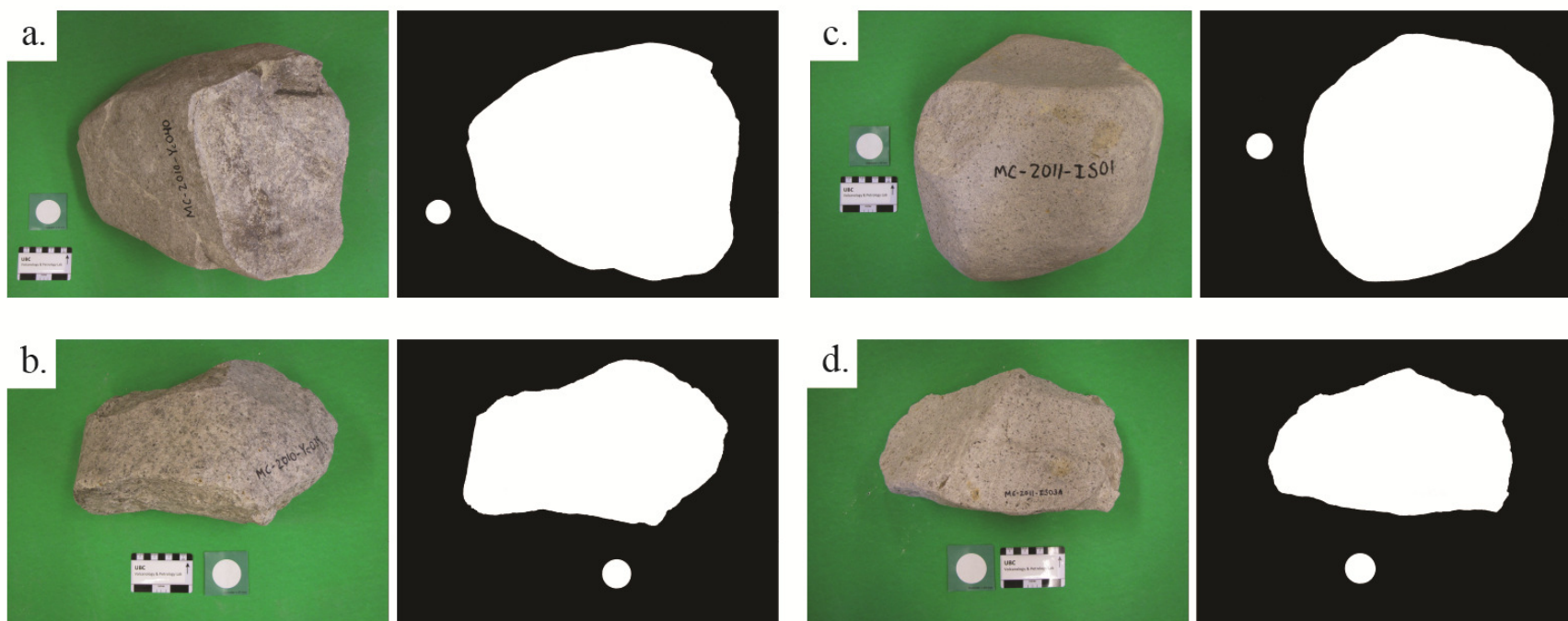
Figure E1-6. Monzogranite accessory lithic samples aligned such that their short axes are vertical. Photos on the left are the originals, while photos on the right are the sample outlines in black and white, created using Adobe Photoshop. The circle in the middle of each photo is a 40 mm diameter standard.

a) IMG_0739.jpg. MC-2010-Yc040.
b) IMG_0746.jpg. MC-2010-Yc039.
c) IMG_0747.jpg. MC-2011-IS01.
d) IMG_0751.jpg. MC-2011-IS03A.
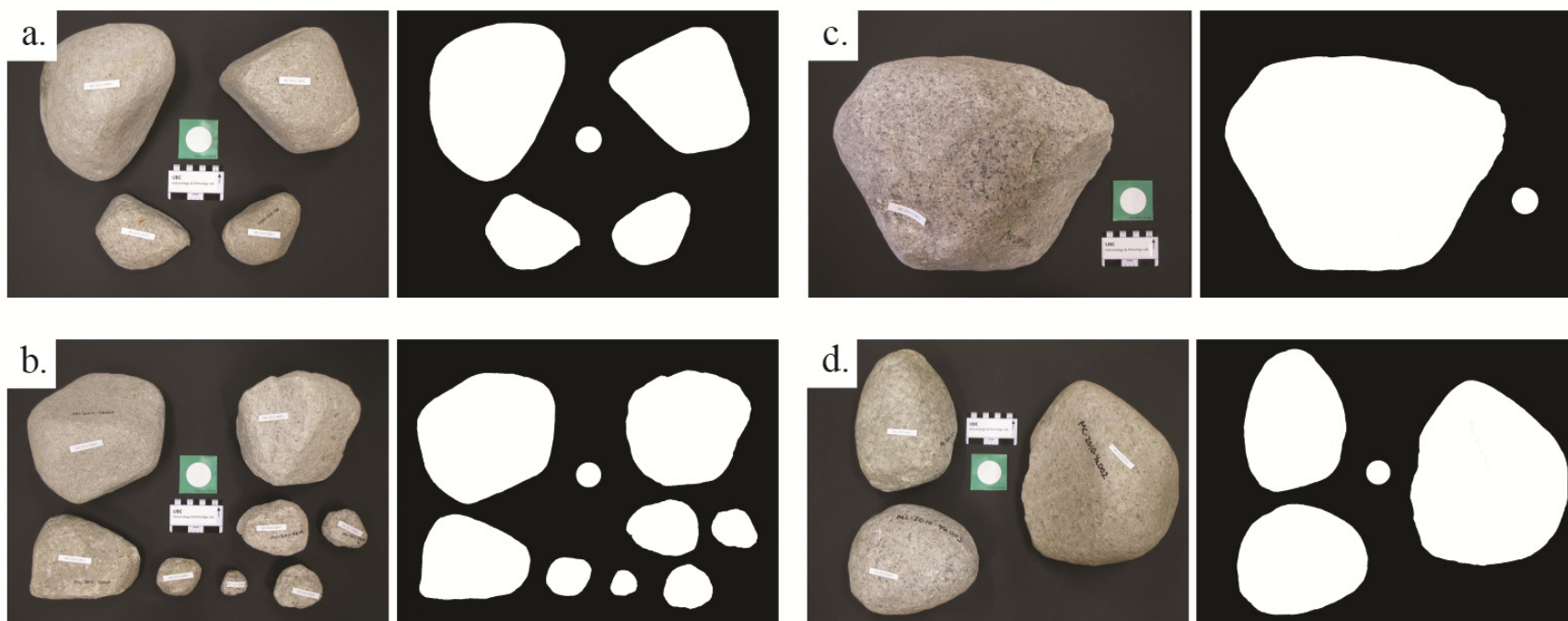
Figure E1-7. Monzogranite accessory lithic samples aligned such that their short axes are vertical. Photos on the left are the originals, while photos on the right are the sample outlines in black and white, created using Adobe Photoshop. The circle in the middle of each photo is a 40 mm diameter standard.

a) IMG_0790.jpg. CW from bottom left: MC-2012-Yd012, MC-2012-Yd001, MC-2012-Yd002, MC-2012-Yd011.
b) IMG_0791.jpg. CW from bottom left: MC-2012-Yd010, MC-2012-Yd003, MC-2012-Yd004, MC-2012-Yd005, MC-2012-Yd006, MC-2012-Yd007, MC-2012-Yd008, MC-2012-Yd009.
c) IMG_0793.jpg. MC-2012-Yd013.
d) IMG_0797.jpg. CW from bottom left: MC-2010-Ya003, MC-2010-Ya001, MC-2010-Ya002.
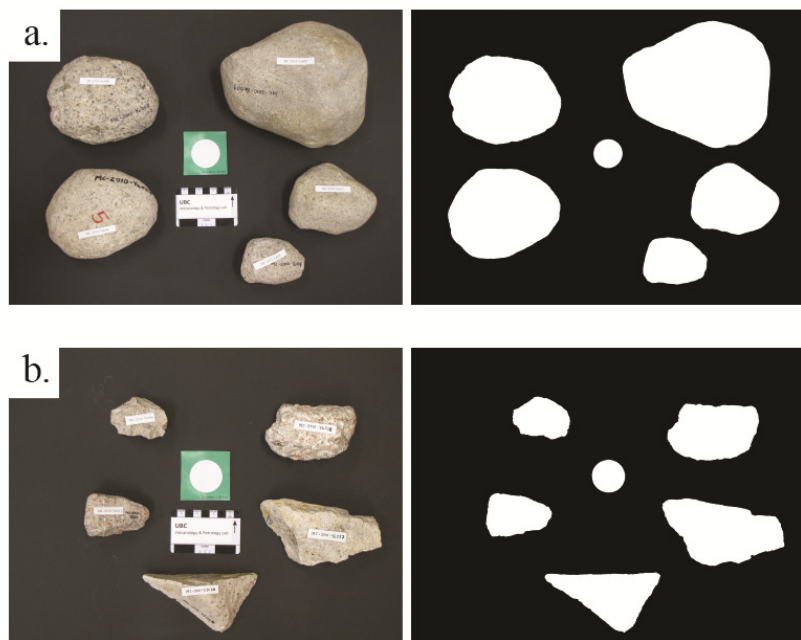
Figure E1-8. Monzogranite accessory lithic samples aligned such that their short axes are vertical. Photos on the left are the originals, while photos on the right are the sample outlines in black and white, created using Adobe Photoshop. The circle in the middle of each photo is a 40 mm diameter standard.

a) IMG_0790.jpg. CW from bottom left: MC-2010-Ya004, MC-2010-Ya008, MC-2010-Ya009, MC-2010-Ya010, MC-2010-Ya014.
b) IMG_0791.jpg. CW from bottom left: MC-2011-IS03B, MC-2010-Yb011, MC-2010-Yb036, MC-2010-Yb038, MC-2010-Ya037.
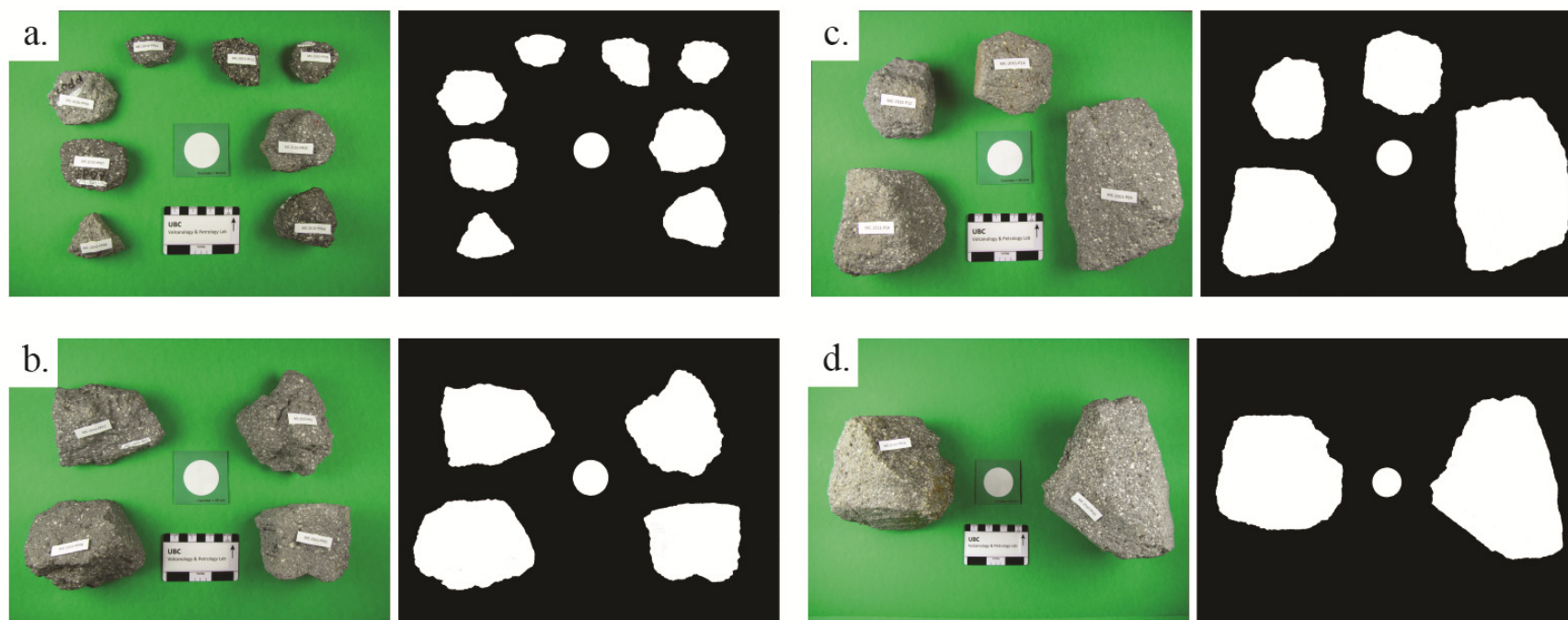
Figure E1-9. Dacite accessory lithic samples aligned such that their short axes are vertical. Photos on the left are the originals, while photos on the right are the sample outlines in black and white, created using Adobe Photoshop. The circle in the middle of each photo is a 40 mm diameter standard.

a) IMG_0699.jpg. CW from bottom left: MC-2011-PP06, MC-2010-PP07, MC-2010-PP09, MC-2010-PP12, MC-2010-PP13, MC-2010-PP02, MC-2010-PP03, MC-2010-PP04.
b) IMG_0701.jpg. CW from bottom left: MC-2010-PP08, MC-2010-PP11, MC-2010-PP01, MC-2010-PP05.
c) IMG_0702.jpg. CW from bottom left: MC-2011-P04, MC-2011-P12, MC-2011-P14, MC-2011-P03.
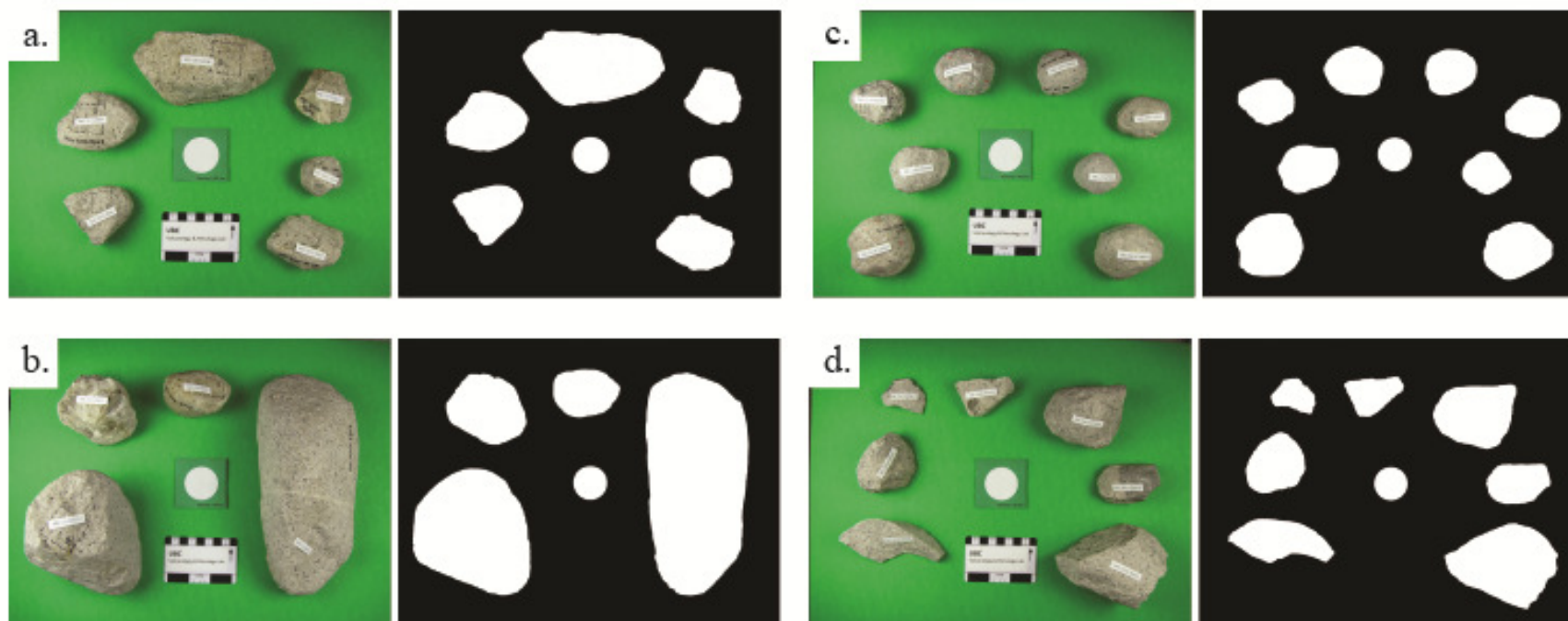d) IMG_0704.jpg. Left to right: MC-2010-PP14, MC-2010-PP10.
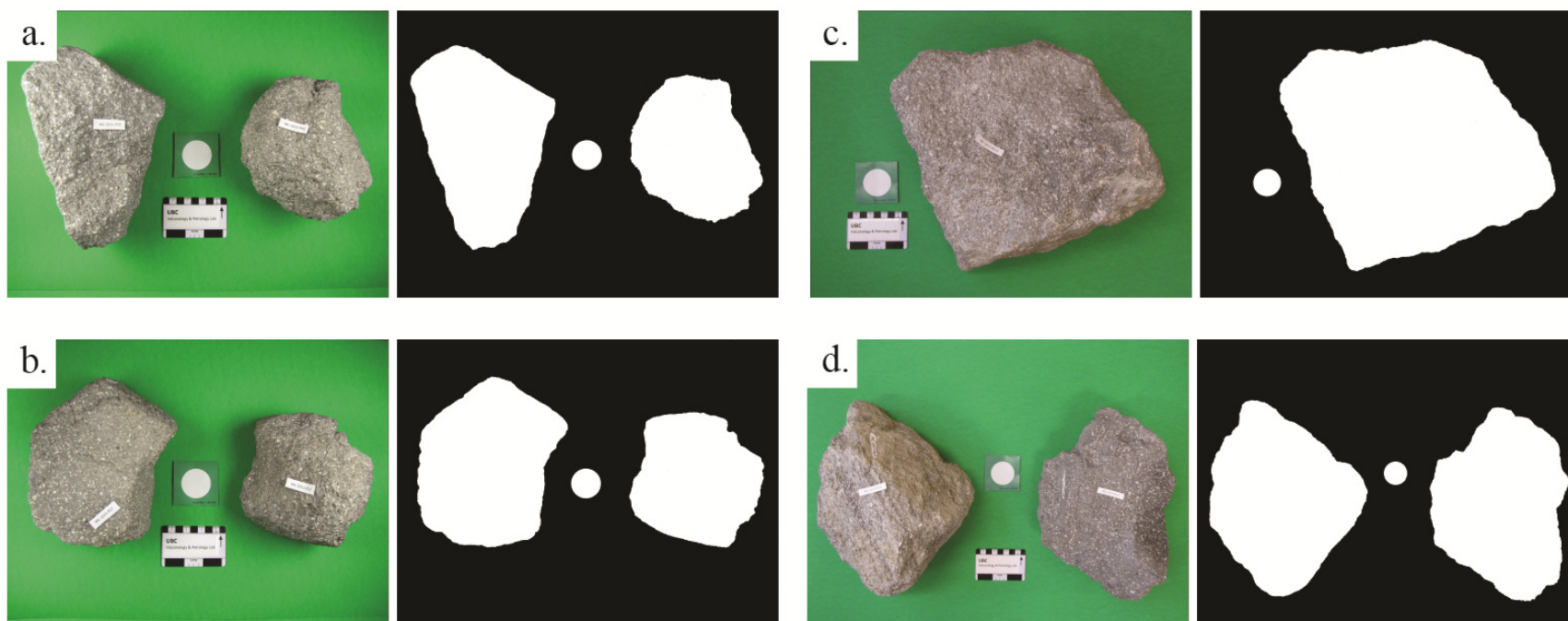
Figure E1-10. Dacite accessory lithic samples aligned such that their short axes are vertical. Photos on the left are the originals, while photos on the right are the sample outlines in black and white, created using Adobe Photoshop. The circle in the middle of each photo is a 40 mm diameter standard.

a) IMG_0705.jpg. Left to right: MC-2011-P05, MC-2011-P01.
b) IMG_0706.jpg. Left to right: MC-2011-P17, MC-2011-P13.
c) IMG_0800.jpg. MC-2012-PL02.
d) IMG_0801.jpg. Left to right: MC-2012-PL02, MC-2012-PL03.
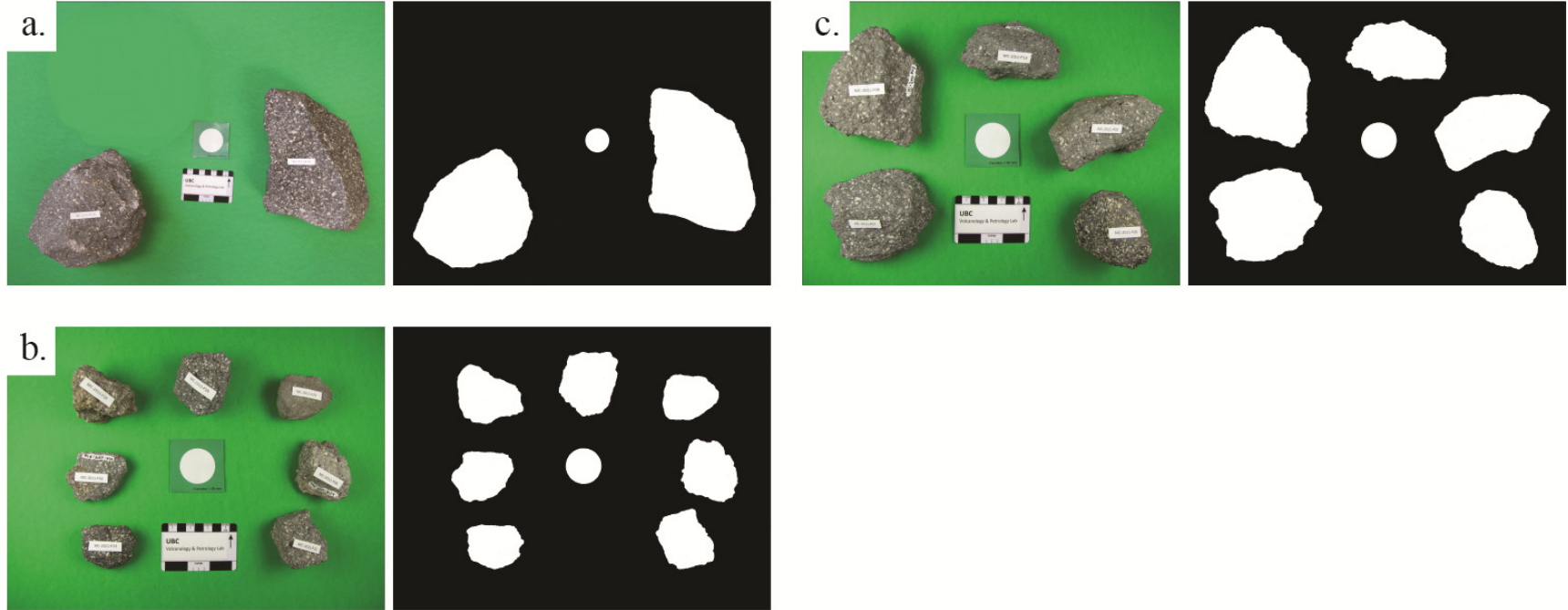
Figure E1-11. Dacite accessory lithic samples aligned such that their short axes are vertical. Photos on the left are the originals, while photos on the right are the sample outlines in black and white, created using Adobe Photoshop. The circle in the middle of each photo is a 40 mm diameter standard.

a) IMG_0802.jpg. Left to right: MC-2012-PL04, MC-2012-PL06.
b) IMG_0695.jpg. CW from bottom left: MC-2011-P15, MC-2011-P16, MC-2011-P18, MC-2011-P19, MC-2011-P20, MC-2011-P09, MC-2011-P11.
c) IMG_0698.jpg. CW from bottom left: MC-2011-P07, MC-2011-P08, MC-2011-P10, MC-2011-P02, MC-2011-P06.

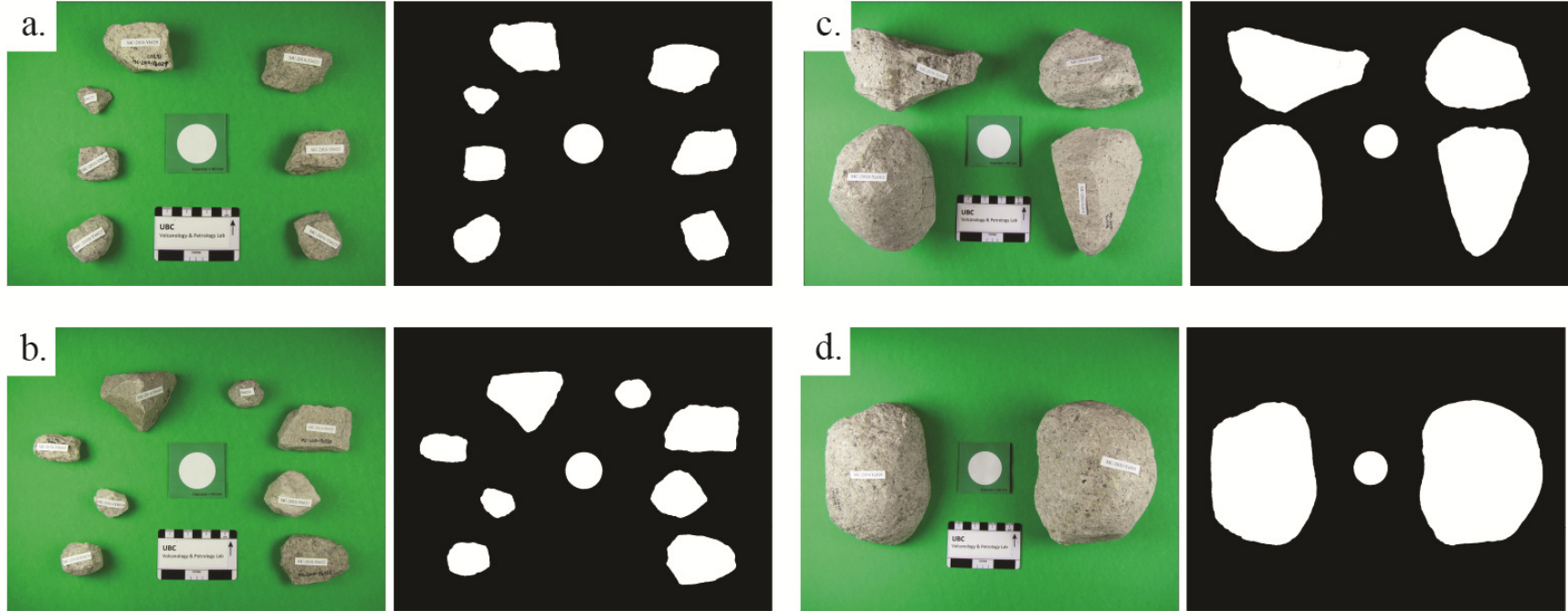*Supplementary small volume sample set monzogranite clasts*
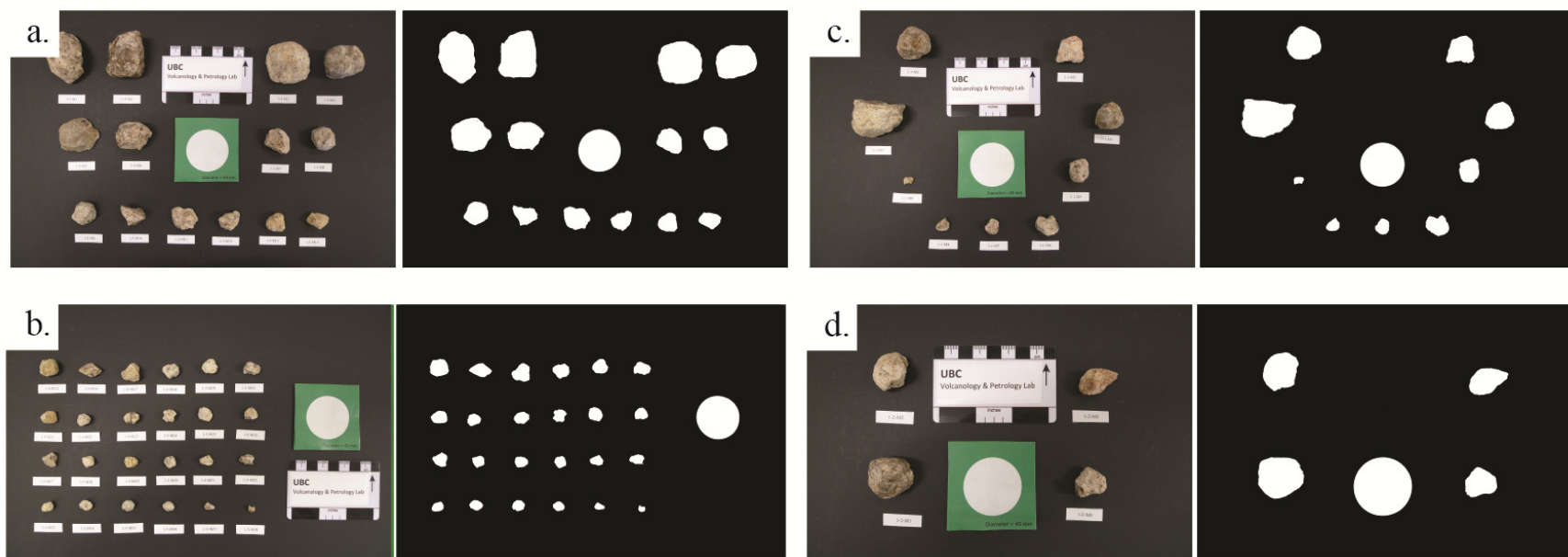
Figure E1-12. Monzogranite accessory lithic samples aligned such that their short axes are vertical. Photos on the left are the originals, while photos on the right are the sample outlines in black and white, created using Adobe Photoshop. The circle in the middle of each photo is a 40 mm diameter standard.

a) P1060581.jpg. Left to right, top to bottom: 1-5-M1, 1-5-M2, 1-5-M3, 1-5-M4, 1-5-M5, 1-5-M6, 1-5-M7, 1-5-M8, 1-5-M9, 1-5-M10, 1-5-M11, 1-5-M12, 1-5-M13, 1-5-M14.
b) P1060579.jpg. Left to right, top to bottom: 1-5-M15, 1-5-M16, 1-5-M17, 1-5-M18, 1-5-M19, 1-5-M20, 1-5-M21, 1-5-M22, 1-5-M23, 1-5-M24, 1-5-M25, 1-5-M26, 1-5-M27, 1-5-M28, 1-5-M29, 1-5-M30, 1-5-M31, 1-5-M32, 1-5-M33, 1-5-M34, 1-5-M35, 1-5-M36, 1-5-M37, 1-5-M38.
c) P1060582.jpg. CW from far left: 1-1-M1, 1-1-M2, 1-1-M3, 1-1-M4, 1-1-M5, 1-1-M6, 1-1-M7, 1-1-M8, 1-1-M9.
d) P1060583.jpg. CW from bottom left: 1-2-M1, 1-2-M2, 1-2-M3, 1-2-M4:
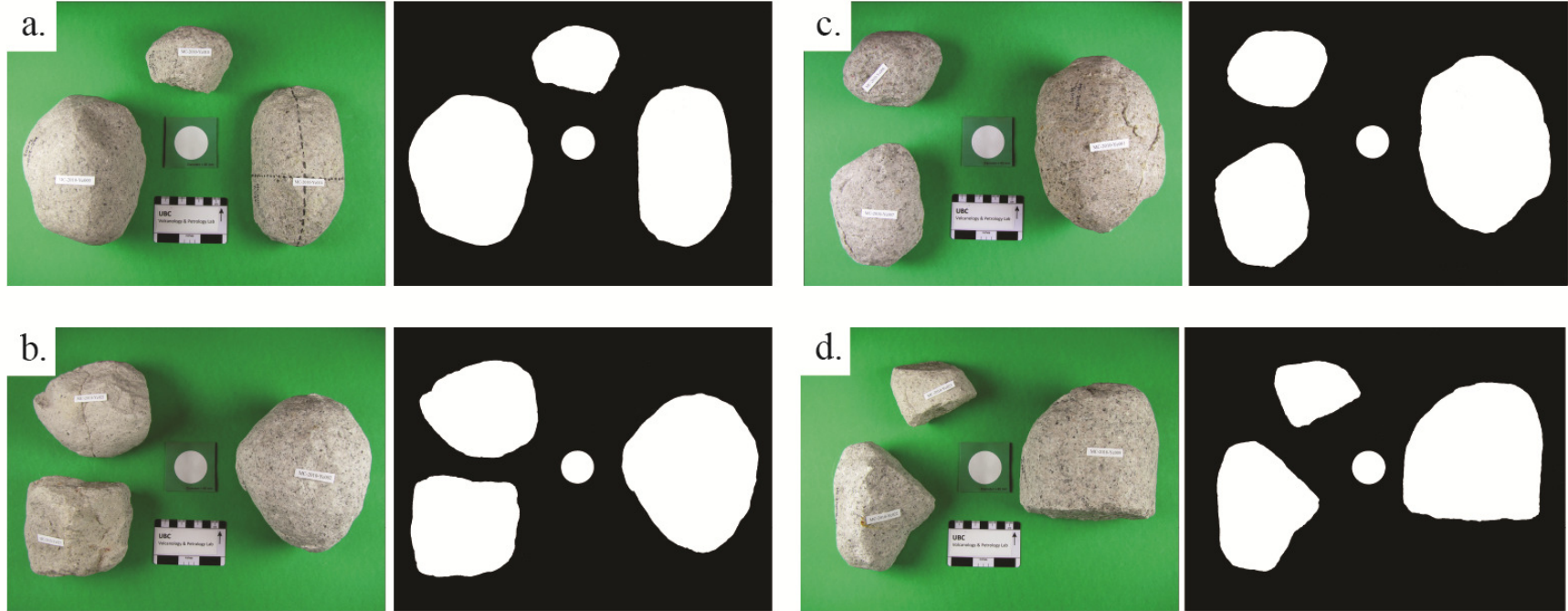
Supplementary small volume sample set dacite clasts
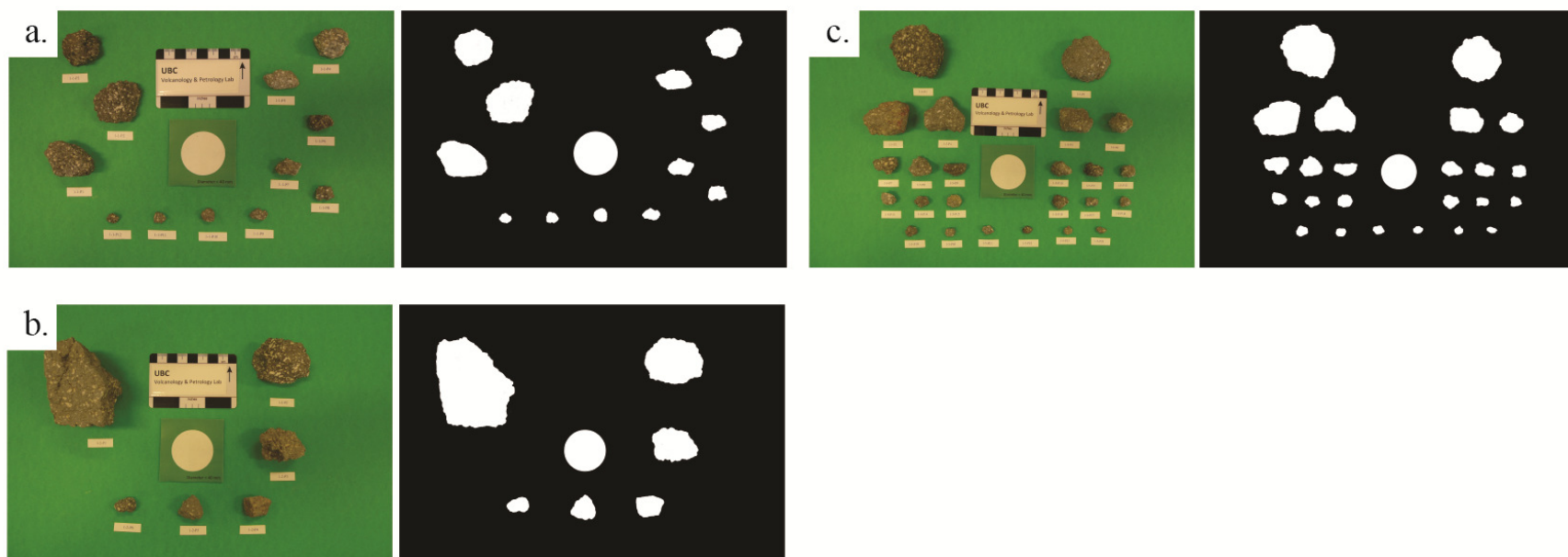
Figure E1-13. Dacite accessory lithic samples aligned such that their short axes are vertical. Photos on the left are the originals, while photos on the right are the sample outlines in black and white, created using Adobe Photoshop. The circle in the middle of each photo is a 40 mm diameter standard.

a) P1060584.jpg. CW from top left: 1-1-P3, 1-1-P4, 1-1-P5, 1-1-P6, 1-1-P7, 1-1-P8, 1-1-P9, 1-1-P10, 1-1-P11, 1-1-P12, 1-1-P1, 1-1-P2.
b) P1060586.jpg. CW from top left: 1-2-P1, 1-2-P2, 1-2-P3, 1-2-P4, 1-2-P5, 1-2-P6.
c) P1060587.jpg. Left to right, top to bottom: 1-5-P1, 1-5-P2, 1-5-P3, 1-5-P4, 1-5-P5, 1-5-P6, 1-5-P7, 1-5-P8, 1-5-P9, 1-5-P10, 1-5-P11, 1-5-P12, 1-5-P13, 1-5-P14, 1-5-P15, 1-5-P16, 1-5-P17, 1-5-P18, 1-5-P19, 1-5-P20, 1-5-P21, 1-5-P22, 1-5-P23, 1-5-P24.

Appendix E2: Image Analysis Matlab Script

```
%%% ROCK SHAPE ANALYSIS PROJECT %%%
% By: Michelle E. Campbell
% June 2011


%%%%%%%%%%%%%%%%%%%%%%%%%%%%%
% Part 2: 2D Image Analysis %
%%%%%%%%%%%%%%%%%%%%%%%%%%%%%


% Based on Matlab script from "Manga, M., A. Patel, and J. Dufek. 2011.
% Rounding of pumice clasts during transport: field measurements and
% laboratory studies. Bulletin of Volcanology, vol. 73, 321-333."


%*************************************************************************
% NECESSARY INPUT: You must first copy the image you want to analyze into *
% the Matlab folder containing this script, and then change the filename  *
% on line 27 to the filename of this image.                               *
%*************************************************************************


%% Step 1: Read image of lithic samples

% Note: Samples should be photographed against a dark background, and well
% lit, as to minimize the presence of shadows in the photo. Multiple
% samples may be photographed together.

% Input filename in single quotation marks, e.g. 'filename.jpg'
RGB = imread('IMAGENAME.jpg');
imshow(RGB);


%% Step 2: Prepare image for analysis

% Convert imported image to grayscale:
GRAY = rgb2gray(RGB);
% Black and white threshold of 0.4:
threshold = .24;
% Convert image to black and white:
bw = im2bw(GRAY,threshold);
imshow(bw);


% Use every 3rd pixel of the shape boundaries for the perimeter calculation
% (appears to provide truest estimate of perimeter):
s_wavelength=3;


% Remove the noise from the image, by deleting all of the "specks" on the
% image which do not belong the samples of interest (<10000 pixels):
bw = bwareaopen(bw,1000);


% Fill in any holes within the samples' boundaries:
bw = imfill(bw,'holes');


%% Step 3: Trace the boundaries of the lithic samples

[B,L,NumberOfObjects] = bwboundaries(bw,'noholes');
```

```
% Option to display number of detected objects:
NumberOfObjects;

% Display image with a grayish background ([.5 .6 .6]), where the
% samples are shown coloured according the the 'summer' colour map, and
% outlined with a white line of width 2:
imshow(label2rgb(L, @summer, [.5 .6 .6]))
hold on
for k = 1:length(B)
boundary = B{k};
plot(boundary(:,2), boundary(:,1), 'w', 'LineWidth', 2)
end

%% Step 4: Calculate properties of samples' images

% Note: the circular standard is 40mm across

stats =
regionprops(L,'Area','Centroid','MajorAxisLength','MinorAxisLength','Convex
Area');

for k = 1:length(B)
boundary = B{k};
A = size(boundary);
boundary2 = boundary(s_wavelength:s_wavelength:A(1,1),:);
delta_sq = diff(boundary2).^2;
perimeter = sum(sqrt(sum(delta_sq,2)));
area2 = stats(k).Area;
area = polyarea(boundary2(:,1),boundary2(:,2));
% Metric for roundness: 4*pi*area/perimeter^2, which = 1 for a circle, and
% which < 1 for any other shape:
metric = 4*pi*area/perimeter^2;
metric_string = sprintf('%2.2f',perimeter);
metric_string2 = sprintf('%2.2f',stats(k).MajorAxisLength);
metric_string3 = sprintf('%2.2f',stats(k).MinorAxisLength);
metric_string4 = sprintf('%2.2f',stats(k).Area);
metric_string5 = sprintf('%2.2f',stats(k).ConvexArea);
metric_string6 = sprintf('%2.2f',metric);

% Put title and legend on figure:
figure(1)
title('Roundness, Perimeter Major Axis and Minor Axis of Perfect
Ellipses','FontSize',14,'FontWeight','bold')
% Insert text box with sample set name:
figure(1)
legend('\fontsize{11}\color(Blackwelder)Perimeter',...
    '\fontsize{11}\color{blue}Major Axis Length',...
    '\fontsize{11}\color{cyan}Minor Axis Length',...
    '\fontsize{11}\color{magenta}Area',...
    '\fontsize{11}\color{red}Convex Area',...
    '\fontsize{11}\color(Blackwelder)Circularity Metric',...
    'Location','SouthOutside');

text(boundary(1,2)-80,boundary(1,1)+0,metric_string,'Color','k',...
'FontSize',12,'FontWeight','bold');
```

```
text(boundary(1,2)-80,boundary(1,1)+30,metric_string2,'Color','blue',...
'FontSize',12,'FontWeight','bold');
text(boundary(1,2)-80,boundary(1,1)+60,metric_string3,'Color','c',...
'FontSize',12,'FontWeight','bold');
text(boundary(1,2)-80,boundary(1,1)+90,metric_string4,'Color','magenta',...
'FontSize',12,'FontWeight','bold');
text(boundary(1,2)-80,boundary(1,1)+120,metric_string5,'Color','r',...
'FontSize',12,'FontWeight','bold');
text(boundary(1,2)-80,boundary(1,1)+150,metric_string6,'Color','k',...
'FontSize',12,'FontWeight','bold');

end
```

Appendix E3: Image Analysis Data

Table E3-1. Image analysis data for main monzogranite and dacite accessory lithic clast sample set.

Sample #	Image (.jpg)	Volume (Wet-Dry) (cm³)	Perimeter (pixels)	Long Axis (pixels)	Short Axis (pixels)	Area (pixels)	Convex Hull Area (pixels)	Circularity C	Ellipticity E	Convexity C_vx
Intact Monzogranite Accessory Lithic Clasts: Main Sample Set										
MC-2010-Ya001	IMG_0797	2470	2912	1047	752	613282	616846	0.91	0.98	0.99
MC-2010-Ya002	IMG_0797	6769	4068	1345	1160	1209747	1220152	0.92	0.97	0.99
MC-2010-Ya003	IMG_0797	2483	2868	979	802	613383	616870	0.94	0.98	0.99
MC-2010-Ya004	IMG_0798	675	2317	801	633	396492	399260	0.93	0.98	0.99
MC-2010-Ya008	IMG_0798	644	2352	800	631	394913	399703	0.90	0.96	0.99
MC-2010-Ya009	IMG_0798	1866	3191	1073	872	720979	728028	0.89	0.96	0.99
MC-2010-Ya010	IMG_0798	377	1814	625	488	235878	239209	0.90	0.97	0.99
MC-2010-Ya014	IMG_0798	177	1331	468	345	124880	126759	0.89	0.97	0.99
MC-2010-Yb001	IMG_0710	83	1171	387	339	102455	103542	0.94	0.97	0.99
MC-2010-Yb002	IMG_0710	69	1175	411	310	99818	101238	0.91	0.97	0.99
MC-2010-Yb003	IMG_0710	60	1051	348	299	81211	82156	0.92	0.97	0.99
MC-2010-Yb004	IMG_0710	161	1487	512	399	159279	161047	0.91	0.97	0.99
MC-2010-Yb005	IMG_0710	129	1576	500	464	181456	184658	0.92	0.96	0.98
MC-2010-Yb006	IMG_0710	90	1319	464	341	123131	125252	0.89	0.96	0.98
MC-2010-Yb007	IMG_0710	79	1209	414	323	104351	106121	0.90	0.96	0.98
MC-2010-Yb008	IMG_0710	105	1289	442	358	124240	125646	0.94	0.98	0.99
MC-2010-Yb009	IMG_0711	263	1828	617	474	222171	227054	0.84	0.94	0.98
MC-2010-Yb011	IMG_0799	97	1336	485	305	111521	114842	0.78	0.94	0.97
MC-2010-Yb024	IMG_0713	15	767	260	216	43918	44558	0.94	0.98	0.99
MC-2010-Yb034	IMG_0713	12	759	263	199	40627	41826	0.89	0.96	0.97
MC-2010-Yb035	IMG_0713	23	996	374	217	63037	65090	0.80	0.95	0.97
MC-2010-Yc001	IMG_0723	1565	3725	1302	981	999286	1012590	0.91	0.97	0.99
MC-2010-Yc002	IMG_0722	1488	3463	1148	972	869075	877834	0.91	0.96	0.99
MC-2010-Yc003	IMG_0721	1048	3337	1127	914	805827	813101	0.91	0.96	0.99
MC-2010-Yc004	IMG_0726	1262	3404	1213	878	832877	839864	0.90	0.97	0.99
MC-2010-Yc005	IMG_0726	1180	2800	918	816	585128	589458	0.94	0.97	0.99
MC-2010-Yc006	IMG_0723	378	2152	744	572	332761	335517	0.90	0.96	0.99
MC-2010-Yc007	IMG_0723	581	2648	921	701	502149	508131	0.90	0.97	0.99
MC-2010-Yc008	IMG_0720	1099	3371	1111	935	807806	819152	0.89	0.96	0.99

Sample #	Image (.jpg)	Volume (Wet-Dry) (cm³)	Perimeter (pixels)	Long Axis (pixels)	Short Axis (pixels)	Area (pixels)	Convex Hull Area (pixels)	Circularity C	Ellipticity E	Convexity C_{vx}
MC-2010-Yc013	IMG_0727	1980	3846	1327	1015	1030540	1038572	0.88	0.96	0.99
MC-2010-Yc021	IMG_0722	593	2590	865	716	481104	486417	0.90	0.96	0.99
MC-2010-Yc025	IMG_0719	373	2290	776	584	351937	357226	0.84	0.94	0.99
MC-2010-Yc030	IMG_0729	3206	3714	1253	1051	1031005	1036604	0.94	0.98	0.99
MC-2010-Yc038	IMG_0732	2640	3468	1188	948	867885	872421	0.91	0.97	0.99
MC-2011-IS01	IMG_0747	15973	5986	1966	1715	2638186	2652503	0.93	0.97	0.99
MC-2011-IS04	IMG_0708	35	1011	325	292	74022	75771	0.91	0.96	0.98
MC-2011-IS07	IMG_0708	104	1685	595	420	193505	197964	0.86	0.95	0.98
MC-2011-IS09	IMG_0709	1418	4130	1697	778	1020068	1033087	0.75	0.97	0.99
MC-2012-Yd001	IMG_0790	3264	3477	1228	926	878209	881644	0.91	0.98	1.00
MC-2012-Yd002	IMG_0790	2596	3062	1010	849	650317	655158	0.87	0.96	0.99
MC-2012-Yd003	IMG_0791	2542	3188	1082	893	754694	758566	0.93	0.98	0.99
MC-2012-Yd004	IMG_0791	1940	2885	937	835	609326	617466	0.92	0.97	0.99
MC-2012-Yd005	IMG_0791	363	1543	535	406	168895	171104	0.89	0.96	0.99
MC-2012-Yd006	IMG_0791	99	1025	350	273	74174	75493	0.89	0.96	0.98
MC-2012-Yd007	IMG_0791	141	1114	361	322	90603	92122	0.92	0.96	0.98
MC-2012-Yd008	IMG_0791	27	626	201	185	28799	29422	0.92	0.97	0.98
MC-2012-Yd009	IMG_0791	119	997	337	285	75055	75836	0.95	0.98	0.99
MC-2012-Yd010	IMG_0791	886	2417	837	632	403256	407626	0.87	0.96	0.99
MC-2012-Yd011	IMG_0790	405	1757	641	439	218006	220081	0.89	0.97	0.99
MC-2012-Yd012	IMG_0790	466	1958	674	504	260372	264302	0.85	0.95	0.99
MC-2012-Yd013	IMG_0793	12307	5980	1985	1630	2489814	2516680	0.87	0.95	0.99
							Mean:	**0.90**	**0.96**	**0.99**
							1σ:	**0.04**	**0.01**	**0.01**
							Max.:	**0.95**	**0.98**	**1.00**
							Min.:	**0.75**	**0.94**	**0.97**

Broken Monzogranite Accessory Lithic Clasts: Main Sample Set

Sample #	Image (.jpg)	Volume (Wet-Dry) (cm³)	Perimeter (pixels)	Long Axis (pixels)	Short Axis (pixels)	Area (pixels)	Convex Hull Area (pixels)	Circularity C	Ellipticity E	Convexity C_{vx}
MC-2010-Yb010	IMG_0711	89	1293	481	303	113131	115647	0.85	0.97	0.98
MC-2010-Yb013	IMG_0711	368	2303	787	566	338730	347758	0.80	0.93	0.97
MC-2010-Yb015	IMG_0711	70	1857	762	295	167254	185744	0.61	0.94	0.90
MC-2010-Yb016	IMG_0711	104	1414	473	392	143986	146160	0.91	0.96	0.99
MC-2010-Yb017	IMG_0711	14	973	334	232	57419	61566	0.76	0.92	0.93
MC-2010-Yb019	IMG_0711	38	1209	426	275	84036	87751	0.72	0.92	0.96
MC-2010-Yb020	IMG_0712	56	1485	524	359	145609	150789	0.83	0.94	0.97

Sample #	Image (.jpg)	Volume (Wet-Dry) (cm^3)	Perimeter (pixels)	Long Axis (pixels)	Short Axis (pixels)	Area (pixels)	Convex Hull Area (pixels)	Circularity C	Ellipticity E	Convexity C_{vx}
MC-2010-Yb021	IMG_0726	230	1980	732	439	243433	250482	0.78	0.94	0.97
MC-2010-Yb022	IMG_0712	52	1402	508	321	125233	129008	0.80	0.94	0.97
MC-2010-Yb023	IMG_0712	30	1183	386	322	96344	98826	0.86	0.94	0.97
MC-2010-Yb025	IMG_0712	30	1146	387	299	89780	92198	0.86	0.94	0.97
MC-2010-Yb026	IMG_0712	19	1047	333	280	71980	73823	0.83	0.92	0.98
MC-2010-Yb027	IMG_0712	6	745	252	191	36395	38046	0.82	0.94	0.96
MC-2010-Yb028	IMG_0726	146	1658	591	406	182687	189185	0.83	0.95	0.97
MC-2010-Yb029	IMG_0712	75	1578	542	380	157171	163143	0.79	0.92	0.96
MC-2010-Yb030	IMG_0713	61	1652	591	370	167305	172920	0.77	0.93	0.97
MC-2010-Yb031	IMG_0713	47	1183	389	334	100923	102485	0.91	0.96	0.98
MC-2010-Yb032	IMG_0713	54	1497	522	369	149195	152313	0.84	0.94	0.98
MC-2010-Yb033	IMG_0713	27	955	328	254	65029	66255	0.90	0.96	0.98
MC-2010-Yb036	IMG_0799	43	1190	417	285	91914	95759	0.82	0.93	0.96
MC-2010-Yb037	IMG_0799	287	2322	871	438	282936	298095	0.66	0.91	0.95
MC-2010-Yb038	IMG_0799	240	1842	666	417	214443	221506	0.79	0.94	0.97
MC-2010-Yb039	IMG_0713	99	1644	540	430	166748	173294	0.77	0.93	0.96
MC-2010-Yc009	IMG_0724	1310	3622	1146	1034	909048	920700	0.87	0.95	0.99
MC-2010-Yc010	IMG_0721	242	1875	643	488	243632	248054	0.87	0.95	0.98
MC-2010-Yc012	IMG_0719	688	2803	948	778	577082	581625	0.92	0.97	0.99
MC-2010-Yc014	IMG_0721	741	3224	1231	729	700777	706341	0.85	0.97	0.99
MC-2010-Yc015	IMG_0725	1170	3787	1288	964	923307	939354	0.81	0.94	0.98
MC-2010-Yc016	IMG_0725	1234	3413	1195	833	750321	774904	0.81	0.94	0.97
MC-2010-Yc017	IMG_0727	390	2107	710	515	274368	280958	0.78	0.92	0.98
MC-2010-Yc018	IMG_0719	465	2744	968	634	458790	465368	0.77	0.93	0.99
MC-2010-Yc019	IMG_0720	647	3140	1082	818	688952	696828	0.88	0.96	0.99
MC-2010-Yc020	IMG_0727	756	3463	1270	728	675120	709269	0.71	0.92	0.95
MC-2010-Yc022	IMG_0724	588	2774	946	716	510243	522896	0.83	0.95	0.98
MC-2010-Yc023	IMG_0724	197	1820	620	464	217788	222230	0.83	0.94	0.98
MC-2010-Yc024	IMG_0728	296	2146	720	548	304448	313726	0.83	0.93	0.97
MC-2010-Yc026	IMG_0719	405	2827	1043	551	408150	441619	0.64	0.91	0.92
MC-2010-Yc027	IMG_0722	669	2769	867	792	526868	537728	0.86	0.94	0.98
MC-2010-Yc028	IMG_0728	291	2452	807	615	375591	389306	0.78	0.92	0.96
MC-2010-Yc029	IMG_0728	971	3767	1218	907	782617	898472	0.69	0.89	0.87
MC-2010-Yc031	IMG_0729	2855	3884	1328	1023	1022285	1036524	0.85	0.95	0.99
MC-2010-Yc032	IMG_0730	2588	3975	1474	905	1024809	1042394	0.81	0.95	0.98

Sample #	Image (.jpg)	Volume (Wet-Dry) (cm^3)	Perimeter (pixels)	Long Axis (pixels)	Short Axis (pixels)	Area (pixels)	Convex Hull Area (pixels)	Circularity C	Ellipticity E	Convexity C_{vx}
MC-2010-Yc033	IMG_0731	863	3102	1016	812	602118	626248	0.79	0.93	0.96
MC-2010-Yc034	IMG_0730	2152	4026	1569	796	958844	990866	0.74	0.95	0.97
MC-2010-Yc035	IMG_0731	1388	3048	1084	705	578564	590910	0.78	0.93	0.98
MC-2010-Yc036	IMG_0731	976	2537	922	613	437882	448218	0.85	0.96	0.98
MC-2010-Yc037	IMG_0732	2402	3703	1216	983	913997	932868	0.84	0.94	0.98
MC-2010-Yc039	IMG_0746	6274	5366	2004	1129	1737134	1821048	0.76	0.94	0.95
MC-2010-Yc040	IMG_0739	19900	6248	2049	1728	2724115	2768878	0.88	0.95	0.98
MC-2011-IS02	IMG_0708	61	1347	409	398	125286	129103	0.87	0.94	0.97
MC-2011-IS03A	IMG_0751	2992	4920	1845	1038	1476458	1528573	0.77	0.94	0.97
MC-2011-IS03B	IMG_0799	112	2167	751	403	195649	210679	0.52	0.86	0.93
MC-2011-IS05	IMG_0708	83	1589	557	383	165456	171041	0.82	0.94	0.97
MC-2011-IS06	IMG_0708	74	1497	478	413	147681	151478	0.83	0.94	0.97
MC-2011-IS08	IMG_0708	346	2644	1027	539	427680	436186	0.77	0.95	0.98
MC-2011-IS10	IMG_0709	757	2916	974	818	613033	617780	0.91	0.97	0.99
MC-2011-IS11	IMG_0709	204	1778	594	486	224468	228394	0.89	0.96	0.98
MC-2011-IS12	IMG_0709	112	1383	503	350	137626	138937	0.90	0.98	0.99
							Mean:	**0.81**	**0.94**	**0.97**
							1σ:	**0.08**	**0.02**	**0.02**
							Max.:	**0.92**	**0.98**	**0.99**
							Min.:	**0.52**	**0.86**	**0.87**

Dacite Accessory Lithic Clasts: Main Sample Set

Sample #	Image (.jpg)	Volume (Wet-Dry) (cm^3)	Perimeter (pixels)	Long Axis (pixels)	Short Axis (pixels)	Area (pixels)	Convex Hull Area (pixels)	Circularity C	Ellipticity E	Convexity C_{vx}
MC-2010-PP01	IMG_0701	324	2544	729	671	370857	393632	0.72	0.87	0.94
MC-2010-PP02	IMG_0699	40	1174	363	310	87417	91068	0.80	0.90	0.96
MC-2010-PP03	IMG_0699	184	1743	549	475	202589	209182	0.84	0.92	0.97
MC-2010-PP04	IMG_0699	115	1516	469	422	149901	155399	0.82	0.92	0.96
MC-2010-PP05	IMG_0701	325	2409	748	618	352143	369252	0.76	0.89	0.95
MC-2010-PP06	IMG_0699	44	1245	381	328	90331	94904	0.73	0.90	0.95
MC-2010-PP07	IMG_0699	72	1576	535	399	166200	170546	0.84	0.94	0.97
MC-2010-PP08	IMG_0701	369	2680	888	667	461142	475144	0.81	0.92	0.97
MC-2010-PP09	IMG_0699	62	1585	498	416	161312	167595	0.81	0.91	0.96
MC-2010-PP10	IMG_0704	1940	3801	1230	888	819042	851939	0.71	0.88	0.96
MC-2010-PP11	IMG_0701	267	2563	839	615	391388	409780	0.75	0.90	0.96
MC-2010-PP12	IMG_0699	29	1038	370	238	68372	70893	0.80	0.93	0.96
MC-2010-PP13	IMG_0699	47	1277	423	302	97417	102119	0.75	0.90	0.95

Sample #	Image (.jpg)	Volume (Wet-Dry) (cm^3)	Perimeter (pixels)	Long Axis (pixels)	Short Axis (pixels)	Area (pixels)	Convex Hull Area (pixels)	Circularity C	Ellipticity E	Convexity C$_{vx}$
MC-2010-PP14	IMG_0704	1131	3216	954	884	652646	673179	0.79	0.90	0.97
MC-2011-P01	IMG_0705	1335	3496	1116	870	750391	786606	0.77	0.90	0.95
MC-2011-P02	IMG_0698	228	2339	876	478	319366	339821	0.73	0.93	0.94
MC-2011-P03	IMG_0702	914	3853	1310	899	906571	933302	0.77	0.91	0.97
MC-2011-P04	IMG_0702	447	2916	888	799	541085	557040	0.80	0.91	0.97
MC-2011-P05	IMG_0705	1979	4177	1498	925	1033989	1069066	0.74	0.92	0.97
MC-2011-P06	IMG_0698	194	1947	645	493	246458	253265	0.82	0.92	0.97
MC-2011-P07	IMG_0698	255	2614	796	684	419737	441177	0.77	0.89	0.95
MC-2011-P08	IMG_0698	324	2912	861	772	503307	528190	0.75	0.88	0.95
MC-2011-P09	IMG_0695	71	1566	483	392	146577	153947	0.75	0.88	0.95
MC-2011-P10	IMG_0698	164	2110	754	428	248327	264557	0.70	0.90	0.94
MC-2011-P11	IMG_0695	73	1493	470	375	135451	142236	0.76	0.89	0.95
MC-2011-P12	IMG_0702	188	1997	619	543	261526	270420	0.82	0.92	0.97
MC-2011-P13	IMG_0706	1365	3396	1013	937	731871	764313	0.80	0.90	0.96
MC-2011-P14	IMG_0702	259	2125	627	601	293357	302884	0.82	0.91	0.97
MC-2011-P15	IMG_0695	40	1331	427	337	111020	115779	0.78	0.90	0.96
MC-2011-P16	IMG_0695	40	1414	463	359	128414	134953	0.81	0.92	0.95
MC-2011-P17	IMG_0706	1511	3968	1282	1020	1007601	1056247	0.80	0.91	0.95
MC-2011-P18	IMG_0695	81	1567	523	386	151084	159001	0.77	0.92	0.95
MC-2011-P19	IMG_0695	85	1633	497	420	161071	167517	0.76	0.88	0.96
MC-2011-P20	IMG_0695	45	1272	427	341	112093	114685	0.87	0.95	0.98
MC-2012-PL01	IMG_0800	11577	6224	1960	1587	2361205	2451791	0.77	0.90	0.96
MC-2012-PL02	IMG_0801	5079	4209	1329	1077	1089388	1124363	0.77	0.90	0.97
MC-2012-PL03	IMG_0801	3575	4187	1356	1003	1033569	1096609	0.74	0.89	0.94
MC-2012-PL04	IMG_0802	1869	2912	925	762	544494	558805	0.81	0.91	0.97
MC-2012-PL06	IMG_0802	2610	3253	1140	739	635872	666801	0.76	0.92	0.95
							Mean:	0.78	0.91	0.96
							1σ:	0.04	0.02	0.01
							Max.:	0.87	0.95	0.98
							Min.:	0.70	0.87	0.94

194

Table E3-2. Image analysis data for supplementary small volume monzogranite and dacite accessory lithic clast sample set.

Sample #	Image (.jpg)	Volume (Wet-Dry) (cm³)	Perimeter (pixels)	Long Axis (pixels)	Short Axis (pixels)	Area (pixels)	Convex Hull Area (pixels)	Circularity C	Ellipticity E	Convexity C_{vx}
Intact Monzogranite Accessory Lithic Clasts: Supplementary Small Volume Sample Set										
1-1-M2	P1060582	9.9	1078	339	317	83775	85354	0.91	0.96	0.98
1-1-M3	P1060582	5.1	955	295	262	57426	61037	0.79	0.92	0.94
1-1-M4	P1060582	5.8	899	286	264	58560	59634	0.91	0.96	0.98
1-1-M5	P1060582	3.0	727	242	200	37752	38789	0.90	0.96	0.97
1-1-M7	P1060582	0.6	484	158	134	16402	17042	0.88	0.95	0.96
1-2-M1	P1060583	8.7	1429	458	409	145781	148257	0.90	0.95	0.98
1-2-M2	P1060583	4.9	1203	390	327	99335	102395	0.86	0.94	0.97
1-5-M04	P1060581	13.7	1231	421	330	108238	110120	0.90	0.96	0.98
1-5-M06	P1060581	8.1	1081	352	276	75482	78517	0.81	0.92	0.96
1-5-M09	P1060581	3.1	757	243	216	40756	41931	0.89	0.95	0.97
1-5-M12	P1060581	1.9	663	221	167	28254	29596	0.81	0.92	0.95
1-5-M13	P1060581	1.8	625	195	187	27827	28555	0.90	0.96	0.97
1-5-M14	P1060581	1.7	617	218	152	25609	26369	0.85	0.95	0.97
1-5-M15	P1060579	1.6	593	189	173	25476	26268	0.91	0.96	0.97
1-5-M17	P1060579	1.4	600	188	168	23672	24982	0.83	0.93	0.95
1-5-M18	P1060579	0.9	518	165	138	17643	18506	0.83	0.92	0.95
1-5-M19	P1060579	0.9	479	151	144	16755	17295	0.92	0.97	0.97
1-5-M22	P1060579	0.6	416	136	115	12010	12390	0.87	0.95	0.97
1-5-M25	P1060579	0.6	457	149	129	14972	15471	0.90	0.96	0.97
1-5-M26	P1060579	0.5	419	134	117	11945	12527	0.86	0.94	0.95
1-5-M29	P1060579	0.4	395	134	108	11227	11552	0.90	0.97	0.97
1-5-M30	P1060579	0.4	376	118	113	10337	10661	0.92	0.96	0.97
1-5-M33	P1060579	0.3	349	125	91	8793	9072	0.90	0.97	0.97
1-5-M34	P1060579	0.4	369	131	98	10006	10359	0.92	0.98	0.97
1-5-M35	P1060579	0.4	382	124	106	10249	10702	0.88	0.95	0.96
1-5-M36	P1060579	0.3	332	114	93	8252	8474	0.94	0.98	0.97
1-5-M37	P1060579	0.1	280	103	66	5099	5395	0.82	0.96	0.95
							Mean:	0.88	0.95	0.95
							1σ:	0.04	0.02	0.02
							Max.:	0.94	0.98	0.98
							Min.:	0.79	0.92	0.92

Sample #	Image (.jpg)	Volume (Wet-Dry) (cm^3)	Perimeter (pixels)	Long Axis (pixels)	Short Axis (pixels)	Area (pixels)	Convex Hull Area (pixels)	Circularity C	Ellipticity E	Convexity C$_{vx}$
Broken Monzogranite Accessory Lithic Clasts: Supplementary Small Volume Sample Set										
1-1-M1	P1060582	20.3	1590	538	373	151397	158044	0.75	0.91	0.96
1-1-M6	P1060582	2.1	738	239	187	34308	36692	0.79	0.91	0.94
1-1-M8	P1060582	0.4	412	141	112	12036	12425	0.89	0.97	0.97
1-1-M9	P1060582	0.1	301	107	72	5851	6266	0.81	0.94	0.93
1-2-M3	P1060583	3.1	1058	388	239	71187	73404	0.80	0.94	0.97
1-2-M4	P1060583	2.8	996	322	275	67234	69625	0.85	0.94	0.97
1-5-M01	P1060581	17.3	1444	506	356	140501	144193	0.85	0.94	0.97
1-5-M02	P1060581	19.4	1483	493	378	142258	147564	0.81	0.93	0.96
1-5-M03	P1060581	17.8	1435	447	426	149232	151702	0.91	0.96	0.98
1-5-M05	P1060581	7.2	1198	392	330	100907	103769	0.88	0.95	0.97
1-5-M07	P1060581	3.9	811	274	217	45715	46827	0.87	0.95	0.98
1-5-M08	P1060581	3.5	777	252	222	43760	44677	0.91	0.96	0.98
1-5-M10	P1060581	2.6	753	249	174	31675	34720	0.85	0.89	0.91
1-5-M11	P1060581	2.3	815	268	217	44817	46722	0.81	0.94	0.96
1-5-M16	P1060579	1.0	556	206	125	19841	20435	0.81	0.95	0.97
1-5-M20	P1060579	0.8	502	172	121	15896	16922	0.79	0.93	0.94
1-5-M21	P1060579	0.7	470	164	125	15922	16307	0.91	0.97	0.98
1-5-M23	P1060579	0.7	436	152	115	13717	14150	0.91	0.97	0.97
1-5-M24	P1060579	0.6	453	133	124	12454	13636	0.76	0.89	0.91
1-5-M27	P1060579	0.6	469	143	134	14460	15289	0.83	0.93	0.95
1-5-M28	P1060579	0.4	387	122	112	10515	10949	0.88	0.95	0.96
1-5-M31	P1060579	0.4	372	132	95	9561	9862	0.87	0.96	0.97
1-5-M32	P1060579	0.3	428	147	96	10745	11728	0.74	0.90	0.92
1-5-M38	P1060579	0.1	220	73	60	3314	3581	0.86	0.95	0.93
							Mean:	0.84	0.94	0.96
							1σ:	0.05	0.02	0.02
							Max.:	0.91	0.97	0.98
							Min.:	0.74	0.89	0.91

Sample #	Image (.jpg)	Volume (Wet-Dry) (cm^3)	Perimeter (pixels)	Long Axis (pixels)	Short Axis (pixels)	Area (pixels)	Convex Hull Area (pixels)	Circularity C	Ellipticity E	Convexity C$_{vx}$
Dacite Accessory Lithic Clasts: Supplementary Small Volume Sample Set										
1-1-P1	P1060584	14.1	1418	503	333	129430	133690	0.81	0.94	0.97
1-1-P2	P1060584	13.9	1555	490	400	152273	159220	0.79	0.90	0.96
1-1-P3	P1060584	9.0	1213	378	345	101758	105103	0.87	0.94	0.97
1-1-P4	P1060584	6.4	1078	343	295	78666	81777	0.85	0.93	0.96
1-1-P5	P1060584	3.0	910	345	192	51457	53550	0.77	0.95	0.96
1-1-P6	P1060584	1.5	683	250	158	30238	31573	0.81	0.95	0.96
1-1-P7	P1060584	1.6	709	252	159	30823	32793	0.77	0.92	0.94
1-1-P8	P1060584	1.0	581	191	148	21466	22956	0.80	0.92	0.94
1-1-P9	P1060584	0.6	481	174	110	14760	15669	0.80	0.94	0.94
1-1-P10	P1060584	0.6	439	139	133	14419	14754	0.94	0.97	0.98
1-1-P11	P1060584	0.3	382	124	110	10479	10848	0.90	0.96	0.97
1-1-P12	P1060584	0.3	359	120	95	8838	9209	0.86	0.94	0.96
1-2-P1	P1060586	123.3	2951	963	679	499835	528088	0.72	0.88	0.95
1-2-P2	P1060586	31.8	1777	577	451	203029	210721	0.81	0.91	0.96
1-2-P3	P1060586	12.6	1396	455	328	114683	121301	0.74	0.89	0.95
1-2-P4	P1060586	4.1	820	278	216	46225	47556	0.86	0.95	0.97
1-2-P5	P1060586	3.4	800	238	232	41798	43538	0.82	0.92	0.96
1-2-P6	P1060586	1.5	631	227	146	25467	26741	0.80	0.94	0.95
1-5-P1	P1060587	55.5	1799	558	479	208329	217701	0.81	0.91	0.96
1-5-P2	P1060587	33.1	1526	464	430	155477	162008	0.84	0.92	0.96
1-5-P3	P1060587	25.9	1380	466	335	120671	125212	0.80	0.92	0.96
1-5-P4	P1060587	17.9	1294	408	339	101538	109717	0.76	0.91	0.93
1-5-P5	P1060587	9.7	1019	352	251	68047	71053	0.82	0.94	0.96
1-5-P6	P1060587	4.5	712	227	190	33415	35073	0.83	0.92	0.95
1-5-P7	P1060587	3.6	716	248	161	30092	32362	0.74	0.91	0.93
1-5-P8	P1060587	3.5	697	217	191	31767	33331	0.82	0.92	0.95
1-5-P9	P1060587	2.0	626	237	124	22161	23388	0.71	0.93	0.95
1-5-P10	P1060587	1.9	576	207	138	21992	23038	0.83	0.95	0.95
1-5-P11	P1060587	1.8	557	202	128	19942	21028	0.81	0.94	0.95
1-5-P12	P1060587	1.2	457	145	127	14162	14968	0.85	0.93	0.95
1-5-P13	P1060587	1.3	457	156	115	13886	14429	0.84	0.94	0.96
1-5-P14	P1060587	0.8	418	144	107	11967	12574	0.86	0.95	0.95
1-5-P15	P1060587	1.1	452	150	126	14819	15367	0.91	0.96	0.96
1-5-P16	P1060587	1.1	480	155	129	15328	16278	0.84	0.93	0.94
1-5-P17	P1060587	0.6	365	131	89	8841	9397	0.83	0.96	0.94
1-5-P18	P1060587	0.6	356	112	101	8597	9037	0.85	0.94	0.95

Sample #	Image (.jpg)	Volume (Wet-Dry) (cm^3)	Perimeter (pixels)	Long Axis (pixels)	Short Axis (pixels)	Area (pixels)	Convex Hull Area (pixels)	Circularity C	Ellipticity E	Convexity C_{vx}
1-5-P19	P1060587	0.5	365	120	100	9317	9779	0.88	0.95	0.95
1-5-P20	P1060587	0.5	314	105	85	6935	7176	0.89	0.95	0.97
1-5-P21	P1060587	0.4	329	113	86	7457	7810	0.87	0.95	0.95
1-5-P22	P1060587	0.3	274	99	72	5571	5778	0.93	0.98	0.96
1-5-P23	P1060587	0.3	266	87	79	5252	5526	0.93	0.98	0.95
1-5-P24	P1060587	0.2	270	103	60	4771	5029	0.82	0.96	0.95
							Mean:	0.83	0.94	0.95
							1σ:	0.05	0.02	0.01
							Max.:	0.94	0.98	0.98
							Min.:	0.71	0.88	0.93

Appendix F: Discussion of Whole Rock 3-D Scan Modes and Resolutions

Conducting 3-D scans with the NextEngine^{TM} Scanner requires the selection of a scanning mode: 'Macro' mode is suitable for smaller objects, measuring up to 7.6 cm wide and up to 12.7 cm long (approximately < 900 cm^3), while 'Wide' mode is suitable for larger objects, measuring up to 25.4 cm wide and up to 33 cm long. After selection of the scanning mode, one of the preset scanning resolutions must be selected, which will determine the overall number of data points in the produced point clouds as well as control what size surface features will be resolvable on the final scan. Scanning at higher resolutions produces highly detailed surface scans, but requires longer scan times and greater computing power, and can produce unmanageably large data point files. The use of Macro mode allows objects to be scanned at higher resolutions than are possible with Wide mode.

In order to determine which resolution setting to use for the smaller samples, scans were made of two monzogranite accessory lithic samples at seven different resolutions using the Macro mode: 1700; 2500; 4000; 10,000; 16,000; 28,400; and 64,500 points/cm^2. It should be noted that it is possible to scan samples at three higher resolutions in Macro mode (114,000, 258,000 and 1,032,000 points/cm^2), but that the computer set-up we used was not able to process the highly populated point clouds produced at these resolutions. The surface areas of the scans made at the various resolutions were computed using the NextEngine^{TM} ScanStudio software. Figures F-1a and F-1c display the variation in measured surface area with increasing scan resolution for each of the two monzogranite samples. Surface area will always tend to increase with increasing scan resolution; as resolution increases, the number of tiny pits and bumps being recorded increases, at an increasingly finer scale. The computed volumes of the fused scans, obtained in Matlab®, are shown in Figures F-1b and F-1d, plotted against the scan resolution. The wet-dry volumes of the two samples are also included on Figures F-1b and F-1d for reference. Because the laser of the NextEngine^{TM} 3-D scanner cannot probe the depths of any deep pits or cracks on a clast's surface, the 3-D scans produced tend to slightly overestimate the volume of the sample. The surface area results (Figures F-1a, F-1c) and Matlab® computed volume results (Figures Appendix F-b, Appendix F-d) of these trial resolution scans indicate that the data produced for sample scans does not improve considerably above a resolution of 28,400 points/cm^2. Consequently, I have decided to select a scan resolution of 28,400 points/cm^2 for all samples scanned using Macro mode.

The use of Wide mode to produce 3-D scans requires a considerably greater amount of computing power, and therefore scans must be produced at lower resolutions. The highest scan resolution possible in Wide mode, using our computer workstation, is 7,100 points/cm^2: this is the resolution that I will use for samples scanned in Wide mode.
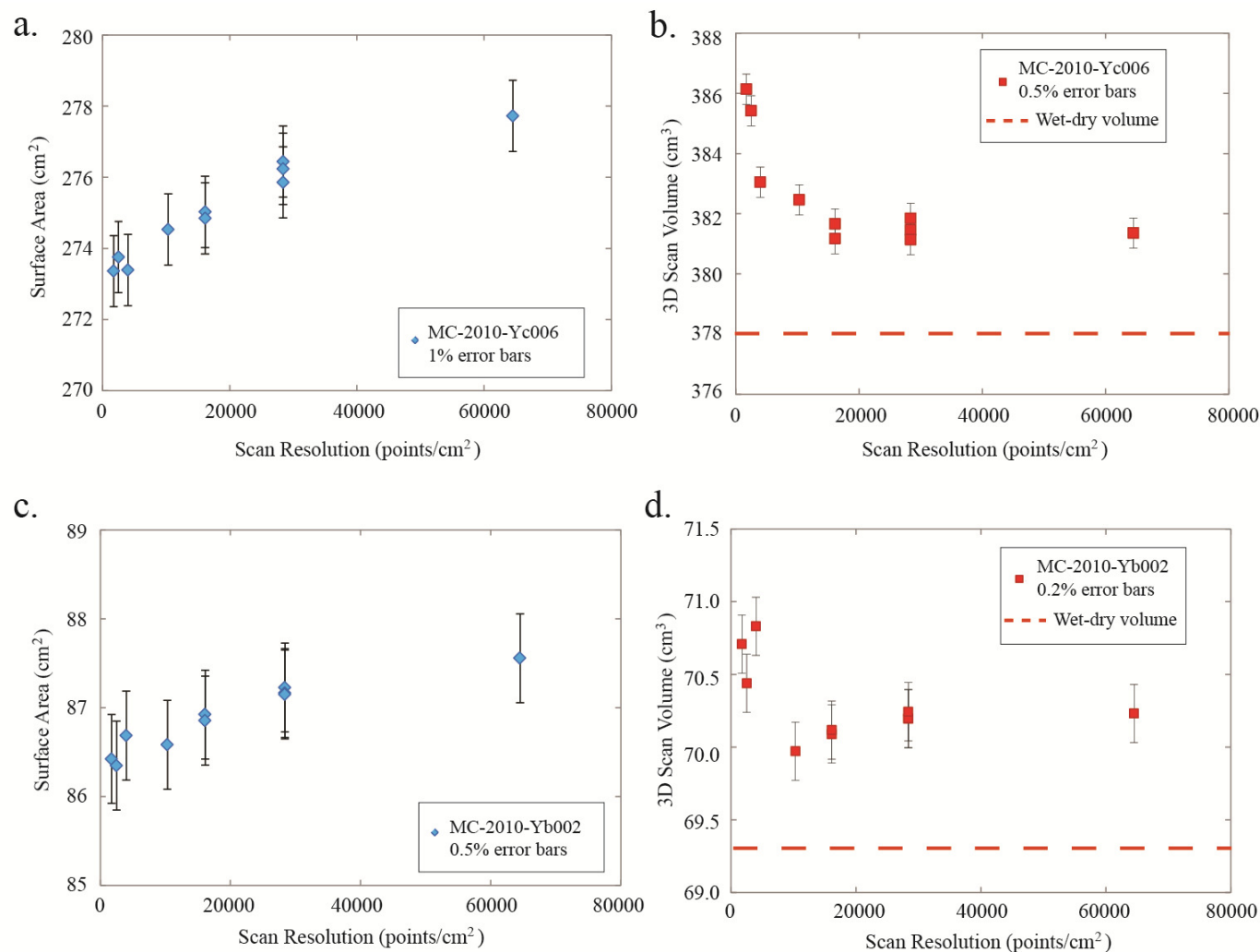
Figure F-1. Resolution test 3-D scans of whole rock samples. a) Surface area results at various resolutions for sample MC-2010-Yc006. b) Volume results for sample MC-2010-Yc006, showing the volume measured using the wet-dry technique for comparison. c) Surface area results at various resolutions for sample MC-2010-Yb002. b) Volume results for sample MC-2010-Yb002, showing the volume measured using the wet-dry technique for comparison.

Appendix G: Maximum Surface Smoothness Data

Table G-1. Maximum Surface Smoothness data for select monzogranite and dacite clasts.

Sample #	Volume (cm^3)	Approximate Scanned Region Size (mm x mm)	Planar Projected Area of Scanned Region (A_{proj}; cm^2)	Measured Area of Scanned Region (A_{meas}; cm^2)	Maximum Surface Smoothness (S_{max})
Monzogranite Accessory Lithic Samples					
MC-2010-Yb024	15	15 x 15	2.342	2.394	0.98
MC-2010-Yb035	23	15 x 15	2.223	2.490	0.89
MC-2011-IS04	35	15 x 15	2.207	2.361	0.93
MC-2010-Yb002	69	15 x 15	2.381	2.418	0.98
MC-2011-IS07	104	20 x 20	3.937	4.167	0.94
MC-2010-Yd007	141	20 x 20	4.084	4.473	0.91
MC-2010-Yb004	161	20 x 20	4.125	4.201	0.98
MC-2010-Yb009	263	30 x 30	9.066	9.344	0.97
MC-2010-Yd005	363	30 x 30	9.280	9.718	0.95
MC-2010-Ya010	377	30 x 30	8.950	9.090	0.98
MC-2010-Yc007	581	30 x 30	9.271	9.499	0.98
MC-2010-Ya004	675	40 x 40	16.265	16.678	0.98
MC-2011-Yd010	886	40 x 40	16.288	16.639	0.98
MC-2010-Yc008	1099	40 x 40	16.184	16.570	0.98
MC-2011-IS09	1418	40 x 40	16.170	16.630	0.97
MC-2012-Yd004	1940	40 x 40	16.183	16.514	0.98
MC-2012-Yd002	2596	40 x 40	15.990	16.380	0.98
MC-2010-Yc030	3206	40 x 40	16.088	16.627	0.97
MC-2010-Ya002	6769	40 x 40	16.281	16.599	0.98
MC-2012-Yd013	12307	40 x 40	15.950	16.356	0.98

Sample #	Volume (cm^3)	Approximate Scanned Region Size (mm x mm)	Planar Projected Area of Scanned Region (A$_{proj}$; cm^2)	Measured Area of Scanned Region (A$_{meas}$; cm^2)	Maximum Surface Smoothness (S$_{max}$)
Dacite Accessory Lithic Samples					
MC-2010-PP12	29	15 x 15	2.454	2.894	0.85
MC-2011-P16	40	15 x 15	2.425	2.690	0.90
MC-2010-PP07	72	20 x 20	4.188	5.014	0.84
MC-2010-PP03	185	20 x 20	4.082	4.590	0.89
MC-2011-P07	255	30 x 30	9.107	10.458	0.87
MC-2011-P08	324	30 x 30	9.192	11.095	0.83
MC-2011-P04	447	30 x 30	9.009	10.472	0.86
MC-2011-P03	914	40 x 40	15.840	17.670	0.90
MC-2010-PP14	1131	40 x 40	15.939	18.868	0.84
MC-2011-P01	1335	40 x 40	16.224	20.007	0.81
MC-2011-P13	1365	40 x 40	16.237	18.095	0.90
MC-2011-P17	1511	40 x 40	16.145	17.926	0.90
MC-2011-P05	1979	40 x 40	16.117	18.548	0.87
MC-2012-PL06	2610	40 x 40	15.877	18.777	0.85
MC-2012-PL03	3575	40 x 40	16.168	18.379	0.88
MC-2012-PL02	5079	40 x 40	16.356	18.426	0.89
MC-2012-PL01	11577	40 x 40	16.137	19.307	0.84